SEGREGATION AND REACTIVITY IN BI-CATIONIC OXIDE CATALYSTS

Pip Hellier

A thesis submitted for the degree of Doctor of Philosophy

June 2019

Declaration

This thesis is the result of my own independent work, except where otherwise stated, and the views expressed are my own. Other sources are acknowledged by explicit references. The thesis has not been edited by a third party beyond what is permitted by Cardiff University's Use of Third Party Editors by Research Degree Students Procedure.

Signed: (candidate) Date:

Statement 1

This thesis is being submitted in partial fulfilment of the requirements for the degree of Doctor of Philosophy.

Signed: (candidate) Date:

Statement 2

This work has not been submitted in substance for any other degree or award at this or any other university or place of learning, nor is it being submitted concurrently for any other degree or award (outside of any formal collaboration agreement between the University and a partner organisation).

Signed: (candidate) Date:

Statement 3

I hereby give consent for my thesis, if accepted, to be available in the University's Open Access repository (or, where approved, to be available in the University's library and for inter-library loan), and for the title and summary to be made available to outside organisations, subject to the expiry of a University-approved bar on access if applicable.

Signed: (candidate) Date:

Word count: 68545 (Excluding summary, acknowledgements, declarations, contents pages, appendices, tables, diagrams and figures, references, bibliography, footnotes and endnotes)

Abstract

The influence of segregation on shell-core selective oxidation catalysts has been investigated in this thesis in three main areas. Novel shell-core catalysts, namely VO_x/Fe_2O_3 catalysts, are selective to formaldehyde during reaction with methanol, indicating that the core Fe_2O_3 is sufficiently segregated, while VO_x remains at the surface. Significant structural understanding has been gained, suggesting VO_4 tetrahedra constitute the active site at the surface. With the soundness of the shell-core model further confirmed by VO_x/Fe_2O_3, other reactions of interest can be investigated with shell-core catalysts.

While VO_x and MoO_x/Fe_2O_3 function well as shell-core catalysts, benefitting from greater surface area and amenability to analysis, NbO_x/Fe_2O_3 catalysts are unable to achieve the necessary segregation during calcination, resulting in exposed Fe_2O_3 at the surface, worsening their selectivity. This is attributed to the notably higher Tamman temperature of NbO_x which is never reached during calcination, preventing the spreading of the NbO_x across the Fe_2O_3 required for shell-core formation.

The properties of Al dopants in Fe_2O_3 cores have also been examined. The addition of up to 20 wt% Al in Fe_2O_3 can increase surface area fourfold, enhancing catalytic activity in turn; however, detrimental effects on catalyst selectivity are seen for higher Al loadings, indicating a degree of structural disruption. It is now known that Al can only occupy sites in the Fe_2O_3 structure at low Al loadings, above which the impetus to phase separate increases.

Magnetocatalysis has also been investigated using shell-core catalysts based on zinc-doped cobalt ferrite. Clear evidence of selectivity manipulation by applying an external field during reaction has been obtained. Additionally, strong indications of internal magnetocatalytic effects have been observed, which are those effects on selectivity caused by magnetisation changes in the ferrite support.

Overall, these studies have further emphasised the importance of multicomponent catalysts, and the need to carefully control catalyst speciation.

Acknowledgements

This thesis has been possible only with the assistance of many people. First and foremost, I would like to thank my supervisor, Prof. Mike Bowker, for the opportunity to undertake this doctoral project and his continued guidance and wisdom throughout. In addition, I thank him for all the amusement—intentional or otherwise—resulting from the occasional senior moment. I also thank my co-supervisor Dr Peter Wells for his advice and assistance along the way, and for the many stimulating discussions on tea, horticulture and the merits of Hampshire, to name but a few topics. I thank Dr Diego Gianolio for his assistance with all matters XAS throughout the entire project; he is the embodiment of the helpful, friendly beamline scientist.

I would also like to thank Prof. Michael Claeys for his assistance in organising and supporting my exchange placement at the University of Cape Town; I am wholly grateful to have lived and worked for a short time in the wonderful place that is Cape Town. I express great thanks to my counterpart student at UCT, Adli Peck; it was a delight to work with you, first at Harwell and then subsequently back on your home turf. I commend your resilience in the face of adversity; while my exposure to the foibles of the magnetometer was limited by the duration of my stay, you were granted no such respite. My thanks also go to the other students of the Claeys group, who all helped make my time in Cape Town so enjoyable.

For the friendly and entertaining atmosphere over the last three years, I express my gratitude to my lab colleagues, fellow PhD students and postdocs. In particular, I wish to convey special thanks to Rachel Blackmore, who, in spite of exhausting illness, provided sterling assistance during my beamtime at the ESRF in December 2017, and helped make it a success despite the myriad difficulties encountered. In addition, as the fellow resident of the small (and clearly superior) office, special thanks goes to Emma Campbell, for livening up the place with her characteristic Welsh cheer and geniality.

Nothing happens in science without funding support, and this thesis has been no exception. I thank Diamond Light Source for contributing to the funding of this doctoral project and the financing of conference travel, and additionally I thank the Newton Fund for supporting the exchange with UCT.

Most importantly of all, I express my strongest thanks to Beatrice Tyrrell, who has kept me constantly amused and happy over the past three years. Finally, for all your fluffy cuddles and entertaining antics throughout this project and particularly during the writing of this thesis, thank you Mittens.

List of Acronyms

AFM Atomic Force Microscopy

AHM Ammonium heptamolybdate

ATR Attenuated Total Reflectance

BET Brunauer-Emmett-Teller (theory)

CCD Charge-coupled Device

DME Dimethyl ether

DMFC Direct Methanol Fuel Cell

DMM Dimethoxymethane

DOS Density of States

DRIFTS Diffuse Reflectance Infrared Fourier Transform Spectroscopy

EDX Energy Dispersive X-ray Spectroscopy

EELS Electron Energy Loss Spectroscopy

ESCA Electron Spectroscopy for Chemical Analysis

EXAFS Extended X-ray Absorption Fine Structure

FTIR Fourier Transform Infrared

FWHM Full Width at Half Maximum

GTL Gas-to-liquids

HAADF High-angle annular dark-field

HR(S)TEM High Resolution (Scanning) Transmission Electron Microscopy

HSA High Surface Area

HTF Heat Transfer Fluid

IR Infrared

IUPAC International Union of Pure and Applied Chemistry

LCF Linear Combination Fitting

LEIS Low-Energy Ion Scattering

LPM Low Pressure Methanol

MFC Mass Flow Controller

MID Multiple Ion Detection

ML Monolayer(s)

MS Mass Spectrometry

MTBE Methyl *tert*-butyl ether

MTG Methanol-to-gasoline

MTH Methanol-to-hydrocarbons

MTO Methanol-to-olefins

MVK Mars-van Krevelen (mechanism)

NMR Nuclear Magnetic Resonance

PCS Pulse Chemisorption System

PFR Pulsed Flow Reaction

PID Proportional-integral-derivative

SEM Secondary Electron Multiplier

STEM Scanning Transmission Electron Microscopy

STM Scanning Tunnelling Microscopy

TEM Transmission Electron Microscopy

TEY Total Electron Yield

TOF Turnover frequency

TPD Temperature Programmed Desorption

UCT University of Cape Town

UV-Vis Ultraviolet-Visible

WAXS Wide Angle X-ray Scattering

XANES X-ray Absorption Near Edge Structure

XAS X-ray Absorption Spectroscopy

XPS X-ray Photoelectron Spectroscopy

XRD X-ray Diffraction

x ZnCoFe $Zn_xCo_{1-x}Fe_2O_4$

Contents

List of Figures

List of Tables

Chapter 1

Introduction

1.1 Catalysis

1.1.1 A brief explanation and history

Catalysis is the process by which the rate of a chemical reaction may be increased through the addition of a catalyst. Importantly, a catalyst does not alter the overall energy change between reactants and products.[1] Rather, rate increases are made possible by the provision of an alternative, less energetically demanding reaction pathway (Figure 1.1). This pathway proceeds *via* transition states and intermediates stabilised by the participation of the catalyst, reducing the activation energy of the reaction. Catalysts are regenerated during the reaction, and can repeatedly catalyse the same reaction: consequently, very little catalyst is required to achieve significant increases in overall reaction rate. In general, catalysts display specificity towards certain reactions, with catalysts tuned by experiment to achieve maximum efficacy. Importantly, catalysts are not just found in the chemical laboratory; many biological systems rely on enzymes (macromolecular biological catalysts) to function properly. The possibility of applying enzymes as catalysts for organic synthesis has been of interest in recent years, and several novel synthetic pathways in organic chemistry have been discovered which utilise these biological catalysts.[2] Laboratory use of enzymes to yield complex synthetic products is a modern accomplishment, but humans have been utilising biological catalysts for fermentation for millennia.[3]

Chemists have experimented with the phenomenon known now as catalysis for hundreds of years. In 1552, the German physician Valerius Cordus made reference to an early example of deliberate catalysis, in which he utilised sulphuric acid to synthesise diethyl ether from ethanol, while the English chemist Elizabeth Fulhame posited in 1794 that water was necessary to oxidise CO.[4,5] Later scientists, such as Davy and Faraday, explored

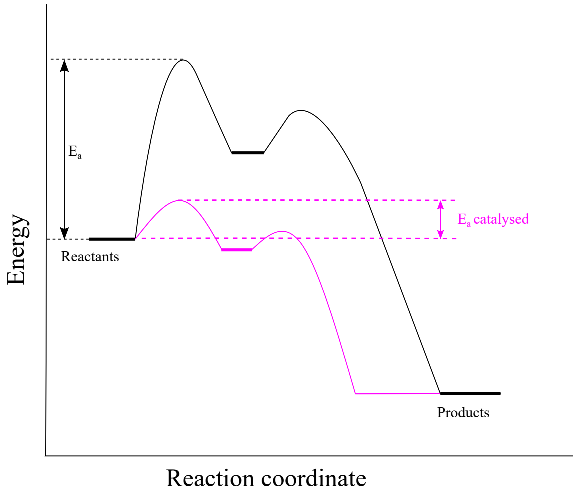

Figure 1.1: An example potential energy profile of an exothermic reaction. The uncatalysed reaction profile is shown in black, with the catalysed profile shown in pink. The thermodynamics of the overall reaction remain unchanged.

the phenomenon further and contributed to the growing evidence of the effects of catalysis.[6,7] In 1835, the Swedish scientist Berzelius studied, among other reactions, the effects of sulphuric acid on ethanol and the production of sugar from starch and noticed the similar behaviour: it was he who first used the word *catalysis* to describe this behaviour.[8] The term itself derives from the Ancient Greek καταλυω, meaning "I loosen" or "I unbind", representing the role of the catalyst as a facilitator of reactions. Rapid progress was made thereafter, such that by 1877 Lemoine had demonstrated that while the addition of a catalyst to a reaction could hasten the rate at which equilibrium is achieved, the position of equilibrium is not disturbed.[9] The discoveries made during the latter half of the 19th century heralded the birth in the early 20th century of large-scale chemical industries reliant upon catalysts to produce valuable chemicals.

An early industrial use for catalysts was in the contact process, used to manufacture sulphuric acid. The original system devised in 1831 consisted of a Pt catalyst and was a marked improvement on the prior lead chamber method;[10] however, catalyst poisoning was a significant hindrance, reducing the efficacy of this process, although some progress was made towards mitigating catalyst deactivation. In 1900 the Pt catalyst was superseded by a vanadium oxide catalyst, which, while unreliable initially, became a mainstay of chemical industry thereafter.[10,11] Perhaps the most famous example of industrial catalysis from the early 20th century is the Haber-Bosch process, in which hydrogen and nitrogen are reacted in the presence of a catalyst to produce ammonia, a crucial fertiliser feedstock. The initial reactions in 1909 utilised osmium and uranium catalysts, which were subsequently replaced by cheaper and more obtainable Fe catalysts alongside promoters; the resultant catalyst is a mixture of iron oxides, metallic iron and other metal (e.g. K, Ca, Al) oxides, and it remains in use in the 21st century for ammonia production.[12]

1.1.2 Homogeneous and heterogeneous catalysis

There exist two broad categories into which catalysts can be divided, namely homogeneous and heterogeneous catalysts. Catalysts of the former type interact in the same phase as the reactants, e.g. in solution, while for the latter category catalysis occurs at the interface between the catalyst phase and the reactant phase. There are substantial differences in catalytic behaviour for the two types, and there are advantages and disadvantages to each type of catalyst (Table 1.1).[13] Examples of homogeneous catalysts include organometallic complexes, acid catalysts and certain biological catalysts; heterogeneous catalysts include metals, metal oxides and nanoparticulate metal catalysts. Enzymes can belong to either group depending on the circumstance and purpose of the enzyme, and can sometimes share properties from both groups.

Table 1.1: Advantages and disadvantages of homogeneous and heterogeneous catalysts.

Catalyst type	Advantages	Disadvantages
Homogeneous	Full mixing of catalyst and reactants	Difficult to recover catalyst
	High selectivity and activity	Expensive catalyst losses
	Well-understood mechanisms	Limited applicability
Heterogeneous	Easy separation from products	Only surface atoms are active
	Widely applicable	Mass transfer limitations can be severe

Homogeneous catalysts are generally more active than heterogeneous catalysts, as they inhabit the same phase as the substrates. This affords a large effective surface area on which catalysis can take place, boosting the activity of the catalyst and permitting the use of lower reaction temperatures. For heterogeneous catalysts, where reactants occupy a different phase to that of the catalyst, only the surface area directly at the interface between the phases can be utilised during catalysis. Reactions using homogeneous catalysts will typically involve the catalyst producing an intermediate species by interacting with a reactant in solution, which, upon further reaction, regenerates the catalyst and yields the products. Heterogeneous catalysts rely instead on surface adsorption, in which reactants approach the catalyst surface, are adsorbed at the active site, and can then roam across the surface. The catalyst surface can facilitate the reaction in multiple ways: by adsorbing reactant species to a surface and confining them there, the effective local concentration of reactants can be increased; by affecting the bonding energies in the adsorbate molecule; and by prompting the adoption of favourable geometric orientations.[14] Due to the costs and difficulties encountered when separating homogeneous catalysts and products, most bulk industrial processes use heterogeneous catalysts, including the Haber-Bosch and contact processes.

1.2 Selective oxidation catalysis

Modern chemical industry is dependent upon heterogeneous selective oxidation catalysts to produce approximately a quarter of all significant organic chemicals used as manufacturing feedstocks for consumer goods or important industrial products, including acrolein, acrylonitrile and maleic anhydride.[15] These catalysts have attracted considerable research interest and popularity since the latter half of the 20th century. Compared to historical catalytic systems, more modern selective oxidation catalysts are notably more environmentally friendly. The chemical industry today is aware of the need to enhance its green credentials and to reduce its impact on the environment: this has been a significant impetus towards the testing of novel selective oxidation catalysts. The changes necessary to mitigate the environmental harm caused by chemical industries are codified in the twelve principles of green chemistry.[16] Of these principles, the idea of *atom economy* is particularly important, and is defined as:

$$\text{Atom economy} = \frac{\text{Molecular weight of intended product}}{\text{Molecular weight of all reactants}} \times 100\%$$

Rather than focus solely on chemical yield, it is more important to consider the amount of waste a reaction generates as a means of gauging the inherent "greenness" of the reaction. Rearrangements, isomerisations and addition reactions are all examples of fully atom efficient reactions, while catalytic reactions frequently exhibit atom economies far better than stoichiometric counterparts.

The precise reaction mechanisms and kinetics during reaction on selective oxidation catalysts remain poorly understood;[17] however, it has been proposed that there are certain fundamental tenets relevant to all selective heterogeneous oxidation catalysis. These are described by Grasselli as:[15,17,18]

(i) lattice oxygen: the lattice oxygen of a metal oxide species can be a more favourable oxidiser than gaseous oxygen present above the catalyst;

(ii) metal-oxygen bond strength: the bond strength must be of moderate value, for too strong a bond will prevent reaction, while too weak a bond will permit over-oxidation (thus losing selectivity);

(iii) host structure: the structure of the metal oxide must be sufficiently accommodating to permit rapid lattice oxygen translation and electron transfer;

(iv) redox properties: the depletion of lattice oxygen in the catalyst during substrate oxidation must be easily restored by gaseous oxygen, and the re-oxidation of the reduced form of the catalyst must occur more rapidly than the initial reduction for it to serve as a catalyst;

(v) active site multifunctionality: the active sites must be capable of undertaking various roles in the catalytic cycle;

(vi) site isolation: lattice oxygen near the catalyst surface must be corralled into specific clusters, which contain the correct number of oxygen species to achieve the desired degree of oxidation;

(vii) phase cooperation: in cases where a single phase is unable to perform all crucial catalytic functions, it is necessary to employ two or more phases whose respective behaviours differ *per se* but complement each other to provide the overall desired catalytic behaviour when used in concert.

Since being reported, these precepts have been applied as guidelines for catalyst design efforts, and have succeeded in amplifying the desirable properties of modern catalysts.[19]

In general, selective oxidation processes proceed by a redox mechanism with two steps:

(i) The reduction of the catalyst by the incoming starting material:

$$\mathrm{X{-}O} + \mathrm{R} \longrightarrow \mathrm{X} + \mathrm{OR}$$

(ii) The reduced catalyst is then reoxidised by gas phase oxygen:

$$\mathrm{X} + \frac{1}{2}\,\mathrm{O_2} \longrightarrow \mathrm{X{-}O}$$

where X is an example catalyst and R is the starting reagent. The reaction rates for both processes will be the same under steady-state conditions. To serve as an example, consider this (unbalanced) schematic mechanism for the oxidation of methanol on molybdena:

$$\mathrm{Mo^{VI}} + \mathrm{CH_3OH} \xrightarrow{\text{- H}_2\text{O}} \mathrm{Mo^{IV}(OCH_3)}$$

$$\mathrm{Mo^{IV}(OCH_3)} \xrightarrow[\text{- H}_2\text{O}]{\text{- H}_2\text{CO}} \mathrm{Mo^{IV}}$$

$$\mathrm{Mo^{IV}} + \mathrm{O_2} \longrightarrow \mathrm{Mo^{VI}}$$

In 1954 Mars and Van-Krevelen first proposed their eponymous reaction mechanism in which the lattice oxygen of metal oxide catalysts (in this instance vanadium oxides) participated in the reaction as an oxidant alongside gas phase oxygen. This result has been corroborated in many later studies of catalysts systems, including bismuth molybdates for propylene oxidation and molybdenum oxide for methanol oxidation.[20–27]

1.3 Methanol oxidation

The production of formaldehyde from methanol represents one of the key selective oxidation processes required to sustain our modern ways of living. The industrial catalysts vital to this process have been in use for more than half a century, yet precise information regarding catalyst surfaces, structures and active sites is still being uncovered today. It is this avenue of research, into methanol selective oxidation and the catalysts employed therein, that is one of the fundamental themes of this thesis. It is necessary to discuss the significant compounds and reactions both in industrial contexts and as they relate more directly to these studies. It is only by understanding the context in which these substances and processes exist, that one may perceive the rationale and expectations of this project.

1.3.1 Methanol

Methanol (CH_3OH but frequently denoted MeOH) is a naturally occurring compound synthesised by the anaerobic metabolism of many bacteria and is hence common globally in small quantities. It has historically been known as wood alcohol due to its former production from the destructive distillation of wood, but is today produced chiefly by hydrogenation of carbon monoxide.[28] It is a volatile, flammable, toxic liquid with an odour similar to ethanol, with density 0.792 $\mathrm{g\,cm^{-3}}$, melting point -97.6°C and boiling point 64.7°C.[29] Methanol has been produced and utilised by humans for several millennia; the embalming fluids used by the Ancient Egyptians were known to contain methanol, which was obtained from the pyrolysis of wooden material. Several millennia passed until methanol itself was isolated, which was achieved in 1661 by Robert Boyle (who later denoted it *pyroxylic spirit*) through the distillation of *Buxus* (box) plant matter.[30] It was not until 1834 that its elemental composition was deduced by French chemists Dumas and Peligot.[31] Its original name, methylene, derived from two Greek words, μεθυ meaning wine and υλη meaning woodland, representing its production from wood: interestingly, the name *methyl* to denote the $-CH_3$ group is a back-formation from the name methylene.

In 1923 Mittasch and Pier, two German chemists in the employ of industrial chemical company BASF, developed the forerunner of the modern synthetic route, producing methanol from synthesis gas (syngas, a mixture of CO, CO_2 and H_2).[32] Alongside a mixed chromium and manganese oxide catalyst, it was necessary to use intense reaction conditions, viz. pressures up to 220 atm and temperatures approaching 450°C. Since the development of the Low Pressure Methanol (LPM) method by ICI in the 1960s, modern industrial production uses catalysts (normally mixed copper, alumina and zinc oxide) capable of operating at lower temperatures and pressures, greatly lessening the energetic demands of production.[33] Several further improvements have been made to the LPM process, including the Synetix LPM process which uses a mixed copper, zinc and chromium catalyst and more enhanced reactor engineering to improve yields.[33] In addition, the contemporary source of syngas in 1923 would have been from coal gasification; modern production of methanol derives from natural gas supplies instead, reacting steam with methane to produce syngas *in situ*:

$$CH_4 + H_2O \rightleftharpoons CO + 3\,H_2$$

This is called steam reforming and is a strongly endothermic reaction ($\Delta H_r = 206$ $kJ\,mol^{-1}$). Due to the high operating temperatures of this reaction (700-1100°C), normal diffusion processes can be affected; catalysts with high surface-area-to-volume ratio are favoured as a means of diminishing the severity of the diffusion limitations.[34] Methane can also react with molecular oxygen directly:

$$CH_4 + \frac{1}{2}\,O_2 \rightleftharpoons CO + 2\,H_2$$

This secondary reaction is mildly exothermic and assists in achieving the temperatures required for the main reaction. When these two methods are combined in one reactor, the result is autothermal reforming (ATR), which can use either CO_2 or steam to generate syngas:

$$\text{With } CO_2\text{: } 2\,CH_4 + O_2 + CO_2 \longrightarrow 3\,CO + 3\,H_2 + H_2O$$

$$\text{With steam: } 4\,CH_4 + O_2 + 2\,H_2O \longrightarrow 10\,H_2 + 4\,CO$$

A significant advantage with ATR is the tunability of the H_2:CO ratio, which is particularly beneficial for the production of certain second-generation biofuels (such as DME) by chemical routes.

Applications of methanol

Methanol is widely used industrially *qua* methanol and as a means to access further commodity chemicals. Internal combustion engines can be designed to run on methanol alone, affording a cleaner burn, increases in thermal efficiency and benefitting fuel sustainability; however, the energy density of methanol is markedly lower than that of gasoline, increasing fuel consumption. In addition, the water produced upon combustion of methanol generates acidic products in the engine, accelerating wear of cylinders, valves and gaskets. Corrosion is worsened by methanol fuel, as only rarely can methanol be obtained without contaminants, especially when produced in large volumes. These contaminants include halide ions, which directly attack passivating oxide layers on engine components and increase the electrical conductivity of the fuel mixture, promoting galvanic and electric corrosion.[35] Consequently, mainstream use of methanol for internal combustion engine fuels is constrained to use as a low percentage additive in existing gasoline fuels to enhance octane rating (i.e. as an anti-knocking agent). For specialised automotive situations like racing, however, methanol is in widespread use: for example, American Indy car racing and monster truck championships mandate the use of methanol fuel. The primary motivation behind this is the vastly superior safety case compared to gasoline fuel. In the event of an accident, methanol fires do not produce opaque smoke clouds and can be extinguished with water; in contrast, gasoline fires are more difficult to extinguish and create dense clouds of smoke, impeding the visibility of other racers and emergency personnel.

A wide array of vital industrial chemicals can be produced from methanol, including formaldehyde (by the Formox process), acetic acid (by the Cativa process) and methyl *tert*-butyl ether (MTBE, an octane rating booster added to gasoline).[36,37] In addition, methanol is widely used in gas-to-liquids (GTL) processes, e.g. methanol-to-hydrocarbons (MTH), methanol-to-olefins (MTO) and methanol-to-gasoline (MTG).[38,39]

Direct methanol fuel cells (DMFCs), which use methanol solution at ambient pressures, represent a significant line of interest as a means to improve the practicalities of existing fuel cell technology. In comparison to hydrogen, transporting methanol is trivial; it is sufficiently energy-dense yet a stable liquid under all environmental conditions encountered in the natural world. The drawback of DMFCs is their low efficiency, which limits their current use to applications wherein portability and power density are more important. It is hoped that advances in DMFC efficiencies can be achieved in the near future, which would potentially enable methanol to be adopted as a general means of transporting energy: ideas akin to this are key to the suggestion of a future methanol economy.

First proposed in the 1990s by George Olah as an alternative to the hydrogen economy, a methanol economy is one in which fossil fuels are replaced by methanol and dimethyl ether (DME) as materials for energy storage, transportation fuel and synthetic feedstocks for commodity chemicals.[40–42] There is a wide variety of methods for the production of methanol, ranging from still-plentiful fossil fuel sources to biomass and agricultural waste: importantly, producing methanol for the methanol economy may represent a key means to recycle CO_2, a vital consideration for the future energy sector.[43]

1.3.2 Formaldehyde

Formaldehyde, (CH_2O or less commonly, methanal), is a colourless gas with boiling point $-19\,^{\circ}C$ and is the simplest aldehyde; however, its apparent simplicity belies its true complexity.[44] It is seldom found as gaseous monomeric formaldehyde, instead occurring more often either in solution or as a polymerised solid. Of the former category, a saturated aqueous solution of formaldehyde (40% by volume or 37% by mass) named formalin is the most common. This solution is typically treated with stabilisers (e.g. methanol) to prevent polymerisation or oxidation. Of the latter category, the cyclic trimer metaformaldehyde (1,3,5-trioxane) and linear polymer paraformaldehyde are the commonest, but a wide range of oligomers of different structures can be formed (reversibly) from formaldehyde. In general, when formaldehyde *per se* is required in the laboratory, formalin is used.

Formaldehyde has been a vital industrial chemical for over a century, and since the advent of efficient synthesis routes and catalysts in the mid-20th century, production has been in the order of millions of tonnes each year, with demand set to grow further still.[45] A synthesis of formaldehyde was first reported in 1859 by the Russian chemist Aleksandr Butlerov, but it was ten years later that the compound was definitively identified by renowned German organic chemist August Wilhelm von Hofmann when he passed methanol vapours in air across a hot platinum spiral.[46,47] In 1909, Leo Baekeland reacted formaldehyde with phenol under pressure and in the presence of a catalyst (HCl or $ZnCl_2$) or in basic conditions to produce Bakelite, the first synthetic plastic.[48] In doing so, Baekeland triggered the great commercial demand for plastics and resins which continues to this day, and still accounts for the largest portion of industrial formaldehyde usage.

In industry, formaldehyde is produced by catalytic oxidation of methanol using either of two main routes. The first system comprises a silver oxide-based catalyst which, when used between 500 and 600°C in a methanol-rich atmosphere, affords 89% yield to formaldehyde.[49,50] There are two reactions which occur on the silver catalyst: i) partial oxidation and ii) dehydrogenation:[45]

$$\text{i)}\quad CH_3OH + \frac{1}{2}O_2 \longrightarrow H_2CO + H_2O$$

$$\text{ii)}\quad CH_3OH \longrightarrow H_2CO + H_2$$

Careful control of the methanol:oxidant ratio, temperature and water content of the input feeds must be maintained to achieve optimal results. Further oxidation products, for instance formic acid, are generated from oxidation of the formaldehyde formed. Despite the good yields obtained by this system, the catalyst is liable to deactivate over extended periods at operating temperatures; the temperatures must be high enough (approximately 600°C) to elicit sufficient activity, but this initiates detrimental sintering processes within the catalyst. The H_2 produced during the process is combusted, helping to maintain the high temperatures necessary for this endothermic reaction.

The second—and increasingly popular—method, involving a long-lasting iron molybdate catalyst at 400°C achieving yields in excess of 95% under an oxygenic atmosphere, originates from studies by Adkins et al. in 1931.[51] The process operates at lower temperatures in a single step, with efficient conversion below 400°C. The metal oxide catalyst utilised in this process has many advantages, namely:

(i) greater yield: the formaldehyde solution which results has fewer methanol impurities;

(ii) greater longevity: the catalyst is stable for longer durations at working temperatures;

(iii) greater stability: the catalyst is more resistant to poisoning, obviating the need to use any intake air filters; and

(iv) greater safety: the reactor concentration of methanol is lower, lessening fire and explosion risks.

Applications of formaldehyde

Formaldehyde has a wide array of uses, both industrially and on smaller scales. Its primary industrial significance derives from the useful commodity chemicals which are themselves produced from formaldehyde. Resins and polymers (e.g. melamine and polyacetal) used in textiles, manufacturing and automotive engineering are responsible for over half of all formaldehyde consumption; equally important are the other valuable feedstock chemicals (e.g. methylene diphenyl diisocyante, a key intermediate *en route* to polyurethane) produced from formaldehyde.[52] In addition, formaldehyde is used in the production of paints and explosives.[53] There are a number of smaller-scale uses of formaldehyde beyond industry, for example as a common embalming agent and as a disinfectant, but these are minor in comparison to industry.

1.3.3 Industrial production of formaldehyde

The original 1931 study and subsequent development culminated in the Formox process, the leading process by which formaldehyde is produced today. Methanol is reacted over an iron molybdate (or occasionally iron vanadate) catalyst between 300 and 400°C, generating formaldehyde only by partial oxidation: unlike the Ag-based catalyst, dehydrogenation is not significant. The chemical engineering involved in the Formox process is best understood with the aid of a process flow diagram (Figure 1.2). Air from the atmosphere is drawn in by fans and compressors and combined with gas being recycled from a later stage in the process (labelled *process gas*), generating a 11 mol% O_2 gas mixture. This gas mixture is piped into a vaporiser module to which methanol is simultaneously added. The resulting methanol/gas mixture is then introduced into the reactor module at a pressure of 1.4 bar: this module contains many thousands of individual reactor tubes (typically 8000-16000) whose lengths are generally between 12 and 14 metres. These tubes contain four main layers:

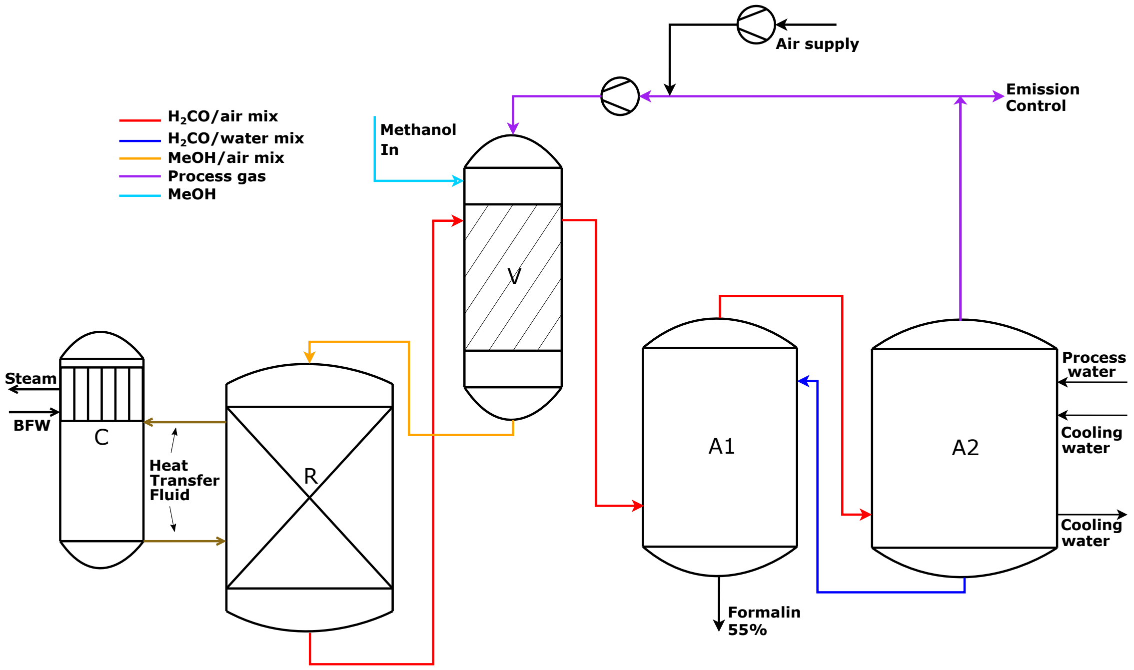

Figure 1.2: A process flow diagram of a formaldehyde production facility utilising the Formox process. (Abbreviations: C - condenser; R - reactor; V - vaporiser; A1 - absorber 1; A2 - absorber 2; BFW - boiler feed water).

(i) A layer of inert ceramic rings, which heat the incoming gas while increasing the space between catalyst pellets. Since the reaction is strongly exothermic, spreading the catalyst pellets more widely allows greater distribution of the heat generated during reaction.

(ii) A mixed layer of inert material and catalyst to preclude the formation of hotspots, which can otherwise contribute to catalyst deactivation.

(iii) A pure layer of catalyst placed relatively far along the reactor tube to boost methanol conversion: by this stage, the methanol concentration has diminished sufficiently that heat generation is no longer as problematic, permitting a pure catalyst phase.

(iv) A final layer containing only inert material, which cools the product before it leaves the reactor module.

Thermocouples are situated throughout certain reactor tubes to report the temperatures at different stages of the reactor: this is important, as the reactor has a non-uniform heat profile. The reactor temperature is maintained by a closed-loop constant flow of Heat Transfer Fluid (HTF, normally a Dowtherm™ hot oil): this heats the reactor inlets while cooling the areas heated by reaction exotherms. Under operating conditions, HTF must be used at its boiling point; to modify the HTF temperature (and hence that of the reactor), HTF pressure is modified, allowing changes in temperature while remaining at the boiling point. During the early stages of operation, HTF temperature is set between 250 and 260°C. As the catalyst deactivates over prolonged operating periods, HTF temperature is raised to 320°C to maintain high product yields. Vaporised HTF is returned to a condenser heat exchanger, generating steam and liquid HTF; liquefied HTF is returned to the reactor to repeat the cycle, while the steam generated is utilised for electricity production or local domestic heating (as occurs near the Perstorp facility in Sweden).

The hot H_2CO/process gas mix generated in the reactor is directed towards and through the vaporiser, where its heat assists the vaporisation of incoming methanol. It then enters a section of heated piping to reach two absorber tanks wherein the formaldehyde is absorbed in process water (to yield formalin): the piping must be heated between vaporiser and absorbers, lest solid polymerisation products be formed in the pipes. The quantity of water added to the absorber tanks can be adjusted to produce a range of formalin concentrations up to 55% formaldehyde. Caustic NaOH is added to the process water in minute quantities to promote the absorption of formaldehyde in the water; however, Na is highly poisonous to the reaction catalyst. Consequently, great care is taken to prevent the retrograde flow of process water towards the catalyst. Increases in temperature caused by the heat of absorption are moderated by a cooling water flow, which expedites further absorption, while the absorber tank head temperature is controlled to minimise the amount of water and formaldehyde remaining in the process gas. A portion of this process gas is recycled, but the remainder is directed to an emissions control unit containing a heat exchanger and a Pt catalyst: this oxidises any remaining volatile organic compounds, rendering the exhaust gas safe for release.

The Formox process achieves a yield of approximately 93% overall.[54] The minority products in the formaldehyde produced (which, unless specified otherwise, is 37% in water) include unconverted methanol (0.3-0.5 wt%), DME, CO, CO_2 and formic acid (0.01-0.03 wt%). Per tonne of formaldehyde produced, the Formox process uses 421-426 kg of methanol, 30-70 kWh of electricity for air blowers, 35 m^3 of cooling water, 0.03-0.5 kg of catalyst and produces 780 kg of steam (which can be utilised further). Approximately 20000-30000 kg of formaldehyde can be produced per kg catalyst (subject to operating conditions).

The Formox catalyst

The Formox process relies on an iron molybdate catalyst, which is synthesised for industrial purposes by co-precipitation. Through combination of $FeCl_3$ and $(NH_4)_6Mo_7O_{24}$ and subsequent acidification, a precipitate is formed, which is filtered and dried to remove up to 70% water: if more is removed, the pore structure of the catalyst can be compromised. A binding agent is added to the dried mixture before pelletisation and calcination, producing catalysts ready for industrial employment. The Mo:Fe ratio in industrial catalysts is greater than that required to produce stoichiometric $Fe_2(MoO_4)_3$: this is discussed in detail in a later section, but it is required to promote catalyst longevity.

Post-mortem examinations on catalysts retrieved from industrial reactors have afforded a wealth of information regarding the impact of prolonged durations at high temperatures. It has been observed that the surface area of the catalyst is not constant along the reactor tube, instead declining as a function of distance through the catalyst bed.[55] The lowest surface area and hence activity was observed at a hotspot, with regions either side seen to be more active (albeit not as active as unused catalyst). In terms of selectivity, regions of the catalyst beyond the hotspot (i.e. further from the entrance) were the most selective, indeed outstripping the selectivity of the original catalyst. This redistribution of selectivity towards the end of the catalyst bed at the expense of activity is the inexorable effect of prolonged high temperature operation. The catalyst adjacent to the reactor tube inlet experiences greater heating by reaction exotherms in comparison to catalyst later in the bed, due to the greater methanol concentration present. These higher temperatures accelerate the volatilisation of Mo from the catalyst, which sublimes, becomes displaced by the gas flow and then condenses in the cooler latter sections of the catalyst as MoO_3. It is these crystallites of MoO_3 on the external faces of the catalyst ring which boost selectivity and dampen activity towards the end of the catalyst.[56]

1.3.4 The thermodynamics of methanol selective oxidation

To understand the niceties behind effective selective oxidation catalysts for methanol oxidation, it is vital to consider the thermodynamics of the various reactions methanol can undertake. Detailed below are the significant reactions occurring during the selective oxidation of methanol and the key thermodynamic values for each reaction (Table 1.2):[57]

Oxidative dehydrogenation:

$$CH_3OH + \frac{1}{2}O_2 \longrightarrow H_2CO + H_2O \qquad \Delta G^\circ = -123\ \mathrm{kJ\,mol^{-1}} \tag{1.1}$$

Dehydrogenation:

$$CH_3OH \longrightarrow H_2CO + H_2 \qquad \Delta G^\circ = 145\ \mathrm{kJ\,mol^{-1}} \tag{1.2}$$

$$CH_3OH \longrightarrow CO + H_2 \qquad \Delta G^\circ = 216\ \mathrm{kJ\,mol^{-1}} \tag{1.3}$$

Combustion:

$$CH_3OH + \frac{3}{2}O_2 \longrightarrow CO_2 + 2\,H_2O \qquad \Delta G^\circ = -678\ \mathrm{kJ\,mol^{-1}} \tag{1.4}$$

$$CH_3OH + O_2 \longrightarrow CO + 2\,H_2O \qquad \Delta G^\circ = -324\ \mathrm{kJ\,mol^{-1}} \tag{1.5}$$

Other processes:

$$CH_3OH \longrightarrow CH_4 + \frac{1}{2}O_2 \qquad \Delta G^\circ = 153\ \mathrm{kJ\,mol^{-1}} \tag{1.6}$$

$$2\,CH_3OH \longrightarrow CH_3OCH_3 + H_2O \qquad \Delta G^\circ = -34\ \mathrm{kJ\,mol^{-1}} \tag{1.7}$$

The Ag-based catalyst operates most efficiently with methanol-rich reducing atmospheres (in which the reactions (1.2) and (1.1) are favoured), while the oxide process is more suited to methanol-poor oxidising atmospheres (in which (1.1) is the main route). It is clear, however, that the combustion processes are the most thermodynamically favourable

Table 1.2: Values of key thermodynamic parameters for the possible oxidation reactions of methanol.

Equation №	$\Delta H°$ ($\mathrm{kJ\,mol^{-1}}$)	$\Delta S°$ ($\mathrm{J\,K^{-1}\,mol^{-1}}$)	$\Delta G°$ ($\mathrm{kJ\,mol^{-1}}$)
(1.1)	-159	-72	-123
(1.2)	84	-122	145
(1.3)	97	-245	216
(1.4)	-674	-55	-678
(1.5)	-389	-145	-324
(1.6)	124	-53	153
(1.7)	-27	15	-34

reactions by some degree. To prevent the dominance of combustion during methanol oxidation, the catalyst must be able to adequately promote both (1.2) and (1.1) for the Ag-based system, and solely (1.1) for the oxide process.

1.4 Materials of interest: background and structural properties

This thesis details the investigations of bi-cationic metal oxide selective oxidation catalysts, primarily within the context of methanol oxidation. It is important, however, to understand the natures and behaviours of more fundamental materials, e.g. metals or single component metal oxides. By studying the properties of simpler oxide species, the examination of more complex multicomponent systems in due course is greatly facilitated. This section will explore the backgrounds of the elements and compounds of relevance to methanol selective oxidation.

1.4.1 Iron

Iron, atomic number 26, is the element inhabiting the eighth group and fourth period of the periodic table (in the first transition series). Immediately adjacent are manganese and cobalt to the left and right respectively, while ruthenium resides below. As a free metal, its electron configuration is [Ar] $3d^6$ $4s^2$. It is the most abundant terrestrial element by mass, constituting the major parts of the outer and inner core of the Earth; in the Earth's crust alone, it is the fourth most abundant element (behind oxygen, silicon and aluminium in that order). Iron is the most widely used metal by a significant margin, accounting for over 90% of total global metal production, and has been a crucial material throughout the history of mankind. The high strength and inexpensive production of iron imbue it with huge value in engineering applications, including use as a structural component in building construction, the manufacture of hulls for large sea vessels and in the assembly of machinery and machine tools.[58] Iron in its pure form, however, is relatively soft: it is necessary to alloy it with other elements (e.g. carbon) to obtain suitable hardness and strength in the final product (e.g. as steel). While the vast majority of all iron is produced for metallurgical purposes, there exists a rich vein of iron chemistry used both in industry and elsewhere. A number of vital industrial processes would not be feasible were it not for iron catalysts, including the Haber-Bosch and Fischer-Tropsch processes to name but two. Nor is the chemical use of iron compounds limited to catalysis: iron(III) chloride, for example, has a multitude of uses, including as a dyeing agent, in sewage treatment and to etch printed circuit boards.[59]

Iron is produced industrially by extraction from its ores, chiefly haematite Fe_2O_3 and magnetite Fe_3O_4, by a two-stage process. The first stage is achieved in a blast furnace at temperatures of approximately 2000°C and in the presence of coke (carbon) and a flux material (e.g. limestone, to remove silicaceous matter from the ore) to produce pig iron, and is described as a carbothermic reaction. Air, heated to 900°C, is blasted into the base of the furnace which reacts with the coke present to produce carbon monoxide:

$$2\,\mathrm{C} + \mathrm{O_2} \longrightarrow 2\,\mathrm{CO}$$

The carbon monoxide now reduces the iron ore (in this instance, haematite) producing molten metallic iron and carbon dioxide:

$$\mathrm{Fe_2O_3} + 3\,\mathrm{CO} \longrightarrow 2\,\mathrm{Fe} + 3\,\mathrm{CO_2}$$

In addition, in the base of the furnace where temperatures are higher, iron ore is able to directly react with the coke:

$$2\,\mathrm{Fe_2O_3} + 3\,\mathrm{C} \longrightarrow 4\,\mathrm{Fe} + 3\,\mathrm{CO_2}$$

Once the pig iron has been produced, it is then converted into steel, cast or wrought iron as required. Alternative laboratory methods exist for synthesising small quantities of pure metallic iron, such as forming and then thermally decomposing iron pentacarbonyl to produce pure iron, but these are bench-scale processes only. All industrial production of iron uses either the blast furnace method or direct iron reduction: in this latter method, iron ore is exposed to syngas (a mixture of hydrogen and carbon monoxide) at high temperature to yield a spongiform iron usable in steelmaking.

All lifeforms irrespective of size or complexity require iron to function, albeit for different purposes. In humans and mammals, the iron-containing protein haemoglobin is responsible for the carriage and storage of oxygen within the body. Consequently, achieving an adequate iron intake is crucial for health. Insufficient iron, or anaemia, is a common condition causing lethargy, nausea and many other symptoms as a result of insufficient cellular oxygen levels.[60] Injurious effects can also arise from a surfeit of bodily iron levels, including organ damage and heart complications. Unlike anaemia, however, there is normally an underlying cause, either acquired or genetic, which predisposes iron overload.[61,62]

1.4.2 Molybdenum

Molybdenum, atomic number 42, is the element occupying the sixth group and fifth period of the periodic table, residing in the second row of the transition metals. In its metallic state, it possesses the electron configuration [Kr] $4d^5$ $5s^1$. Its periodic neighbours are niobium and the synthetic element technetium, while its group neighbours are chromium above and tungsten below. It is obtained primarily from molybdite ore and its name derives ultimately from the Greek μολυβδος, *molybdos*, meaning lead: molybdite shares many properties both visually with lead ore (galena, PbS) and as a lubricant with graphite, and consequently was misidentified. It was not until 1778 that the (oft-overlooked) Pomeranian chemist Carl Wilhelm Scheele definitively stated that molybdite was neither graphite nor galena, but instead the ore of an undiscovered element.[63,64] It is reported that molybdenum was used as an additive to steel in 14th century Japan for swordsmithing purposes to enhance blade hardness, but it is doubtful whether this was intentional; the technique was lost to history with few known surviving examples.[65] In 1781, Swedish chemist Peter Jacob Hjelm succeeded in isolating molybdenum itself through treatment of the ore with carbon and linseed oil.[66] Contemporary metallurgy was insufficiently developed to extract molybdenum in any significant quantities, affording it no industrial significance throughout the 19th century.[67] In 1906, American engineer William Coolidge patented a method for the ductilisation of molybdenum: this permitted its employment as, for example, a heating element and a support in tungsten-filament incandescent light bulbs, yet supply remained problematic. In 1913, engineer Frank Elmore developed the first commercially viable froth flotation process for the beneficiation of ores obtained from a copper mine in Llanelltyd, Wales, including molybdite. This significant increase in the supply of molybdenum greatly whetted industrial appetites: molybdenum-doped steel for armour plating was in particular demand given the events of the succeeding four years. Industrial production and use of molybdenum grew strongly throughout the 20th century. Even today, it is the beneficial metallurgical properties of molybdenum in alloys which are responsible for the greatest molybdenum consumption (approximately 86% of all produced). In order of decreasing significance, molybdenum is used in structural steel, stainless steel, chemicals, high-speed (tool) steels, cast iron, as elemental molybdenum and in superalloys.

Molybdenum in metallic form is not found naturally on Earth, but rather it exists as a range of oxidation states in minerals. As a free metal, it has a melting point of 2623°C, the sixth-highest of the elements. While molybdenum remained undiscovered by humans until relatively recently, its presence in the environment is nothing new. Indeed, molybdenum-bearing enzymes are the commonest bacterial catalysts for breaking the extremely strong triple bond in N_2 during biological nitrogen fixation. More than 50 enzymes in bacteria, plants and animals are now known to contain molybdenum, but only those found in bacteria (called nitrogenases) are able to fix nitrogen. This is due to the oxidation state of molybdenum in the respective enzymes. In plants, animals and higher organisms, molybdenum in the molybdenum cofactor exists as fully-oxidised Mo(VI); however, in bacteria, reduced molybdenum is present, either as Mo(III) or Mo(V).[68]

The catalytic abilities of molybdenum compounds derive from the wide range of oxidation states accessible by molybdenum, ranging from -2 to +6 (Table 1.3).[69] Higher oxidation states are more prevalent in terrestrial circumstances and in biological systems, with lower oxidation states arising in metal clusters and the lowest in organomolybdenum compounds.

Table 1.3: The oxidation states of molybdenum.

Oxidation state	Example compound
-2	$Na_2[Mo_2(CO)_{10}]$
0	$Mo(CO)_6$
1	$Na[C_6H_6Mo]$
2	$MoCl_2$
3	$Na_3[Mo(CN)]_6$
4	MoS_2
5	$MoCl_5$
6	MoO_3

In humans and other mammals molybdenum is an essential trace dietary element (approximately 0.07 mg/kg in humans), responsible for the generation of four key enzymes, viz. sulphite oxidase, aldehyde oxidase, xanthine oxidoreductase and mitochondrial amidoxime reductase. Where bodily levels of molybdenum are insufficient, sulphite oxidases are unable to properly function, causing toxic reactions to sulphite-containing foods.[70] In contrast, overly high quantities of molybdenum can impede the uptake of dietary copper: this is rarely a problem in humans, but can become serious in ruminant livestock.

1.4.3 Vanadium

Vanadium, atomic number 23, is the element in the fifth group and fourth period of the periodic table, in the first row of the transition metals: its periodic neighbours are titanium and chromium, and it sits above niobium. Metallic vanadium has the electron configuration $[\mathrm{Ar}]\ 3\mathrm{d}^3\ 4\mathrm{s}^2$. While vanadium compounds in ores are relatively abundant on Earth (occurring in more than 60 ores), metallic vanadium is only found in nature in the extremely scarce mineral *native vanadium*, which is present in vanadium-rich soils around the fumaroles of a volcano in Colima in Mexico.[71] Historically, the main vanadium ores of practical interest have been patrónite (VS_4) and carnotite ($K_2(UO_2)_2(VO_4)_2 \cdot 3\,H_2O$). A large quantity of the former was unearthed during the early 20th century, while the increasing production of radium from carnotite in the 1910s boosted the quantities of vanadium generated as a by-product. Today, most vanadium (in the form of vanadium oxide) is extracted as slag from vanadium-bearing magnetite and titaniferous magnetite ores during the production of steel.[72]

In 1801, the Spanish mineralogist Andrés Manuel del Río discovered vanadium by extraction from an ore of $Pb_5(VO_4)_3Cl$, then called "brown lead" but today called vanadinite. Despite successfully forming a wide range of differently-coloured vanadium salts, however, del Río was misinformed by French chemist Collet-Descotils to believe that he had in fact extracted an impure form of chromium, and so retracted his claim to a new element. It was only three decades later in 1831 that vanadium was rediscovered in iron ores by Swedish chemist Nils Selfström, who named it vanadium partly after the Old Norse name for the goddess of beauty (on account of the many attractive colours exhibited by vanadium compounds) and because no element names thus far had commenced with the letter v.[73] Attempts to isolate metallic vanadium were undertaken by contemporary chemists, including Berzelius who instead produced vanadium nitride, but it was not until 1867 that (impure) elemental vanadium was successfully obtained by British chemist Henry Roscoe, who reduced vanadium(II) chloride with hydrogen gas.[74] Another fifty years would pass until pure vanadium was effectively produced by reduction of vanadium pentoxide with calcium.[75]

Similarly to molybdenum, vanadium is mostly employed as a steel additive; with vanadium added, the tensile strength of the steel is greatly multiplied through the formation of stable vanadium carbides and nitrides within the steel.[76] Vanadium steel is widely employed in load-bearing steels, such as crankshafts, axles and bogies: indeed one of the first major industrial applications of vanadium steel alloys was in the chassis of the first assembly-line-produced automobile, the Ford Model T.[77] Alloys containing higher proportions of vanadium (up to 5%) are utilised in the manufacture of high-speed steel, which can withstand higher temperatures without losing its temper. This allows steel blades to cut faster (as faster blade speeds generate higher blade temperatures), hence the name high-speed steel. The vanadium quotient in alloys can be expanded further (up to 18%) to supplement the wear resistance of tools and blades.[78] When titanium is alloyed with vanadium, its strength and temperature stability are improved considerably. In conjunction with aluminium, titanium-vanadium alloy is extensively used in aeronautical engineering to manufacture jet engines, turbine blades and high-speed surfaces: since aircraft experience larger frictional forces at higher airspeeds, temperature stability is a critical consideration in high-performance airframes.

Vanadium-containing catalysts are in widespread use in chemical industry, ranging from simple vanadium pentoxide in the contact process to more complex mixed metal oxide catalysts such as those utilised in the oxidation and ammoxidation of propane and propylene to acrolein and acrylonitrile (both key polymer feedstocks) respectively. A significant disadvantage of vanadium is its toxicity: there are no vanadium compounds known to be safe for humans, with respiratory exposure posing the greatest risk to the user.

1.4.4 Iron(III) oxide

Iron(III), or ferric, oxide (Fe_2O_3) is a compound of great relevance to this thesis as a support material in catalysts. It can occur in a range of polymorphs, but is typically found as either α-Fe_2O_3 or γ-Fe_2O_3 with an octahedral coordination environment about the iron. While the name haematite strictly refers to the mineral form of α-Fe_2O_3, it is regularly used synecdochally to refer to α-Fe_2O_3 as a compound (as indeed it is throughout this thesis). Similarly, the compound γ-Fe_2O_3 is often referred to by its mineral name, maghaemite. Fe_2O_3 is one of the three main oxides of iron alongside iron(II,III) oxide, Fe_3O_4 (also known as magnetite), and iron(II) oxide, FeO. Iron(III) oxide is frequently mislabelled as rust; however, rust in fact comprises **hydrated** iron(III) oxide and iron(III) oxide-hydroxide.

Structure

Most commonly, iron(III) oxide occurs in its α-Fe_2O_3 haematite structure, exhibiting a rhombohedral crystal structure with lattice parameters a = 5.038 Å and c = 13.772 Å and space group R$\bar{3}$c (Figure 1.3).[79,80] In this structure, sheets of octahedrally-coordinated Fe^{3+} cations are stacked between two layers of oxygen anions. Only two of every three oxygen octahedra are occupied by cations, as each oxygen anion shares four cations.

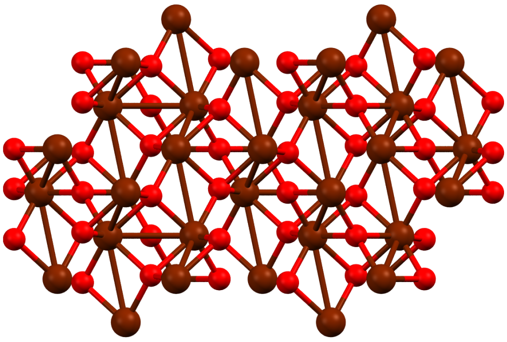

Figure 1.3: Structure of α-Fe_2O_3 viewed along cell axis c: Fe cations are brown, O anions are red.

The significant other phase, γ-Fe_2O_3, exists as a strongly magnetic cubic spinel structure, with lattice parameters a = 8.347 Å and c = 25.042 Å and space group $P4_12_12$.[81,82] This phase can form from α-Fe_2O_3 during prolonged exposure to high temperatures. The Fe cations in γ-Fe_2O_3 exist in either of two coordination geometries: eight Fe cations possess tetrahedral coordination geometries and $13^1/_3$ reside in octahedral sites. Unlike α-Fe_2O_3, there are no oxygen vacancies. Several other phases have been reported, including β-Fe_2O_3 which adopts a cubic body-centred structure; however, this structure is metastable and readily converts to α-Fe_2O_3 when heated above 500°C.[80] ε-Fe_2O_3 has also been studied, albeit with difficulty. It is a rhombic structure with properties from both α- and γ-Fe_2O_3 and is thought to display interesting magnetic properties. It too is metastable, rapidly forming α-Fe_2O_3 above 500°C.[83,84]

1.4.5 Molybdenum trioxide

Molybdenum trioxide (MoO_3, also referred to as molybdena) is the most widely-produced compound of molybdenum. It occurs naturally, but only in the rare mineral molybdite. Instead, it is generated industrially through the roasting of the major molybdenum ore, molybdenum disulphide:[85]

$$2\,\mathrm{MoS_2} + 7\,\mathrm{O_2} \longrightarrow 2\,\mathrm{MoO_3} + 4\,\mathrm{SO_2}$$

MoO_3 has a range of industrial uses, including as a means to adhere enamel to metal surfaces. Crucially it is a co-catalyst in the ammoxidation of propylene to acrylonitrile: this is a vital industrial process, producing approximately five million tonnes of acrylonitrile each year. In addition, the production of metallic Mo, an industrially-important additive to steel and corrosion-resistant alloys, is achieved by treatment of MoO_3 with hydrogen at high temperatures:

$$\mathrm{MoO_3} + 3\,\mathrm{H_2} \longrightarrow \mathrm{Mo} + 3\,\mathrm{H_2O}$$

MoO_3 has attracted considerable interest in recent years as a component of electrochemical display devices due to facile Mo(VI)/Mo(V) coupling and its foliated structure.[86] In addition, an antimicrobial effect arising from MoO_3 in contact with water has been observed, in which bacteriotoxic H^+ ions are formed; however, this usage has yet to be developed, as there are a number of practical considerations (e.g. catalyst cleanliness) which must be addressed first.[87]

Structure

The structure of α-MoO_3 was first detailed in 1963 by Kihlborg, revealing it to have an orthorhombic crystal structure with space group Pnma, with lattice parameters a = 3.962 Å, b = 13.858 Å and c = 3.607 Å.[88] The structure contains distorted MoO_6 octahedra arranged in two layers held together by interplanar van der Waals forces. The octahedra are connected in one dimension by shared corners and in another by shared edges.[89,90] The oxygen anions exist in any of three states, namely terminal, symmetric and asymmetric: these are connected to one, two or three Mo atoms respectively (Figure 1.4).

The layers align with the (010) plane, which is the most stable with only oxygen anions exposed at the very surface. The precise nature of the surface of molybdena remains poorly understood, particularly with respect to the role of molybdena during catalysis. Nonetheless, the adoption of such an irregular structure hinders interaction with incoming reactants, permitting reaction only on certain faces. A monoclinic form β-MoO_3, of space group $P2_1/c$ and lattice parameters a = 7.122 Å, b = 5.374 Å and c = 5.565 Å, also exists. In this form it is isostructural with ReO_3 and the distorted octahedra share corners.

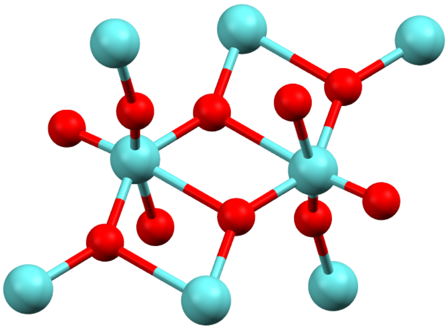

Figure 1.4: Structure of α-MoO_3, showing MoO_6 units: Mo cations are blue, O anions are red.

1.4.6 Vanadium(V) oxide

Vanadium(V) oxide (V_2O_5), more commonly called vanadia, is a yellow/orange solid commonly used as an oxidising agent. It is the most industrially significant vanadium compound, being the precursor to a multitude of vanadium alloys and being widely utilised *per se* as an industrial catalyst.[91] It is produced mainly by reacting vanadium ores or residues (e.g. certain furnace slags) with sodium carbonate and ammonium salts to yield sodium metavanadate, which then precipitates upon acidification to pH 2 with sulphuric acid. This precipitate is heated to 700°C whereupon it melts, producing crude V_2O_5. Vanadia does occur naturally in the mineral shcherbinaite, albeit extremely rarely: its existence is almost exclusively limited to volcanic fumaroles.

The predominant industrial application (by mass) of vanadia is to produce ferrovanadium, a steel additive used to enhance strength and corrosion resistance.[58] Sulphuric acid, a vital industrial chemical, is produced by the vanadia-catalysed contact process.[20,92] In this process, the exothermic oxidation of sulphur dioxide to sulphur trioxide is achieved with a vanadium catalyst between 400 and 620°C. Below 400°C, the catalytic activity of vanadia is poor; above 620°C, catalyst stability suffers. The suggested catalytic cycle proceeds thus:

$$\mathrm{SO_2 + V_2O_5 \longrightarrow SO_3 + 2\,VO_2}$$

$$\mathrm{2\,VO_2 + \frac{1}{2}\,O_2 \longrightarrow V_2O_5}$$

This particular chemistry can also be environmentally deleterious. Vanadia catalysts are often used in power station emissions scrubbers for NO_x selective catalytic reduction; however, the ability of vanadia to oxidise SO_2 to SO_3 necessitates the use of low-sulphur fuels or careful temperature management, lest sulphuric acid be formed from the SO_3 generated by vanadia. Other oxidation processes can be catalysed by vanadia, including, *inter alia*, the oxidation of butane to maleic anhydride and the oxidation of carbohydrates to oxalic acid. Additionally, vanadia has less prominent electrochemical usages, including as a sensing material in bolometers (devices to gauge the power of electromagnetic radiation) and in flow batteries for energy storage.[91,93–95]

Structure

Vanadium(V) oxide adopts an orthorhombic structure, with lattice parameters a = 11.544 Å, b = 4.383 Å and c = 3.574 Å and space group Pmmn, in which the vanadium cations in the structure possess square pyramidal coordination geometry (Figure 1.5).[96,97] In its bulk crystalline form, the layers oriented with the (010) plane contain VO_5 square pyramidal units which share edges and corners. There are six planar layers of atoms in the structure, four oxygen anion layers and two vanadium layers constituting one overall "slab". Three distinct inequivalent oxygen environments are present, namely bridging oxygens coordinated to three vanadium centres, bridging oxygens coordinated to two vanadium centres and terminal vanadyl oxygens.[98]

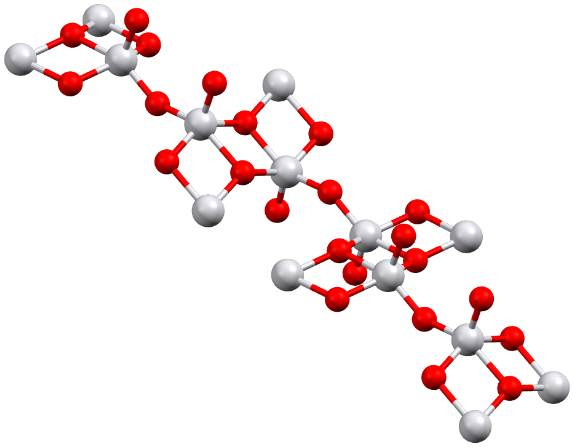

Figure 1.5: Structure of V_2O_5, incorporating square pyramidal VO_5 units: V cations are grey, O anions are red.

1.4.7 Iron molybdate

Iron molybdate, $Fe_2(MoO_4)_3$, is widely employed as an industrial catalyst for the selective oxidation of methanol to formaldehyde. It is an effective catalyst, producing high yields (>90%) of formaldehyde for prolonged periods; however, in order to achieve such longevity, an excess of molybdena is required to be present in the catalyst. The catalytic behaviour of iron molybdate and its important features are discussed in greater detail in a later section.

Structure

$Fe_2(MoO_4)_3$ exists as a monoclinic structure with lattice parameters a = 15.693 Å, b = 9.235 Å and c = 18.218 Å and space group $P2_1$.[99] The coordination geometry around each Mo cation is broadly tetrahedral, with an average Mo-O distance of 1.756 Å, while each Fe cation inhabits an octahedral environment (Figure 1.6). Octahedral FeO_6 units are linked to MoO_4 tetrahedra by oxygen atoms—each oxygen anion connects one octahedron and one tetrahedron—expanding the intrastructural spacing and affording a shortest Fe-Fe distance of 5.03 Å.

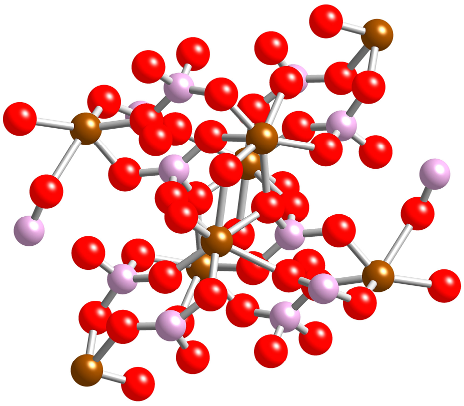

Figure 1.6: Structure of $Fe_2(MoO_4)_3$, incorporating tetrahedral MoO_4 units: Mo cations are lilac, Fe cations are brown and O anions are red.

This monoclinic iron molybdate can also undergo a reversible phase transition to β-$Fe_2(MoO_4)_3$, generating an orthorhombic structure akin to scandium tungstate, $Sc_2(WO_4)_3$, or scandium molybdate, $Sc_2(MoO_4)_3$. This structure possesses lattice parameters a = 9.683 Å, b = 13.317 Å and c = 9.591 Å and space group Pnca.[100,101]

When excess MoO_3 is present in α-$Fe_2(MoO_4)_3$, an expansion of the unit cell has been observed along certain planes, which is not apparent in stoichiometric iron molybdate. This is suggested to be due to defects in the structure arising from substitution of Mo^{6+} cations for Fe^{3+} cations, with additional oxygen anions present to preserve charge neutrality. It is these supplementary oxygens that elicit the observed structural changes.[102]

1.5 Reactivity of methanol selective oxidation catalysts

The oxidation of methanol to formaldehyde has been extensively studied over a range of metal oxide catalysts.[57,102–112] By assessing and probing reaction intermediates absorbed on catalysts during the catalytic cycle, the significance of particular catalyst surfaces can be revealed.[113,114] Molybdenum-containing catalysts have been regarded as the most effective—indeed they are employed industrially to produce formaldehyde—but other metal oxides are equally worthy of interest. It is hoped that, by comparing catalytically-relevant metal oxides in the same reaction, greater insight can be gained into the particular properties of a catalyst which enhance selectivity during reaction.

An overarching motif in this thesis is the shell-core catalyst (discussed in more detail in section 1.6). These catalysts comprise MO_x shells (where M = transition metal, e.g. Mo) around haematite cores. To properly comprehend the catalytic behaviour exhibited by such shell-core catalysts, it is vital to have a thorough appreciation of the reactivities of shell and core moieties in isolation.

1.5.1 Haematite

Viewed from the standpoint of intended formaldehyde production, Fe_2O_3 acquits itself poorly: it is an extremely efficient combustor of methanol, affording large quantities of CO_2.[57] From a disinterested perspective, however, Fe_2O_3 displays much interesting chemistry. Using X-ray photoelectron spectroscopy (XPS) and infrared (IR) spectroscopy, the interactions between Fe_2O_3 surfaces and incoming reductants, such as methanol and formic acid, have been explored.[115,116] It is apparent that methanol can adsorb in either a dissociative or a molecular mechanism: in the former, hydroxy and methoxy adsorbates are generated, while in the latter methanol interacts with Lewis acidic and Lewis basic sites on the Fe_2O_3 surface. As methanol chemisorbs to the surface, it is partially oxidised and the Fe_2O_3 is accordingly reduced: this is corroborated by a noticeable diminution of the O:Fe ratio from 1.5 to 1.3. Upon heating to 125°C, a formate species is formed on the surface. This is suggested to arise from the combination of methoxy adsorbates with Fe_2O_3 lattice oxygen, since the formate appears irrespective of external oxygen concentration (and indeed this process can be monitored spectroscopically). Increasing the temperature beyond 220°C prompts decomposition of the formate intermediate, yielding H_2, CO, CO_2 and H_2O. Additionally, any formaldehyde formed on Fe_2O_3 is inclined to undergo further oxidation, hence only combustion products are observed.[117] Formate species are also formed on Fe_2O_3 in the presence of formic acid, while they do not form with formaldehyde present.[118] By an analogous mechanism, acetate groups are formed following the adsorption of ethanol on Fe_2O_3.[119]

Mass spectral analysis of the products of methanol temperature programmed desorption (TPD) has supplied crucial information regarding the formate intermediate formed on Fe_2O_3.[57] The selectivity to formaldehyde in TPD from Fe_2O_3 is nil, instead methanol combustion dominates: the significant desorption is CO_2 at 300°C, with two H_2 desorptions at 200°C and 290°C respectively and a broad water desorption throughout. With pulsed-flow studies under an oxygenic atmosphere, no significant methanol conversion occurs until 250°C: it is suggested that the bidentate formate species is stable enough until this temperature, inhibiting interaction between the methanol and the Fe_2O_3 surface. Like in TPD, the only products observed are those of combustion. Since no CO is seen, it is assumed that the combustion pathway requires the formation of a formate intermediate, which decomposes to yield CO_2, H_2 and water. This decomposition is propounded to be the rate-limiting step in the reaction, due to the high temperature stability of the formate species on the surface.[57,115] Subsequent studies of modified Fe_2O_3 systems (e.g. enrichment of the surface with Mo) have determined that surface cation proximity is a crucial consideration when determining methanol oxidation selectivity. In Mo-deficient iron molybdates and Fe_2O_3, the Fe cations at the surface are pressed closer together due to their high concentration at the surface. Since the formate intermediate is bidentate, there is a limit on the distance between Fe cations if the formate is to be stable. This is hugely significant: formate intermediates, and by extension direct selectivity to combustion, can only exist where multiple Fe cations are exposed at the surface, and these cations are sufficiently close to interact.[120–122]

1.5.2 Molybdena

Unlike Fe_2O_3, MoO_3 is highly selective (>90%) to formaldehyde in both TPD and under oxygenic reaction conditions. Methanol is known to adsorb either as a chemisorbed methoxy species or as undissociated methanol, jointly achieving a surface coverage of 3-4%.[57,123] The undissociated methanol is weakly chemisorbed to MoO_3 lattice oxygen via a hydrogen bond: chemisorption on MoO_3 is feeble, and the efficiency of methanol oxidation even in ultra-high vacuum (UHV) scarcely exceeds 40%.[124] Formate species are not formed on MoO_3, and consequently neither are combustion products. A range of higher order oxidation by-products can occur during reaction of methanol with MoO_3, arising from the condensation of methoxy intermediates, particularly at lower temperatures and with insufficient oxygen. Nonetheless, the degree of formation of such by-products from acidic oxides like MoO_3 is constrained by energetic barriers larger than those for the formation of formaldehyde.[123]

The mechanism and activity of MoO_3 during oxidation have historically attracted considerable interest. The most exposed faces of α-MoO_3 are (010), (100) and (001+100): the relative proportions of these faces are contingent on the method used during synthesis.[125] These faces are important as they influence the means by which methanol reacts, either by the Mars-van Krevelen (MVK) mechanism or by the Eley-Rideal mechanism. It has been suggested that the defect sites and edge facets of MoO_3 are the commonest sites upon which methanol adsorbs, since the uptake of methanol at saturation correlates with the quantity of available active sites on non-basal planes.[126] The (010) face occupies only 10% of the surface of MoO_3, but possesses the lowest free energy of all faces.[109,126] When considered in conjunction with experimental data demonstrating that catalytically active sites represent only approximately 12% of MoO_3 surface sites, it suggests that the (010) face is the crucial face for formaldehyde production via dehydrogenation of methanol. *Ab initio* computational investigations have proposed that dual-dioxo sites on the MoO_3 (010) face are the location of methanol adsorption, but this is contradicted by studies showing that any methanol adsorbing on the (010) does so associatively, and does not afford formaldehyde.[126,127] Instead, it is thought that methanol chemisorption occurs on defects and other faces adjacent to under-coordinated Mo sites. Atomic force microscopy (AFM) has since probed the anaerobic reaction of methanol with these Mo sites, supporting this line of enquiry.[128] Crystal faces other than (010) exhibit acid-base sites, comprising an unsaturated Mo cation and a vicinal terminal oxygen: it is on these bi-functionalised sites that dissociative chemisorption transpires. The unsaturated cation (O$-$Mo$-$O) is Lewis acidic and binds the methoxy moiety; the terminal oxygen forms a hydroxyl species by proton abstraction from the methoxy (lengthening the M=O bond from 1.66 Å to 1.89 Å).[125] The reduced surface sites weaken the C$-$H bond in the methanol, while simultaneously strengthening the methoxy C$-$O bond, boosting the proportion of products deriving from hydrogen abstraction. Formaldehyde can be oxidised further to CO or CO_2 under suitable conditions; however, it has been shown that undissociated methanol and water on the MoO_3 surface inhibit further oxidation of formaldehyde by physically obstructing adsorption sites.[129]

Subsequent *in situ* examinations of the dehydrogenation of methanol on MoO_3 have been undertaken with a range of techniques, including ultraviolet-visible (UV-Vis) and Raman spectroscopy, Wide Angle X-ray Scattering (WAXS) and mass spectrometry. These stated that an MVK mechanism delivering lattice oxygen to the surface is responsible for reoxidation of the active sites, enabling successful catalysis.[130] Further anaerobic pulsed flow reactor experiments demonstrated prolonged selectivity to formaldehyde at low temperatures, bolstering the suggestion that an MVK mechanism underpins the catalytic processes.[131,132] MoO_3, however, possesses low catalytic activity in spite of its excellent selectivity. The low inherent surface area of MoO_3 impairs the activity, as does its inefficient lattice oxygen mobility: since the MVK mechanism relies upon lattice oxygen movement to complete the cycle, the poor mobility impairs the activity.

1.5.3 Vanadia

Similarly to MoO_3, V_2O_5 is selective to formaldehyde, achieving selectivities in excess of 85% under ideal conditions.[133] It attracted some interest in the 1920s as a potential methanol oxidation catalyst to formaldehyde, but has since been replaced by molybdenum-containing catalysts.[134] In methanol oxidation to formaldehyde, V_2O_5 is more active than MoO_3, but demonstrates worse selectivity.[133,135] The kinetics of methanol oxidation on V_2O_5 have been widely studied, revealing that it too proceeds by an MVK redox mechanism.[136] Experiments by Roozenboom et al. determined that while formaldehyde selectivity is high at 250°C, formaldehyde selectivity is diminished by DME production at lower temperatures and carbon oxide (CO_x) production at higher temperatures.[112] Notwithstanding these studies, the subsequent investigations by Tatibouët et al. unearthed significantly more complexity during methanol oxidation by probing the link between product distribution and reaction conditions. It was found that at low conversions, dimethoxymethane (DMM), $H_2C(OCH_3)_2$, is the major product in conjunction with lesser quantities of DME. By 190°C methanol conversion becomes significant and selectivity to formaldehyde dominates. At temperatures thereafter, however, methyl formate and CO_x preponderate. Tatibouët et al. indicated that a rake-type mechanism (wherein, over a series of consecutive steps, intermediate complexes are formed, which then either desorb or transform into the next intermediate in the series) where the series of intermediates comprises methanol, formaldehyde and formic acid accounts for the product distribution.[137] Kinetic analysis of the reaction unveiled that DMM and formaldehyde form by dissimilar routes in the early stages of the reaction, as their respective formation kinetics follow different orders with respect to oxygen.[137]

Significant efforts have been made to rationalise the reactivity of V_2O_5 in structural terms, focussing particularly on the influence of microcrystal morphology on methanol oxidation over V_2O_5.[138,139] It has been reported that the (001) basal plane of V_2O_5 is more selective to DMM—albeit less active—than the side faces (mostly (100) faces), which display no selectivity preference.[109] Considering that the structure of the (001) plane consists of square pyramidal vanadium with alternating vanadyl (V=O) units projecting above and below the plane, Tatibouët posited that the DMM selective site comprises a upwards-pointing vanadyl unit and an adjacent oxygen vacancy near an opposite direction vanadyl vanadium.[109]

The properties of V_2O_5 crystallinity on methanol oxidation were further examined by Gasser and Baiker.[140] Instead of using crystalline V_2O_5, they monitored changes in catalytic properties manifested by an amorphous V_2O_5 precursor. Substantial increases in catalytic activity were observed with longer time on stream alongside significantly greater activity in steady-state conditions than seen for crystalline V_2O_5.[140] At steady-state, this material was revealed to be a mixture of crystalline V_2O_5 and V_3O_7, evincing the greater reducibility of amorphous vanadia compared to crystalline V_2O_5.

Measurements by IR spectroscopy have been undertaken to scrutinise the mechanism by which methanol reacts on a V_2O_5 surface. It was found that methoxy groups are formed in a manner similar to the process on MoO_3, either by dissociative or condensative adsorption; formaldehyde adsorption, whether produced in series from methoxy groups or directly adsorbed, affords dioxymethylene species, which possess poor higher temperature stability. When methanol conversion is low during reaction, dioxymethylene units can react with methanol to produce DMM, while at higher temperatures formaldehyde is produced preferentially. It is the fragility of formaldehyde adsorption which is considered to be essential to highly selective catalysts. This reaction process, *via* DMM to formaldehyde, is thought to occur primarily on the (100) face, which is rich in under-coordinated vanadium.[141] Notwithstanding this assertion by Busca, Sambeth et al. have utilised experimental methods and computational studies to investigate the active site of V_2O_5 in greater detail.[142] They indicate that an active site on the (001) face is more energetically favourable and mechanistically suitable for DMM generation (and hence formaldehyde production) than the (100) face or other defect sites.

1.5.4 Iron molybdate

As a widely used industrial catalyst, iron molybdate has been extensively investigated to better understand its reactivity for over half a century. It is known that all industrial iron molybdate catalysts contain a surplus of molybdenum (as MoO_3) over that required to produce stoichiometric iron molybdate. Without excess MoO_3, the longevity of the catalyst under working conditions is severely hindered. The actual identity of the active phase has triggered much debate, with some suggesting that ferric molybdate itself is the active phase, while others consider the active phase to exist at the boundary between the iron molybdate bulk and the excess Mo. A study of $Fe_2(MoO_4)_3$ alongside MoO_3 and mixtures of single metal oxides for methanol oxidation was performed, revealing that all tested combinations and substances elicited formaldehyde production; it was notable, however, that CO generation is only observed for catalysts containing a Fe_2O_3 moiety.[143] The activation energy for the reaction on iron molybdate was reported as 45.2 $\mathrm{kJ\,mol^{-1}}$, with first order kinetics with respect to oxygen. A separate examination of the mass balance of the reaction noted a loss during pulsed-flow reaction of methanol over iron molybdate with excess MoO_3.[24] It was later shown that, despite good activity in pulsed-flow reaction, pure iron molybdate performs poorly under continuous flows of methanol. The suggested explanation for this difference in reactivity was that reoxidation of iron molybdate during catalysis is difficult, which, when combined with poisoning effects by intermediates and products, impacted the activity of the catalyst. Formaldehyde yield in this experiment was independent of the flow rate, but methanol conversion is not: this led to the erroneous suggestion that the rate-limiting step was the desorption of formaldehyde. A subsequent study noted no major differences in activity for iron molybdate catalysts with Mo:Fe rations between 1.5 and 3.[144]

The importance of the redundant MoO_3 in iron molybdate catalysts has long attracted significant attention. Trifiro et al. surmised that it was necessary for three reasons: to improve the mechanical properties of the catalyst; to ensure the presence of a Mo:Fe ratio greater than 1.5 in the active phase; and to generate *in situ* the MoO_3 required to reoxidise β-$FeMoO_4$ to $Fe_2(MoO_4)_3$.[145] Similarly, Grasseli suggested that excess Mo was necessary to achieve optimal catalytic behaviour (though here for ammoxidation catalysis). This excess MoO_3 was proposed to be a mobile spectator phase whose function is to furnish the reduced catalyst with MoO_3 or $MoO(OH)_2$ with which to reoxidise.[146] The general consensus is now that the active phase is $Fe_2(MoO_4)_3$ and excess MoO_3 is needed to replace the Mo lost through volatilisation.[147]

Irrespective of differing Mo:Fe ratios, surplus quantities of Mo are always found.[148] It was noted that a correlation exists not between excess Mo in the bulk and catalytic activity, but between excess Mo at the surface and selectivity. Additionally, the excess

Mo slightly enhanced the surface area and mechanical strength of the catalyst. Calcination temperature is also known to be highly relevant to the efficacy of an iron molybdate catalyst. Popov et al. determined that, for a stoichiometric iron molybdate, the optimal calcination temperature is 400°C.[149] When calcination is performed below 400°C, the resulting catalyst is not fully crystalline, but rather retains significant amorphous character: it is the properly-formed crystallinity of the 400°C catalyst which affords superior catalytic properties. Calcination at 500 and 600°C also yields effective catalysts, albeit with lesser selectivity and activity than for 400°C. This can be rationalised by considering that once the structure is crystalline (by 400°C), no further heating is required. Indeed such heating is injurious to catalytic properties, for instance through surface area reductions.[149]

Burcham et al. used methanol chemisorption to more intricately examine the active sites of iron molybdate and supported metal oxide catalysts.[114] On a supported MoO_3 catalyst, it was seen that 0.3 methoxy species existed on the surface for each active metal oxide atom at the surface, with steric factors limiting the quantity of methoxy formed. They reported that methanol typically adsorbs as CH_3OH_{ads} on Lewis acid sites and as OCH_{3ads} (methoxy) on Lewis base (or less Lewis acidic) sites. On the iron molybdate surface, the adsorption sites are Mo cations, which due to their inherent acidity, tend to support CH_3OH_{ads}. Interestingly, it was observed that the catalytic properties (in this instance turnover frequencies, TOFs) for bulk metal oxide catalysts and supported single oxides do not differ significantly. The authors attribute this to the formation of a molybdenum oxide monolayer at the surface of the bulk metal oxides. It appears that electronic ligand effects control TOF during methanol oxidation, with increases in ligand electronegativity accompanied by reductions in TOF. They concluded that disparities in the electronics of Mo-O-ligand bonds induced the observed differences in TOF.[114] More recent studies have modelled the surface of $Fe_2(MoO_4)_3$ by utilising MoO_3 atop Fe_2O_3.[107,150] These catalysts possess a Mo-rich surface, whose outermost layer resembles MoO_3: this provides further credibility to the suggestion that the outermost surface of iron molybdate is indeed a molybdenum oxide monolayer.

During the production of formaldehyde, despite the excellent selectivity of iron molybdate, by-products can still form. In a review of iron molybdate catalysts, Tatibouët discussed the alternative reactions which can occur over iron molybdate, and developed a reaction scheme which showed that, with the exception of DME, all product-forming reactions have a prerequisite oxidation step (Figure 1.7).[109] He proposed further that product selectivity derived directly from structural differences in the catalyst, in particular acid-

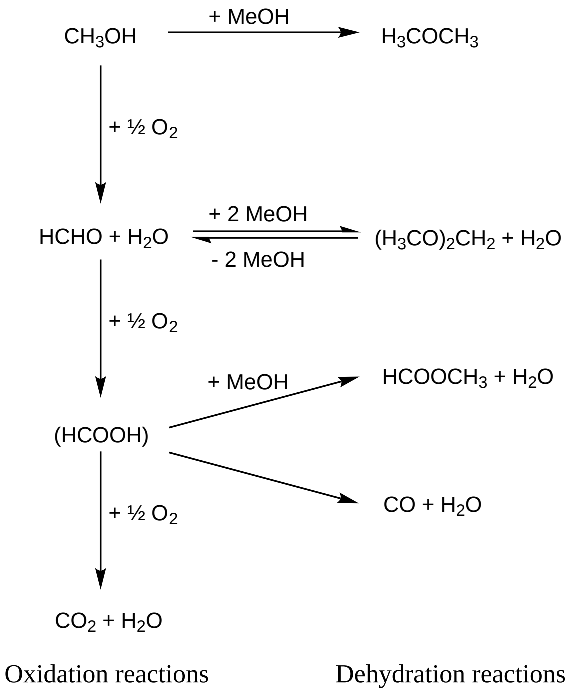

Figure 1.7: A summary of the reactions which can occur on iron molybdate catalysts in the presence of methanol.

base properties. Selectivity to formaldehyde increases with greater methanol conversion until high conversions, after which production of CO—the major by-product—commences in earnest. CO usually arises from the oxidation of selectively formed formaldehyde, but at high temperatures can form directly from the oxidation of reactant methanol.[151]

In summary, while some debate continues regarding the precise nature of the active sites on iron molybdate catalysts, it is accepted that the $Fe_2(MoO_4)_3$ catalyst supports a selective Mo-rich monolayer at the surface.[107,150,152] This is an important consideration for the works reported in this thesis, as it directly leads to the principle of modelling iron molybdate by using shell-core molybdena on haematite catalysts.

1.5.5 Summary of metal oxide methanol oxidation reactivities

There are several reasons why one must heed the selectivities displayed by simple metal oxides and bulk metal oxides when considering MO_x/Fe_2O_3 shell-core catalyst structures. Firstly, knowledge of these oxides can direct the choice of shell material to maximise the return on research efforts invested: in other words, the oxide in question must be suitably selective and sufficiently "interesting" to warrant investigation. Secondly, the precise behaviour of each component in a shell-core catalyst must be understood when employed in isolation: the techniques used to gauge the degree of shell-core segregation demand that sufficiently different reactivity is demonstrated by shell and core sections. To assist with this, it is useful to summarise the fundamental reactivities of oxides pertinent to this thesis (Table 1.4):

Table 1.4: A comparison of reactivities for metal oxide catalysts in methanol selective oxidation, as measured by the author during the work reported in this thesis. Each sample mass: 250 mg.

Catalyst	Major selective product(s)	50% conversion temperature (°C)
MoO_3	Formaldehyde	350
$Fe_2(MoO_4)_3$	Formaldehyde	240
V_2O_5	Formaldehyde	250
$FeVO_4$	Formaldehyde	230
WO_3	Formaldehyde	400
Ta_2O_5	Formaldehyde & DME	400
Nb_2O_5	DME	350
Al_2O_3	DME	200

1.6 Shell-core catalysts

The abilities and utility of iron molybdate catalysts are well known, but full understanding of the active surface has remained elusive. If one wishes to improve heterogeneous catalysts like iron molybdate, one must firstly completely understand the surface of the catalyst. This is, however, an arduous proposition. The difficulties encountered during attempts to elucidate the nature of the surface are compounded by the structure of iron molybdate: as a proportion of the overall structure, the surface layers of a bulk iron molybdate catalyst are a distinct minority. The solution is to produce structures supporting more surface, while reducing the amount of bulk material present.

It is known that the surface layers of iron molybdate catalysts are rich in molybdenum (likely in the form of MoO_3-like units, MoO_x, which accumulate only at the surface), and these are considered to be the active site for methanol oxidation.[107,150,152] The corollary of this is that synthesis of similar model surfaces rich in MoO_x on other supports with a range of properties might represent an easier analytical target. Using synthetic techniques which favour surface segregation and ensure Mo does not enter the bulk, all Mo characterisation data obtained from such samples will be from the surface. This methodology is particularly useful for techniques like X-ray Absorption spectroscopy (XAS), a bulk averaging but element-specific technique. If the element of interest exists only at the surface, then all acquired XAS data from that element originates from the surface; in other words, such segregated catalysts render the technique “quasi-surface sensitive”.

A multitude of studies have been reported detailing experiments with model supported molybdena catalysts, typically covering those using haematite supports, though some interest has been directed to supported iron molybdate catalysts also.[106,153] Other iron oxide supports have also been employed, such as Fe_3O_4, which was investigated as a support for molybdena by Bamroomgwongdee et al. in 2013.[154] The relationship between the Mo-rich surface and reactivity was investigated using filament deposition of Mo on iron oxide supports: the quantity of Mo atop the surface greatly influences reactivity with methanol. Once placed on the surface, the Mo exists as stable Mo(VI), its highest oxidation state. Beyond 300°C, however, the surface Mo is observed to migrate into the iron oxide support, forming a thin layer of $Fe_2(MoO_4)_3$ across the entire surface.

Routray et al. probed the surface of model MoO_x/Fe_2O_3 system, and by extension the surface of iron molybdate, using Low-Energy Ion Scattering (LEIS).[152] MoO_x/Fe_2O_3 catalysts (of 2.3 and 3 wt% MoO_x) were prepared by incipient wetness impregnation using ammonium heptamolybdate and analysed by LEIS. It was seen that the outermost surface layers were Mo-enriched, and Fe was only observed after several sputtering scans had removed sufficient surface material. They concluded that, at 2.3 wt%, a full monolayer of MoO_x was present at the surface of the catalyst.[152] Supporting MoO_x layers atop Fe_2O_3 confers many advantages upon the resulting catalytic behaviour: using a Fe_2O_3 support can greatly improve surface area, benefit surface morphology and increase lattice oxygen mobility (a crucial factor in the MVK mechanism by which methanol oxidation proceeds).

MoO_x/Fe_2O_3 shell-core catalysts have been an ongoing subject of interest within the Bowker group, and indeed are a fundamental theme of this thesis. In 2008, House et al. surveyed both iron molybdate and MoO_x/Fe_2O_3 catalysts to discern important structural information about the surface of the catalysts.[107] Using aberration-corrected electron microscopy with spectroscopic techniques, a line-scan revealed an abundance of Mo at either surface of a particle of iron molybdate, confirming the hypothesis that the surface is rich in Mo species. Subsequently, in an attempt to clarify whether $Fe_2(MoO_4)_3$ acts merely as a benign support or as a direct participant in catalysis, Brookes et al. examined monolayers of MoO_x atop Fe_2O_3 cores spectroscopically. They found that the surface of such shell-core catalysts are similarly Mo-enriched, with electron microscopy showing clear segregation of Mo to the surface layers of imaged particles.[155] The precise surface species in MoO_x/Fe_2O_3 catalysts (and by extension in iron molybdate) have yet to be definitively identified, but XAS suggests that the surface consists of molybdena-like units. XAS enables oxidation states and coordination geometry to be relatively easily discerned, and can (albeit with more difficulty) also provide significant structural information (e.g. neighbouring atomic distances). The XAS studies conducted by Brookes et al. determined that the outermost surface layer comprised octahedral MoO_x units, and with density functional theory (DFT) computational studies suggested that the active species resembled MoO_3 directly atop Fe_2O_3.[150] XAS is rarely, however, conclusive. The coordination geometry of MoO_3 is commonly denoted as octahedral, particularly in prior XAS studies, but this is an oversimplification. In reality, it is the coordination environment of **crystalline** MoO_3 that is octahedral, and even then it is heavily distorted. MoO_3 does not exclusively exist as octahedral MoO_3: indeed, a range of structures is accessible depending on the situation in which MoO_3 exists.[156–158] Importantly, it has been reported that MoO_3 adopts a tetrahedral structure when dispersed as a monolayer phase across a metal oxide support.[159] As a corollary, it cannot be assumed that MoO_x units atop Fe_2O_3 will exist octahedrally: many other structures are possible.

Considerable insight into how to synthesise, analyse and utilise MoO_x/Fe_2O_3 catalysts has been gained over the past few years within the Bowker group. A fundamental requirement of MoO_x/Fe_2O_3 shell-core catalysts is that the shell and core components be properly segregated. Due to the inherent differences in reactivity with methanol between MoO_x and Fe_2O_3 (namely that MoO_x is selective to formaldehyde while Fe_2O_3 combusts to CO_2), great care must be taken to ensure the catalyst displays the desired behaviour. To achieve this, it is necessary that the Fe_2O_3 portion be unable to directly participate in the catalysis at the surface, lest methanol be (very readily) combusted. This is accomplished by ensuring that the MoO_x shell encapsulates the Fe_2O_3 core to the greatest possible extent, and requires careful control of calcination temperatures.[155] The mainstay technique for determining efficacious core segregation is temperature programmed desorption (TPD), an inherently surface-sensitive technique. For MoO_x/Fe_2O_3 catalysts, if CO_2 production is witnessed during TPD, the shell is insufficiently formed and the core is exposed. It is known that methanol combustion on Fe_2O_3 proceeds *via* a bidentate formate intermediate, and that its formation requires multiple Fe sites in close proximity to be accessible to incoming methanol. Accordingly, should CO_2 arise from MoO_x/Fe_2O_3 during TPD, it can be inferred that significant portions of the Fe_2O_3 core are exposed to methanol, providing the multiple Fe sites required for the thermodynamically preferred combustion process. This is a pivotal consideration for all metal oxide shell-haematite core catalysts.

Since comparisons of novel catalyst reactivities are frequently made with existing MoO_x/Fe_2O_3 catalytic behaviour throughout this thesis, it is necessary to understand the fundamental reactivity of MoO_x/Fe_2O_3 catalysts. This is best shown in TPD (Figure 1.8) and in pulsed-flow reaction studies (Figure 1.9); the niceties of these techniques are discussed elsewhere, but it is important at this stage to understand the major trends. In methanol TPD, MoO_x/Fe_2O_3 catalysts perform well, producing large quantities of formaldehyde alongside CO: crucially there is no CO_2 observed by TPD for a properly formed MoO_x/Fe_2O_3 catalyst. Similarly, when exposed to methanol under oxygenic conditions, MoO_x/Fe_2O_3 catalysts demonstrate strong formaldehyde selectivity and appreciable activity, with an overall formaldehyde yield of approximately 85%. CO_2 is observed when under oxygen, though this arises not from improper selectivity but the subsequent combustion of selectively formed products. It is worthwhile to be cognisant of these reactivity trends when perusing the later chapters.

1.7 Research objectives

While significant headway has been made in exploring metal oxide selective oxidation catalysts, a rich vein of new catalysts and applications remains to be explored. Molybdenum-containing catalysts are widely regarded as the most effective choice for formaldehyde production, and consequently have been the focus of attention thus far. MoO_x/Fe_2O_3 shell-core catalysts are convenient model systems to represent the surface layers of the iron molybdate catalysts used in industry, and notable progress has been made in exploring the formation of these systems, their structural constitution and their catalytic behaviour. This thesis will continue the study of such systems. Alongside further exploration of MoO_x systems, the first chapter of results will detail the logical development of the shell-core concept demonstrated by MoO_x/Fe_2O_3: namely, to extend it to alternative metal oxides of relevance to selective oxidation, such as vanadia. It is hoped that the significant analytical advantages acquired through shell-core catalysts (e.g. XAS "surface-sensitivity") might facilitate the exploration of the niceties of other selective oxidation catalysts and other catalytic processes. While vanadia catalysts are more typically renowned in catalytic processes other than methanol oxidation (e.g. propane/propylene oxidation), the novel selective materials in this chapter will be explored in the context of methanol oxidation. In this manner, the validity of the shell-core design to other metal oxides can be fairly assessed.

The second chapter will concern modifications to the haematite core used in MO_x/Fe_2O_3

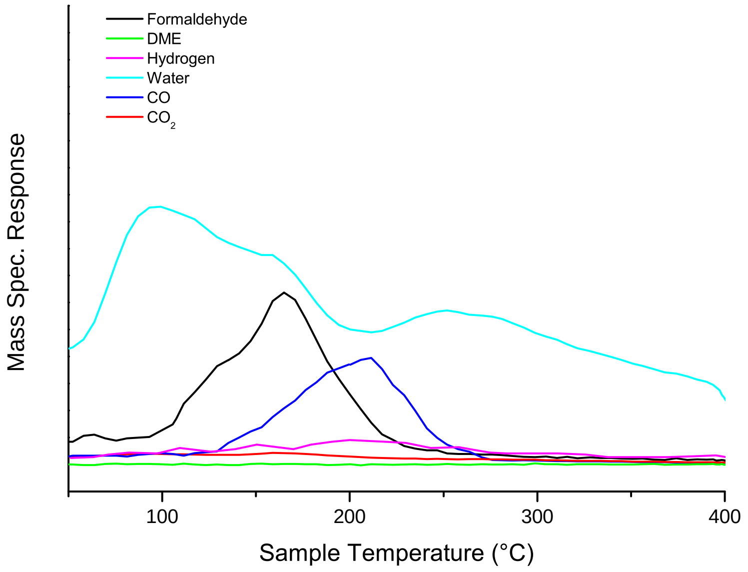

Figure 1.8: Methanol TPD data for a MoO_x/Fe_2O_3 catalyst. Gas flow: 30 mL/min pure He. Catalyst mass: 250 mg.

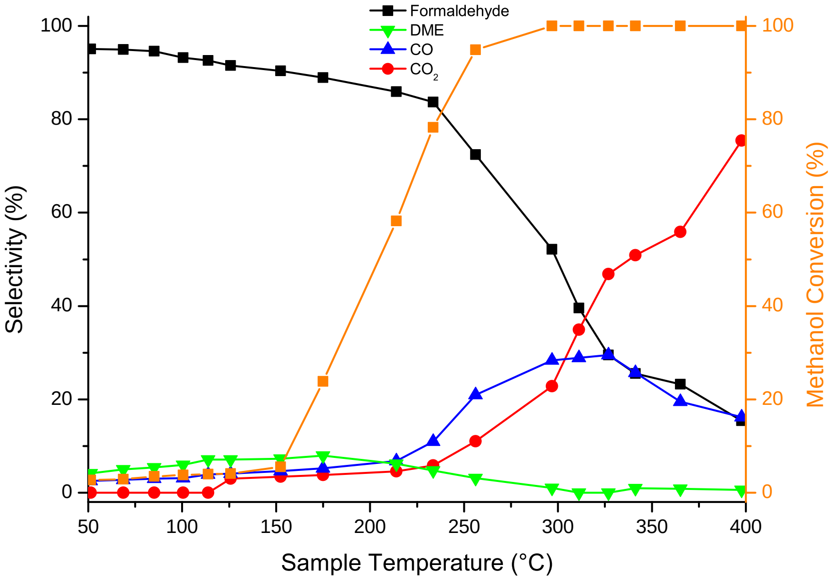

Figure 1.9: Methanol pulsed flow reaction data for a MoO_x/Fe_2O_3 catalyst. Gas flow: 30 mL/min 10% O_2 in He. Catalyst mass: 250 mg.

catalysts (where M = Mo, V, etc.). It has been shown previously that surface area can be influenced by dopants in Fe_2O_3. Given that the success of a catalyst is influenced strongly by surface area, any means to enhance it are worthy of study. The addition of aluminium dopants to Fe_2O_3 will be examined in terms of surface area benefits, and also in terms of any changes to the resulting catalysis. In other words, increases in catalytic activity through higher surface areas must not materialise to the detriment of selectivity. The available quantities of dopants, their impact on reactivity and their structural effects on haematite will be studied, both when used as a catalyst directly and also when used as a support for a selective metal oxide like MoO_3.

In the third chapter, the concept of magnetocatalysis will be explored. Magnetocatalysis is a relatively novel field, but has attracted only niche interest in the last several decades. The intention herein is to examine the effects on selectivity afforded by inherent magnetism and changes in magnetism during catalysis. Since selectivity derives from the energetic differences of electronic orbitals, and these can be influenced by magnetic fields, whether such influence is enough to shift product distributions during reaction will be examined. Methanol oxidation will remain the reaction of interest, due to the large body of prior research which will assist in understanding any magnetic effects. Shell-core catalysts represent a promising means to test a proof of concept for magnetocatalytic effects. Instead of incorporating Fe_2O_3 cores, these shell-core catalysts will contain a magnetically active core material, namely cobalt ferrite. These supports will, like MoO_x/Fe_2O_3, be dosed with monolayer MoO_x to produce selective magnetic catalysts. Additionally, methods to modify the magnetic properties of magnetic materials will be explored, particularly focussing on means to modify the Curie temperature of a catalyst support. In doing so, the effects of inherent magnetism together with the consequences of applying or removing magnetic fields during catalysis will be explored.

References

(1) K. J. Laidler, in *IUPAC Recommendations 1996*, 1, 1996, vol. 68, ch. A glossary of terms used in chemical kinetics, including reaction dynamics, p. 149.

(2) G. M. Whitesides and C.-H. Wong, *Angewandte Chemie International Edition in English*, 1985, **24**, 617–638.

(3) P. E. McGovern, J. Zhang, J. Tang, Z. Zhang, G. R. Hall, R. A. Moreau, A. Nunez, E. D. Butrym, M. P. Richards, C.-s. Wang, G. Cheng, Z. Zhao and C. Wang, *Proceedings of the National academy of Sciences of the United States of America*, 2004, **101**, 17593–17598.

(4) B. Lindström and L. J. Pettersson, *CATTECH*, 2003, **7**, 130–138.

(5) J. W. Mellor, *The Journal of Physical Chemistry*, 1902, **7**, 557–567.

(6) H. Davy, *Philosophical Transactions of the Royal Society of London*, 1817, **107**, 77–85.

(7) M. Faraday, *Philosophical Transactions of the Royal Society of London*, 1834, **124**, 55–76.

(8) J. Berzelius, *Årsberättelse om framstegen i fysik och kemi*, Norstedt, 1835.

(9) G. Lemoine, *Annales de Chimie et de Physique*, 1877, **5**, 145–253.

(10) L. Lloyd, *Handbook of Industrial Catalysts*, Springer US, 2011.

(11) E. Oppermann, *Process of treating organic substances in presence of vanadium compounds.* US Patent 823435, 1906.

(12) *Ammonia, Ullmann's Encyclopedia of Industrial Chemistry*, Wiley-VCH Verlag GmbH, 2000.

(13) D. J. Cole-Hamilton and R. P. Tooze, *Homogeneous Catalysis — Advantages and Problems*, ed. D. J. Cole-Hamilton and R. P. Tooze, Springer Netherlands, Dordrecht, 2006, pp. 1–8.

(14) N. Mizuno and M. Misono, *Chemical Reviews*, 1998, **98**, 199–218.

(15) R. K. Grasselli, *Topics in Catalysis*, 2002, **21**, 79–88.

(16) P. T. Anastas and J. C. Warner, in *Green Chemistry: Theory and Practice*, Oxford University Press, 2000.

(17) R. Schlögl, *Topics in Catalysis*, 2016, **59**, 1461–1476.

(18) R. G. Teller, J. F. Brazdil, R. K. Grasselli and W. Yelon, *Journal of the Chemistry Society, Faraday Transactions 1: Physical Chemistry*, 1985, **81**, 1693–1704.

(19) G. Mestl, J. L. Margitfalvi, L. Vegvari, G. P. Szijjarto and A. Tompos, *Applied Catalysis A: General*, 2014, **474**, B. Delmon Honor Special Issue, 3–9.

(20) P. Mars and D. van Krevelen, *Chemical Engineering Science*, 1954, **3**, The Proceedings of the Conference on Oxidation Processes, 41–59.

(21) C. N. Satterfield, *AIChE Journal*, 1981, **27**, 174–176.

(22) G. W. Keulks, *Journal of Catalysis*, 1970, **19**, 232–235.

(23) R. Wragg, P. Ashmore and J. Hockey, *Journal of Catalysis*, 1971, **22**, 49–53.

(24) G. Liberti, N. Pernicone and S. Soattini, *Journal of Catalysis*, 1972, **27**, 52–55.

(25) N. Pernicone, F. Lazzerin, G. Liberti and G. Lanzavecchia, *Journal of Catalysis*, 1969, **14**, 293–302.

(26) N. Pernicone, F. Lazzerin, G. Liberti and G. Lanzavecchia, *Journal of Catalysis*, 1969, **14**, 391–393.

(27) C. Doornkamp and V. Ponec, *Journal of Molecular Catalysis A: Chemical*, 2000, **162**, In honour of Prof. H. Knözinger on the occasion of his 65th, 19–32.

(28) E. Fiedler, G. Grossmann, D. B. Kersebohm, G. Weiss and C. Witte, in *Ullmann's Encyclopedia of Industrial Chemistry*, American Cancer Society, 2000, ch. Methanol.

(29) D. Lide, *CRC Handbook of Chemistry and Physics 86th Edition*, Taylor & Francis, 2005.

(30) R. Boyle, *The Sceptical Chymist*, J. Cadwell, 1661.

(31) Procès-verbaux des séances de l'Académie, 1834.

(32) A. Mittasch and M. Pier, US Patent 1569775, 1926.

(33) S. Lee, J. Speight and S. Loyalka, *Handbook of Alternative Fuel Technologies, Second Edition*, Taylor & Francis, 2014.

(34) R. Reimert, F. Marschner, H.-J. Renner, W. Boll, E. Supp, M. Brejc, W. Liebner and G. Schaub, in *Ullmann's Encyclopedia of Industrial Chemistry*, Wiley, 2011, ch. Gas Production, 2. Processes.

(35) N. D. Brinkman, R. Halsall, S. W. Jorgensen and J. E. Kirwan, SAE Technical Paper, SAE International, 1994.

(36) A. M. Bahmanpour, A. Hoadley and A. Tanksale, *Reviews in Chemical Engineering*, 2014, **30**, 583–604.

(37) G. J. Sunley and D. J. Watson, *Catalysis Today*, 2000, **58**, 293–307.

(38) U. Olsbye, S. Svelle, M. Bjorgen, P. Beato, T. V. W. Janssens, F. Joensen, S. Bordiga and K. P. Lillerud, *Angewandte Chemie International Edition*, 2012, **51**, 5810–5831.

(39) P. Tian, Y. Wei, M. Ye and Z. Liu, *ACS Catalysis*, 2015, **5**, 1922–1938.

(40) G. A. Olah, *Chemical & Engineering News Archive*, 2003, **81**, 5.

(41) G. A. Olah, *Angewandte Chemie International Edition*, 2005, **44**, 2636–2639.

(42) G. A. Olah, A. Goeppert and G. K. S. Prakash, *The Journal of Organic Chemistry*, 2009, **74**, PMID: 19063591, 487–498.

(43) G. A. Olah, *Angewandte Chemie International Edition*, 2013, **52**, 104–107.

(44) R. C. Weast, *CRC Handbook of Chemistry and Physics. 62nd Edition*, CRC Press, 1983.

(45) A. W. Franz, H. Kronemayer, D. Pfeiffer, R. D. Pilz, G. Reuss, W. Disteldorf, A. O. Gamer and A. Hilt, *Ullmann's Encyclopedia of Industrial Chemistry*, 2000, 1–34.

(46) J. Liebig, *Annalen der Chemie und Pharmacie*, C.F. Winter'sche, 1859.

(47) O. L. Erdmann, *Journal für praktische Chemie*, J. A. Barth., 1868.

(48) J. Meikle, *American Plastic: A Cultural History*, Rutgers University Press, 1995.

(49) Y. Cao, W.-L. Dai and J.-F. Deng, *Applied Catalysis A: General*, 1997, **158**, L27–L34.

(50) M. Qian, M. Liauw and G. Emig, *Applied Catalysis A: General*, 2003, **238**, 211–222.

(51) H. Adkins and W. R. Peterson, *Journal of the American Chemical Society*, 1931, **53**, 1512–1520.

(52) G. Reuss, W. Disteldorf, A. O. Gamer and A. Hilt, in *Ullmann's Encyclopedia of Industrial Chemistry*, American Cancer Society, 2000, ch. Formaldehyde.

(53) H. Schurink, *Organic Syntheses*, 2003, **4**, 53–53.

(54) H.-J. Arpe and S. Hawkins, *Industrial Organic Chemistry*, Wiley, 2010.

(55) B. I. Popov and N. G. Skomorokhova, *Reaction Kinetics and Catalysis Letters*, 1982, **18**, 101–105.

(56) A. Andersson, M. Hernelind and O. Augustsson, *Catalysis Today*, 2006, **112**, 40–44.

(57) M. Bowker, R. Holroyd, A. Elliott, P. Morrall, A. Alouche, C. Entwistle and A. Toerncrona, *Catalysis Letters*, 2002, **83**, 165–176.

(58) N. Greenwood and A. Earnshaw, *Chemistry of the Elements*, Elsevier Science, 2012.

(59) E. Wildermuth, H. Stark, G. Friedrich, F. L. Ebenhöch, B. Kühborth, J. Silver and R. Rituper, in *Ullmann's Encyclopedia of Industrial Chemistry*, American Cancer Society, 2000, ch. Iron Compounds.

(60) B. Rodak, G. Fritsma and K. Doig, *Hematology: Clinical Principles and Applications*, Saunders Elsevier, 2007.

(61) R. C. Hider and X. Kong, in *Interrelations between Essential Metal Ions and Human Diseases*, ed. A. Sigel, H. Sigel and R. K. Sigel, Springer Netherlands, Dordrecht, 2013, ch. Iron: Effect of Overload and Deficiency, pp. 229–294.

(62) N. C. Andrews, *New England Journal of Medicine*, 1999, **341**, 1986–1995.

(63) Der Königl. Schwedischen Akademie der Wissenschaften neue Abhandlungen aus der Naturlehre, Haushaltungskunst und Mechanik, 1783.

(64) J. Emsley, *Nature's Building Blocks: An A-Z Guide to the Elements*, Oxford University Press, 2003.

(65) A. Iron and S. Institute, *Steel Facts*, American Iron and Steel Institute, 1948.

(66) Der Königl. Schwedischen Akademie der Wissenschaften neue Abhandlungen aus der Naturlehre, Haushaltungskunst und Mechanik, 1789.

(67) C. Gupta, *Extractive Metallurgy of Molybdenum*, Taylor & Francis, 1992.

(68) R. Bjornsson, M. U. Delgado-Jaime, F. A. Lima, D. Sippel, J. Schlesier, T. Weyhermüller, O. Einsle, F. Neese and S. DeBeer, *Zeitschrift für anorganische und allgemeine Chemie*, 2015, **641**, 65–71.

(69) M. Schmidt, in *Anorganische Chemie II*, Bibliographisches Institut, 1969, ch. VI. Nebengruppe, pp. 119–127.

(70) H. J. Cohen, R. T. Drew, J. L. Johnson and K. V. Rajagopalan, *Proceedings of the National Academy of Sciences*, 1973, **70**, 3655–3659.

(71) M. Ostrooumov and Y. Taran, *Mineralogical Magazine*, 2018, 371–382.

(72) E. Hukkanen and H. Walden, *International Journal of Mineral Processing*, 1985, **15**, 89–102.

(73) N. G. Sefström, *Annalen der Physik*, 1831, **97**, 43–49.

(74) H. E. Roscoe, *Proceedings of the Royal Society of London*, 1870, **18**, 37–42.

(75) J. W. Marden and M. N. Rich, *Industrial & Engineering Chemistry*, 1927, **19**, 786–788.

(76) H. Chandler, *Metallurgy for the Non-Metallurgist*, Taylor & Francis, 1998.

(77) F. Betz, *Managing Technological Innovation: Competitive Advantage from Change*, Wiley, 2003.

(78) N. Yefimov, S. Naboychenko, O. Neikov, I. Mourachova, V. Gopienko, I. Frishberg and D. Lotsko, *Handbook of Non-Ferrous Metal Powders: Technologies and Applications*, Elsevier Science, 2009.

(79) S. W. Lovesey, A. Rodriguez-Fernandez and J. Blanco, *Physical Review B*, 2011, **83**.

(80) T. Zhai and J. Yao, *One-Dimensional Nanostructures: Principles and Applications*, Wiley, 2013.

(81) J.-E. Jørgensen, L. Mosegaard, L. E. Thomsen, T. R. Jensen and J. C. Hanson, *Journal of Solid State Chemistry*, 2007, **180**, 180–185.

(82) R. Grau-Crespo, A. Y. Al-Baitai, I. Saadoune and N. H. De Leeuw, *Journal of Physics: Condensed Matter*, 2010, **22**, 255401.

(83) J. Tuček, R. Zbořil, A. Namai and S.-i. Ohkoshi, *Chemistry of Materials*, 2010, **22**, 6483–6505.

(84) J. López-Sáñchez, A. Muñoz-Noval, A. Serrano, M. Abuín, A. de la Figuera, J. F. Marco, L. Pérez, N. Carmona and O. Rodríguez de la Fuente, *RSC Advances*, 2016, 46380–46387.

(85) R. F. Sebenik, A. R. Burkin, R. R. Dorfler, J. M. Laferty, G. Leichtfried, H. Meyer-Grünow, P. C. H. Mitchell, M. S. Vukasovich, D. A. Church, G. G. Van Riper, J. C. Gilliland and S. A. Thielke, in *Ullmann's Encyclopedia of Industrial Chemistry*, American Cancer Society, 2000, ch. Molybdenum and Molybdenum Compounds.

(86) F. Ferreira, T. G. S. Cruz, M. Fantini, M. Tabacniks, S. C. de Castro, J. Morais, A. de Siervo, R. Landers and A. Gorenstein, *Solid State Ionics*, 2000, **136-137**, Proceedings of the 12th International Conference on Solid State Ionics, 357–363.

(87) C. Zollfrank, K. Gutbrod, P. Wechsler and J. P. Guggenbichler, *Materials Science and Engineering: C*, 2012, **32**, 47–54.

(88) L. Kihlborg, *Acta Chemica Scandinavica*, 954–962.

(89) N. A. Chernova, M. Roppolo, A. C. Dillon and M. S. Whittingham, *Journal of Materials Chemistry*, 2009, **19**, 2526–2552.

(90) D. O. Scanlon, G. W. Watson, D. J. Payne, G. R. Atkinson, R. G. Egdell and D. S. L. Law, *The Journal of Physical Chemistry C*, 2010, **114**, 4636–4645.

(91) G. Bauer, V. Güther, H. Hess, A. Otto, O. Roidl, H. Roller and S. Sattelberger, in *Ullmann's Encyclopedia of Industrial Chemistry*, American Cancer Society, 2000, ch. Vanadium and Vanadium Compounds.

(92) P. Pareish, *Journal of the Society of Chemical Industry*, 1925, **44**, 451–451.

(93) M. H. Chakrabarti, S. A. Hajimolana, F. S. Mjalli, M. Saleem and I. Mustafa, *Arabian Journal for Science and Engineering*, 2013, **38**, 723–739.

(94) A. A. Shinkle, A. E. S. Sleightholme, L. T. Thompson and C. W. Monroe, *Journal of Applied Electrochemistry*, 2011, **41**, 1191–1199.

(95) S. Roe, C. Menictas and M. Skyllas-Kazacos, *Journal of The Electrochemical Society*, 2016, **163**, A5023–A5028.

(96) V. Shklover, T. Haibach, F. Ried, R. Nesper and P. Novák, *Journal of Solid State Chemistry*, 1996, **123**, 317–323.

(97) I. E. Wachs and B. M. Weckhuysen, *Applied Catalysis A: General*, 1997, **157**, Vanadia catalysts for selective oxidation of hydrocarbons and their derivatives, 67–90.

(98) A. Chakrabarti, K. Hermann, R. Druzinic, M. Witko, F. Wagner and M. Petersen, *Physical Review B*, 1999, **59**, 10583–10590.

(99) M. H. Rapposch, J. B. Anderson and E. Kostiner, *Inorganic Chemistry*, 1980, **19**.

(100) Y. Zhou, S. Adams, R. P. Rao, D. D. Edwards, A. Neiman and N. Pestereva, *Chemistry of Materials*, 2008, **20**, 6335–6345.

(101) N. Imanaka, S. Tamura, Y. Kobayashi, Y. Okazaki, M. Hiraiwa, T. Ueda and G. Adachi, *Journal of Alloys and Compounds*, 2000, **303-304**, 303–306.

(102) G. Fagherazzi and N. Pernicone, *Journal of Catalysis*, 1970, **16**, 321–325.

(103) S. H. Taylor, J. S. J. Hargreaves, G. J. Hutchings and R. W. Joyner, in *Methane and Alkane Conversion Chemistry*, Springer, 1995, ch. Methanol Oxidation Over Oxide Catalysts, pp. 339–345.

(104) G. Deo and I. Wachs, *Journal of Catalysis*, 1994, **146**, 323–334.

(105) H. Hu and I. E. Wachs, *The Journal of Physical Chemistry*, 1995, **99**, 10911–10922.

(106) G. Jin, W. Weng, Z. Lin, N. F. Dummer, S. H. Taylor, C. J. Kiely, J. K. Bartley and G. J. Hutchings, *Journal of Catalysis*, 2012, **296**, 55–64.

(107) M. P. House, M. D. Shannon and M. Bowker, *Catalysis Letters*, 2008, **122**, 210–213.

(108) P. Hellier, P. P. Wells, D. Gianolio and M. Bowker, *Topics in Catalysis*, 2018, **61**, 357–364.

(109) J. Tatibouët, *Applied Catalysis A: General*, 1997, **148**, 213–252.

(110) L. J. Burcham, G. Deo, X. Gao and I. E. Wachs, *Topics in Catalysis*, 2000, **11**, 85–100.

(111) P. Forzatti, E. Tronconi, A. S. Elmi and G. Busca, *Applied Catalysis A: General*, 1997, **157**, 387–408.

(112) F. Roozeboom, P. D. Cordingley and P. J. Gellings, *Journal of Catalysis*, 1981, **68**, 464–472.

(113) G. Centi, S. Perathoner and S. Tonini, *Catalysis Today*, 2000, **61**, 211–221.

(114) L. J. Burcham, L. E. Briand and I. E. Wachs, *Langmuir*, 2001, **17**, 6164–6174.

(115) A. Glisenti, G. Favero and G. Granozzi, *Journal of the Chemical Society, Faraday Transactions*, 1998, **94**, 173–182.

(116) A. Glisenti, *Journal of the Chemical Society, Faraday Transactions*, 1998, **94**, 3671–3676.

(117) J. Nováková, P. Jíru and V. Zavadil, *Journal of Catalysis*, 1971, **21**, 143–148.

(118) G. Busca and V. Lorenzelli, *Journal of Catalysis*, 1980, **66**, 155–161.

(119) V. Lorenzelli, G. Busca and N. Sheppard, *Journal of Catalysis*, 1980, **66**, 28–35.

(120) M. Bowker, R. Holroyd, M. House, R. Bracey, C. Bamroongwongdee, M. Shannon and A. Carley, *Topics in Catalysis*, 2008, **48**, 158–165.

(121) E. Söderhjelm, M. P. House, N. Cruise, J. Holmberg, M. Bowker, J.-O. Bovin and A. Andersson, *Topics in Catalysis*, 2008, **50**, 145.

(122) M. P. House, A. F. Carley, R. Echeverria-Valda and M. Bowker, *The Journal of Physical Chemistry C*, 2008, **112**, 4333–4341.

(123) R. P. Groff, *Journal of Catalysis*, 1984, **86**, 215–218.

(124) T. Wadayama, T. Saito and W. Suëtaka, *Applications of Surface Science*, 1984, **20**, 199–201.

(125) J. Tatibouët and J. Germain, *Journal of Catalysis*, 1981, **72**, 375–378.

(126) U. Chowdhry, A. Ferretti, L. Firment, C. Machiels, F. Ohuchi, A. Sleight and R. Staley, *Applications of Surface Science*, 1984, **19**, 360–372.

(127) J. N. Allison and W. A. Goddard, *Journal of Catalysis*, 1985, **92**, 127–135.

(128) R. L. Smith and G. S. Rohrer, *Journal of Catalysis*, 1996, **163**, 12–17.

(129) W.-H. Cheng, *Journal of Catalysis*, 1996, **158**, 477–485.

(130) M. G. O'Brien, A. M. Beale, S. D. M. Jacques, T. Buslaps, V. Honkimaki and B. M. Weckhuysen, *The Journal of Physical Chemistry C*, 2009, **113**, 4890–4897.

(131) M. Bowker, A. F. Carley and M. House, *Catalysis Letters*, 2007, **120**, 34.

(132) W. E. Farneth, F. Ohuchi, R. H. Staley, U. Chowdhry and A. W. Sleight, *The Journal of Physical Chemistry*, 1985, **89**, 2493–2497.

(133) M. Ai, *Journal of Catalysis*, 1978, **54**, 426–435.

(134) G. C. Bailey and A. E. Craver, US Patent 1383059, 1921.

(135) R. Mann and M. Dosi, *Journal of Catalysis*, 1973, **28**, 282–288.

(136) S. Bhattacharyya, K. Janakiram and N. Ganguly, *Journal of Catalysis*, 1967, **8**, 128–136.

(137) J. Tatibouët and J. Germain, *Comptes rendus hebdomadaires des séances de l'Académie des sciences. Série C, Sciences chimiques*, 1979, **289**, 305.

(138) J. Tatibouët and J. Germain, *Comptes rendus de l'Académie des Sciences*, 1983, **296**, 613.

(139) A. Baiker and D. Monti, *Journal of Catalysis*, 1985, **91**, 361–365.

(140) D. Gasser and A. Baiker, *Journal of Catalysis*, 1988, **113**, 325–333.

(141) G. Busca, *Journal of Molecular Catalysis*, 1989, **50**, 241–249.

(142) J. Sambeth, L. Gambaro and H. Thomas, *Adsorption Science & Technology*, 1995, **12**, 171–180.

(143) K. Habersberger and P. Jíru, *Collection of Czechoslovak Chemical Communications*, 1972, **37**, 535–540.

(144) T. H. Kim, B. Ramachandra, J. S. Choi, M. B. Saidutta, K. Y. Choo, S.-D. Song and Y.-W. Rhee, *Catalysis Letters*, 2004, **98**, 161–165.

(145) F. Trifirò, M. Carbucicchio and P. Villa, *Hyperfine Interactions*, 1998, **111**, 17–22.

(146) R. K. Grasselli and M. A. Tenhover, in *Handbook of Heterogeneous Catalysis*, American Cancer Society, 2008, ch. Ammoxidation, pp. 3489–3517.

(147) A. P. V. Soares, M. F. Portela and A. Kiennemann, *Catalysis Reviews*, 2005, **47**, 125–174.

(148) T. Nguyen Van, P. Tittarelli and P. L. Villa, 3rd International Conference on the Chemistry and Uses of Molybdenum, 1979, p. 161.

(149) B. I. Popov and N. G. Smokorokhova, *Reaction Kinetics and Catalysis Letters*, 1982, **18**, 107–110.

(150) C. Brookes, P. P. Wells, N. Dimitratos, W. Jones, E. K. Gibson, D. J. Morgan, G. Cibin, C. Nicklin, D. Mora-Fonz, D. O. Scanlon, C. R. A. Catlow and M. Bowker, *The Journal of Physical Chemistry C*, 2014, **118**, 26155–26161.

(151) A. V. Soares, M. F. Portela and A. Kiennemann, in *Reaction Kinetics and the Development and Operation of Catalytic Processes*, ed. G. Froment and K. Waugh, Elsevier, 2001, vol. 133, pp. 489–494.

(152) K. Routray, W. Zhou, C. J. Kiely, W. Grünert and I. E. Wachs, *Journal of Catalysis*, 2010, **275**, 84–98.

(153) G. Shi, T. Franzke, M. D. Sánchez, W. Xia, F. Weis, M. Seipenbusch, G. Kasper and M. Muhler, *ChemCatChem*, 2012, **4**, 760–765.

(154) C. Bamroongwongdee, M. Bowker, A. F. Carley, P. R. Davies, R. J. Davies and D. Edwards, *Faraday Discussions*, 2013, **162**, 201–212.

(155) C. Brookes, P. P. Wells, G. Cibin, N. Dimitratos, W. Jones, D. J. Morgan and M. Bowker, *ACS Catalysis*, 2014, **4**, 243–250.

(156) H. Hu, I. E. Wachs and S. R. Bare, *The Journal of Physical Chemistry*, 1995, **99**, 10897–10910.

(157) S. C. Street and D. W. Goodman, *Journal of Vacuum Science & Technology A*, 1997, **15**, 1717–1723.

(158) H. Tian, C. A. Roberts and I. E. Wachs, *The Journal of Physical Chemistry C*, 2010, **114**, 14110–14120.

(159) W. Shi, X. Cai, J. Wei, J. Ma, T. Hu, N. Wu and Y. Xie, *Surface and Interface Analysis*, 2001, **32**, 202–204.

Chapter 2

Experimental

2.1 Introduction

In this chapter the preparation of catalyst materials will be detailed, alongside discussion of the characterisation techniques used in their analysis. All starting materials and reagents used during synthesis were commercially obtained (unless noted otherwise). All distilled water utilised in these studies was obtained from a Thermo Scientific Barnstead NANOpure Water Purification System. Carbolite laboratory furnaces were employed for drying and calcination; all calcinations were performed in air, unless otherwise stated.

2.1.1 Co-precipitation

Defined by IUPAC as "the simultaneous precipitation of a normally soluble component with a macro-component from the same solution by the formation of mixed crystals, by adsorption, occlusion or mechanical entrapment",[1] co-precipitation is a highly popular means of synthesising catalysts, both in research settings and in industry. The products of co-precipitation reactions can be significantly altered by changes in solution concentration, acidity, temperature and degree of agitation during reaction. Consequently, these factors must all be carefully controlled to minimise differences between product batches.

2.1.2 Incipient wetness impregnation

Incipient wetness impregnation is commonly used in the synthesis of heterogeneous catalysts, and is a technique of particular relevance to the studies detailed in this thesis. The technique broadly involves:

(i) calculating the internal pore volume of the support material. This is achieved by dosing the support with successive small increments of the solvent (typically water or a volatile organic) and mixing until the material appears wet. The volume of solution used to reach the point of wetting is therefore the volume required to fill the pores;

(ii) determining the quantity of reagent to dissolve in the known solvent volume. As an example, when synthesising shell-core catalysts of MoO_x/Fe_2O_3 with particular monolayer (ML) coverage, the relevant amount of ammonium heptamolybdate (the Mo source) must be determined (see below);

(iii) adding the reagent solution dropwise to the support with thorough mixing, until the point of wetness is reached;

(iv) drying the catalyst at moderate temperatures (typically above 100°C), during which time the volatile solvent phase is removed from the sample, depositing the solute across all surfaces of the support.

Calcination of the catalyst is frequently performed after drying to complete catalyst formation. Incipient wetness impregnation is a reliable method for achieving excellent coverage across the surface of the support, due to rapid uptake of the solution into support pores by capillary action.

Reagent calculations

For each shell-core catalyst synthesised by incipient wetness impregnation, it is necessary to calculate the amount of the appropriate shell oxide precursor required for the reaction to yield the desired depth of shell coverage in the resultant catalyst. The following calculation is a worked example, in this instance to produce a 3 ML MoO_x/Fe_2O_3 catalyst:

- Approximate number of surface atoms = 10^{15} atoms per cm^2 = 10^{19} atoms per m^2.
- 3 ML of MoO_x on the surface are required, hence: $(3)(1\times10^{19}) = 3\times10^{19}$ atoms per m^2.
- The surface area of the calcined Fe_2O_3 used is 20 m^2 g^{-1}.
- Volume of water required to reach the wetting point of one gram of Fe_2O_3 = 0.6 mL.
- The number of atoms required for one gram of $Fe_2O_3 = 6 \times 10^{20}$, all dissolved in 0.6 mL H_2O.
- Scaling up to a litre quantity of reagent solution yields: 9.9996×10^{23} atoms L^{-1}.
  - This in turn reveals that 1.66 moles of Mo are required per litre of solution.

- The molecular mass of the Mo precursor, ammonium heptamolybdate (AHM) = 1236 g mol^{-1}

  $$\text{Mass of AHM in solution} = \frac{(1/7)(1236)(1.66)}{4}$$

  It is assumed for the benefit of the calculation that surface Mo consists of species similar to MoO_3, yielding the divisor expressed in the above equation.

  $$\text{Mass of AHM in solution} = 74 \text{ g L}^{-1}$$

- Since litre quantities of reagent solution are impractical for small-scale synthesis, the quantity of AHM required to produce a 3 ML MoO_x/Fe_2O_3 catalyst can be expressed more usefully thus:

  $$\text{Mass of AHM in solution} = 0.74 \text{ g per 10 mL } H_2O$$

This methodology can be applied to other systems, e.g. VO_x/Fe_2O_3 or MoO_x/Al-Fe_2O_3, but consideration must be made for differences in molecular masses, support surface area and the desired final ML coverage. In addition, certain experimental techniques may require modification if alternative solvents are employed; compared to water, more viscous solvents (e.g. ethanolamine) mix less easily with solid supports.

2.2 Catalyst preparation

In general, bulk multi-component metal oxides (e.g. $FeVO_4$) were synthesised by co-precipitation, while shell-core catalysts were produced *via* incipient wetness impregnation.

2.2.1 Single oxides

Single metal oxides, such as Fe_2O_3, V_2O_5 and Nb_2O_5, were obtained commercially from Sigma Aldrich and calcined at 500°C before catalytic testing or use in synthesis as supports. V_2O_5 has also been produced by the decomposition of ammonium metavanadate, NH_4VO_3, at high temperatures.

2.2.2 Iron molybdates

Iron molybdate was prepared as a reference material to gauge the efficacy of novel MoO_x/VO_x catalysts, and was prepared by co-precipitation of iron(III) nitrate nonahydrate and AHM. The mass of AHM required to achieve the desired Mo loading was dissolved in 100 mL of distilled water, forming a colourless solution, which was then acidified through the addition of dilute HNO_3 (33% dilution) to pH 2. The requisite quantity of $Fe(NO_3)_3 \cdot 9\,H_2O$ was dissolved in 50 mL of distilled water, affording a vividly orange solution, and placed in a dropping funnel. The solution of AHM was heated to 60°C with continuous stirring and positioned beneath the dropping funnel containing $Fe(NO_3)_3 \cdot 9\,H_2O$, which was then added to the solution below in a dropwise fashion. A canary yellow precipitate formed, and following complete addition of the $Fe(NO_3)_3 \cdot 9\,H_2O$ the reaction mixture was heated to 90°C to evaporate most of the water. A wet yellow slurry resulted, which was allowed to air dry for three hours; this was followed by drying overnight in a furnace at 120°C. The resultant dried product was then calcined at 500°C to yield the desired iron molybdate catalyst, $Fe_2(MoO_4)_3$ (Fe:Mo, 1:1.5).

2.2.3 MoO_x/Fe_2O_3 shell-core catalysts

Shell-core catalysts of the form MoO_x/Fe_2O_3, where a shell of MoO_x encapsulates a Fe_2O_3 core, are prepared by incipient wetness impregnation. These catalysts can possess different ML thicknesses of the surface MoO_x depending on the concentration of Mo in the solution. The relevant quantity of AHM to achieve a particular ML coverage was dissolved in a known volume of water, and added slowly to Fe_2O_3 (Sigma Aldrich, calcined at 500°C) with thorough mixing. The wet solid material was then dried overnight at 120°C (yielding a dull red powder) and calcined at 500°C for 24 hours (yielding a more vibrantly red powder, the desired catalyst).

2.2.4 High Surface Area Fe_2O_3

High Surface Area (HSA) Fe_2O_3 was synthesised by co-precipitation of iron(III) nitrate nonahydrate (Sigma Aldrich, $\geq$ 99.95%) and aluminium(III) nitrate nonahydrate (Sigma Aldrich, 99.997%). The appropriate quantity of aluminium(III) nitrate nonahydrate to achieve 5, 10, 15 or 20 wt% Al in the resulting HSA Fe_2O_3 was dissolved in water, acidified to pH 2 with HNO_3 (70%, Sigma Aldrich) and stirred continuously at 60°C. Aqueous iron(III) nitrate nonahydrate was then added dropwise over a period of time, after which stirring was continued for a further thirty minutes. The solution was then evaporated almost to dryness at 90°C, yielding a wet red solid material to be dried overnight at 120°C in a furnace. After drying, the dried product was gently ground by spatula to improve particle size homogeneity. This powdered product was then calcined at 500°C for 24 hours to afford the final product, HSA Fe_2O_3.

2.2.5 MoO_x/HSA Fe_2O_3 shell-core catalysts

These catalysts were produced by incipient wetness impregnation in the same manner as MoO_x/Fe_2O_3 catalysts. Due to the larger surface areas supported by HSA Fe_2O_3, the quantity of AHM required to make the same equivalent ML coverage is increased, resulting in a greater absolute quantity of Mo in the surface layers for the same notional ML coverage.

2.2.6 VO_x/Fe_2O_3 shell-core catalysts

Shell-core catalysts comprising VO_x layer(s) around a Fe_2O_3 core were synthesised by incipient wetness impregnation using Fe_2O_3 as the support and a solution of ammonium metavanadate, NH_4VO_3, in ethanolamine. Due to the poor aqueous solubility of NH_4VO_3, ethanolamine was employed, in which it is sufficiently soluble. The relevant amount of NH_4VO_3 for a specific ML coverage was dissolved in a quantity of ethanolamine known to equal the pore volume of the Fe_2O_3 and mixed thoroughly. The mixture was then dried at 120°C overnight (liberating ammonia and depositing VO_x across the Fe_2O_3 surface), before calcination at 500°C. Lesser temperature calcinations were performed to study the formation of VO_x/Fe_2O_3 catalysts as a function of temperature and calcination duration.

2.2.7 Iron vanadate

Bulk iron vanadate was prepared by co-precipitation of $Fe(NO_3)_3$ and NH_4VO_3 in water. 0.4 g of $Fe(NO_3)_3$ was dissolved in 30 mL H_2O, while 0.11 g of NH_4VO_3 was separately dissolved in 30 mL H_2O. The vanadate solution was stirred and heated to 80°C, forming initially a pale green solution followed by a transparent solution after some time at 80 °C. This was then added dropwise to the solution of $Fe(NO_3)_3$ under constant stirring. The pH of the reaction mixture was then increased through the addition of 2 M NaOH solution, after which the temperature of the reaction mixture was reduced to 55°C; this temperature was maintained with constant stirring for a period of 24 hours, yielding a dark orange precipitate which was collected by vacuum filtration, and washed with liberal quantities of water and ethanol.

2.2.8 NbO_x/Fe_2O_3 shell-core catalysts

Repeated attempts to produce shell-core catalysts with a NbO_x shell were made by incipient wetness impregnation: the relevant quantity of ammonium niobate oxalate hydrate required for a certain ML coverage was dissolved in a quantity of H_2O known to equal the pore volume of the Fe_2O_3 support. The niobate solution was added dropwise with thorough mixing, after which it was dried at 120°C overnight. Calcinations for 24 hours at a range of temperatures from 200 to 500°C were performed, to produce the final catalyst at high temperature and gauge the formation process at lower temperatures. It was observed that NbO_x does not perform similarly to MoO_x or VO_x, but instead fails to form a shell-core catalyst; nonetheless, for consistency these materials are described here as (attempted) shell-core catalysts.

2.2.9 Iron niobate

Bulk iron niobate was prepared by co-precipitation of $Fe(NO_3)_3$ and ammonium niobate oxalate hydrate in water. $Fe(NO_3)_3$ was dissolved in water, heated to 60°C and acidified to pH 2 with HNO_3: thereafter, ammonium niobate oxalate hydrate in water was added dropwise. The resulting mixture was stirred and heated to 80°C, darkening in the process. It was evaporated to dryness, and the solid residue was dried overnight at 120°C before being calcined for 24 hours at 500°C.

2.2.10 Cobalt ferrite

Cobalt ferrite, $CoFe_2O_4$ was synthesised by co-precipitation of iron(III) nitrate nonahydrate and cobalt(II) nitrate hexahydrate in water. 42.6 mL of 0.5 M $Co(NO_3)_2$ and 85.2 mL of 0.5 M $Fe(NO_3)_3$ were mixed, stirred and heated to 60°C, after which 116 mL of 1 M ammonium hydroxide was added dropwise until pH 9 was attained. The resulting claret solution was stirred for a further three hours at 85°C; the precipitate was then collected by vacuum filtration and dried initially on the filter, then overnight in the furnace at 120°C. Following drying, the sample was calcined for four hours at 500°C.

2.2.11 Zn-doped cobalt ferrites

The preparation of Zn-doped cobalt ferrite samples, in which Zn is substituted for a proportion of the Co, proceeded similarly by co-precipitation. A variety of compounds were produced, described by the general formula $Zn_xCo_{1-x}Fe_2O_4$, with differing ratios of starting materials depending on the desired Zn-doping level (Table 2.1). Aqueous solutions of $Zn(NO_3)_2$, $Fe(NO_3)_3$ and $Co(NO_3)_2$ were mixed and heated to 60°C, whereupon 1 M Na_2CO_3 solution was added slowly until pH 10 was reached. After a further hour, the precipitate was obtained by vacuum filtration and washed with distilled water. The resulting solid was dried at 120°C overnight and then calcined at 500°C for four hours.

Table 2.1: Volumes of starting materials required to achieve particular Zn loadings (CoFe denotes cobalt ferrite for clarity).

Zn proportion	$Zn(NO_3)_2$ (mL)	$Co(NO_3)_2$ (mL)	$Fe(NO_3)_3$ (mL)
$Zn_{0.35}$CoFe	17.7	32.9	101.4
$Zn_{0.4}$CoFe	20.2	30.4	101.2
$Zn_{0.45}$CoFe	22.7	27.9	101.1

2.2.12 MoO_x/ZnCoFe shell-core catalysts

Shell-core catalysts comprising MoO_x shells on Zn-doped cobalt ferrite (denoted ZnCoFe for brevity) core supports were synthesised by incipient wetness impregnation. The relevant quantity of AHM (normally sufficient to achieve 6 ML) was dissolved in a quantity of H_2O known to match the internal pore volume of the relevant ZnCoFe support: this solution was added to the ZnCoFe and mixed thoroughly, before being dried overnight at 120°C. After drying, the samples were calcined at 500°C for 24 hours.

2.3 Catalyst characterisation and testing

2.3.1 Brunauer-Emmett-Teller theory

Background theory

Brunauer-Emmett-Teller (BET) theory attempts to understand the physical multilayer adsorption of gas molecules upon a solid surface, and is an excellent tool for the determination of specific surface area. In general, unreactive gaseous adsorbates—such as N_2—are used to probe the surface and quantify the surface area of the sample. The theory is an extension of the Langmuir adsorption model for monolayers to multilayer systems, but with the following postulates:

(i) gas molecules adsorb physically on a solid surface in layers without limit;

(ii) the molecules within one layer can only interact with layers immediately adjacent;

(iii) the Langmuir theory applies to each layer.

With these points considered, this is the BET equation:

$$\frac{1}{v[(p_0/p)-1]} = \frac{c-1}{v_m c}\left(\frac{p}{p_0}\right) + \frac{1}{v_m c} \tag{2.1}$$

where p and p_0 are the equilibrium and saturation pressure of adsorbates at the adsorption temperature, v is the quantity of adsorbed gas, v_m is the quantity of adsorbate per monolayer and c is the BET constant, which is defined as:

$$c = \exp\left(\frac{E_1 - E_L}{RT}\right) \tag{2.2}$$

where E_1 is the heat of adsorption for the first layer, and E_L is the heat of adsorption for the second and subsequent layers (equivalent to the heat of liquefaction).

The BET equation above is an adsorption isotherm, plottable as a straight line with p/p_0 on the x-axis and $1/v[(p_0/p) - 1]$ on the y-axis (although linearity is maintained only for $0.05 < p/p_0 < 0.35$): the resulting graph is a BET plot (Figure 2.1). The BET constant and the value of v_m are obtained from the plot using the slope, A, and the intercept with the ordinate, I, using the following equations:

$$c = 1 + \frac{A}{I} \tag{2.3}$$

$$v_m = \frac{1}{A + I} \tag{2.4}$$

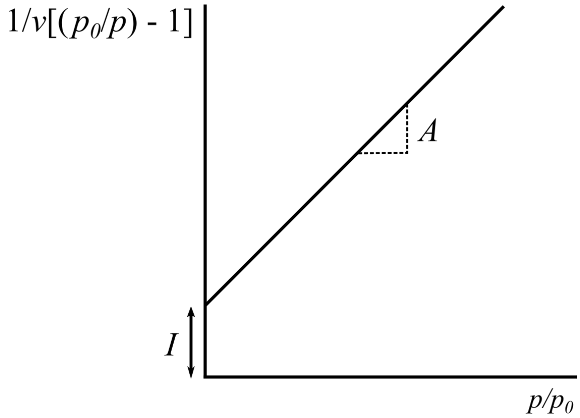

Figure 2.1: The BET plot.

Calculation of the total surface area, S_{total}, and the specific surface area, S_{BET}, can be achieved with the following equations:

$$S_{\text{total}} = \frac{(v_m \cdot N_A \cdot s)}{V} \tag{2.5}$$

$$S_{\text{BET}} = \frac{S_{\text{total}}}{a} \tag{2.6}$$

where v_m must be in units of volume, N_A is the Avogadro constant, s is the adsorption cross section of the sample undergoing measurement, V is the molar volume of the adsorbate and a is the sample mass.

Experimental

BET measurements were performed using a Quantachrome Quadrasorb Evo analyser and all samples were degassed overnight before analysis under strong vacuum and at elevated temperature. Several measurements of gas pressure were recorded and plotted to produce an adsorption isotherm: this isotherm can then be used with the BET equation to calculate surface area values. Each sample tube was placed into a dewar of liquid nitrogen for the entire duration of the measurement.

2.3.2 CATLAB techniques

The Hiden CATLAB reactor system was heavily used throughout the entire range of studies reported in this thesis. Essentially, it is a catalyst microreactor designed to mimic industrial processes on a smaller scale, possessing a powerful furnace, multiple mass flow controllers (MFCs) and a highly sensitive quadrupole mass spectrometer. This section will detail the instrumentation and experimental methods relating to the microreactor: information on the mass spectrometer is discussed elsewhere (section 2.3.5).

Equipment

The CATLAB suite of equipment is split into three major components: the mass flow controllers, the valves and the switches therein; the CATLAB reactor itself, which comprises a furnace around a reactor tube through which gas flows; and the mass spectrometer for data acquisition (Figure 2.2).

The delivery of carefully-controlled gas mixtures to the sample is essential for reliable catalytic testing. A bank of eight MFCs, comprising two carrier gas lines and six lines capable of being routed into the pulsing system. Seven MFCs deliver reliable flow rates of 3-100 mL/min, with the other MFC specialised as a high-flow MFC capable of sustaining 200 mL/min of gas for long periods: the minimum supply pressure for all MFCs is 3 bar. Common gases and those in regular use are connected by metal Swagelok tubing directly from the laboratory gas system, while cylinders of lesser used gases can be connected to one MFC port easily with flexible or metal tubing.

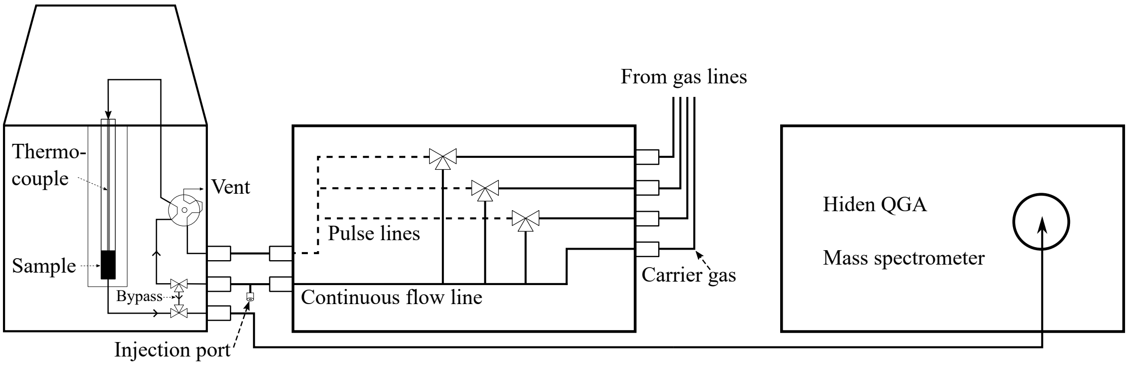

Figure 2.2: A schematic diagram of the interior layout of the Hiden CATLAB catalyst testing reactor (not to scale). Vent lines and outlets are not displayed.

The CATLAB reactor itself contains a large proportional-integral-derivative (PID)-controlled furnace capable of reaching 1000°C, into which the sample is placed. Each sample is placed into a quartz sample tube, the base of which has been bored through to allow the passage of gas flow: quartz wool is compacted at the bottom of the tube, and the sample is placed atop the wool. Gas flow is directed from the side of the apparatus to the top and then down through the sample: in this way, the undesired movement of powdered samples is hindered by a positive gas pressure acting downwards. A thermocouple is inserted into the sample bed to gather accurate measurements of sample temperature and to provide temperature control inputs. Post-reaction gas mixtures are then moved by positive pressure through the base of the furnace and towards the mass spectrometer sampling capillary, which uses vacuum pressure from a scroll pump beyond the spectrometer to draw in gas. A bypass mode is fitted, which enables measurements and calibrations to be performed without disturbing the sample itself; however, caution must be used when calibrating with the bypass. Since the bypass route is considerably shorter in terms of tubing distance (and distance through the catalyst bed) than the equivalent analysis line, differences in gas pressure and sample concentrations are often noticed on the mass spectrometer upon switching from bypass to analysis. Upon reaching the capillary, gas is moved to the mass spectrometer for analysis.

A pulsing mode is fitted to the reactor setup, allowing computer-controlled dosing of set quantities of gas mixtures at certain intervals. Instead of gas passing through the constant flow lines, gas is instead directed through the pulse lines. The Pulse Chemisorption System (PCS) switching valve is normally set to allow the carrier flow to pass through to the sample tube. With the pulse mode activated, however, this valve will switch to allow a sample loop to fill with a set quantity of gas, and then will switch again to direct the carrier flow to push the contents of the loop towards the sample.

Temperature Programmed Desorption

Temperature Programmed Desorption (TPD) analysis has been a cornerstone of all the works reported in this thesis. It is an extremely useful technique for the surface scientist and catalysis researcher, and works by probing the surface of a material to elucidate the types, quantity and strengths of surface sites on catalysts. In addition, a wealth of topological information can be obtained regarding, for example, surface coverage, surface area and adsorption/desorption kinetics.[2–6] It is assumed in Langmuir-Hinshelwood kinetics that reactions occur between surface adsorbates, and that stronger adsorption to the surface impedes reaction by lowering the reactant surface coverage.[7] Thermal desorption from a surface is described by a modified form of the Arrhenius equation:

$$r(t) = -\frac{\mathrm{d}\sigma}{\mathrm{d}t} = v_n \sigma^n \exp\left(\frac{-E_a}{RT}\right) \tag{2.7}$$

where $r(t)$ is the desorption rate, n is the order of desorption, σ is the surface coverage, v_n is the pre-exponential factor (Hz), E_a is the activation energy of desorption, R is the gas constant and T is the temperature in Kelvin.

Using the Redhead method, which assumes the pre-exponential factor and energy of desorption to be independent of surface coverage, a simplified equation for first order processes is obtained:[8]

$$\frac{E_a}{R{T_m}^2} = \frac{v_1}{\beta} \exp\left(\frac{-E_a}{RT_m}\right) \tag{2.8}$$

where β is the heating rate in $\mathrm{K\,s^{-1}}$.

For TPD experiments, samples (all of particle size 450-600 µm) were placed into the quartz sample tube, which itself was then mounted in the CATLAB reactor. Under a 30 mL/min helium flow at constant low temperature for fifteen minutes, 1 µL aliquots of methanol were injected manually by syringe to saturate the catalyst surface. The temperature is then ramped to 400°C at a constant rate of 8°C $\mathrm{min^{-1}}$, during which time the mass spectrometer is constantly sampling. At certain temperatures, the surface adsorbates will attain energy greater than that required to desorb from the surface: this desorption is observed by the mass spectrometer.

Temperature Programmed Pulsed Flow Reaction

While TPD measurement is quick and easy to perform, the reactivity data obtained is limited to product selectivities: to explore both selectivity and substrate conversion an alternative method is required, namely Temperature Programmed Pulsed Flow Reaction (PFR). The technique explores catalytic behaviour under conditions more similar to those used for working catalysts, and consequently can yield information regarding the light-off/effective operating temperatures of the catalyst. With all samples prepared as for TPD, 1 µL aliquots of methanol are injected into a constant flow of 10% O_2 in He at two-minute intervals over the course of a temperature ramp from room temperature to 500°C, throughout which the reaction mixture is being monitored by mass spectrometry. The gradient of the temperature ramp can be adjusted to suit the purposes of the experiment, but the in general the value was set at 10°C/min. The general behaviour displayed by selective oxidation catalysts during methanol oxidation is described below:

(i) Initial methanol injections appear equal in size, with an array of methanol cracking fragments observed. The first methanol peak is often slightly smaller, due to methanol adsorbing on the catalyst: subsequent injections of methanol are not sequestered by the now-saturated catalyst.

(ii) Once the temperature increase has commenced, small changes in selectivities can be observed: typically, strong selectivity to formaldehyde is observed at low to medium temperatures. Note, however, that conversion at this point is low: in other words, of the little methanol being converted, almost all of it is converted to formaldehyde.

(iii) At medium temperatures methanol conversion starts in earnest, accompanied by an increase in combustion selectivity at the expensive of selective oxidation. Nonetheless selective oxidation remains the major process at this temperature.

(iv) At high temperatures selective oxidation declines considerably, and combustion processes dominate the product distribution.

The short duration during which the methanol is around the catalyst provides two significant advantages over constant flow methods. Firstly, small transient pulses do not deactivate the catalyst quickly; after each pulse has passed, the gas conditions reoxidise the catalyst to its original state before the next pulse arrives. Secondly, a vast quantity of data is obtained with each pulse, greatly facilitating comparative experiments with different gas conditions or temperature settings.

Before quantitative analysis of the mass spectra from PFR experiments can occur, all mass spectral overlaps must be resolved: this is discussed in detail elsewhere (Section 2.3.5). Along with the need to resolve relative contributions, the effects of the mass spectrometer filament must be minimised. This is achieved by calibration using blank catalyst tubes or the bypass line to probe any methanol cracking on the filament itself. The quantity of each species present in spectra is obtained from the integral of the curves: since each injection and its corresponding MS pattern is discrete, the integral limits can be set to the edges of the peak. The integral values can then be used to calculate product selectivity and methanol conversion for each injection. The quantity of methanol conversion at time t is determined by:

$$X_i = 100 - \left(\frac{n_t}{n_{\text{unreacted}}} \right) \times 100 \tag{2.9}$$

where X_i is conversion expressed as a percentage, n_t is the integral of the methanol pulse at a time t during the reaction and $n_{\text{unreacted}}$ is the integral of the methanol pulse at low temperature with no conversion.

Integrals of all species of interest (post-spectral overlap resolution) can be used to compute selectivities by the following method:

$$S_p = \left(\frac{S_d}{\sum_i S_i} \right) \times 100 \tag{2.10}$$

where S_p is the selectivity of product p, S_d is the mass spectral integral of the desired species d and $\sum_i S_i$ is the sum of the integrals of all products.

The yield of the reaction can be determined by combining conversion and selectivity thus:

$$Y_p = X_i S_p \tag{2.11}$$

where Y_p is the overall yield of the reaction expressed as a percentage.

Depending on the sample undergoing PFR, exotherms of different strengths are visible coincident with methanol injections at higher temperatures. This is often a measure of the inherent activity of the catalyst (and therefore normally a reflection of its surface area). In this manner, the CATLAB reactor can be used as a calorimeter, by monitoring the size of the temperature increases upon methanol injection and noting the time required to resettle at the setpoint temperature. For these experiments, isothermal stages are required; instead of a constant ramp to high temperature, long plateaus are built into the temperature profile to allow the baseline to settle and to permit sensible comparison of multiple injections.

2.3.3 Infrared spectroscopy

Background theory

Infrared spectroscopy is a popular technique for determining sample composition in terms of functional groups or bonds of interest: it relies on the absorption of certain frequencies of light characteristic of particular molecular structures and the resultant increase in the amplitude of the vibrational mode in question. The frequencies absorbed will be resonant, i.e. the energy of the incident radiation equals that of the vibrational frequency. Due to the relative weakness of infrared radiation, only rotational or vibrational modes can be excited: electronic excitation is not possible.

For a particular motion to be visible by IR spectroscopy, it must be *IR active*, i.e. it must cause a change in dipole moment. A permanent dipole is unnecessary: it is the change in dipole which matters. Molecules can vibrate in a range of different patterns, called vibrational modes: the number of such vibrational modes available to a molecule depends on its structure. For a molecule containing N atoms, a linear molecule possesses $3N-5$ degrees of vibrational freedom, while a non-linear molecule possesses $3N-6$. It can therefore be determined that simple diatomic molecules, such as O_2, will not be seen by IR spectroscopy: as a symmetrical molecule with only one degree of freedom, the dipole moment does not change with vibration. Vibrational modes can be classified according to their motions during vibration (Table 2.2).

Table 2.2: A summary of IR vibrational modes.

Description	Symmetric	Asymmetric
Radial	Symmetric stretching	Asymmetric stretching
Longitudinal	Scissoring: bond angle decreases	Rocking: motion in plane, angle constant
Latitudinal	Wagging: motion perpendicular to plane	Twisting: opposite motion perpendicular to plane

A wide variety of IR spectroscopic techniques are used currently to measure a range of samples, including, *inter alia*, classic solid preparations in mulling agent (e.g. Nujol), liquids, gases, and unprepared solids (by using an Attenuated Total Reflectance (ATR) setup allowing for direct powder measurement). Modern measurements are largely made with using Fourier Transform Infrared (FTIR) instruments, which allow quicker measurement while improving the signal-to-noise ratio. These operate in a fundamentally different manner to traditional IR instruments. Instead of shining monochromatic light at a sample and measuring the absorption for each wavelength, a beam of many frequencies is directed at the sample through an interferometer and its absorption is measured. The frequencies in the beam are then altered to a different set of frequencies, and the new absorption measured. This process continues, eventually yielding an interferogram which displays absorption as a function of mirror position in the interferometer. This data can be converted by Fourier transform to afford absorption as a function of wavelength, the desired result.

A classic dispersive IR spectrometer requires a monochromator containing entrance and exit slits; slits reduce the transmission of radiant energy. Since an FTIR system possesses no slits, no energy is lost, and power transmission is considerably greater than dispersive spectrometers at similar resolutions. This increase is referred to as *Jacquinot's throughput advantage*, the magnitude of which depends on wavelength.[9] While FTIR systems can be disadvantageous for certain specialised systems, for example those utilising sensitive thermocouples, in the large majority of cases FTIR spectrometers are superior.

Diffuse Reflectance Infrared Fourier Transform Spectroscopy

Diffuse Reflectance Infrared Fourier Transform Spectroscopy (DRIFTS) is a versatile technique of particular interest in catalysis research. By utilising a probe molecule, DRIFTS enables surface sensitive measurements to be made; the samples require no preparation, and are simply placed as powder into a small cup within the spectrometer. While standard IR techniques rely on the transmission of light through a sample to record a spectrum, a DRIFTS instrument utilises the radiation which is otherwise scattered to produce a spectrum. Instead of an illumination source being positioned perpendicular to the sample (in order to maximise transmission to the detector), in DRIFTS it is placed at an angle to the surface in order to graze the surface. A range of processes can occur upon irradiation by IR light, including absorption, specular and internal reflection, or multi-directional diffusion. It is this latter process which is exploited in DRIFTS measurements. When the incident light is diffusely reflected by the sample, it is modified by passing through the sample structure, and then is picked up by the optical accessories and rerouted to the detector. Crucially, due to the shallow angle with which incident light is introduced to the sample, the incident beam penetrates a greater quantity of the surface material than it would otherwise, were it to be perpendicular for transmission measurements. Consequently, the surface layers make a greater relative contribution to the overall signal, affording DRIFTS greater surface sensitivity than standard IR/FTIR techniques. The instrumental setup required to perform DRIFTS measurements differs greatly to that used for standard transmission or ATR IR spectroscopy (Figure 2.3). The cup into which powdered sample is placed is itself housed within a metal dome, containing two Se_2Zn windows: this window material is thermally stable and has negligible effect on the incident and reflected beams, hence is ideal for this use. The sample environment can be made gas-tight and connected to gas tubing to provide specific atmospheric conditions during the measurement. A cooling system is fitted, in which vaporised liquid nitrogen is introduced into the sample cell through an inlet below the sample, flowing through the sample space to an outlet above, providing a constant flow of cooling gas. Without a cooling system, the focussed IR laser would thermally damage the sample.

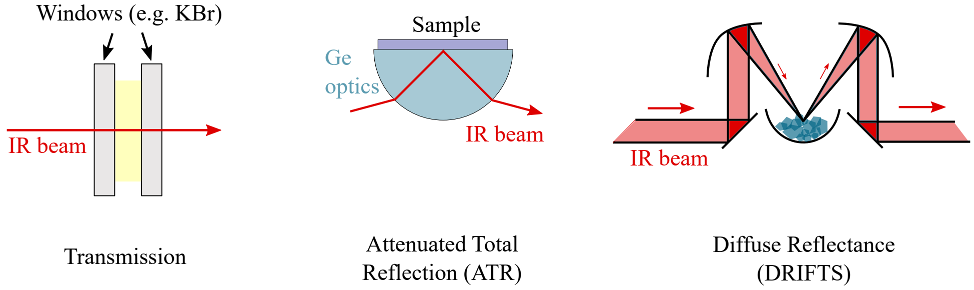

Figure 2.3: Differences in instrumental sample environment for each type of IR spectroscopy measurement.

Experimental

DRIFTS measurements were performed using an Agilent Technologies Cary 600 FTIR spectrometer with DRIFTS modifications containing the sample holder and the focussing mirrors. A Harrick Praying Mantis optical accessory was employed to harvest diffuse reflectance data, and measurements were carried out on catalysts up to 500°C. A Hiden quadrupole mass spectrometer was connected to the vent line from the DRIFTS sample cell, permitting mass spectral analysis during DRIFTS measurements.

2.3.4 Magnetometry

A portion of this thesis concerns the investigation of novel shell-core catalysts employing magnetic cobalt ferrites as a core support, and whether their resulting catalytic behaviour could be influenced by magnetic means. To this end, *ex situ* measurements of magnetic susceptibility were performed in the Research Complex at Harwell and further *in situ* magnetometry was performed at the University of Cape Town. The term magnetometry in these contexts refers to measurement of magnetic susceptibility, which is the measure of the degree to which a material will be magnetised in an applied magnetic field. There are three variants of magnetic susceptibility, viz. volume (or bulk), mass and molar susceptibility: it is volume susceptibility which is measured herein. Volume susceptibility, χ_v, is the ratio of magnetic moment per unit volume (magnetisation) $\mathbf{M}$ to the applied field intensity $\mathbf{H}$ and can be expressed mathematically thus:[10]

$$\mathbf{M} = \chi_v \mathbf{H} \tag{2.12}$$

where **M** and **H** are measured in $\mathrm{A\,s^{-1}}$, hence χ_v is dimensionless. Including SI units, magnetic field strength **H** is related to magnetic induction **B**:

$$\mathbf{B} = \mu_0(\mathbf{H} + \mathbf{M}) = \mu_0(1 + \chi_v)\mathbf{H} = \mu\mathbf{H} \tag{2.13}$$

where μ_0 is the permeability of free space, $(1 + \chi_v)$ is the relative permeability of the material and μ is the magnetic permeability. Magnetic susceptibility is normally discussed in terms of **H** and **M**, but less commonly can be discussed in terms of the intensity of magnetisation, **I**, and **B**:

$$\mathbf{I} = \mu_0 M \tag{2.14}$$

From equation 2.13, one can see that volume magnetic susceptibility and magnetic permeability are related:

$$\mu = \mu_0(1 + \chi_v) \tag{2.15}$$

This equation is used by all magnetometers during measurements, recording values for μ and μ_0 to compute magnetic susceptibility. The resolution of the benchtop magnetometer used in these studies exceeds one ppm, permitting highly accurate determination of magnetic susceptibility.

Experimental

The Curie temperatures ($\mathrm{T_c}$) of samples were measured using a Bartington Instruments temperature-programmable MS2 Magnetic Susceptibility System, comprising a power supply, a magnetic susceptibility sensor/meter and a furnace (with water cooling system). This instrument relies on the change in inductance occurring within an inductor when the core magnetic permeability is modified. A reference state is measured when the sensor contains nothing but air, since the permeability of air is approximated to be the permeability of free space: measurement after determination of a reference yields the permeability of the material itself. Due to the elevated operating temperatures of the equipment, it is necessary to eliminate sensor drift by re-establishing an air reference periodically. Values are displayed digitally during a measurement, and recorded for analysis on GeoLabsoft software. The exact position of the $\mathrm{T_c}$ of a material remains the subject of some debate. In general, it is accepted to be the intercept with the abscissa from a tangent drawn from the steepest linear-like portion of the magnetic susceptibility curve (Figure 2.4). This method notwithstanding, it is occasionally reported as the inflection point immediately before loss of magnetic susceptibility: for the purposes of these studies, the generally-accepted method is used.

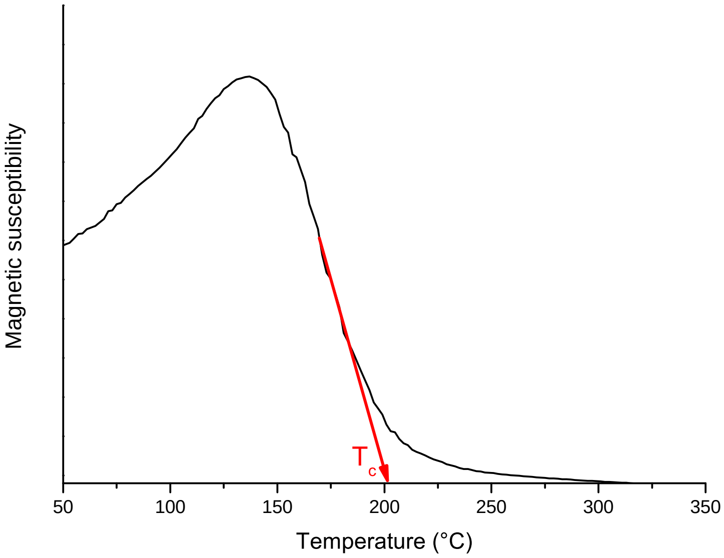

Figure 2.4: Determination of the Curie temperature (T_c) from a typical magnetic susceptibility curve: magnetic susceptibility is a dimensionless value.

In situ magnetometry was conducted on a specially designed magnetometer/reactor in the Department of Chemical Engineering, University of Cape Town.[11] The setup comprised: a series of mass flow controllers for control of reaction gas mixtures; a linearly-oscillating heated reactor tube (up to 500°C) in which the sample is placed; and the electromagnets which surround the reactor tube space. A mass spectrometer and gas chromatograph can be connected to the outlet tubing permitting live sample analysis during magnetic field application experiments. The magnetic flux density produced by these electromagnets ranges from $-2\,\mathrm{T}$ to $2\,\mathrm{T}$. A range of experimental conditions in terms of magnetic field and temperature was used for these studies. A typical experiment involved prolonged dwell periods at 100 and 300°C; halfway through each dwell period, a 2T magnetic field was applied. Alternative conditions included stepped temperature ramps over long time periods with a variety of magnetic conditions. Considerable experimental error was encountered in these studies, both from equipment failure and unexpected magnetic interference. The reliability of mass spectrometry measurements was severely compromised by proximity to the electromagnet. The possibility of such interference had been considered and mitigated against, but the degree of mitigation required was greater than thought initially. The mass spectrometer was positioned at as great a distance from the magnetometer as possible to reduce magnetically-induced noise in the data; however, this required greater lengths of MS sampling capillary tubing, increasing dead volume and causing a significant delay in MS response.

2.3.5 Mass spectrometry

Mass spectrometry (MS) has been a mainstay for all aspects of this thesis, and is one of the most important techniques available to the modern chemist. The principle of the technique is to ionise species and sort the resulting ions or molecular fragments by mass-to-charge ratio (m/Q, though more commonly m/z), thereby enabling assessment of sample constituents both qualitatively and quantitatively.

Background theory

A mass spectrometer comprises three main components, viz. the ion source (or ioniser), a mass analyser and a detector; however, the nature and effects of these components can vary between types of mass spectrometer. There exists a wide range of ionisation methods utilised by mass spectrometers, the choice of which depends on the sample phase and the ionisation efficiency for the sample in question. Ions are extracted from a sample and directed through the mass analyser, which contains electromagnetic fields: these exert force on ions passing through the analyser, altering their speed or trajectory. The degree to which an ion is diverted is dependent on its mass: since Newton's Second Law states $F = ma$, lighter ions are more affected by magnetic force than heavier ones. In this way, the ions are spatially separated by mass and arrive at the detector in different positions across the detector surface. The detector registers the relative abundance of each mass and reports these to the user. The original mass spectrometers were of sector-type, and these are still used today for certain purposes: these contain a mass spectral analyser whose shape roughly represents a sector of a circle (Figure 2.5).

Quadrupole mass analysers

For the studies detailed in this thesis, quadrupole mass spectrometers were utilised for all MS measurements. Quadrupole mass analysers consist of four parallel cylindrical metal rods, wherein opposing pairs of rods are electrically connected (Figure 2.6). In an ideal case, these rods would be hyperbolic, but manufacturing such items is not trivial: instead, fully cylindrical rods with known diameter-to-spacing ratio adequately approximate hyperbolas while offering easier manufacturing. A variable radio-frequency voltage is applied between the two pairs of rods, generating oscillating electric fields along the length of the analyser. Ions are directed down the centre of the analyser, but only ions with certain m/z

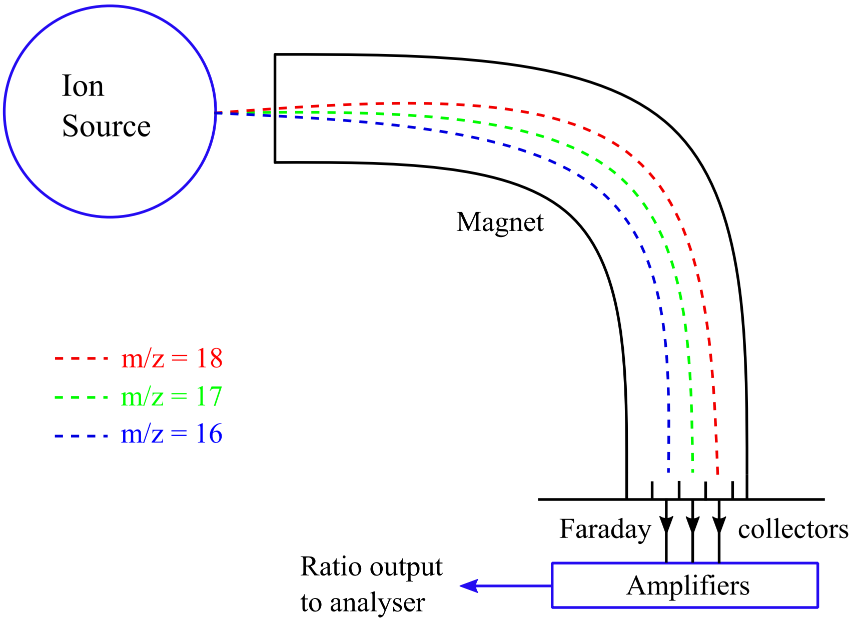

Figure 2.5: A schematic diagram of a typical sector-type mass spectrometer: the lower m/z values are deflected to a greater degree by the magnet.

values will reach the detector with a given ratio of voltages; the other non-selected ions will have unstable trajectories through the electric fields and will collide with the rods.

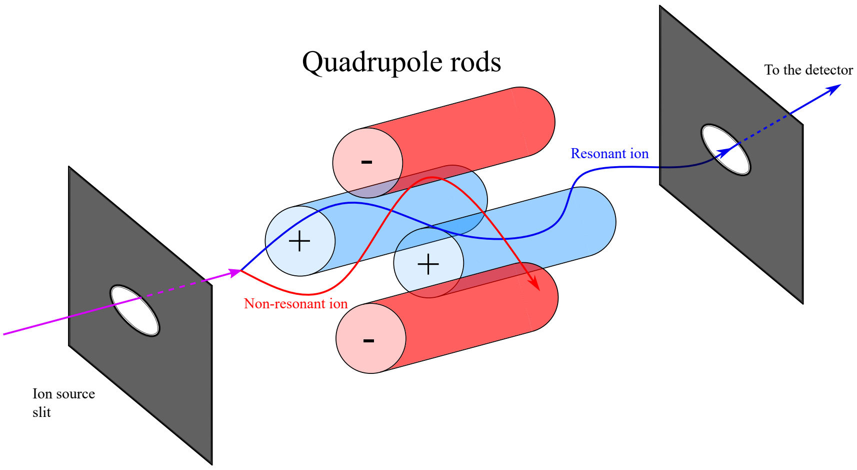

Figure 2.6: A schematic diagram of a quadrupole mass analsyer: resonant ions travel through the poles while non-resonant ions collide with the rods, becoming neutralised.

Quadrupole instruments afford significant advantages for the types of chemistry explored throughout these studies. Since they can remain tuned on a single ion m/z for extended periods, they excel at monitoring a set of known, predefined masses over time. This property is utilised by the Multiple Ion Detection (MID) mode on the spectrometer, and has been the basis of all CATLAB measurements. This does, however, come with a significant disadvantage: since only preset masses are analysed, one cannot easily measure speculatively over a range, as with a conventional mass analyser.

Secondary Electron Multipliers

Upon emerging from the quadrupole mass analyser, ions arrive at a secondary electron multiplier (SEM): as ions collide with the layer of secondary-emissive material (e.g. BeO or GaP) on the first dynode, the emission of one to three electrons can result. This process is referred to as secondary emission, and the number of electrons emitted per incident charged particle dictates the secondary emission yield. The secondary electrons are accelerated by an electric field and are directed to the next dynode to repeat the process: in this way, a large shower of electrons can be produced from only one original incident ion (Figure 2.7). Since the process relies on electronic collisions, a small period of dead time is allowed between electron multiplication events in order to restore the surfaces within the multiplier to their original conditions. The mass spectrometer used for the vast majority of these studies contained two detection mechanisms: a less sensitive but quicker Faraday collector, and the more sensitive but slower secondary electron multiplier.

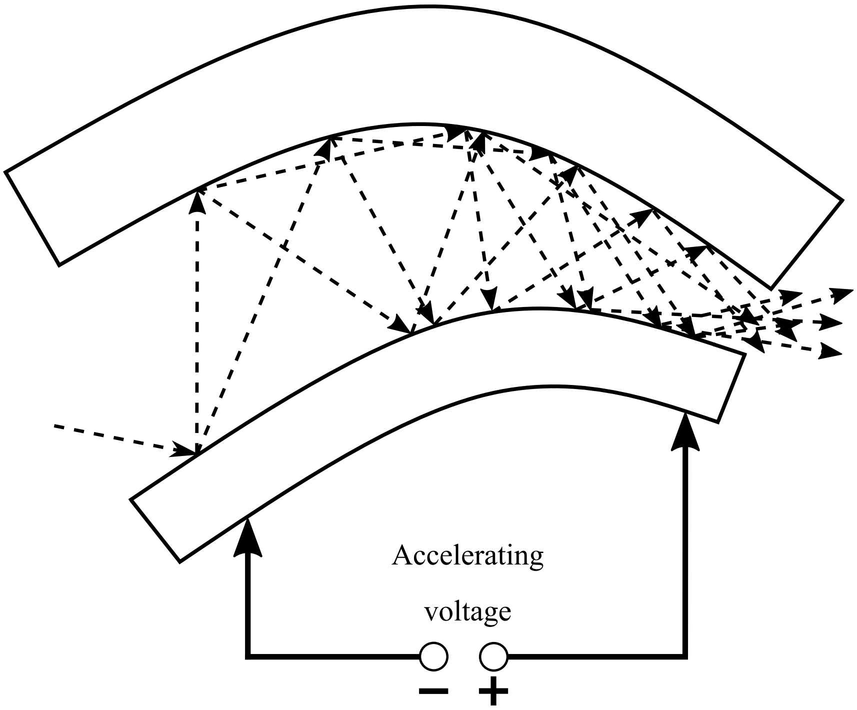

Figure 2.7: The operating principle of a continuous secondary electron multiplier.

Practical determination of molecular fragmentation

In a reaction with only one species of interest, the analysis of mass spectral data is straightforward. With multiple products present, however, spectral overlap becomes significant and the resulting analysis is often not trivial. Since different species can fragment to produce fragments with the same m/z, to work out the true quantities of a certain substance present in the mass spectrum it is necessary to deconvolute the data. In most cases, each substance of interest in the mass spectrum will possess a unique peak (i.e. an MS peak unshared with any other species present) somewhere in its cracking pattern. Literature cracking patterns provide a starting point for the resolution of spectral overlaps, but it is important to note that these values will differ slightly from the actual values obtained on a particular mass spectrometer. A summary of cracking patterns reported in literature for molecules of interest to these studies is detailed below (Table 2.3).[12] It is not always the case that the unique peak will be the base peak; indeed, in many reaction mixtures it is often not possible to use the base peak as a unique peak. In such cases, a lesser peak can be used to calculate the contributions of that substance to the base peak and other fragments in the same way that a base peak can be used to work out the relative contributions to cracking pattern peaks. This approach, however, relies on a known environment: if the range of possible products is not known beforehand, resolution of spectral overlaps becomes arduous indeed.

Table 2.3: Reported values for cracking patterns of molecules of interest in this thesis.

Substance	Cracking fractions (Abundance ‰)
Hydrogen	2 (1000), 1 (21)
Water	18 (1000), 17 (211), 16 (9), 19 (5), 20 (3)
Carbon monoxide	28 (1000), 12 (47), 16 (17), 29 (12), 14 (8), 30 (2), 13 (1)
Formaldehyde	29 (1000), 30 (885), 28 (309), 14 (44), 13 (43), 12 (33), 31 (19), 17 (14)
Methanol	31 (1000), 32 (717), 29 (421), 28 (90), 30 (78), 33 (11), 27 (5)
Oxygen	32 (1000), 16 (36)
Carbon dioxide	44 (1000), 16 (94), 28 (82), 12 (67)
Dimethyl ether	45 (1000), 29 (390), 15 (240), 31 (30), 43 (10), 30 (10), 28 (9), 44 (6)

In theory, this methodology should yield reliable mass spectral data; in practice, however, the effects of a hot mass spectrometer filament cannot be disregarded and will complicate mass spectra accordingly. During TPD or pulsed-flow reactor studies with methanol, it was noticed that combustion products were observed well below the operating temperatures of the catalysts under investigation. This arises from the combustion of methanol (which has not reacted with the intended catalyst) on the hot tungsten oxide filament inside the mass spectrometer, and adds to the relative abundance of combustion products in the resulting spectra. This issue can, however, be remedied by calibration prior to experimentation.

Experimental

Mass spectral data from CATLAB experiments were obtained from a Hiden QGA mass spectrometer, using the SEM collection method in almost all cases. For reactions involving high concentrations of reactants/products, a Faraday collector with lower sensitivity but faster response time was selected. A Hiden Quartz Inert Capillary (QIC) draws gas flow from the post-catalyst space in the CATLAB reactor, and delivers it to the mass spectrometer. A large portion of the incoming gas mixture is directed to vent immediately to ensure high vacuum is maintained in the spectrometer. The remaining gas is ionised, routed through the quadrupoles and to the detector. Mass spectral data was processed to remove spectral overlaps and reveal the true relative quantities of substances present. For the experiments conducted on the magnetometer set-up at the University of Cape Town, a Pfeiffer Vacuum OmniStar mass spectrometer was employed. This differed only in lesser sensitivity in comparison to the Hiden QGA instrument, but was vastly more practical to connect to the magnetometer. Due to the strong effects of the electromagnets, considerable interference was seen: to mitigate this, the mass spectrometer was situated several metres distant from the magnetometer (and catalyst therein). Data quality and reliability was markedly increased, but at the cost of significantly greater dead volume and transit time between sample and spectrometer.

2.3.6 Raman spectroscopy

Background theory

Raman spectroscopy offers a useful means of providing a distinct chemical fingerprint of a sample by observing vibrational, rotational and low-frequency modes in a sample, which greatly assists the identification of chemical species. The technique derives from the inelastic scattering (or Raman scattering) of monochromatic light frequently obtained from a normally near-IR, visible or near-UV laser. The incoming laser photons interact inelastically with vibrations, phonons and excitations in the sample, exciting the system to a virtual state. The decay from this system to a final energy level different to the starting level emits a photon, albeit one with different energy to the incident photons. The degree to which the energies of the photons are shifted is indicative of the vibrational modes in the system. Unlike elastic (Rayleigh) scattering, however, spontaneous Raman scattering is feeble: consequently, it is difficult to separate the Raman scattered light from the vastly more common Rayleigh scattered light. When the final state possesses greater energy than the initial state, the scattered photon will be reduced in frequency, hence also energy, in order that energy is conserved: this is called a Stokes shift. If the final state is lower in energy than the initial (excited) state, however, this will provide the scattered photon with extra energy for the same reason: this is called an anti-Stokes shift (Figure 2.8). Since a majority of molecules will be found in their ground states at room temperature, the probability that a photon will be anti-Stokes scattered is low. As a consequence, most Raman measurements are conducted using only Stokes-shifted light.

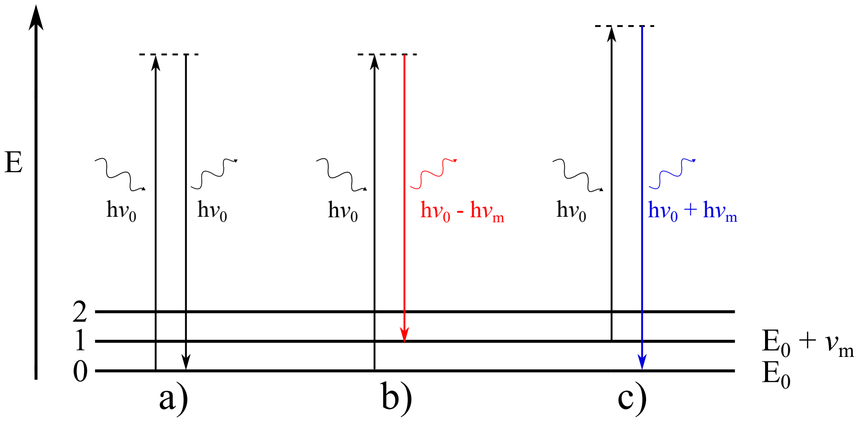

Figure 2.8: Mechanisms for inelastic scattering of incident photons: a) Rayleigh (elastic) scattering; b) Stokes Raman scattering; c) Anti-Stokes Raman scattering.

Raman spectroscopy possesses many advantages: it can analyse a wide range of samples and material types, it is non-destructive (at low laser power) and it requires little time to complete a measurement. Consequently, its use is commonplace in modern chemical laboratories. There are, however, some disadvantages, for example that it cannot be used to measure metals or alloys, but the primary issue is that samples or impurities within the samples are frequently liable to fluoresce when irradiated by the spectrometer laser, masking the Raman spectrum. This can be moderated by careful selection of laser power and wavelength, but remains a continual issue.

Experimental

Samples were analysed using a Renishaw inVia Raman microscope (a schematic of which is detailed in Figure 2.9) kindly provided by the Central Laser Facility. A typical measurement involved the deposition of a small quantity of solid sample upon the sample stage, followed by focussing of the optics using the eyepieces (and on occasion the camera within the instrument when using the laser itself to focus). All spectra detailed in these studies were performed using a laser with wavelength 830 nm. Laser power was minimised to prevent sample damage, and was typically set to 0.1%. Several accumulations of duration twenty seconds were taken at each measurement site; several sites were measured to account for any sample inhomogeneity. The Raman instrument was recalibrated to the internal silicon standard before the initial measurement, and was recalibrated periodically thereafter.

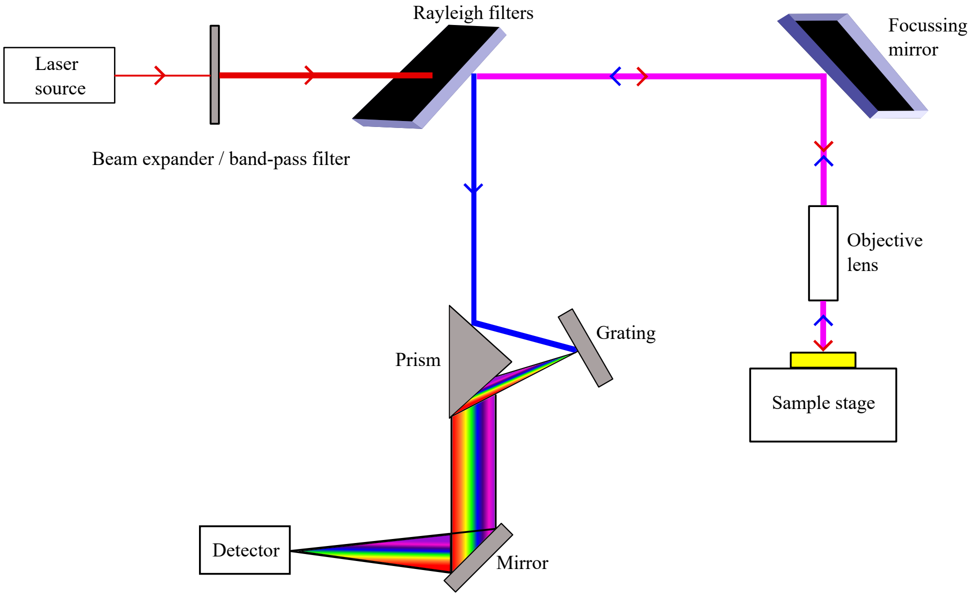

Figure 2.9: A schematic diagram of a Raman microscope. The incident light beam is marked in red, while the reflected/scattered light beam is shown in blue. The pink line represents the simultaneous passage of incident and reflected radiation.

2.3.7 Transmission electron microscopy

Background theory

Transmission electron microscopy (TEM) is a technique in which an electron beam is transmitted through an ultrathin sample (<100 nm in thickness), interacting with the sample as it passes through. The interaction of this beam and the sample creates an image, which is then magnified and focussed onto an imaging device (historically photographic film, but today charge-coupled device (CCD) digital image sensors).

The capability of microscopy using visible light is limited by the relatively long wavelengths of visible light. The maximum resolution obtainable with visible light is:

$$d = \frac{\lambda}{2n \sin \alpha} \approx \frac{\lambda}{2\mathrm{NA}} \tag{2.16}$$

where d is the maximum resolution, λ is the wavelength of the incident photons, n is the refractive index of the medium in which the lens exists, α is the maximum half-angle of the cone of light able to reach the lens and NA is the numerical aperture of the system.

Due to the markedly shorter de Broglie wavelength of electrons, vastly greater resolutions are achievable than with visible or UV light microscopes. As a consequence, highly detailed morphological, compositional and crystallographic information can be obtained. At low magnifications, the contrast obtained in the TEM image arises from differential absorption of the electrons due to disparities in sample composition or thickness; at high magnifications, however, complex wave interactions modulate the intensity of the image, frustrating simple analysis. Numerous operating modes are available to suit different imaging requirements, permitting the determination of, *inter alia*, chemical speciation, crystal alignment and electronic structure. Cutting-edge TEM systems can incorporate aberration-correction equipment, which permits even further gains in resolution (down to picometre scale).

To generate the electrons utilised in the instrument, an electron source sits atop the column, which can be a single crystal of LaB_6 or a tungsten filament.[13] This source is connected to a High Tension tank (a source of high voltage, normally 100-300 kV); when sufficient current is supplied, electrons are emitted by thermionic emission (similar to a classic light bulb) or field electron emission into the vacuum chamber.

In general, a modern TEM will contain three stages of lensing, namely the condenser, objective and projector lenses: the condenser lenses are used for initial formation of the electron beam; the objective lenses focus the beam that passes through the sample; and the projector lenses expand the beam onto an imaging device or viewing screen. Image magnification is dictated by the ratio of the distances between the specimen and the image plane of the objective lenses. Astigmatism in the beam of electrons is removed through the use of stigmators, which apply weak magnetic fields to the beam as it passes. Further corrective processes occur in many instruments and differ depending on the specialism of each TEM: for example, spherical aberration is corrected in microscopes tuned for ultra-high resolution imaging.[14]

TEM instrumentation

A typical TEM consists of a large vacuum column through which the electrons travel, a series of lenses and electrostatic plates permitting guidance of the electron beam, a sample stage and finally an imaging device at the base of the instrument (Figure 2.10). The vacuum level is typically of the order of 10^{-4} Pa, but for high-voltage TEMs higher vacuum levels are required, ranging from 10^{-7} to 10^{-9} Pa to prevent electrical arcing. A range of sample holder environments is available to suit the material in question, from simple *ex situ* grid holders to more complex heated cells for *in situ* measurements.

Scanning Transmission Electron Microscopy

While conventional TEM is a useful and reliable technique, the capabilities of electron microscopy are greatly enhanced by Scanning TEM (STEM). In this mode, the beam of electrons is tightly focussed into a fine spot (of size $\sim$ 0.1 nm) and scanned across the sample to create a raster image (i.e. a rectangular grid of pixels). This rastering process permits other analytic techniques to be conducted simultaneously, for example energy dispersive X-ray spectroscopy (EDX), or electron energy loss spectroscopy (EELS). In addition, operating in STEM mode is required for high resolution imaging techniques, such as annular dark-field imaging (ADF). While conventional dark-field imaging collects only electrons passing through an inserted objective aperture, ADF collects scattered electrons using a ring-shaped dark-field detector around the electron beam: this harvests far greater numbers of electrons than does an objective aperture. As a consequence, the efficiency of signal collection (and hence resultant signal-to-noise) is greatly improved. The bonus of using an annular detector is that the main beam passes through unaffected and can be used by a different analytical technique (e.g. EELS). High-angle annular dark-field imaging (HAADF) is a subsidiary technique which collects only high angle, incoherently scattered electrons: these electrons have experienced Rutherford scattering, in which they are electrostatically repelled by the nucleus itself. Accordingly, the images obtained from HAADF are extremely sensitive to differences in atomic number and nuclear charge.[15]

Spectroscopy and microscopy in concert

Various spectroscopic methods can be employed alongside STEM imaging, of which two of the more common are EDX and EELS. In EDX, inner shell electrons can be excited and ejected by a focussed beam of electrons, creating an electron hole. This hole is then filled by an outer electron higher in energy, which can (but not always will) emit an X-ray, whose energy can be detected by an energy dispersive spectrometer. Since the energy of the X-ray is characteristic of the difference in energy between outer and inner shells, elemental composition can be determined. EELS is a complementary technique in which the kinetic energies of the electrons in the incident beam are constrained to a known range. In passing through the sample, some will experience inelastic scattering, losing energy: the

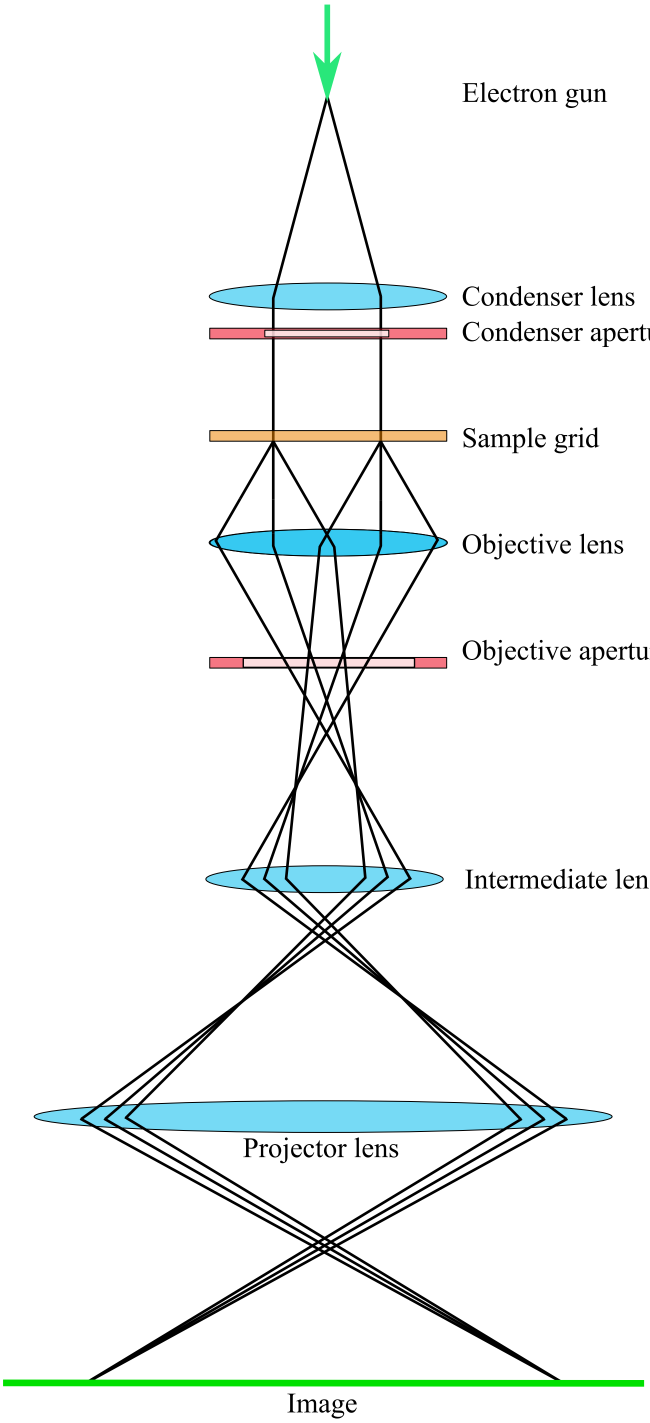

Figure 2.10: Schematic of the imaging mode of a typical transmission electron microscope.

energy lost can be measured by an electron spectrometer. This inelastic scattering arises from many different sources, e.g. inner shell ionisation, and can provide considerable detail on atomic composition, chemical bonding, electronic and surface properties. Traditionally EDX has been the easier technique to perform, more effective for atomic composition and more successful with heavier elements; EELS is more difficult, but prospers at lower atomic numbers and provides considerably more detail.[16,17]

Experimental

TEM analysis was performed on a JEOL JEM-2100 microscope at the Research Complex at Harwell. This microscope is equipped with tilt functionality for tomography measurements, and possesses a STEM operating mode with bright and dark-field detectors. An EDX spectroscopic setup is connected to the microscope, affording information about elemental composition and speciation within samples. Each sample was placed onto a standard copper TEM grid by dissolution in ethanol and subsequent addition by dropping pipette, and each grid was loaded into a standard grid holder. Full microscopic alignments were performed before each imaging session, with regular updates of certain important parameters (e.g. eucentric height).

2.3.8 X-ray absorption spectroscopy

X-ray Absorption Spectroscopy (XAS) is a highly versatile and powerful bulk characterisation technique which can reveal considerable information about the structure, geometry and electronics of a sample. Within the technique are two main divisions, namely X-ray Absorption Near Edge Structure (XANES) and Extended X-ray Absorption Fine Structure (EXAFS). The former region reveals information on oxidation states and local coordination geometry, while the latter can elucidate coordination environment and local structure.

Background theory

As X-rays move through a sample, their intensity is attenuated by interaction with the sample matter, as expressed by:

$$dI = -\mu I_0 dx \tag{2.17}$$

where I is the intensity of the transmitted X-rays, μ is the absorption coefficient (a function of the photon energy E), I_0 is the incident X-ray energy and x is the path length. Integration of this equation over the path length yields the following equation, the Beer-Lambert law:

$$I = I_0 \exp(-\mu E x) \tag{2.18}$$

Absorption of X-rays decreases with increasing incident energy until the absorption edge is reached, at which point there is a sharp increase in absorption (Figure 2.11). This energy corresponds to the excitation of a core electron into an excited state or continuum (the photoelectric effect); the position and identity of the absorption edge are dictated by the quantum number of the orbital from which the excited electron originates. The ejected electron is described as a spherical wave function with wave vector k:

$$k = \sqrt{\left(\frac{8\pi^2 m_e}{h^2}\right)(h\nu - E_0)} \tag{2.19}$$

where m_e is the electron rest mass and E_0 is the zero point energy.

The presence of neighbouring atoms causes the outgoing wave to experience backscattering, and as such the wave function of the final state must be considered:

$$\phi_{\text{final}} = \phi_{\text{outgoing}} + \phi_{\text{backscattered}} \tag{2.20}$$

The type and degree of coherence occurring between the two waves influences the variation in the total absorption coefficient (Figure 2.12), affording EXAFS features extending up to 1 keV beyond the absorption edge in question. While many EXAFS datasets can be satisfactorily analysed by considering only single-scattering paths (in other words, one return journey to and from a near neighbour scatterer), detailed modern analysis requires that multi-scattering paths and corrections for curved waves be considered.[18]

Oscillations in the EXAFS region of the spectrum are denoted by χ, the normalised value of μ. This is generated by subtraction of the absorption of an isolated atom arising from elastic and inelastic X-ray scattering, μ_0, from μ. The resultant EXAFS signal, $\chi(k)$, is obtained as a function of the wave vector k:

$$\chi(k) = \frac{(\mu - \mu_0)}{\mu_0} \tag{2.21}$$

This function comprises an amplitude term and a phase component, and can be expressed as the EXAFS equation, which is used to model the EXAFS region:

$$\chi(k) = S_0^2 \sum_j \frac{N_j}{kR_j^2} F_j(k) \exp\left(\frac{-2R_j}{\lambda_j(k)}\right) \exp(-2k^2\sigma_j^2) \sin[2kR_j + \Phi_j(k)] \tag{2.22}$$

where N_j is the coordination number; R_j is the interatomic distance; σ_j^2 constitutes the mean-square disorder in the distance between absorber and scatterer; F_j is the scattering

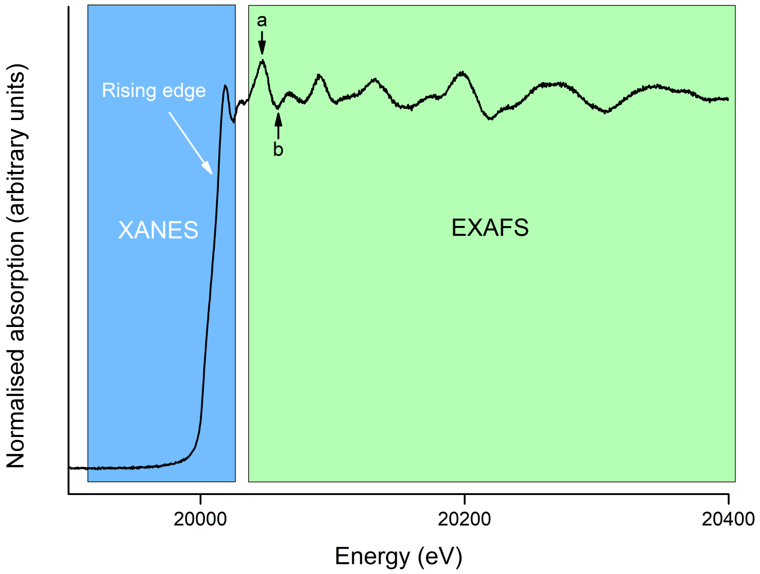

Figure 2.11: XAS spectrum of Mo foil at the Mo K-edge (20.0005 keV) displaying the XANES and EXAFS regions. The EXAFS region displays: a) constructive interference; and b) destructive interference.

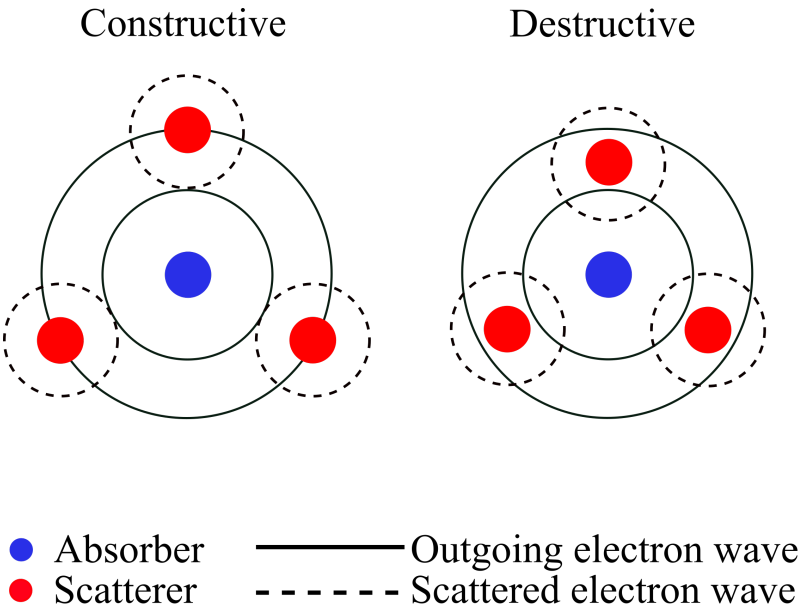

Figure 2.12: A schematic diagram of the interference processes which generate EXAFS features.

amplitude of the photoelectron and $\Phi_j(k)$ its corresponding phase; S_0^2 is the amplitude reduction factor (which accounts for absorber relaxation due to multi-electron excitations occurring simultaneously to the presence of the core electron hole); $\exp[-2R_j/\lambda_j(k)]$ is a gauge of the lifetime of the excited state and $\lambda_j(k)$ is the inelastic mean free path of the photoelectron; and $\exp(-2k^2\sigma_j^2)$ is the Debye-Waller factor, which represents static disorder and thermal vibration.[19–21]

The onset of the EXAFS region is considered to be approximately 50 eV after the relevant absorption edge. The signal before this is incorporated into the XANES region; however, interpretation of this section is nontrivial, due to the greater photoelectron scattering amplitudes encountered at these energies causing multiple-scattering modes to dominate.

Data analysis

Data processing was undertaken with IFEFFIT using the Demeter package (including Athena and Artemis).[22,23] Raw XAS data were imported into Athena, deglitched where necessary and merged into single datasets with one spectrum per sample. The number of raw spectra used in this process varied, depending on the beamline used to perform XAS measurements and the experimental conditions in use. Processing the data proceeds *via* the following stages:

(i) The parabolic background of the spectrum is removed through fitting pre- and post-edge lines, normalising the scale of intensity such that the absorption edge increase equals one;

(ii) The value for E_0 is fixed at 0 eV relative to the energy scale, which is accomplished by setting E_0 atop the maximum of the first derivative;

(iii) The application of splines erases the contribution to the spectrum from the absorption of an isolated atom.

The oscillations now visible in the χ plot should be of equal size either side of the horizontal; subjecting this plot to a Fourier Transform yields a pseudo-radial spectrum, indicative of the atoms vicinal to the absorbing atom (Figure 2.13). With these stages of processing complete, the datasets can be imported into Artemis, a program designed for EXAFS fitting. Through careful assessment of the data, reasonable estimation of structural composition and comparison with similar model structures, values for coordination number, radial distances and mean-squared disorder can be obtained. The inherent quality of each fit is listed by its R-factor—values of R-factor below 0.05 are acceptably reliable. A good fit is seldom obtained initially; instead, adopting an iterative approach in which each fit is successively improved upon by modifying its parameters affords the best results.

Transmission measurements

Wherever possible XAS measurements are run in transmission mode—due to its simplicity and superior data quality—in which X-ray absorption is measured as a function of energy. The intensity of the incident X-ray beam is assessed by ion chambers, of which there are three: I_0 determines incident intensity, I_t measures post-sample intensity and I_ref gauges the beam intensity post-sample and after passing through a reference metal foil. The chambers are filled with a known quantity of inert gas such that a certain amount of incident flux is absorbed. Metal plates either side of the ion chambers exert a constant electrical potential on the chambers: ionisation induces an electrical current from the movement of ionised gas molecules to the negative plate and electrons to the positive plate respectively. The magnitude of this current is directly proportional to the intensity of the photon beam entering the chamber. It is important to ensure that I_ref is recorded throughout XAS measurements. Due to the shift of energy readings over time, a metal reference foil allows post-processing of the measured data to calibrate the absorption edge position: this is particularly relevant in the XANES region, in which the precise position of edges provides important information.

Successful measurement in transmission mode requires careful control of sample quantity. If the analyte concentration is too small, few X-rays are absorbed, worsening signal-to-noise. Conversely, if the analyte concentration is too high, too many X-rays are absorbed leaving few to reach the detector. Whether a sample can be run in transmission mode depends not only on the concentration and absorption properties (e.g. attenuation coefficient) of the target element, but also those of all other sample constituents. In general, acceptable values for absorption edge, μx, range from 0.1 to 1.5 (1 is ideal). The mass required to achieve the desired absorption edge value is calculated using this equation:

$$\mathrm{Mass} = \frac{(\mu x)(a)}{\left(\frac{\mu}{\rho}\right)} \tag{2.23}$$

where a is the sample cross-sectional area and ρ is the sample density.

This equation can be rearranged to calculate the total absorption from all sample constituents (which generally must be below 2.5). For the XAS studies performed on B18 at Diamond Light Source, samples were pelletised (diameter 8 or 13 mm) while samples

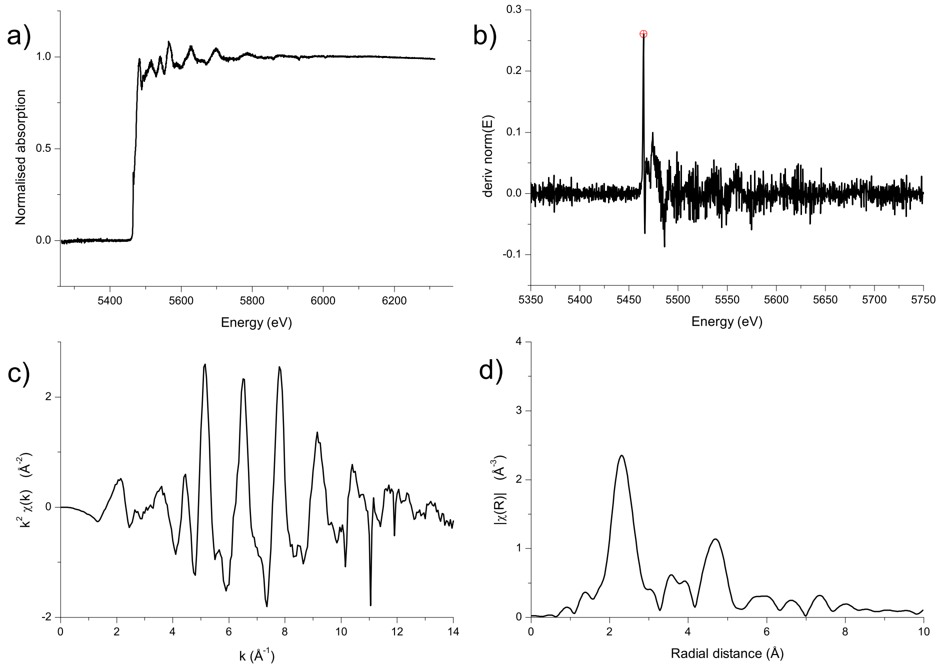

Figure 2.13: A graphical overview of steps encountered during XAS data processing in Athena, using vanadium foil as an example: a) normalised XAS data; b) identification of the E_0 position using the derivative (peak marked by circle); c) χ data plotted in k-space; d) Fourier Transformed χ data plotted in R-space.

run on XMaS at the European Synchrotron Research Facility (ESRF) were pressed into a sample holder without prior pelletising.

Fluorescence measurements

In cases where a low concentration of a target element is present, for instance as would be found in a low metal loading catalyst, the absorbance properties of the surrounding matrix will predominate. The resulting low signal-to-noise ratio seriously impedes measurement by transmission mode, requiring fluorescence measurements instead. The radiation released by fluorescence is element specific, but is considerably weaker in intensity compared to the total absorption: this necessitates markedly longer data collection times. Solid-state detectors are positioned orthogonally to the beam direction and at an optimal distance from the sample to harvest the maximum fluorescence radiation possible without saturating the detector (Figure 2.14). Such detectors can be windowed to achieve energy-specfic gathering of fluorescence radiation: certain types can achieve energy resolutions of less than 1 eV by spatial resolution (e.g. with a von Hamos spectrometer).[24]

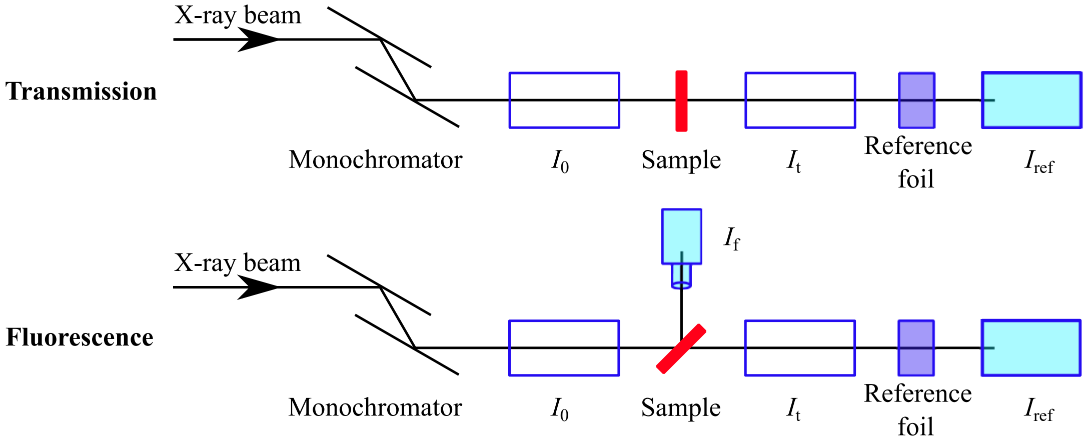

Figure 2.14: A schematic diagram displaying the measurement modes available during XAS measurements.

Synchrotron radiation

When electrons moving at close to the speed of light are forced to change direction by an applied magnetic field, energy is lost. This lost energy is released in the form of X-rays, and in a direction tangential to the path of the electrons. This is the principle by which all synchrotron facilities operate. The X-ray radiation released is known as *synchrotron radiation*, and it possesses many properties advantageous for analytical techniques, namely:

(i) High brilliance: the intensity of the X-rays generated by synchrotrons is several orders of magnitude greater than other X-ray sources;

(ii) High collimation: the angular divergence of the X-ray beam is low;

(iii) Low emittance: the beam particles are confined to a small distance and have similar momentum, enhancing brightness;

(iv) Wide tunability: the energies of the X-rays can be carefully controlled by monochromatisation (ranging from <1 eV to several MeV);

(v) High degree of polarisation: the emitted light is polarised in the plane of the electron motion;

(vi) Pulsed emission: greatly facilitates time-resolved studies (sub-nanosecond pulses are possible).

The importance of high quality X-rays generated in synchrotron sources cannot be overstated, as the techniques which rely upon them find uses in all branches of science, from aeronautical engineering to zoology. Diamond Light Source (the UK's national facility for synchrotron radiation) exemplifies the features of a modern synchrotron and how they are used to generate synchrotron radiation:

(i) A cathode (typically tungsten oxide) is heated under vacuum, resulting in thermionic emission of electrons. A voltage is then applied by separate anodes, generating a directional positive electric field which allows the electrons to escape the cathode; without the voltage applied, there is no net current as the electrons cannot escape and simply fall back into the cathode. The speed at which the electrons are removed from the cathode is dependent on the strength of the applied electric field: for Diamond, the electron beam at this point has energy 90 keV. This device is known as an electron gun.

(ii) The electrons then enter the linear accelerator (linac) and are accelerated to close to the speed of light by a series of alternating electric fields, achieving a relativistic energy of 100 MeV.

(iii) After acceleration in the linac, the electrons enter the booster ring where they are further accelerated to an energy of 3 GeV.

(iv) The electrons are then injected into the polygonal storage ring, which comprises 48 straight sections joined by bending magnets to form a loop (of circumference

562 m). This loop remains under high vacuum during operation to reduce electron energy losses through interaction with matter. Insertion devices (either wigglers or undulators) are positioned on straight sections and permit greater brilliance to be obtained.

(v) The synchrotron radiation generated by the storage ring is then channelled by bending magnets or insertion devices into beamlines, the experimental stations in which analytical techniques are performed.

During operating periods, the storage ring is regularly topped up to maintain a constant electron current and prevent fluctuations in beam properties at the beamlines. An array of interlocks and safety systems is fitted to all beamline facilities due to the dangers inherent to high energy X-rays, and special engineering measures are taken to provide compartmentability. For example, each Diamond beamline has a Front End section, which serves several purposes: to protect the storage ring from leaks or faults in beamlines; to monitor the position of the synchrotron radiation beam; and to remove as much heat from the high energy beam as possible. Beyond this stage each beamline will differ to suit its own analytical requirements and equipment.

Sample preparation

For all experiments performed as part of these studies on B18, Diamond Light Source, samples were pelletised prior to the beamtime. Pelletising sets of diameter 8 or 13 mm were available, and could be used interchangeably depending on sample constitution. The composition of the pelletised sample must be calculated to achieve sufficient absorption from the element of interest without absorbing too strongly overall; if necessary, binding agents like cellulose can be used to improve the physical properties of the pellet (in cases of small sample mass or lack of pellet structural integrity) without significantly affecting the absorption properties of the sample. B18 analysis was normally performed in Quick EXAFS (QEXAFS) mode with a fast scanning Si (111) double crystal monochromator. In general, scan duration was three minutes per scan, with three scans per sample: this afforded sufficiently reliable EXAFS signal out to higher k ranges up to $k = 14$, depending on the sample.

The experimental setup at the XMaS beamline at the ESRF for the experiments reported herein differed significantly. Since these experiments were intended to employ a novel *in situ* apparatus, samples were instead pressed into blocks and then mounted in the cell. Unlike B18, XMaS does not possess a QEXAFS mode and moreover does not yield reliable EXAFS data, instead producing mainly XANES data. Scan duration on XMaS was of the order of 30 minutes per scan, and with a minimum of three scans per sample, each sample required at least 90 minutes for measurement alone. As a consequence, time resolution was markedly poorer: the usefulness of *in situ* measurements decreases with decreasing time resolution, as key reaction changes can pass unnoticed. Regrettably, due to problematic gas containment in the sample cell, the proposed experiment to investigate propane oxidation at XMaS could not proceed: instead, methanol selective oxidation on VO_x/Fe_2O_3 was investigated.

Al K-edge measurements were performed on PHOENIX, Swiss Light Source, using small quantities of sample powders dispersed on carbon tape. Spectra were acquired both in fluorescence and electron yield modes: this latter mode is similar to XPS, relying on the detection of Auger electrons/Auger electron-induced secondary electrons to measure the sample. Due to the limited mean free path of Auger electrons, the results obtained in this mode are strongly surface-sensitive.

2.3.9 X-ray diffraction

Background theory

X-ray diffraction (XRD) is an important technique that permits the rapid determination of the composition and structure of a material; the technique is typically non-damaging to samples during analysis, which is hugely beneficial. When X-rays are directed at a material, some of the incoming X-rays will be elastically scattered through collision with electrons or nuclei in the material, yielding secondary waves which are dispersed. When the material under X-ray illumination possesses a regular, repeating structure (i.e. it is crystalline), an array of scattered waves results (Figure 2.15); most of these waves are removed by destructive interference, but certain scattering angles will afford constructive interference. These points will appear as bright reflections on a diffraction pattern, and their locations are dictated by Bragg's Law:

$$n\lambda = 2d \sin\theta \tag{2.24}$$

where n is an integer, λ is the beam wavelength, d is the diffraction spacing and θ is the angle of incidence.

Since many substances exist in crystalline structures, the scope of analysis by XRD is wide indeed. Measurements can be made on single crystals to determine single crystal structures, or on bulk powders to reveal the crystalline phases present within the material:

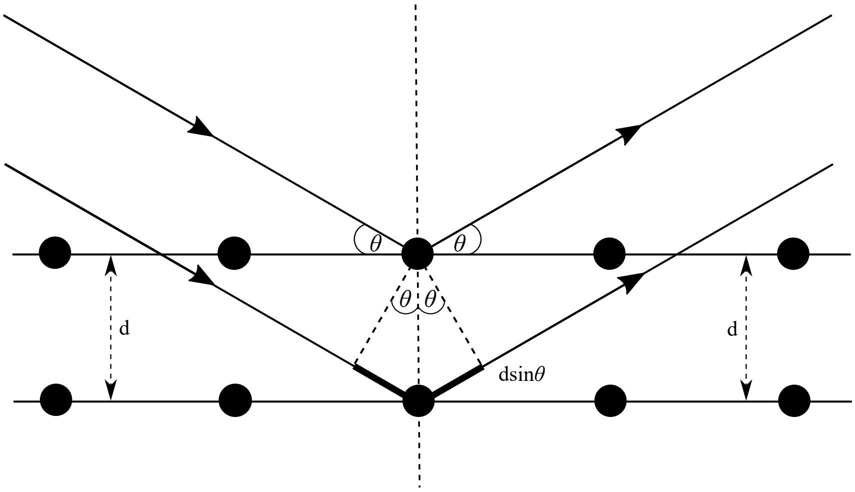

Figure 2.15: A diagram displaying the principle of X-ray diffraction and the relation of Bragg's Law to structural properties.

measurements of this latter type have been performed regularly on catalyst powders. The principle of a typical powder XRD measurement is simple: the sample is illuminated with monochromatic X-rays, while a detector moves about the opposite side of the sample (Figure 2.16). Since the diffraction spacing, wavelength and incident angle remain constant during measurement, Bragg's Law dictates that regions of constructive interference will be traversed by the detector at regular intervals, yielding a diffraction pattern. This pattern will reveal all crystalline materials present in sufficient quantity (i.e. thin layers/monolayers may not be visible), aiding the assessment of sample homogeneity and the revealing the presence of other phases/substances.

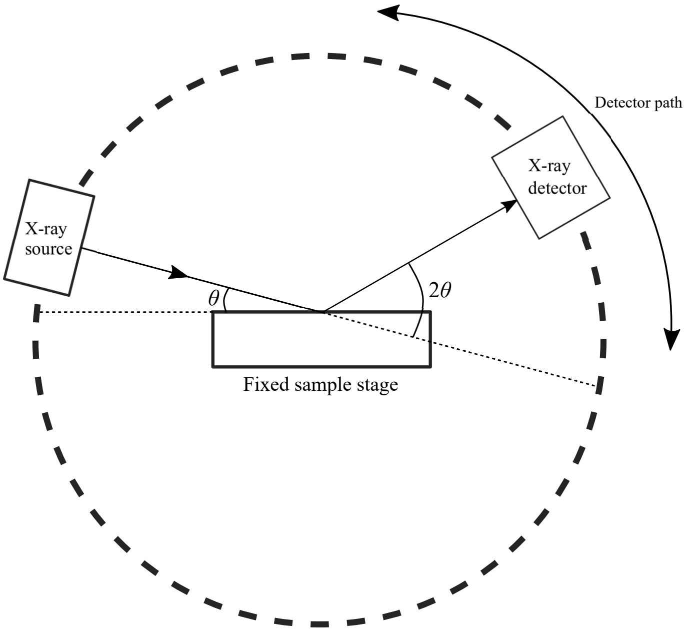

Figure 2.16: A schematic diagram of a typical XRD experiment.

Further information beyond the structure and composition of a material can also be revealed from a diffraction pattern, e.g. the size of crystalline particles in the material: this offers a convenient means to validate particle size measurements obtained by other techniques. Particle size can be determined using the Scherrer equation:

$$\tau = \frac{K\lambda}{\beta \cos\theta} \tag{2.25}$$

where τ is the mean size of the crystalline domains, K is shape factor (dimensionless, typically close to 1), λ is the beam wavelength, β is the line broadening at FWHM and θ is the angle of incidence.

Experimental

XRD has frequently been employed throughout these studies as a means to determine sample quality and probe differences in support materials. For XRD measurements of shell-core catalysts, the shell layers are normally unobserved; in these cases, the diffraction patterns (in which only the haematite support is observed for example) reinforce the suggested behaviour wherein segregated shell and core moieties are formed, and not interspersed phases of bulk support/shell metal oxides (e.g. iron vanadate). XRD was performed on a fifth generation Rigaku MiniFlex 600 benchtop diffractometer (with tube voltage 40kV and tube current 30 mA) using a Cu Kα X-ray source (λ = 0.15418 nm) under ambient conditions: access to the diffractometer (and its supporting lab services) was kindly provided by the Materials Characterisation Laboratory at ISIS Neutron Source. The range of 2θ scanned by the detector can be set beforehand; a majority of scans were performed between 5° and 85°, with each scan typically lasting approximately 30 minutes to improve pattern quality.

2.3.10 X-ray photoelectron spectroscopy

Background theory

X-ray photoelectron spectroscopy (XPS), or alternatively electron spectroscopy for chemical analysis (ESCA), is a surface-sensitive quantitative technique that permits measurement of elemental composition and oxidation state through irradiation of the sample under high or ultra-high vacuum by X-rays, and collection of the emitted photoelectrons by a detector. The technique is rendered surface-sensitive by the relatively short path length of the emitted photoelectrons. Any photoelectrons emitted from too far below the surface cannot escape the sample and reach the vacuum; their passage towards the detector is impeded due to interactions between the newly emitted photoelectron and the material including, *inter alia*, inelastic collision, recombination and sample excitation. The severity of these effects on emitted photoelectrons increases exponentially with sample depth, affording a concomitant decrease in the likelihood of a deeper photoelectron escaping the sample. This drastically reduces the contribution of the sample interior to the XPS spectrum and limits sample acquisition of any quality to the surface layers.

Upon irradiation by X-ray photons, photoelectrons are emitted in accordance with the photoelectric effect (Figure 2.17). Their kinetic energies are expressed by:

$$\text{Kinetic energy} = h\nu - \text{BE} - \phi_{\text{spec}} \tag{2.26}$$

where $h\nu$ is the photon energy, BE is the electron binding energy and ϕ_{spec} is the spectrometer work function. Since each element has a characteristic set of binding energies, the resultant XPS peaks enable element-specific determination of surface composition, electronic configuration and oxidation state. Differences in binding energies can be explained by assessing the chemical state of the electrons in a sample: for example, small differences in electronegativity (as might be expected with changes in oxidation state) significantly alter electron binding energies.

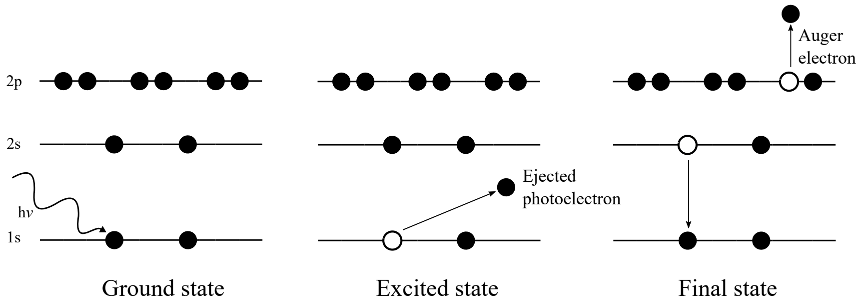

Figure 2.17: Principles of photoemission and Auger emission essential to XPS analysis. Higher energy levels are omitted for clarity.

XPS does not rely solely on photoemission and detection of the ejected photoelectrons to produce signals. The irradiation and ejection of a core electron from the atom produces an excited state, which contains a core hole. An electron in a higher energy level may drop to the core level to fill this vacancy, releasing energy in the process. This excess energy can then be transferred to a secondary outer electron, prompting its ejection from the atom (Figure 2.17). The kinetic energy of the ejected electron corresponds to the difference in energy between the initial electronic transition energy which fills the core vacancy and the ionisation energy of the electron energy level from which the Auger electron originates. Auger emission does not always occur; indeed the excess energy from filling the core hole is more frequently released as a photon.

In a typical high resolution XPS instrument, the sample is placed onto a moveable stage and is irradiated by monochromatic X-rays (Figure 2.18). The electrons thus ejected from the sample move through a series of electron optics, which collect particular electrons and focus them on the entrance point to the hemispherical analyser. Strong electric potentials are maintained within the hemispherical analyser (with different potentials on the inner and outer edges), which permit only electrons with certain energies (so-called pass energies) to reach the detector slits and the detector itself to maintain a consistent energy resolution. Electrons reaching the detector are counted in discrete events, and recorded with their detection time and energy.

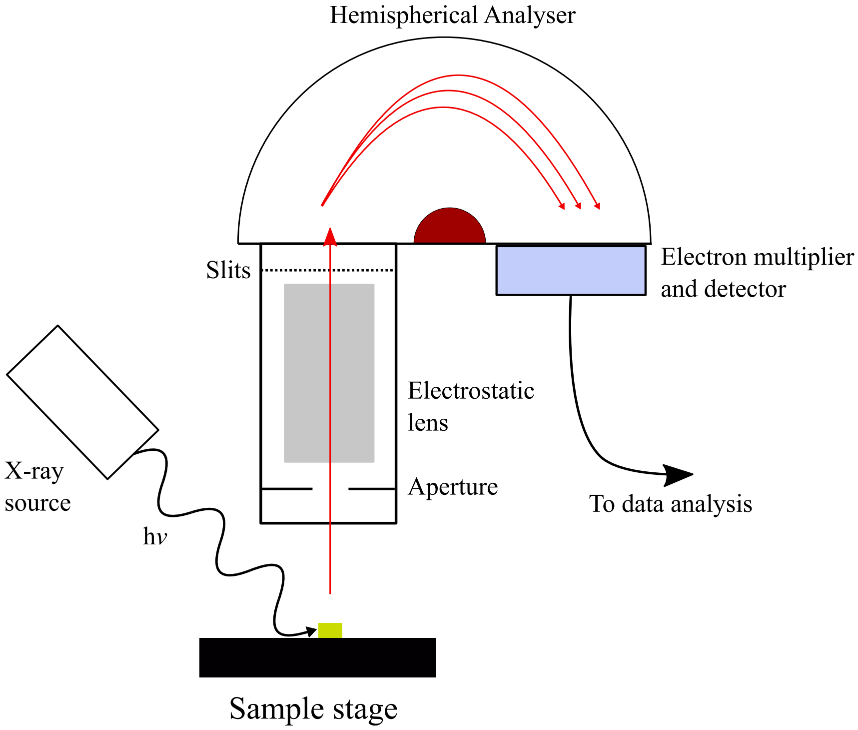

Figure 2.18: A schematic diagram of a typical XPS instrument.

Experimental

Spectra were obtained using a Kratos AXIS Ultra-DLD XPS spectrometer with 1486.6 eV monochromatic Al Kαradiation and 40 eV pass energy. Spectra were referenced to the C 1s peak at 284.7 eV, and processed with CasaXPS software. XPS was performed by David Morgan of Cardiff University, and by Shaoliang Guan at HarwellXPS, the EPSRC National Facility for X-Ray Photoelectron Spectroscopy.

References

(1) IUPAC, *Compendium of Chemical Terminology, 2nd ed.* Ed. A. D. McNaught and A. Wilkinson, Blackwell Scientific Publications, Oxford, 1997.

(2) P. R. Davies and G. G. Mariotti, *The Journal of Physical Chemistry*, 1996, **100**, 19975–19980.

(3) R. Gorte, *Catalysis Today*, 1996, **28**, 405–414.

(4) N.-Y. Topsoe, K. Pedersen and E. G. Derouane, *Journal of Catalysis*, 1981, **70**, 41–52.

(5) J. L. Falconer and J. A. Schwarz, *Catalysis Reviews*, 1983, **25**, 141–227.

(6) R. J. Cvetanovic and Y. Amenomiya, *Catalysis Reviews*, 1972, **6**, 21–48.

(7) C. N. Satterfield, *AIChE Journal*, 1981, **27**, 174–176.

(8) P. Redhead, *Vacuum*, 1962, **12**, 203–211.

(9) R. White, *Chromatography/Fourier Transform Infrared Spectroscopy and its Applications*, Taylor & Francis, 1989.

(10) R. O'Handley, *Modern Magnetic Materials: Principles and Applications*, Wiley, 1999.

(11) M. Claeys, E. van Steen, J. van Steen, J. Visagie and J. van der Loosdrecht, US Patent 20110204884A1, 2010.

(12) G. W. A. Milne, *Biomedical Mass Spectrometry*, 1977, **4**, 68–68.

(13) R. Egerton, *Physical Principles of Electron Microscopy: An Introduction to TEM, SEM, and AEM*, Springer US, 2011.

(14) H. H. Rose, *Science and Technology of Advanced Materials*, 2008, **9**, 014107.

(15) D. Jesson and S. Pennycook, *Proceedings of the Royal Society of London A: Mathematical, Physical and Engineering Sciences*, 1995, **449**, 273–293.

(16) R. F. Egerton, *Reports on Progress in Physics*, 2009, **72**, 016502.

(17) C. Ahn, *Transmission electron energy loss spectrometry in materials science and the EELS atlas*, Wiley-VCH, 2004.

(18) H. Niemantsverdriet, in *Spectroscopy in Catalysis*, John Wiley & Sons, Ltd, 2007, ch. Diffraction and Extended X-Ray Absorption Fine Structure (EXAFS), pp. 147–177.

(19) D. Koningsberger, B. Mojet, G. van Dorssen and D. Ramaker, *Topics in Catalysis*, 2000, **10**, 143–155.

(20) D. E. Sayers, E. A. Stern and F. W. Lytle, *Physical Review Letters*, 1971, **27**, 1204–1207.

(21) J. J. Rehr and R. C. Albers, *Reviews of Modern Physics*, 2000, **72**, 621–654.

(22) M. Newville, *Journal of Synchrotron Radiation*, 2001, **8**, 322–324.

(23) B. Ravel and M. Newville, *Journal of Synchrotron Radiation*, 2005, **12**, 537–541.

(24) J. Szlachetko, M. Nachtegaal, E. de Boni, M. Willimann, O. Safonova, J. Sa, G. Smolentsev, M. Szlachetko, J. A. van Bokhoven, J.-C. Dousse, J. Hoszowska, Y. Kayser, P. Jagodzinski, A. Bergamaschi, B. Schmitt, C. David and A. Luecke, *Review of Scientific Instruments*, 2012, **83**, 103–105.

Chapter 3

Novel shell materials in shell-core methanol oxidation catalysts

3.1 Introduction

This chapter addresses two areas of interest within the context of MO_x/Fe_2O_3 shell-core catalysts. The primary research theme discussed herein is the exploration and development of new metal oxides as shell materials (i.e. different MO_x), though certain continued investigations of MoO_x/Fe_2O_3 will also be discussed. The soundness of the shell-core design for MoO_x/Fe_2O_3 has been demonstrated (examples are provided in section 1.6 and in the cited literature), but so far studies have been limited to Mo-containing catalysts.[1–4] Many of the neighbouring elements to Mo in the periodic table afford catalytically interesting metal oxides, including those useful in methanol selective oxidation, e.g. V_2O_5 or Nb_2O_5. The rationale behind the studies reported in this chapter is best understood by considering by the following questions:

(i) Can other catalytically relevant metal oxides form shell-core catalysts in a manner similar to MoO_x/Fe_2O_3?

(ii) Are any differences in structure or reactivity apparent in novel shell-core catalysts compared to MoO_x/Fe_2O_3?

(iii) What factors affect the validity and applicability of the MO_x/Fe_2O_3 shell-core model?

(iv) Where shell-core formation is not possible, why not?

The exploration of novel shell-core catalysts is greatly facilitated through reflection on the prior knowledge gathered from studies of MoO_x/Fe_2O_3 catalysts. The initial standpoint for these investigations was an assumption, namely that the shell-core model could be extended to other oxides, and that trends like those found for MoO_x/Fe_2O_3 would also be observed in novel shell-core catalysts.

One must recall that MoO_x/Fe_2O_3 catalysts were developed as a means to recreate the hypothesised surface of the iron molybdate industrial catalyst, but in a manner more amenable to superior analysis. At this stage, it is sensible to summarise the characteristics of MoO_x/Fe_2O_3 catalysts to properly understand the shell-core motif. These catalysts consist of a haematite core enwrapped by surface MoO_x units, whose quantity varies depending on notional monolayer (ML) coverage. This coverage can be varied by altering the amounts of Mo-precursor (ammonium heptamolybdate) used during catalyst synthesis (an example calculation for a particular ML coverage is given in Chapter 2).

After aqueous incipient wetness impregnation with ammonium heptamolybdate, the material is dried at 120°C overnight before calcination for 24 hours. To properly form a MoO_x/Fe_2O_3 catalyst requires careful control of calcination temperatures. Essentially, 500°C is necessary to form the desired catalyst, while 400°C generates significant amounts of MoO_3 (as determined by Raman spectroscopy) and lower temperatures leave the MoO_x amorphous (and the catalyst thus unselective).[3] In general, 3 ML MoO_x/Fe_2O_3 catalysts were preferred for investigation, since the methodology used to compute the required quantity of Mo precursor relies on some assumptions. It was considered that a calculated 1 ML MoO_x might undershoot in reality, resulting in a catalyst with less than a full monolayer at the surface. To obviate this, 3 ML MoO_x catalysts were employed, guaranteeing the presence of a full shell layer. In addition, a 3 ML MoO_x catalyst possesses an absolute quantity of Mo threefold greater than 1 ML, improving data quality during analysis.

While Mo is commonly regarded as the metal of choice for formaldehyde production, it is by no means the only catalyst selective to formaldehyde. Vanadium oxide, or vanadia, also displays high selectivity to formaldehyde, achieving selectivities of greater than 85% under the correct conditions.[5] In addition, a range of other important oxidation processes (including propylene and propane oxidation) rely on vanadia-based catalysts. Consequently, vanadia was selected as the first target metal oxide for incorporation into a shell-core catalyst, both for its behaviour during methanol oxidation and for its illustrious history as a catalyst for other reactions. Interest was subsequently directed to the prospects of including niobia in a shell-core catalyst, again due to its catalytic relevance to a range of reactions.

3.2 Experimental

A short description of the synthetic methods and characterisation techniques reported in this chapter is given below: a more complete description is given in Chapter 2 (Experimental).

3.2.1 Catalyst preparation

All catalysts and materials discussed in this chapter were prepared by incipient wetness impregnation of Fe_2O_3 with the relevant quantity of metal oxide precursor. For VO_x catalysts, the precursor is ammonium metavanadate, NH_4VO_3; for NbO_x catalysts, ammonium niobate oxalate hydrate, $C_{10}H_5NbO_{20} \cdot xH_2O$, is used. After thorough mixing, the material is dried and then calcined under air in a muffle furnace for 24 hours. To produce MoO_x/Fe_2O_3 catalysts by incipient wetness impregnation, ammonium heptamolybdate is dissolved in a known quantity of water; ammonium niobate oxalate hydrate is similarly dissolved in water to produce Nb-based catalysts. For VO_x catalysts, however, dissolution of ammonium metavanadate in water is problematic, due to its extremely poor solubility therein. Instead, highly-viscous ethanolamine must be used as the solvent for the incipient wetness impregnation process, a significant hindrance. To successfully impregnate the support with the precursor and ensure sample homogeneity, thorough mixing—typically manually by spatula—of the solution with the solid is required. This is trivial with an aqueous solution, but markedly less trivial with a viscous, corrosive solution. While ammonium metavanadate is more soluble in ethanolamine than water, it is a limited increase. Small ML coverages ($\leq$ 3 ML) are achievable with one dosing, since the quantity of ammonium metavanadate required will dissolve in heated ethanolamine; greater ML coverages necessitate multiple dosing with lesser coverage equivalents (e.g. 12 ML $=$ 4 $\times$ 3 ML).

3.2.2 Characterisation

TPD and TPPFR were the linchpin techniques of this thesis, and particularly of this chapter, and were undertaken on the Hiden CATLAB microreactor. For TPD studies, each sample was placed inside the reactor at ambient temperatures. Under a constant flow of helium, multiple microlitre injections of methanol were introduced to saturate the surface of the catalyst, after which a constant temperature ramp was applied. The mass spectrometer records throughout the entire experiment, both to verify that methanol is successfully being injected, and to monitor the products undergoing desorption. For PFR, each sample was placed in the reactor in a stream of 10% O_2 in He, and heated at a constant rate of 8°C min^{-1} to 500°C with constant monitoring by mass spectrometry. Throughout the experiment, microlitre injections of methanol were made every two minutes. Post-experiment analysis utilises the integrals of each peak to compute methanol conversion and selectivity to various products at each injection. Raman spectroscopy is a crucial technique for understanding the formation process of each catalyst and verifying that the catalyst has formed correctly. XAS studies were conducted to assist the identification of the surface species of each catalyst, and to understand catalyst behaviour during catalysis.

3.3 VO_x/Fe_2O_3 shell-core catalysts

A range of VO_x/Fe_2O_3 shell-core catalysts of varying ML coverage was prepared and found to be effective for methanol selective oxidation catalysis. This section will detail the exploration of these catalysts: parts of this section were published in 2018.[6]

3.3.1 Initial feasibility studies

The objective in the early stages of these studies was to assess the generalisability of the shell-core system, i.e. whether such a system was achievable with alternative metal oxides as shells. A shell-core catalyst whose shell was based on vanadia represented a logical starting point, given the selectivity displayed by vanadia *per se* (Figure 3.1). V_2O_5 is a selective catalyst, generating notable quantities of formaldehyde at approximately 200°C with lesser quantities of CO produced at slightly higher temperatures: importantly, no CO_2 is observed. This is a vital point, as the means of determining the degree to which the haematite core of a shell-core catalyst has been successfully segregated hinges upon the different reactivities of shell and core moieties. If the shell material also displays selectivity to CO_2 in TPD, then TPD cannot be used to measure core inhibition and hence shell-core segregation. In this case, since V_2O_5 does not produce CO_2, the inferences made through TPD are entirely valid.

To explore the possibility of applying vanadia as a shell material, a series of VO_x/Fe_2O_3 catalysts were prepared by incipient wetness impregnation, starting with a 3 ML catalyst. At first, the process was performed using an aqueous solution; however, this afforded a poor catalyst with little vanadium content, no evidence of vanadate by Raman nor selectivity to formaldehyde. Despite some dissolution of ammonium metavanadate in water, this quantity was wholly insufficient, leaving little vanadium in the Fe_2O_3. An alternative solvent was then found, viz. ethanolamine, in which ammonium metavanadate exhibited greater solubility; it is, however, a markedly more viscous solvent. The initial

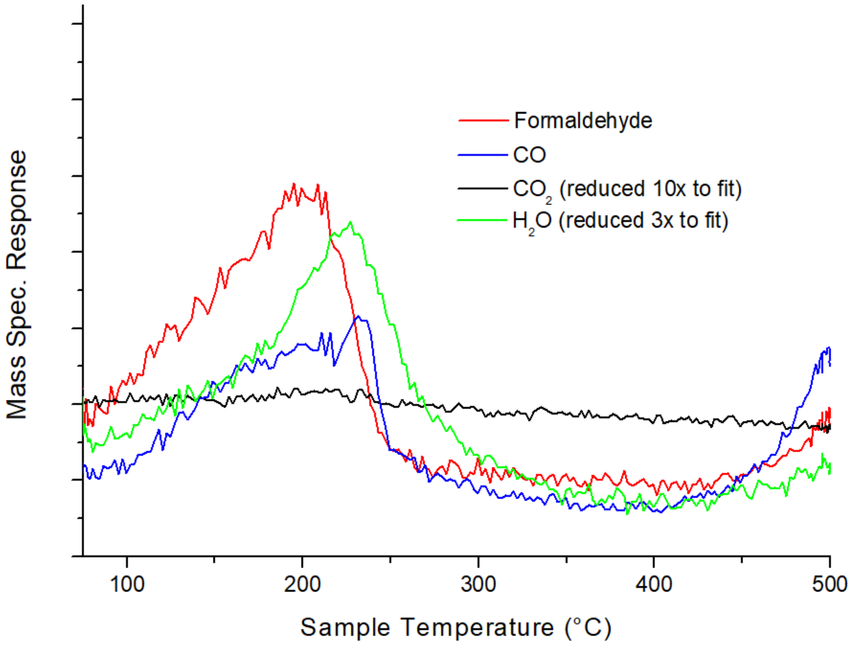

Figure 3.1: TPD data for V_2O_5 after methanol dosing, exhibiting high formaldehyde production (peak at 200°C). Gas flow: 30 mL/min He. Catalyst mass: 250 mg.

attempts to synthesise VO_x/Fe_2O_3 with ethanolamine yielded catalysts with significant inhomogeneity by Raman, which was attributed to problematic mixing due to the higher solvent viscosity. Later attempts to synthesise VO_x/Fe_2O_3 catalysts met with greater success, after the adoption of a modified synthetic method, wherein the mixture of solvent and Fe_2O_3 was partially dosed and left to settle for an hour after thorough mixing. This waiting period allowed the solvent to more effectively penetrate the Fe_2O_3 by capillary action before further addition of precursor solution. This became the standard method for producing VO_x/Fe_2O_3 catalysts.

The 3 ML VO_x/Fe_2O_3 catalyst visually resembles haematite after calcination, with little if any difference in colour between pre- and post-incipient wetness samples. In the prior studies of MoO_x/Fe_2O_3 systems, a temperature of 500°C was deemed necessary to form a successful shell-core catalyst. Consequently, for this initial 3 ML VO_x/Fe_2O_3 proof of concept sample, 500°C was selected as the calcination temperature. By TPD, the results are highly encouraging (Figure 3.2): clear selectivity to formaldehyde without any significant CO_2 production. This clearly suggests that the Fe_2O_3 present is not participating directly in catalysis of the methanol, presenting an encouraging sign that a shell-core system has indeed been developed for 3 ML VO_x/Fe_2O_3.

Analysis of 3 ML VO_x/Fe_2O_3 was also performed by PFR to complement the TPD study of 3 ML VO_x/Fe_2O_3 (Figure 3.3), further demonstrating the validity of the shell-core

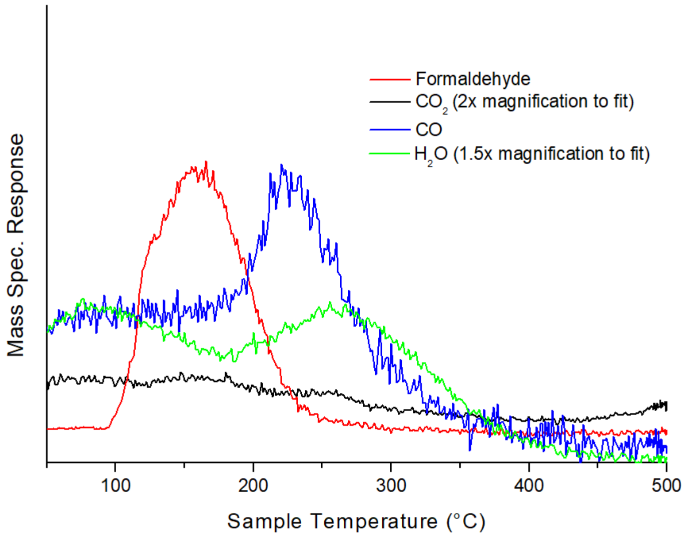

Figure 3.2: TPD data for 3 ML VO_x/Fe_2O_3 feasibility studies. Gas flow: 30 mL/min He. Catalyst mass: 250 mg.

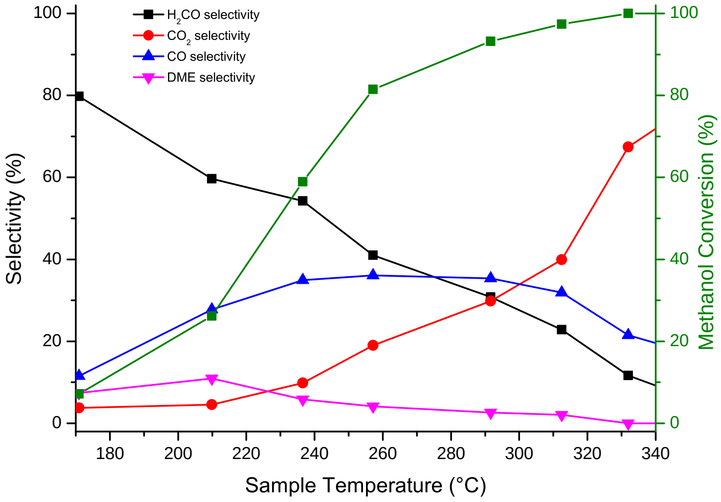

Figure 3.3: Pulsed-flow reaction data for 3 ML VO_x/Fe_2O_3 under a 10% O_2 atmosphere (30 mL/min). Catalyst mass: 250 mg.

catalyst. Formaldehyde selectivity is initially high, exceeding 75%, before CO production begins to dominate at moderate temperatures and CO_2 at higher temperatures. T_{50} was observed at approximately 230°C. Crucially, the CO_2 witnessed in this PFR study does not originate from the Fe_2O_3 portion of the catalyst, but instead arises from oxidation at higher temperatures (and only under O_2) of the earlier selectively formed products. If Fe_2O_3 is participating directly during catalysis, CO_2 is produced from 180°C; since the CO_2 is produced here at temperatures well beyond 180°C, one can be sure that the Fe_2O_3 core is not exposed.

To ensure that the resulting catalyst is not simply a bulk iron vanadate catalyst unintentionally generated by incipient wetness impregnation, the constitution of 3 ML VO_x/Fe_2O_3 was analysed by XRD (Figure 3.4).

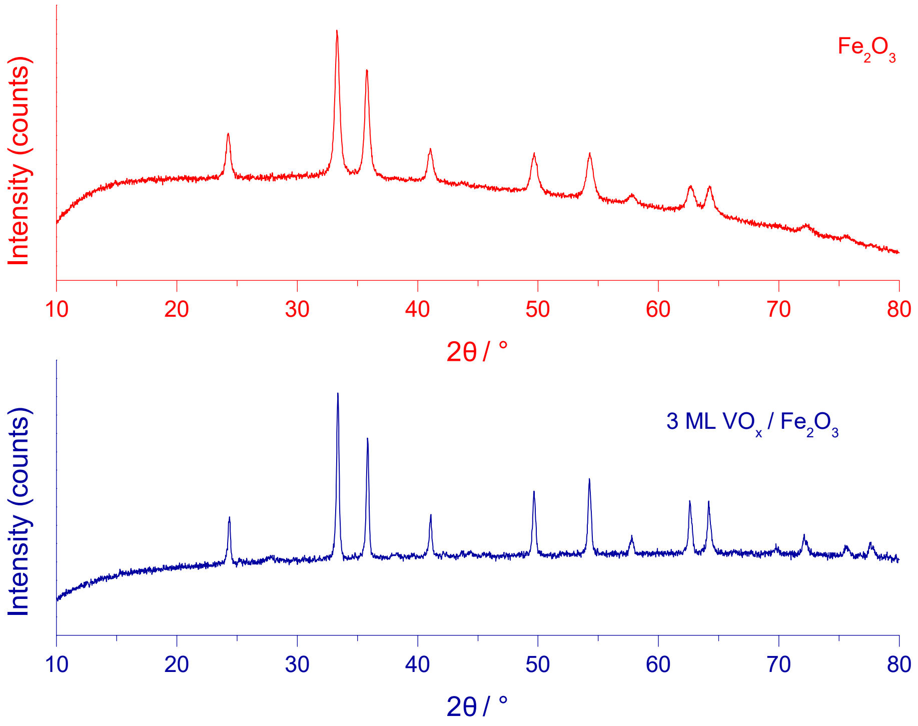

Figure 3.4: A comparison of XRD patterns for Fe_2O_3 and 3 ML VO_x/Fe_2O_3.

By XRD, the post-calcination catalyst resembles Fe_2O_3: this is highly promising. Were a bulk compound to be responsible for selectivity trends seen by TPD and PFR, and not a shell-core catalyst, its presence would be revealed by XRD. Since the XRD data displayed only Fe_2O_3 peaks and yet the TPD and PFR data revealed strong selectivity to formaldehyde, it is reasonable to assert that a VO_x/Fe_2O_3 shell-core catalyst has been formed, as selective oxidation products are unattainable without the successful segregation of the Fe_2O_3 core.

Alongside TPD, XPS is a useful measure of surface speciation and is partially surface-sensitive: this is useful, since all vanadium in a properly-formed VO_x/Fe_2O_3 shell-core catalyst will exist solely in the surface layers. XPS analysis confirms that vanadium remains at the surface, and it is clearly observed in the spectrum (Figure 3.5); however, due to the several-nanometre penetration depth of standard XPS, Fe is also visible (Figure 3.6). The V $2p_{3/2}$ and Fe $2p_{3/2}$ binding energies indicated each element to be in its highest oxidation state, namely V(V) and Fe(III) (Table 3.1).[7]

Table 3.1: Measured XPS peak data for 3 ML VO_x/Fe_2O_3.

Peak identity	Binding energy (eV)
V $2p_{3/2}$	517.92
Fe $2p_{3/2}$	710.92
O 1s	530.92
C 1s	284.92

The nature of the surface can be further clarified by IR spectroscopy, particularly by DRIFTS. With a suitable probe molecule, e.g. methanol, surface-sensitivity can be achieved. 3 ML VO_x/Fe_2O_3 was dosed with methanol, heated gently and monitored by DRIFTS alongside a similarly-treated sample of Fe_2O_3 (Figure 3.7). Striking differences between the spectra are observed, intimating fundamental differences between the surface environments of 3 ML VO_x/Fe_2O_3 and Fe_2O_3. In both spectra, adsorbed methoxy species are observed at 2800-3050 cm^{-1} as expected. The 3 ML VO_x/Fe_2O_3 spectrum shows peaks between 1650 and 2000 cm^{-1}; it has been reported in the literature that the peak at approximately 2050 cm^{-1} arises from a V−O overtone corresponding to V^{4+}−O. This indicates that the V present in the surface layer has been reduced to V(IV) from V(V), a process known to occur during oxidation of the initially-formed methoxy species.[8,9] In the Fe_2O_3 spectrum, peaks are observed between 1360 and 1560 cm^{-1}, which are attributed to the formate intermediate present on the Fe_2O_3 surface during methanol combustion. Since these formate peaks are not observed for 3 ML VO_x/Fe_2O_3, it can be inferred that the surface has been successfully modified with VO_x to preclude the multiple neighbouring Fe sites necessary to support and stabilise formate.

Taken together, the spectroscopic and reactor data from 3 ML VO_x/Fe_2O_3 strongly imply that the segregation necessary for the success of a shell-core catalyst has indeed occurred. With the knowledge that VO_x can be incorporated as a shell material in shell-core catalysts, more detailed and extensive investigations into VO_x/Fe_2O_3 catalysts could

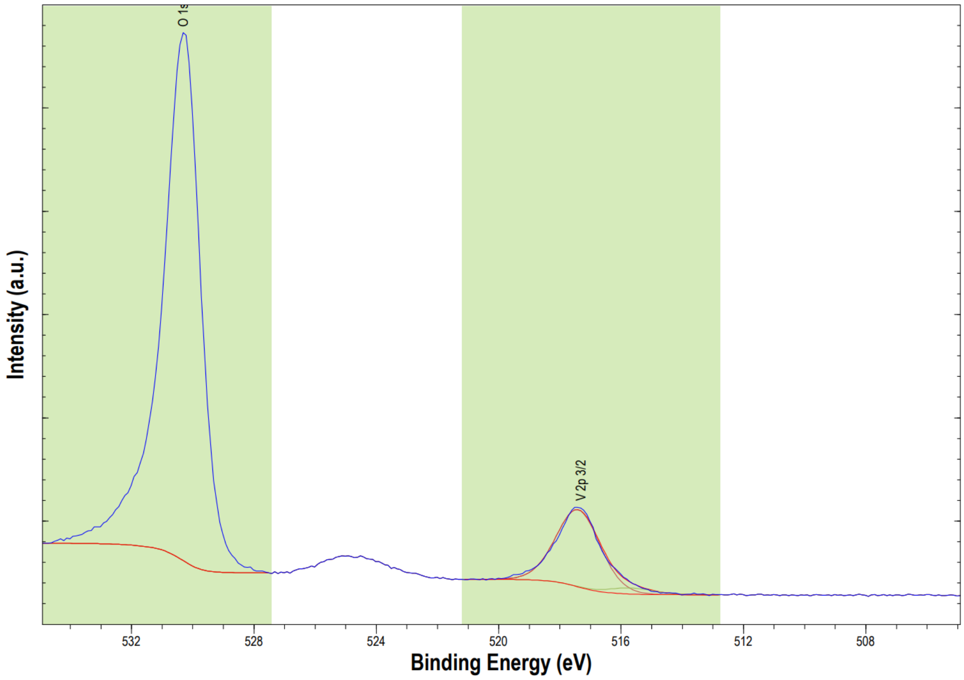

Figure 3.5: XPS spectrum of 3 ML VO_x/Fe_2O_3: V $2p_{3/2}$

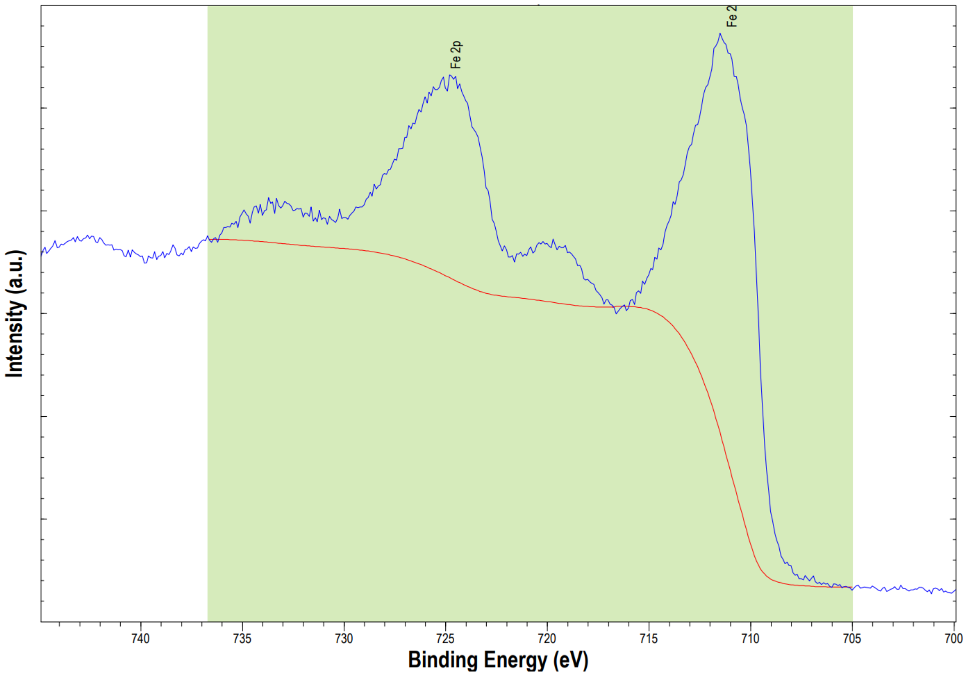

Figure 3.6: XPS spectrum of 3 ML VO_x/Fe_2O_3: Fe 2p and Fe $2p_{3/2}$

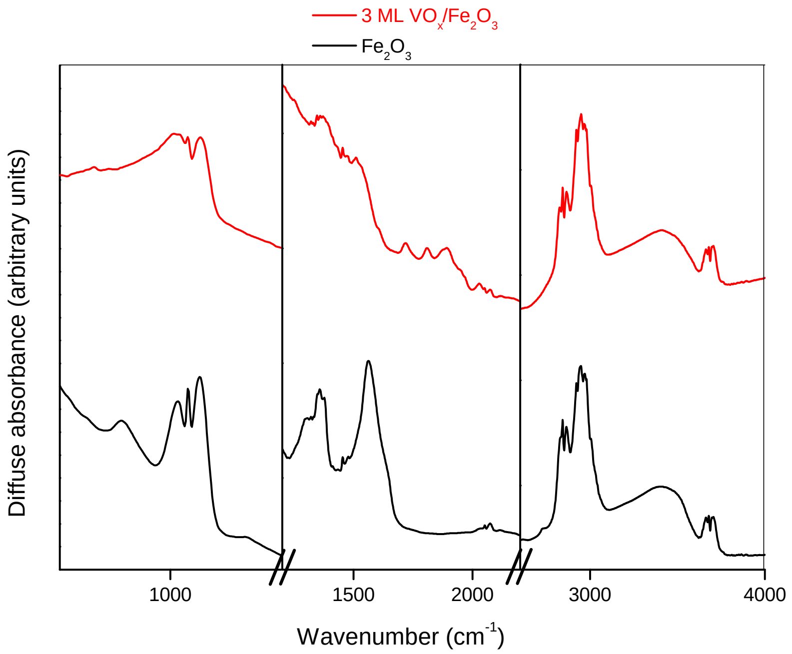

Figure 3.7: A comparison of key regions in the DRIFTS spectra of Fe_2O_3 and 3 ML VO_x/Fe_2O_3 after addition of methanol and temperature ramp to 150°C. Note: magnification differs between panels for clarity.

now be pursued. At this stage, it is useful to consider the theorised structure of the shell-core catalyst in general. For MoO_x/Fe_2O_3 catalysts, the shell-core structure contains:[3]

(i) the core haematite moiety;

(ii) the selective outermost surface monolayer of MoO_x units; and

(iii) for all catalysts with more than 1 ML MoO_x, a layer of iron molybdate sandwiched between the core and outermost layer.

The size of the sandwich iron molybdate layer depends on the number of ML coverages in use: each successive ML beyond 1 ML is incorporated into the sandwich layer. For example, a 3 ML MoO_x/Fe_2O_3 catalyst contains 2 ML of sandwiched iron molybdate, a 6 ML catalyst contains 5 ML of iron molybdate and so on. Importantly, no major differences in reactivity are exhibited between different ML MoO_x/Fe_2O_3 catalysts (when coverage is $\geq$1 ML).

An analogous system is proposed to exist for VO_x/Fe_2O_3 catalysts, comprising a haematite core, a selective outermost layer of VO_x units and a sandwiched layer of iron vanadate for >1 ML catalysts. In order to evaluate the validity of this proposition, it was decided to probe the whole gamut of VO_x/Fe_2O_3 catalysts, spanning single ML catalysts up to 12 ML samples.

3.3.2 Examining the effects of shell thickness in VO_x/Fe_2O_3 shell-core catalysts

With the validity of extending the shell-core motif to include VO_x appropriately demonstrated for 3 ML VO_x/Fe_2O_3, catalysts bearing three other VO_x loadings (namely 1, 6 and 12 ML) were synthesised by the same method for comparison with 3 ML VO_x/Fe_2O_3. For the 6 and 12 ML catalysts, the relatively poor solubility of ammonium metavanadate in ethanolamine necessitated repeated additions of metavanadate solution to achieve the correct ML coverage (see Section 3.2.1).

Surface area measurement

The surface area of a catalyst is highly pertinent to its prospects for success during reaction. If a catalyst affords high selectivity to a chosen product, but fails to convert significant quantities of the reactant under working conditions, its value is called into question. Catalytic activity is markedly influenced by the surface area of the catalyst, with small increases in surface area able to elicit large changes in activity. Consequently, a fair assessment of VO_x/Fe_2O_3 catalysts must commence with measurement of the surface areas of each catalyst post-calcination (Table 3.2). Importantly, surface area is itself impacted by the calcination temperature employed, with overly high temperatures damaging surface area (hence also activity).

Table 3.2: A comparison of BET-derived surface area values for VO_x/Fe_2O_3 catalysts and reference compounds. Where marked, calcination lasted 24 hours at 500°C.

Catalyst	Specific surface area ($m^2\,g^{-1}$)	Calcined?
Commercial V_2O_5	8.6	✓
Lab-produced V_2O_5	4.3	✓
Commercial Fe_2O_3 nanopowder (<50 nm)	21.2	×
Commercial Fe_2O_3 nanopowder (<50 nm)	20.1	✓
Lab-produced $FeVO_4$	10.9	✓
1 ML VO_x/Fe_2O_3	20.2	✓
3 ML VO_x/Fe_2O_3	20.1	✓
6 ML VO_x/Fe_2O_3	20.0	✓
12 ML VO_x/Fe_2O_3	20.2	✓

It is evident from BET measurements that the post-calcination surface area values for VO_x/Fe_2O_3 do not significantly differ, and instead greatly resemble the value obtained for post-calcination Fe_2O_3 alone. This is understandable, since the haematite core constitutes the large majority of each catalyst particle; no differences are observed between ML coverages, as they are all produced by the same method and calcined alike. This is a satisfactory result: no change in surface area was expected after the addition of a surface shell material, and nor was one seen.

Reactivity

Following the initial feasibility study, samples of 1, 3, 6 and 12 ML VO_x/Fe_2O_3 were examined by TPD measurements under He (Figures 3.8, 3.9, 3.10 and 3.11 respectively). No significant differences in reactivity with changes in ML coverage are apparent by TPD. This is unsurprising, since TPD is a surface-sensitive technique. Since all ≥ 1 ML VO_x shell-core catalysts are thought to possess an outermost layer of VO_x units, present irrespective of ML coverage, the surface selectivity will be the same between ML loadings. This finding corroborates the suggestion that each successive ML of VO_x is incorporated into the sandwiched $FeVO_4$ layer between the Fe_2O_3 core and the surface.

It is equally important to understand the behaviour of the catalyst under working conditions, i.e. under an oxygenic atmosphere. If the theorised shell-core structure is indeed formed for all VO_x/Fe_2O_3 catalysts, little reactivity difference is to be expected between different ML loadings during reaction. PFR studies under O_2 revealed that the reactivities observed for the different ML VO_x/Fe_2O_3 catalysts were broadly similar, as exemplified by 1 and 3 ML VO_x/Fe_2O_3 (Figures 3.12 and 3.13). The slight differences in selectivity and conversion can be accounted for by experimental error and post-experiment spectral overlap resolution. In both cases, T_{50} occurs at approximately 230°C, at which point formaldehyde selectivity starts to notably decline. Crucially, in both cases no significant CO_2 is observed at temperatures below 220°C: this is a key indicator that the Fe_2O_3 core is not directly reacting with incoming methanol. The CO_2 seen at higher temperatures originates from combustion of previously-formed selective products, an inexorable process on shell-core catalysts (including MoO_x/Fe_2O_3) during reactions under O_2. The selectivity displayed by the whole range of VO_x/Fe_2O_3 catalysts and the absence of any combustion behaviour further evince the validity of the shell-core catalyst when applied to VO_x.

Spectroscopy

Alongside the TPD and PFR studies, which indicated little difference between ML coverages, it is important to ascertain by spectroscopy whether any differences in structure or speciation are present throughout the range of VO_x/Fe_2O_3 catalysts. Raman spectroscopy

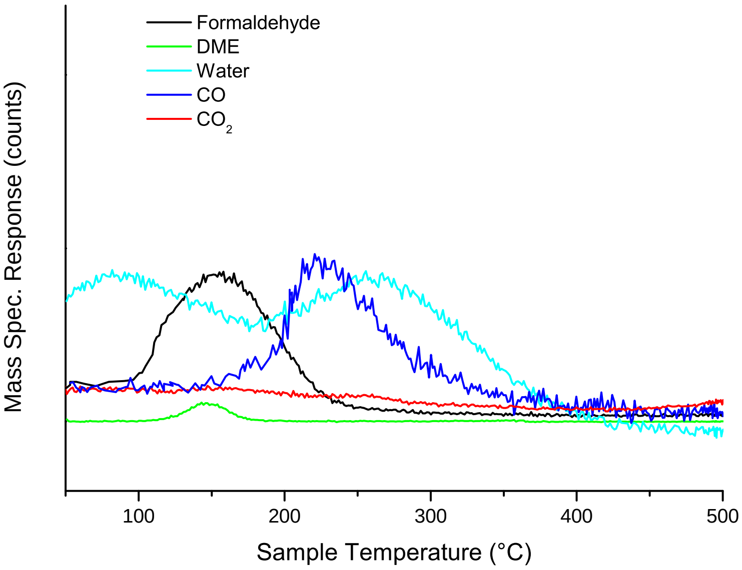

Figure 3.8: TPD data for 1 ML VO_x/Fe_2O_3. Gas flow: 30 mL/min He. Sample mass: 250 mg.

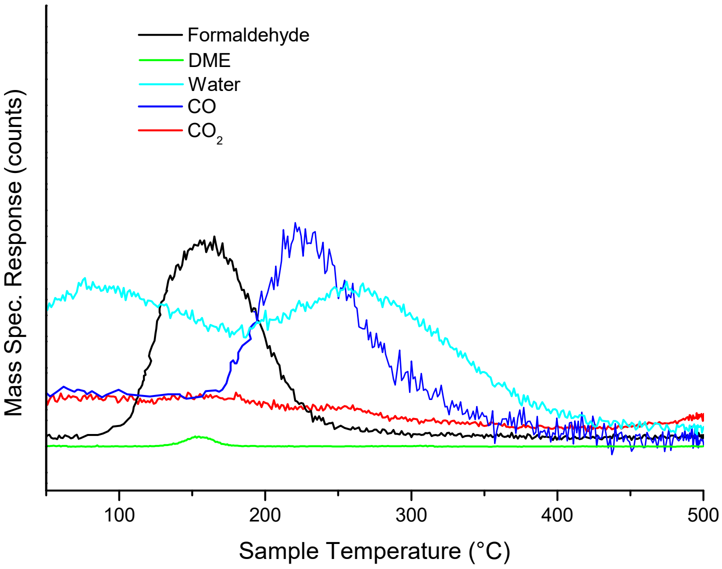

Figure 3.9: TPD data for 3 ML VO_x/Fe_2O_3. Gas flow: 30 mL/min He. Sample mass: 250 mg.

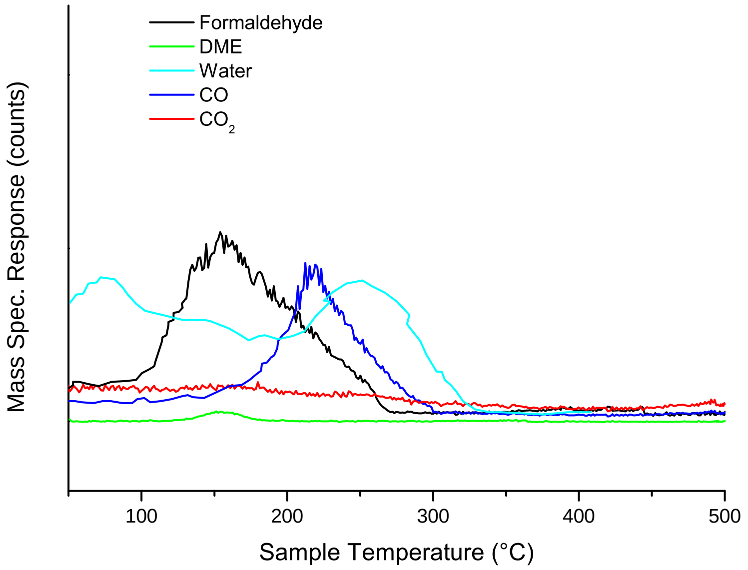

Figure 3.10: TPD data for 6 ML VO_x/Fe_2O_3. Gas flow: 30 mL/min He. Sample mass: 250 mg.

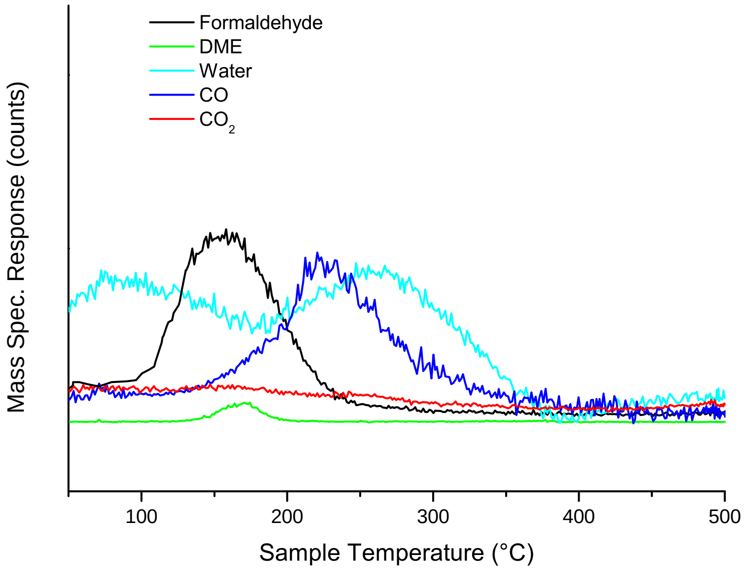

Figure 3.11: TPD data for 12 ML VO_x/Fe_2O_3. Gas flow: 30 mL/min He. Sample mass: 250 mg.

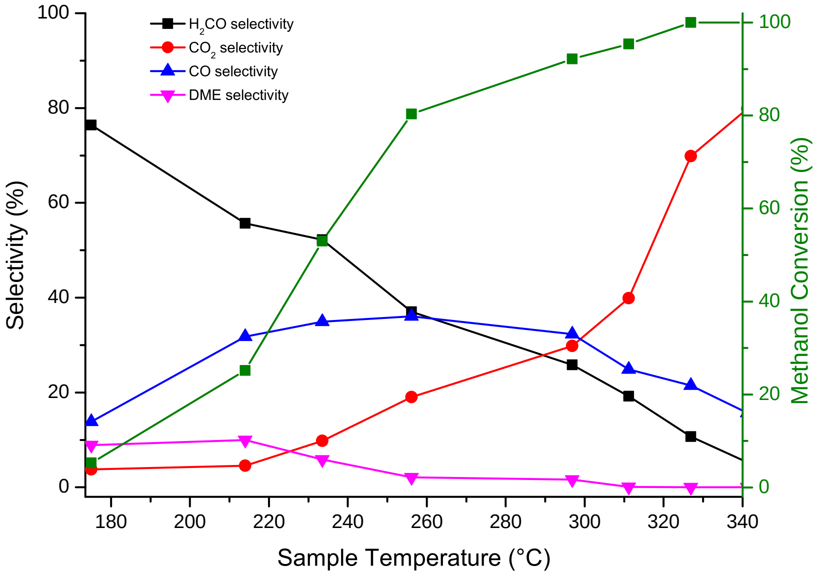

Figure 3.12: Pulsed-flow reaction data for 1 ML VO_x/Fe_2O_3. Methanol conversion is shown in green on the right-hand y-axis. Gas flow: 30 mL/min 10% O_2 in He. Sample mass: 250 mg.

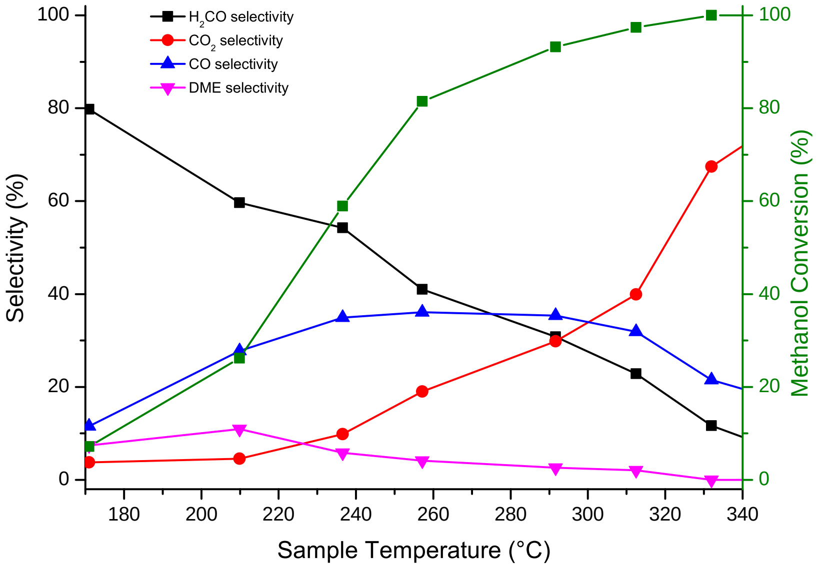

Figure 3.13: Pulsed-flow reaction data for 3 ML VO_x/Fe_2O_3. Methanol conversion is shown in green on the right-hand y-axis. Gas flow: 30 mL/min 10% O_2 in He. Sample mass: 250 mg.

is well suited to this task, and was extensively used during the initial investigations of MoO_x/Fe_2O_3 catalysts for the same purpose.[3]

Samples of 1, 3, 6 and 12 ML VO_x/Fe_2O_3 were examined by Raman spectroscopy to assess any differences in catalyst constitution (Figure 3.14). Since excess ML coverages are presumed to incorporate into the iron vanadate sandwich layer, a reference Raman spectrum of $FeVO_4$ was recorded; the Raman spectrum of V_2O_5 is also included for reference (Figure 3.15). To understand the VO_x/Fe_2O_3 catalyst peaks, a summary of the relevant Raman peak assignments from literature is provided below (Table 3.3).[10,11]

Table 3.3: Raman assignments for peaks relevant to VO_x/Fe_2O_3 catalysts, V_2O_5 and $FeVO_4$.

Wavenumber (cm^{-1})	Raman assignment	Species identity
610	e_g Fe–O stretching	Fe_2O_3
634, 663	V–O–Fe bridging	$FeVO_4$
730-910	Asymmetric VO_4 unit stretching	$FeVO_4$
934, 969	Terminal V=O bond stretching	$FeVO_4$
701	V–O–V deformation	V_2O_5
994	V–O stretching	V_2O_5

The greatest difference in the Raman spectra is observed between the 1 ML and the higher ML samples. Apart from haematite at 610 cm^{-1}, the former spectrum is bereft of Raman signals, while the latter spectra increasingly resemble $FeVO_4$. Due to the limited dimensionality of the outermost surface VO_x layer, it is not expected to be visible by Raman spectroscopy for any VO_x/Fe_2O_3 loading; for 1 ML VO_x/Fe_2O_3, where only the outermost VO_x layer exists, this dimensionality limitation yields an unexciting Raman spectrum. For the 3, 6 and 12 ML VO_x/Fe_2O_3 catalysts, however, the intensities of the non-haematite peaks increase—relative to the size of the haematite peak—with increasing ML coverage, denoting the presence of increasing quantities of $FeVO_4$. This greatly reinforces the proposed structure of the shell-core VO_x/Fe_2O_3 catalyst, providing clear evidence of increased quantities of $FeVO_4$ (i.e. a wider sandwich layer) with increasing ML coverage.

The presence of some V_2O_5 in the 12 ML VO_x/Fe_2O_3 catalyst is attributed to a failure to fully calcine the catalyst through either insufficient temperature or duration: the effects of calcination temperature upon the resultant catalyst material will be detailed in a later section.

Through investigation by spectroscopic and reactor techniques, no significant differences in catalytic behaviour, nor major changes in speciation are apparent between different ML VO_x/Fe_2O_3 catalysts: where small deviations are observed, these are accounted for by experimental error. Given that the whole range of catalysts (for ≥ 1 ML) is effectively interchangeable without prejudice for the purposes of catalysis, to achieve the greatest efficiency from the time available it was decided to focus on fewer ML loadings (primarily 3 ML) for further studies.

3.3.3 Probing the formation process of VO_x/Fe_2O_3 catalysts

It was noted during the early studies of MoO_x/Fe_2O_3 catalysts that small changes in calcination temperature could have an inordinate effect on the abilities of the resultant catalyst.[3] A minimum temperature during calcination of 500°C was found to be necessary to imbue the catalyst with the desired selectivity: in other words, only at 500°C can direct participation of the core moiety in catalysis be sufficiently impeded. Using Raman spectroscopy, the species present in a range of improperly-calcined catalysts were investigated, ultimately indicating that formation proceeds by a stepwise mechanism: crucially, this mechanism passes through a stage at which the Mo is present as MoO_3 crystallites.[3]

Bearing the MoO_x/Fe_2O_3 formation process in mind, interest was similarly directed to the formation process of VO_x/Fe_2O_3. Given the structural and behavioural similarities to MoO_x/Fe_2O_3 manifested by VO_x/Fe_2O_3, it is highly likely that similar dependence on calcination temperature will be observed. Since the fungibility of each ML VO_x/Fe_2O_3 catalyst has been adequately demonstrated, to avoid unnecessary repetition, these temperature studies were performed only on 3 ML VO_x/Fe_2O_3. A large quantity of 3 ML VO_x/Fe_2O_3 was synthesised normally by incipient wetness impregnation and was dried overnight at 120°C: contrary to normal procedure, however, at this stage it was not immediately calcined. Instead, it was separated into four portions, in order to investigate the effects of four different calcination temperatures, viz. 200, 300, 400 and 500°C. Each portion was duly calcined at the appropriate temperature for 24 hours, before being analysed by Raman spectroscopy (Figure 3.16).

From comparing the Raman spectra of samples from each calcination temperature, the

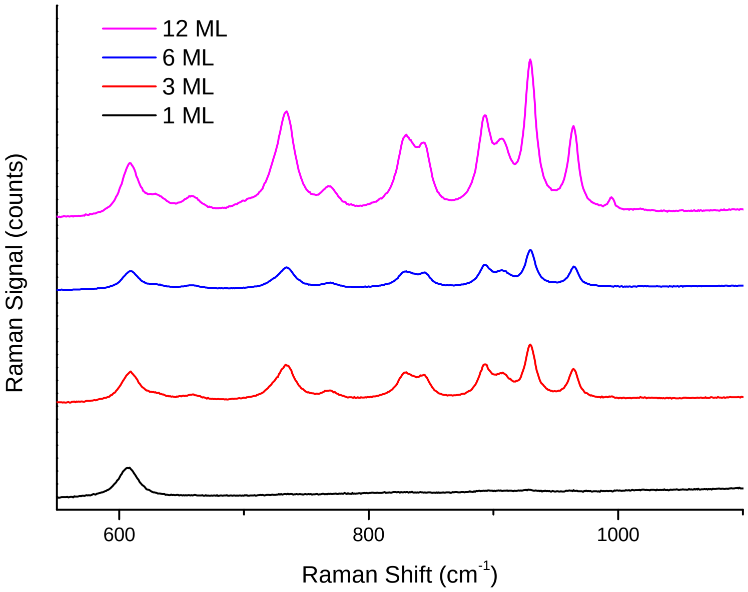

Figure 3.14: Raman spectra from 1, 3, 6 and 12 ML VO_x/Fe_2O_3. Three accumulations, each of 1% laser power and duration 20 seconds, were collected per sample: these samples were liable to fluoresce under the focussed laser.

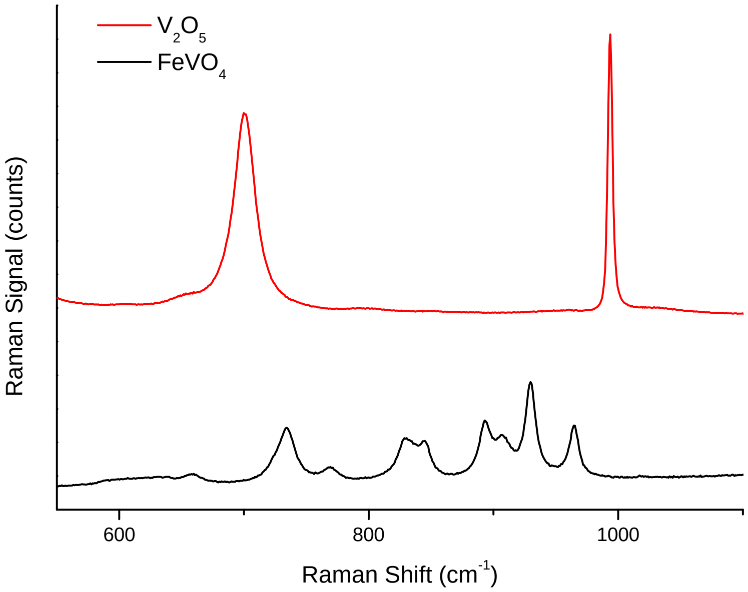

Figure 3.15: Raman spectrum from $FeVO_4$ and V_2O_5. Three accumulations, each of 1% laser power and duration 20 seconds, were collected per sample.

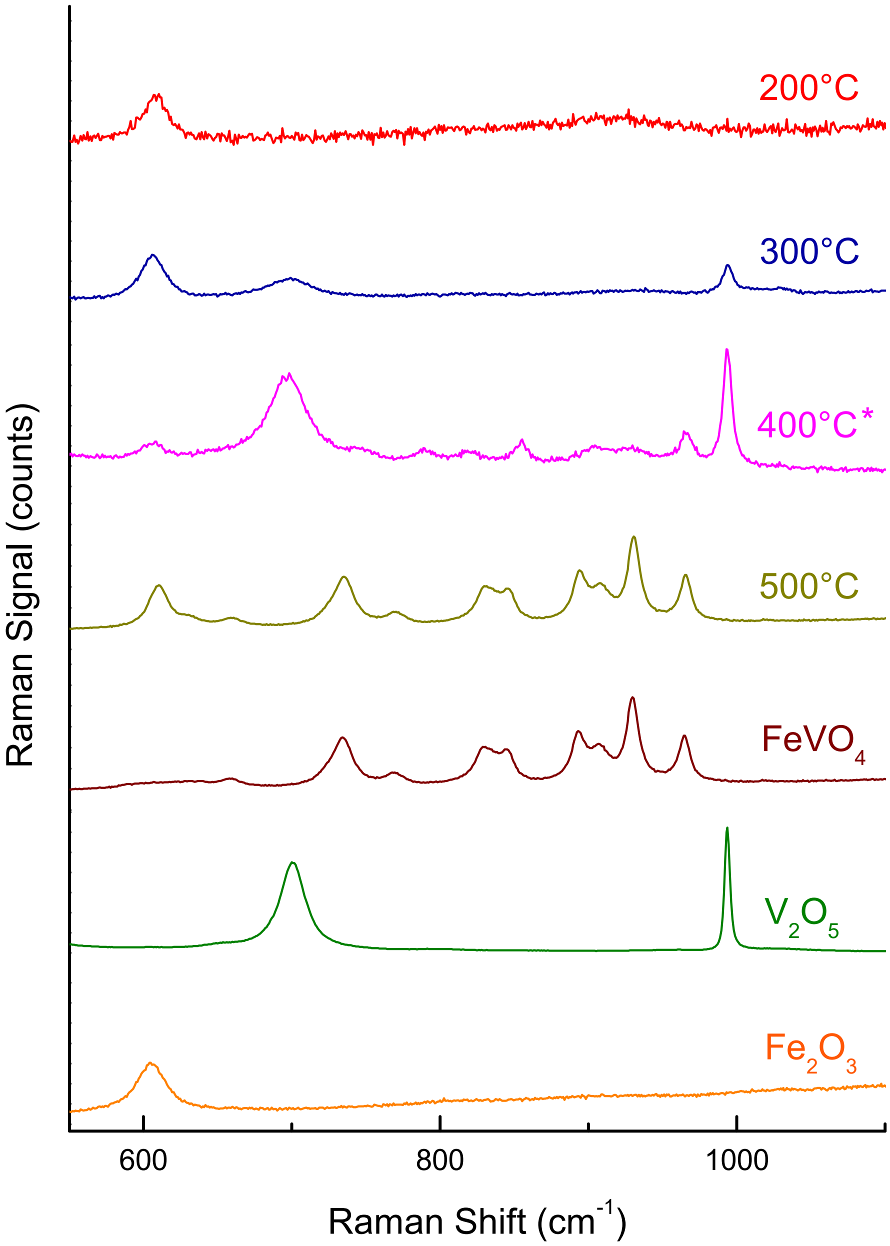

Figure 3.16: Raman spectra of 3 ML VO_x/Fe_2O_3 calcined at 200, 300, 400 and 500°C with $FeVO_4$, V_2O_5 and Fe_2O_3 references (the asterisk represents that spectrum intensity has here been halved to fully display the prominent V_2O_5 peak at 994 cm^{-1}). Three accumulations, each of 1% laser power and duration 20 seconds, were collected per sample.

progression of intermediate species through to the fully calcined catalyst—which as 3 ML VO_x/Fe_2O_3 will resemble $FeVO_4$—during calcination can be charted. At 300°C, sufficient thermal energy has been supplied to the starting material to begin formation of small amounts of V_2O_5; by 400°C this process has intensified, producing significant quantities of V_2O_5. After calcination at 500°C, however, complete conversion to $FeVO_4$ is observed, signifying that the $FeVO_4$ sandwich layer has formed. The lack of visible V_2O_5 at this stage indicates that the spreading of vanadia across the surface is fully accomplished by 500°C, with no isolated V_2O_5 aggregates remaining. As mentioned before, the tenuity of the outermost surface VO_x monolayer precludes its observation by Raman spectroscopy.

This behaviour is comparable to that displayed for MoO_x/Fe_2O_3 catalysts, which further reinforces the validity of the shell-core catalyst model for VO_x/Fe_2O_3 catalysts particularly and more generally the ability of the shell-core system to be applied to alternative systems. With the knowledge that the formation of 3 ML VO_x/Fe_2O_3 involves notable amounts of a V_2O_5 intermediate, a schematic mechanism for catalyst formation was proposed (Figure 3.17).

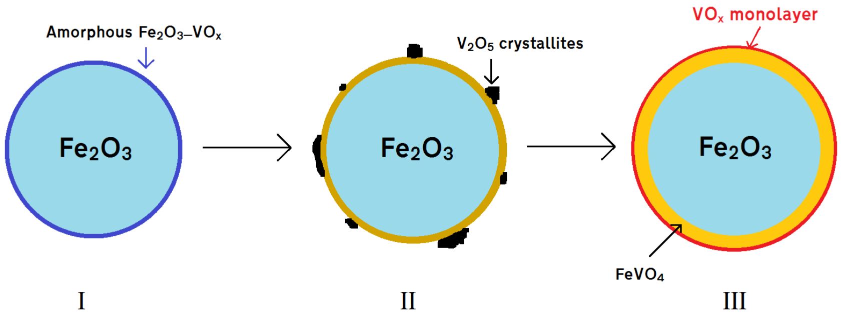

Figure 3.17: A suggested schematic model of the shell-core formation process as a function of increasing calcination temperature for VO_x/Fe_2O_3 catalysts with ≥ 1 ML coverage: I) at low temperatures, the surface comprises amorphous VO_x units residing atop the haematite core; II) by 400°C many isolated V_2O_5 aggregates exist at the surface; III) by 500°C all excess V_2O_5 has been converted into the $FeVO_4$ sandwich layer, separating the surface VO_x layer from the Fe_2O_3 core.

According to this postulated mechanism, it is suggested that after incipient wetness impregnation and the associated drying of the catalyst, the VO_x in the sample exists as amorphous units on the Fe_2O_3 surface. Since the synthetic technique applies the VO_x precursor solution to the Fe_2O_3 and relies on capillary action to generate the catalyst, and not reaction, after removal of the solvent the VO_x will remain at the surface. Between

350 and 400°C, enough thermal energy has been applied to the system to permit a low level of VO_x mobility, which in turn allows the VO_x aggregation and ordering to occur. At 400°C, crystalline, ordered V_2O_5 is formed at the surface in place of the earlier amorphous VO_x. At this stage, the catalytic selectivity to formaldehyde is markedly superior to that of the pre-calcination catalyst, though still displaying small quantities of CO_2 by TPD. This is attributed to gaps remaining at the surface of the Fe_2O_3, which have yet to be filled by VO_x surface spreading. To fully spread VO_x across the surface, however, requires a degree of thermal energy only present at temperatures in excess of 450°C, with complete resemblance—both spectroscopically and catalytically—to the earlier 3 ML catalyst observed by 500°C.

The similar behaviour of VO_x/Fe_2O_3 catalysts to MoO_x/Fe_2O_3 during calcination further substantiates the validity of exporting the shell-core concept to other metal oxides. While variances in the exact temperatures at which certain intermediates are seen (e.g. for MoO_x/Fe_2O_3, MoO_3 is observed from 350°C, while V_2O_5 is observed below 350°C for VO_x/Fe_2O_3), these are small: crucially, the final catalyst is formed in both cases by 500°C. There are important physical parameters affecting structural behaviour during the calcination of MO_x/Fe_2O_3 catalysts, most significantly the mobility of oxide materials at elevated temperatures. The mobilities of VO_x and MoO_x during calcination are both suited to shell-core formation by 500°C. Conversely, the diffusion properties of other metal oxides, e.g. NbO_x, differ enough to compromise effective shell-core formation. The importance of solid mobility, and the reasoning behind the greater suitability of certain metal oxides versus others for shell-core formation will be explored in detail in a later section.

3.3.4 Confirmation of vanadium segregation

By TPD it is possible to strongly infer that the vanadium present in VO_x/Fe_2O_3 catalysts is segregated to the shell layers of the catalyst as theorised. A vital means to categorically substantiate such segregation is electron microscopy, specifically with STEM-EDX or STEM-EELS. High resolution nanometre-scale imaging techniques like STEM/TEM are extremely valuable for investigating shell-core catalysts, enabling the following:

(i) facile determination of particle size, corroborating other surface area and particle size distribution measurements;

(ii) elucidation of structural information from the catalyst (e.g. crystal parameters); and

(iii) measurement of chemical speciation and elemental analysis as a function of position (either in one or two dimensions).

Of these possibilities, perhaps the most beneficial for shell-core catalyst studies is the ability to probe chemical identity as a function of position in the image. Using this technique, the proposition that the vanadium component in VO_x/Fe_2O_3 catalysts is isolated to the surface can easily be verified. To that end, two different loadings of VO_x/Fe_2O_3, 3 and 12 ML, were imaged and investigated by high-resolution STEM. Alongside the acquisition of an image, simultaneous EELS line scan measurements (pixel size 0.5 nm) were performed across a catalyst particle. For the 3 ML VO_x/Fe_2O_3 catalyst, the EELS line scan was directed through a convenient promontory at the surface (Figure 3.18), while for 12 ML VO_x/Fe_2O_3 a scan was aligned through one side of a larger agglomeration of catalyst particles (Figure 3.19). In this latter case, the sample presented several individual particles directly atop each other, impeding attempts to place a line scan across an entire particle: consequently, only one edge of the particle was scanned.

Gratifyingly, for both 3 and 12 ML VO_x/Fe_2O_3 strong vanadium EELS signals were observed only at the edge of the particles: this is clear evidence that vanadium is indeed segregated solely to the surface layers of the catalyst. For 12 ML VO_x/Fe_2O_3, an additional EELS line scan for iron was performed. Upon passing the surface, the iron signal climbs markedly and begins to plateau, while the vanadium signal declines shortly after the surface. This corroborates the presence of a haematite core in the catalyst. Crucially, the increase in the iron signal occurs at slightly greater path distance than the vanadium increase, which is due to the presence of the outermost selective VO_x overlayer. Since this is a 12 ML VO_x/Fe_2O_3 catalyst, 11 ML of $FeVO_4$ are present, which will generate a strong iron EELS signal; however, iron does not occupy the outermost layer, only vanadium as VO_x, hence the iron signal is expected only from the layers beneath the surface layer. This is indeed apparent from the subtle lateral difference of the point at which the iron signal starts to increase relative to the equivalent point for vanadium.

The confirmation that vanadium in VO_x/Fe_2O_3 catalysts exists only at the surface further reinforces the similarity between VO_x/Fe_2O_3 and MoO_x/Fe_2O_3, for which comparable STEM line scans were performed (though by EDX and not EELS), showing molybdenum to exist only at the surface.[2] In addition, by clarifying through electron microscopy that the surface is vanadium-rich, the reliability of TPD measurements as a means of determining surface segregation is further emphasised. The author thanks Dr Qian He of Cardiff University for his assistance with this microscopy.

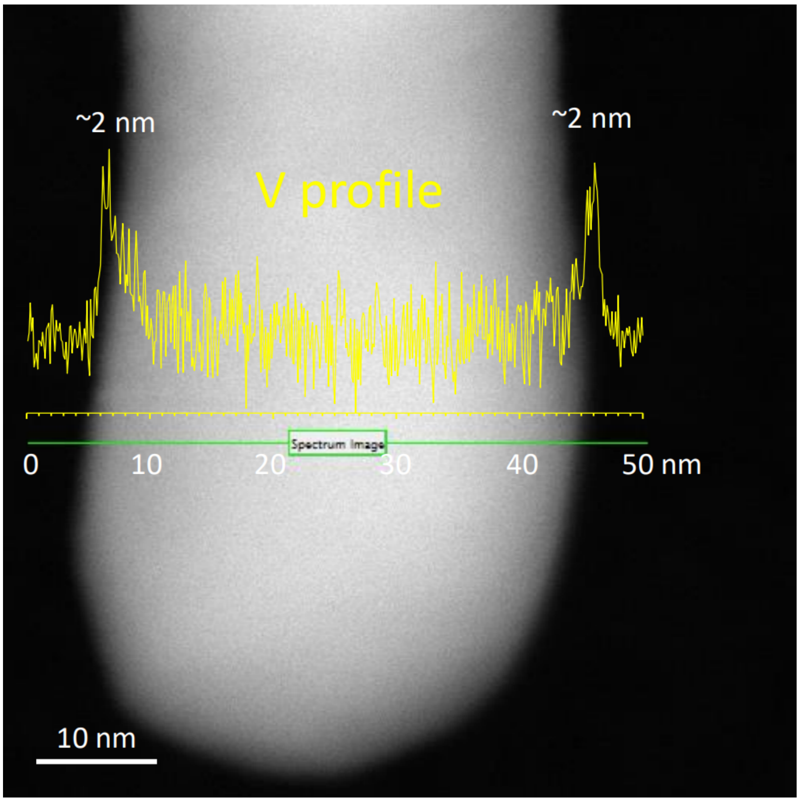

Figure 3.18: HAADF STEM-EELS line scan of a 3 ML VO_x/Fe_2O_3 catalyst.

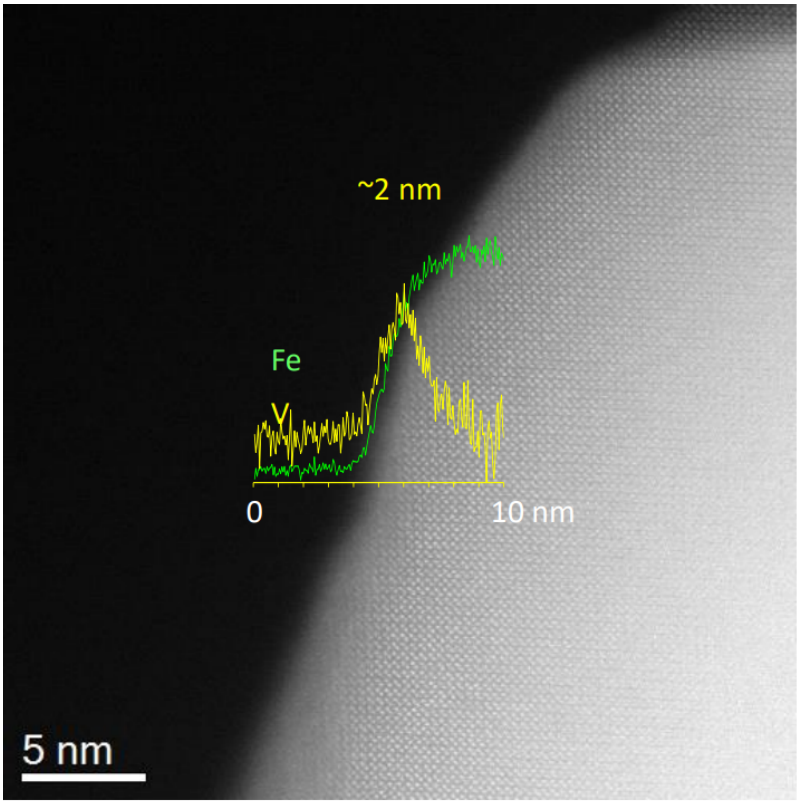

Figure 3.19: HAADF STEM-EELS line scan of a 12 ML VO_x/Fe_2O_3 catalyst.

3.3.5 Sub-monolayer VO_x/Fe_2O_3 catalysts

In accordance with the fundamental hypothesis of the shell-core catalyst model—namely that the haematite core must be fully segregated from direct contact with methanol during catalysis lest the methanol be combusted—studies on VO_x/Fe_2O_3 catalysts have thus far considered only those ML coverages known to display high selectivity to formaldehyde, i.e. ≥ 1 ML. With at least one full monolayer at the surface, the core is sufficiently encapsulated for the catalyst to exhibit high formaldehyde selectivity. As a means to verify the scalability and linearity of different ML coverages, sub-monolayer samples (i.e. < 1 ML) warrant consideration. At this juncture, it is prudent to recall the inherent selectivities evinced with different surface environments (Table 3.4). It is vital to reiterate that full combustion of methanol to CO_2 can only occur when multiple Fe sites are exposed at the surface, since these sites can stabilise the formate intermediate required to form CO_2.

Table 3.4: The effects of MO_x/Fe_2O_3 shell-core catalyst surface speciation on methanol oxidation selectivities (where M = V, Mo).

Species at surface	Selectivity
VO_x	Formaldehyde
Single Fe sites	Carbon monoxide
Multiple neighbouring Fe sites	Carbon dioxide
Fe_2O_3	Carbon dioxide

Four samples were prepared to explore the effects of sub-monolayer catalysts, viz. 0.25, 0.5, 0.75 and 1 ML VO_x/Fe_2O_3, and analysed by TPD focussing on formaldehyde, CO and CO_2 (Figure 3.20). The catalytic behaviour revealed by TPD data from the 0.25 ML VO_x/Fe_2O_3 catalyst is quite unlike that displayed by full ML catalysts. CO_2 is decidedly the major product, which is to be expected: according to the proposed formation model, at this stage VO_x units are a distinct minority at the surface. Instead, the surface is expected to contain large swathes of exposed Fe_2O_3. Given the thermodynamic favourability of combustion over selective oxidation, methanol is now preferentially combusted by the exposed Fe_2O_3 sections, and consequently the TPD behaviour resembles that of Fe_2O_3. The 0.5 ML catalyst is broadly similar to the 0.25 ML catalyst; however, a small quantity of formaldehyde is now observed, arising from those sections of the surface still occupied by VO_x, but this is minor. The major product remains CO_2: again, this indicates significant exposure of Fe_2O_3 at the surface.

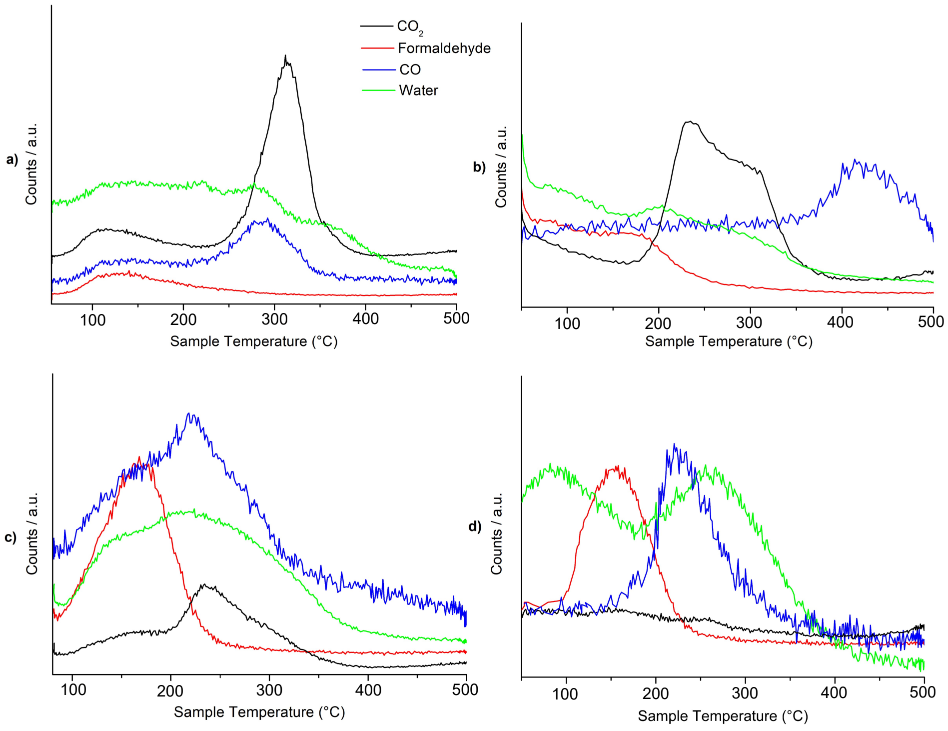

Figure 3.20: A comparison of TPD data for sub-monolayer VO_x/Fe_2O_3 catalysts: a) 0.25 ML; b) 0.5 ML; c) 0.75 ML; d) 1 ML. In all cases, gas flow: 30 mL/min He; sample mass: 220 mg.

By 0.75 ML, the catalytic behaviour has been markedly altered, manifested by strong selectivity to formaldehyde, and a significant reduction in CO_2 production. At this stage the surface comprises mainly VO_x units, eliciting the formaldehyde selectivity, but enough Fe_2O_3 remains exposed at the surface to elicit combustion. This is in accordance with the suggested shell-core model, as the catalyst surface is only expected to be $^3/_4$ covered with VO_x units. The change in the relative quantities of CO and CO_2 produced by 0.75 ML coverage is highly significant. Given the preponderance of CO in comparison to CO_2, it is clear that, of the Fe sites now exposed at the surface, a majority of them are not able to interact with other surface Fe sites. In other words, most Fe sites are effectively isolated "islands", surrounded by VO_x.

Since the surface at 1 ML coverage is effectively covered with VO_x units, very few Fe sites will be exposed at the surface: certainly there will be no exposure of multiple neighbouring Fe sites. This is borne out by the selectivity demonstrated in TPD by 1 ML VO_x/Fe_2O_3, which is selective to formaldehyde and produces no significant CO_2.

In summary, methanol oxidation is initially dominated by combustion for a 0.25 ML VO_x catalyst. Upon increasing the ML coverage to 0.5 ML, the production of CO becomes the major process. Increasing further to 0.75 ML, favourable formaldehyde selectivity appears alongside strong CO generation, while CO_2 production declines noticeably. By 1 ML, the catalyst behaves as a normal VO_x/Fe_2O_3 catalyst. A model for the proposed changes in surface environment as a function of increasing ML coverage for sub-ML VO_x/Fe_2O_3 catalysts is shown below (Figure 3.21).

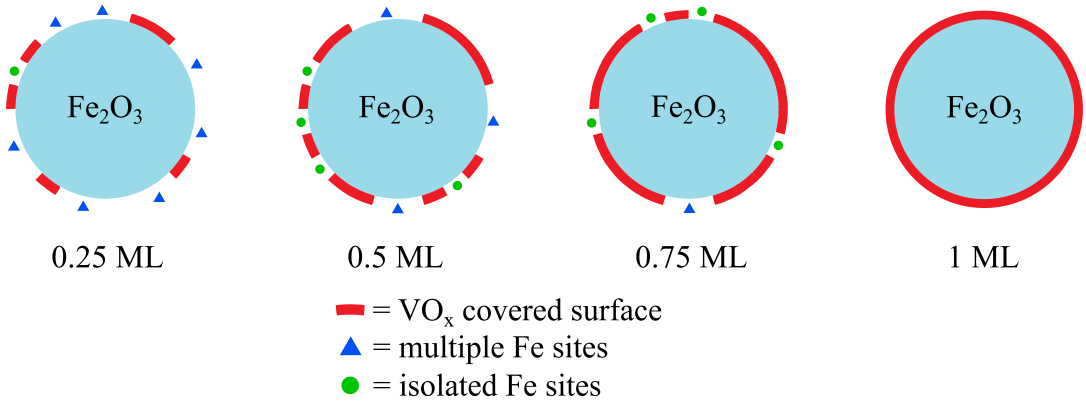

Figure 3.21: A representative schematic of the surface environment for sub-monolayer VO_x/Fe_2O_3 catalysts. At 0.25 ML, combustion predominates due to the large number of Fe sites on the surface within reach of other Fe sites (which stabilise the formate intermediate *en route* to CO_2), while by 1 ML, the Fe_2O_3 core has been properly segregated, eliciting no CO_2 production.

Through TPD analysis of the behaviours of sub-ML catalysts, the continued validity of the shell-core model for both sub-ML and ≥ 1 ML and VO_x/Fe_2O_3 has been confirmed. The changes in selectivity as a function of sub-ML loading correspond to the expected behaviours for haematite-rich and haematite-poor surfaces respectively. Additionally, that the selectivities observed appear at the expected ML coverages reinforces the reliability of the calculations used to compute ML coverages for each sample.

3.3.6 *Ex situ* XAS investigations of VO_x/Fe_2O_3 shell-core catalysts

A significant incentive behind the development of the shell-core catalyst design, originally for MoO_x/Fe_2O_3 and more recently VO_x/Fe_2O_3, was to produce catalytic systems wherein the benefits of XAS studies could be maximised: XAS is a powerful technique, capable of supplying a profusion of structural and electronic information. In catalysis, the possibility of elucidating surface chemistry by XAS is particularly inviting. This can be achieved by ensuring the proper segregation of shell and core components in the catalyst: accordingly, the relevant metal of interest, be it Mo or V, resides only in the surface layers. XAS is not inherently a surface-sensitive technique, but a bulk averaging technique, probing the sample in its entirety. Crucially, however, it is element-specific. Therefore, if the relevant analyte of interest (e.g. V in shell-core VO_x/Fe_2O_3) exists only at the surface, then any XAS information from that element must originate from species at the surface of the catalyst. Since, to a heterogeneous catalysis chemist, the surface environment of a catalyst is the crux of all catalytic processes, the ability to obtain quasi-surface sensitive structural and electronic information from a shell-core catalyst by XAS is a tremendous boon. Two main regions of interest are present in data collected by XAS measurements, namely the XANES and EXAFS regions: the differences between these regions are discussed in detail alongside an overview of XAS from a theoretical perspective in Chapter 2. At this point, it suffices to summarise that the XANES region contains information on coordination geometries and oxidation states, while the EXAFS region reveals coordination environments and local structures.

XAS measurements, both *ex* and *in situ*, have previously been performed on various ML MoO_x/Fe_2O_3 catalysts at the Mo K-edge.[2,3] The XANES data from these studies supported the assertion that each excess ML of MoO_x beyond 1 ML is fashioned into an iron molybdate sandwich layer (in a way akin to iron vanadate for $\geq$ 1 ML VO_x/Fe_2O_3 catalysts), with the 3 and 6 ML MoO_x XANES data resembling iron molybdate. For a 1 ML catalyst, however, no sandwich layer is anticipated. Instead, the XANES signal from 1 ML MoO_x/Fe_2O_3 was comparable to that of a MoO_3 reference.[3] The structure of MoO_3 is frequently stated to be octahedral, and hence 1 ML MoO_x/Fe_2O_3 was similarly labelled, but this is an oversimplification: in reality, MoO_3 adopts a heavily-distorted octahedral structure quite unlike a free octahedral structure, and this is clear from the XANES data. The presence of a strong pre-edge feature at the absorption edge signifies a non-centrosymmetric environment about the absorber, while absorbers occupying centrosymmetric environments generate no such pre-edge features. An octahedral environment is centrosymmetric, therefore it will not produce a pre-edge feature; since 1 ML MoO_x/Fe_2O_3 and MoO_3 generate significant pre-edge features, they are conclusively not octahedral *per se*. This distinction will be discussed together with the latest structural investigations of MoO_x/Fe_2O_3 catalysts by XAS in a later section.

VO_x/Fe_2O_3 catalysts are well suited to *ex situ* XAS investigations, but are more problematic than their MoO_x counterparts for *in situ* studies due to the markedly softer V K-edge energy (5.465 keV compared to 19.999 keV). *In situ* sample cells are often made gastight, but must still incorporate windows to permit the transmission of X-rays. Kapton® tape (full name poly-oxydiphenylene-pyromellitimide) is regarded as the window material *par excellence*, due to its high mechanical stability, fair temperature stability and excellent X-ray transmittance. For low-temperature V XAS studies, thin Kapton® windows are wholly suitable; however, the thermal stability of Kapton® declines above 330°C, limiting the scope of any *in situ* studies. Consequently, for soft-energy *in situ* studies alternative window materials must be considered, which are thermally stable, mechanically capable of maintaining gastightness and suitably transmissive.

XANES analysis

Ex situ XAS measurements of a range of VO_x/Fe_2O_3 catalysts were performed at B18, Diamond Light Source to gather structural information regarding the surfaces of VO_x/Fe_2O_3 catalysts and to further contribute to the body of evidence detailing the validity of the shell-core model as applied to VO_x catalysts. XANES data for four loadings of VO_x/Fe_2O_3 catalysts calcined to 500°C, viz. 1, 3, 6 and 12 ML VO_x/Fe_2O_3, alongside two reference compounds, $FeVO_4$ and V_2O_5 were recorded, and subsequently calibrated, aligned and normalised (Figure 3.22). The main XANES transition at the V K-edge is a dipole-permitted 1s → 4p transition, but also visible are distinct pre-edge features, attributed to dipole-forbidden 1s → 3d transitions. These pre-edge transitions appear regularly in vanadium XANES, and differences in such pre-edge features typically convey significant structural information.[12]

Upon initial observation of the wider spectra, the VO_x/Fe_2O_3 spectra clearly resemble tetrahedral $FeVO_4$ to a significantly greater degree than they do square pyramidal V_2O_5. The V_2O_5 XANES spectrum exhibits a steeper absorption edge with a distinct shoulder between 5480 and 5485 eV, not present for $FeVO_4$ or the VO_x/Fe_2O_3 catalysts: additionally, the pre-edge feature is shifted higher in energy. This is encouraging, since the presence of V_2O_5 is not anticipated in a properly calcined catalyst; conversely, for $> 1\,\text{ML}$ the presence of $FeVO_4$ is. All VO_x/Fe_2O_3 catalyst samples contain fully oxidised vanadium(V), determined by the great similarity between the catalysts and the vanadium(V) standards. By studying the pre-edge region in greater detail, subtler variations between the VO_x/Fe_2O_3 catalysts can be seen more clearly (Figure 3.23). The pre-edge feature for the V_2O_5 reference is noticeably shifted to higher energy in comparison to the other reference, $FeVO_4$. It is clear that the pre-edge peaks for the VO_x/Fe_2O_3 catalysts are co-located with the $FeVO_4$ pre-edge peak, not V_2O_5 (Figure 3.24). There is a significant discrepancy, namely the 1 ML VO_x/Fe_2O_3 catalyst pre-edge peak, which is shifted higher in energy, occurring at an energy between those of the $FeVO_4$ and V_2O_5 pre-edge peaks. There are noticeable differences in pre-edge peak intensity between VO_x ML coverages: this is likely to be due to the adoption of non-ideal geometries within catalyst shells.

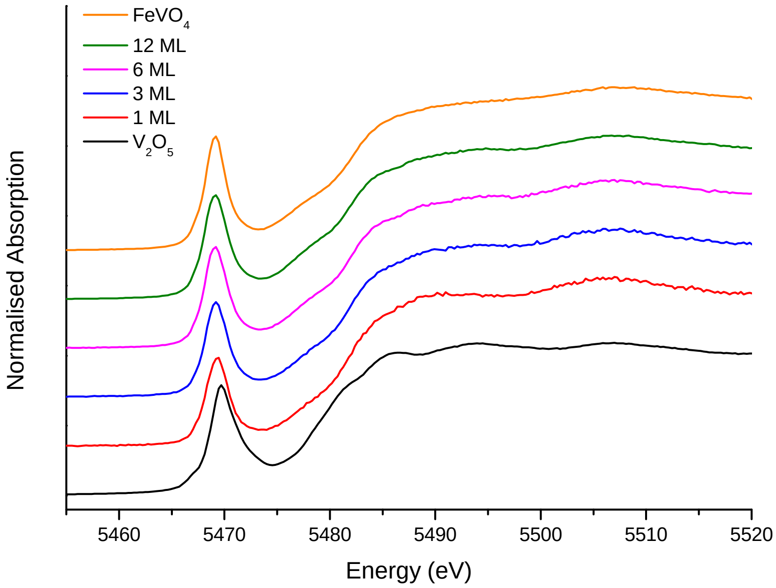

Figure 3.22: Normalised XANES spectra of calcined 1, 3, 6 and 12 ML VO_x/Fe_2O_3, $FeVO_4$ and V_2O_5 at the V K-edge.

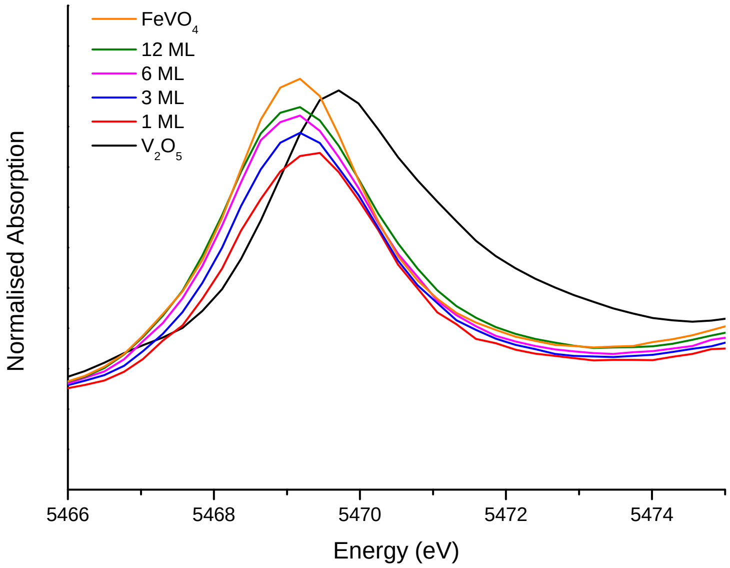

Figure 3.23: Expanded XANES pre-edge region of 1, 3, 6 and 12 $MLVO_x/Fe_2O_3$, $FeVO_4$ and V_2O_5 displaying increased peak intensity with increases in VO_x ML coverage, alongside the shift in the 1s → 3d peak.

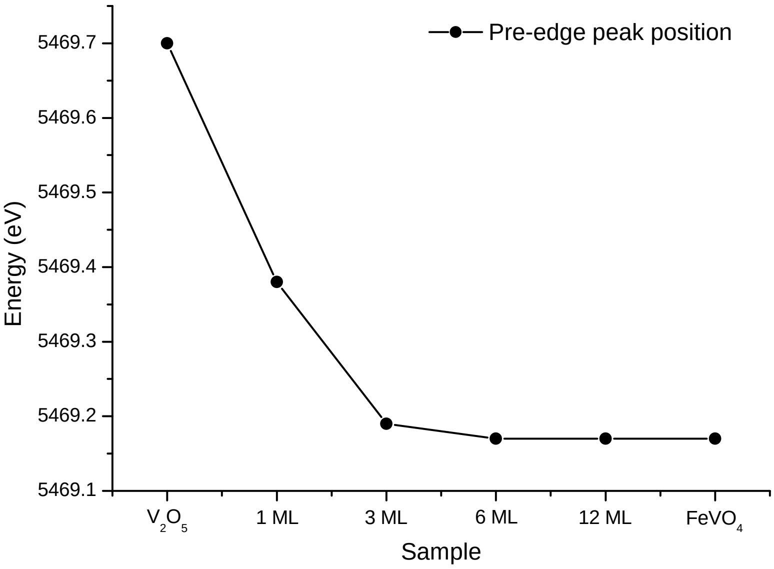

Figure 3.24: A comparison of pre-edge peak positions for 1, 3, 6 and 12 ML VO_x/Fe_2O_3, $FeVO_4$ and V_2O_5.

It has been reported that the intensity of vanadium pre-edge transitions varies depending on the proximity of coordinating nearest-neighbour ligands to the vanadium centre; the more closely packed the local environment, the greater the intensity of the pre-edge peak.[12] For a 1 ML VO_x/Fe_2O_3 catalyst, it is thought that VO_x species in the surface layer are nominally tetrahedral, but considerably distorted from an ideal tetrahedral structure. For greater ML coverages, it is believed that the outermost surface layer consists of similarly distorted tetrahedral units, in this instance forming from a V-terminated $FeVO_4$ layer in which the V−O bonds are elongated. This elongation perturbs the environment around the vanadium, reducing packing concentration and hence the pre-edge peak intensity.

Importantly, VO_x/Fe_2O_3 pre-edge resemblance to tetrahedral $FeVO_4$ increases as a function of increasing ML coverage. This is highly encouraging, since it is known that the relative abundance of $FeVO_4$ in higher ML coverages is greater, producing the trend seen in the pre-edge feature, further corroborating the shell-core model. XAS is a bulk averaging technique, thus all compounds and structures of a particular element will contribute to one overall spectrum. Crucially, differences in relative peak intensities of XANES features do not arise from the absolute quantity of a substance present, but rather from differences in the relative proportions of different compounds of that element. The outermost VO_x layer equivalent to 1 ML VO_x/Fe_2O_3 is present for all VO_x/Fe_2O_3 catalysts, but the degree to which it influences the resulting XANES spectrum depends on the extent to which other

V-containing materials are present. Since multi-ML coverages possess greater relative quantities of $FeVO_4$ sandwich layer (i.e. a 3 ML catalyst contains approximately 2 ML of $FeVO_4$, a 6 ML catalyst 5 ML of $FeVO_4$, etc.), the ratio of V present in the outermost VO_x layer to V present in $FeVO_4$ declines with increasing ML coverage accompanied by lesser contributions of the outermost VO_x layer to each spectrum, thereby generating spectra more similar to that of $FeVO_4$.

In addition to the major influence from changes in the relative abundances of each substance present, structural distortion can also modify the pre-edge peak intensity.[12] While shell-core catalyst particles are not perfectly spherical, they are nonetheless effectively spheroidal. Accordingly, compelling a material—which, in its free state, would be flat—to curve around a spheroidal core imparts a degree of structural strain to the shell material. Depending on the severity of this curvature-induced strain, it is conceivable that the structural properties of a material might be altered, hence also its XANES features. The greatest effects from any such alterations will be witnessed for thinner shell components, while thicker layers at the surface can more easily adapt to alleviate strain effects. Consider the 3 ML VO_x/Fe_2O_3 catalyst, which contains two monolayers of $FeVO_4$ in the sandwich layer. Both $FeVO_4$ monolayers are near the core moiety, and due to curvature the adoption of a "normal" $FeVO_4$ structure is hindered. A 12 ML VO_x/Fe_2O_3 catalyst, however, comprises 11 ML of $FeVO_4$ at each edge. At this thickness, the bulk of the $FeVO_4$ present can minimise strain-derived structural deformities by adopting more ideal structures—which would be thermodynamically favourable—throughout a significant portion of its mass, with major structural distortions limited to the extremities of the sandwich layer. The resulting catalyst is more representative of the structure of free $FeVO_4$, and consequently its XANES features would be also.

The observed behaviour in the 1, 3, 6 and 12 ML VO_x/Fe_2O_3 catalyst XANES pre-edge intensities can be adequately explained by both changes in relative abundance and structural differences from curvature-induced strain. Nonetheless, one cannot dismiss the possibility that the surface comprises a multitude of vanadium species. The paucity of surface species in comparison to the rest of the catalyst impedes attempts to characterise them in greater detail.

Linear combination fitting

Linear combination fitting (LCF) analysis can be performed on XANES data to quantitatively measure the similarity of a sample to a selection of reference material standards.

Since XAS is an averaging technique, all element environments present contribute to the XANES spectrum: this is manifested by shifts in edge/pre-edge positions and changes in the absorption edge shapes relative to the quantities of each environment. LCF analysis enables the deconvolution of the XANES spectrum, by determining the quantities of each component present by their effects on the overall spectrum. To explain this, consider a 50:50 mixture of two vanadium materials. When measured by XAS along with references of the two vanadium materials in isolation, LCF analysis of the XANES obtained will reveal that the sample resembles the two standards equally. For a 90:10 mixture, LCF analysis will reveal a 90% resemblance to sample one and 10% to sample two.

LCF analysis was undertaken on the XANES spectra of 1, 3, 6 and 12 ML VO_x/Fe_2O_3, using $FeVO_4$ and V_2O_5 as the reference materials. In accordance with the shell-core model for VO_x/Fe_2O_3, the greatest quantitative difference by LCF should be observed between 1 ML VO_x/Fe_2O_3 and the higher ML VO_x catalysts due to the absence of the $FeVO_4$ sandwich layer for 1 ML VO_x/Fe_2O_3. Since the structure of the outermost VO_x surface layer (i.e. 1 ML VO_x) is deemed to be distorted tetrahedral, it was anticipated that fitting using tetrahedral $FeVO_4$ and square pyramidal V_2O_5 as standards for comparison would nonetheless suggest greater similarity to $FeVO_4$. This was indeed demonstrated by fitting, but the degree of distortion from an ideal tetrahedral structure is sufficient to increase the statistical unreliability of the fit (Figure 3.25): in other words, there is an observable discrepancy between the original XANES spectrum and the plotted fit. Multiple ML VO_x catalysts, however, relate well to $FeVO_4$, again reinforcing the shell-core model and the growth of the $FeVO_4$ layer with increasing ML coverage (Figure 3.26). In these cases, the LCF fits do not significantly differ in peak shape or position from the original XANES spectra, a signal of reliable fitting. A comparison of the statistical data obtained from LCF analysis of each sample is provided below (Table 3.5).

Table 3.5: LCF statistical fitting data from *ex situ* XANES measurements of 1, 3, 6 and 12 ML VO_x/Fe_2O_3 catalysts.

	Similarity to standards (%)		
Species	V_2O_5	$FeVO_4$	R-factor
1 ML VO_x	6.5	93.4	1.01×10^{-2}
3 ML VO_x	2.3	97.7	4.54×10^{-3}
6 ML VO_x	1.5	98.5	1.73×10^{-3}
12 ML VO_x	1.0	99.0	6.31×10^{-4}

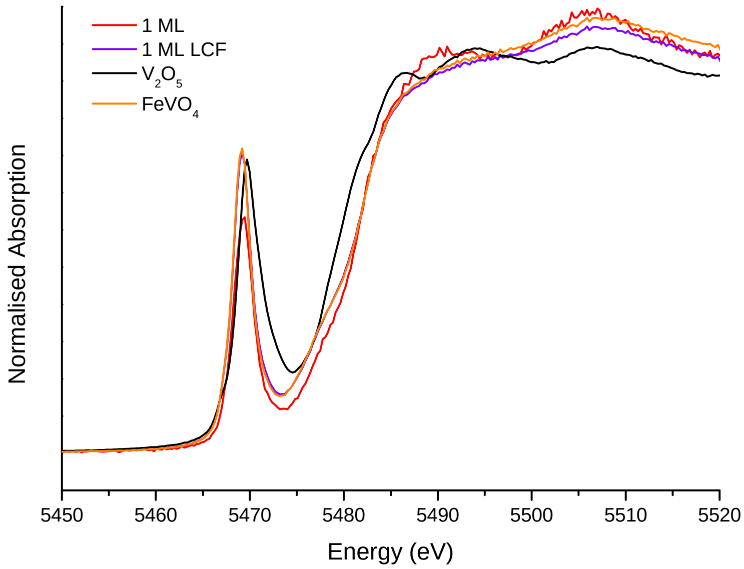

Figure 3.25: Linear combination fit of 1 ML VO_x/Fe_2O_3 with $FeVO_4$ and V_2O_5 as fitting standards with normalised 1 ML VO_x/Fe_2O_3 for comparison.

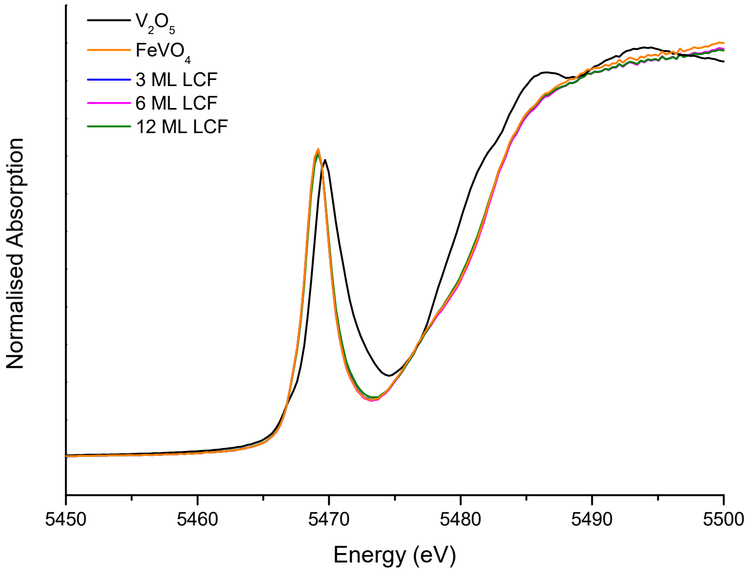

Figure 3.26: Linear combination fit of 3, 6 and 12 ML VO_x/Fe_2O_3 using $FeVO_4$ and V_2O_5 as fitting standards, displaying clear similarity to $FeVO_4$.

LCF analysis, in conjunction with a visual assessment of the XANES spectra obtained from VO_x/Fe_2O_3 catalysts, has significantly bolstered the reliability of the shell-core model, and changes therein as a function of ML coverage. This can be observed qualitatively by visual comparison of the initial XANES spectra with the $FeVO_4$ reference, where the 12 ML VO_x/Fe_2O_3 pre-edge peak is most similar to $FeVO_4$ in intensity and peak position, and quantitatively by LCF analysis, which reveals greater resemblance to $FeVO_4$ and lower statistical errors (i.e. better fits) at higher ML coverage.

EXAFS analysis

In contrast to the XANES region, which divulges knowledge of oxidation states and coordination geometries, the EXAFS region can yield significant information on coordination environments, bonding distances and coordination numbers. While the examination of XANES data is relatively straightforward, analysis of EXAFS data is somewhat more challenging. Through the use of reference crystal structures, known bonding information and computational methods, a series of fits can be developed, which attempt to mimic the EXAFS region of the XAS data to the greatest possible extent. Key to these fits is a series of fitting parameters, including the Debye-Waller factor (a measure of static disorder), σ^2 (mean-squared disorder) and the amplitude reduction factor (which mitigates against absorber relaxation induced by multi-electron excitation): these parameters, and how they relate to the mathematics of EXAFS analysis, are detailed in Chapter 2.

EXAFS analysis was performed on the XAS data from the VO_x/Fe_2O_3 catalysts for two main reasons:

(i) to assess the structural similarity of higher ML VO_x/Fe_2O_3 catalysts to $FeVO_4$;

(ii) to attempt to understand the structure of the outermost VO_x layer (i.e. 1 ML VO_x/Fe_2O_3).

For higher ML catalysts, EXAFS fits should correspond to the bonding distances and coordination numbers encountered in the tetrahedral $FeVO_4$ structure: this will be most pronounced for 12 ML VO_x/Fe_2O_3 due to its greater relative quantity of $FeVO_4$. Conversely, the 1 ML VO_x/Fe_2O_3 is theorised to contain no $FeVO_4$ at all; however, its structure is reasoned to be tetrahedral also—though considerably distorted—hence bonding distances and angles from $FeVO_4$ are a sensible starting point for fitting purposes. Additionally, when fitting 1 ML VO_x/Fe_2O_3, direct V-Fe scattering must be considered, since the VO_x units are sitting directly on a Fe_2O_3 surface: for a high ML sample, this is not a consideration, as little $FeVO_4$ relative to the overall amount present will be close to the Fe_2O_3 core.

From crystallographic studies of $FeVO_4$ reported in the literature, it was determined that the structure of $FeVO_4$ contains a unit of three independent Fe atoms, two distorted octahedral and one distorted trigonal bipyramidal, which produce a doubly-bent chain of six edge-sharing polyhedra: these chains are joined by tetrahedral units of VO_4^{3-}.[13] Each VO_4 tetrahedron contains two distinct V−O bonding distances, namely 1.649 Å and 1.785 Å, which were used to create EXAFS fitting paths: as the most $FeVO_4$-rich sample, fitting was conducted on 12 ML VO_x/Fe_2O_3 with these $FeVO_4$-derived paths (Figure 3.27), affording a reliable fit with an R-factor (a statistical reliability marker) of 0.008 (Table 3.6). R-factor values below 0.05 are accepted to signal a good fit. The value of the amplitude reduction factor was deduced to be 0.65 by fitting the V_2O_5 reference; this value applies to every measured sample.

The fit agrees well with the original Fourier transformed 12 ML VO_x/Fe_2O_3 data, both visually and statistically. A range of coordination numbers for each V−O scattering path was explored, with values between 2.2 and 2.3 providing the lowest R-factor value. Were the sample free, unconstrained $FeVO_4$, a coordination number of two for each path would be expected; however, given the tolerances of EXAFS fitting and the deviation from an ideal $FeVO_4$ structure expected in a shell-core structure, this small deviation from the ideal coordination number does not disquiet. The mean-squared disorder values are encouragingly low, indicating that the V−O scattering path distances are highly similar to the actual bonding distances in the structure. Ultimately, earlier by XANES fitting and now by EXAFS fitting, it can be seen that the vanadium in higher ML coverage catalysts exists mainly in $FeVO_4$, as predicted by the proposed VO_x/Fe_2O_3 shell-core model.

Of all the samples measured by XAS, the 12 ML VO_x/Fe_2O_3 catalyst most exemplifies free $FeVO_4$; in contrast, the 1 ML VO_x/Fe_2O_3 catalyst displays the greatest difference. The position of the 1 ML VO_x/Fe_2O_3 pre-edge feature in the XANES region is shifted higher in energy and lower in intensity than the other VO_x/Fe_2O_3 catalysts and the tetrahedral $FeVO_4$ reference, but this difference is small. Based on literature reports on vanadium XANES, the pre-edge peak shift does not result from the adoption of a fundamentally different structure, but from structural perturbations (in this instance from a distorted tetrahedral structure). Consequently, the 1 ML VO_x/Fe_2O_3 catalyst is expected to display significant tetrahedral character in the EXAFS region of the XAS data. Unlike in 12 ML VO_x/Fe_2O_3, all the VO_x units at the surface in 1 ML VO_x/Fe_2O_3 are directly

Table 3.6: EXAFS fitting parameters for 12 ML VO_x/Fe_2O_3 calcined to 500°C. Preset fitting parameters: $S_0^2 = 0.65$ as calculated from the V_2O_5 standard; range $3.0 > k > 12.9$, $1 > R > 2.5$; no. of independent points = 7.

Abs - Sc	N	R/Å	$2\sigma^2$ / Å^2	E_f/eV	R-factor
V−O (i)	2.2	1.649	0.00049	4.057	0.008
V−O (ii)	2.3	1.785	0.00007		

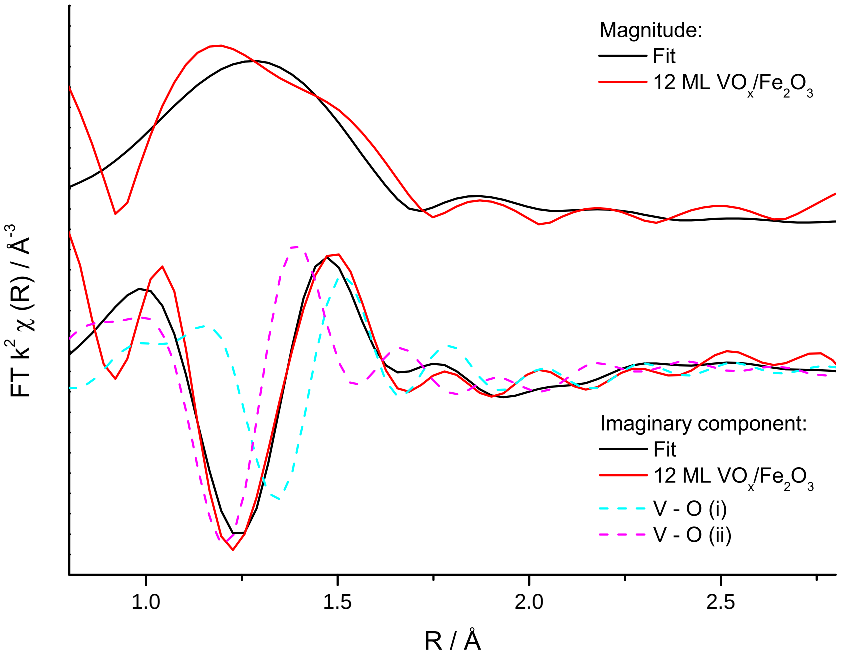

Figure 3.27: Magnitude and imaginary component of the k_2 weighted Fourier transformed fit for the EXAFS data of 12 ML VO_x/Fe_2O_3. Individual scattering paths are displayed in the imaginary component.

adjacent to the Fe_2O_3 surface: accordingly, a direct EXAFS interaction between vanadium and Fe atoms of the Fe_2O_3 is expected.

Using fitting models obtained from the $FeVO_4$ crystal structure, two V−O scattering paths were included in the fit for 1 ML VO_x/Fe_2O_3, at 1.649 Å and 1.785 Å respectively. In addition, due to the proximity of vanadium to the Fe_2O_3, a V−Fe scattering path was included. A range of V−Fe distances were assessed, from which it was determined that a V−Fe distance of 3.10 Å was most appropriate. These scattering paths are explained in the model provided (Figure 3.28). That this is the optimal value is highly encouraging, since in prior studies of the equivalent 1 ML MoO_x/Fe_2O_3 catalyst, the Mo−Fe scattering distance was found to also be 3.10 Å.[2] Fitting 1 ML VO_x/Fe_2O_3 with these scattering paths generates an EXAFS fit of observably high quality throughout the fitting region (Figure 3.29), with reliability retained up to 3.2 Å. The calculated EXAFS fitting parameters reinforce the sensibility of the proposed $FeVO_4$-derived interatomic distances (Table 3.7), while the low R-factor of 0.01 attests to the statistical reliability of the fit.

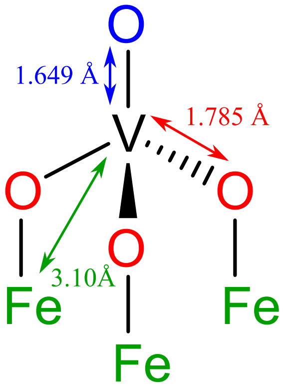

Figure 3.28: A schematic model of scattering distances in the proposed VO_x surface unit. Atoms with equivalent scattering distances share a colour: blue denotes the terminal oxygen, red the downward-pointing oxygens and green the Fe beneath.

Based on the 1 ML VO_x/Fe_2O_3 XANES data, the structure of the 1 ML VO_x layer was stated to be distorted tetrahedral based on the shift in pre-edge peak position. Consequently, while the coordination environment will not be identical to that of $FeVO_4$ or the higher ML catalysts, it will not be grossly dissimilar. The significant difference for EXAFS fitting between 1 ML VO_x/Fe_2O_3 and $FeVO_4$ is the existence of V−Fe scattering paths. The XAS data in question lack the requisite range to reliably see or fit the greater V−Fe distances in $FeVO_4$ (and hence the larger ML catalysts); however, an equivalent is observable for 1 ML VO_x/Fe_2O_3. Considering a hypothetical 1 ML VO_x distorted tetrahedron (i.e. VO_4) on a Fe_2O_3 surface, the most energetically stable structure will contain

Table 3.7: EXAFS fitting parameters for 1 ML VO_x/Fe_2O_3 calcined to 500°C. Preset fitting parameters: $S_0^2 = 0.65$ as calculated from the V_2O_5 standard; range $3.0 > k > 10.5$, $1 > R > 3.2$; no. of independent points = 10.

Abs - Sc	N	R/Å	$2\sigma^2$ / Å^2	E_f/eV	R-factor
V−O (i)	1	1.649	0.02003		
V−O (ii)	3	1.785	0.00146	6.359	0.01
V−Fe	3	3.10	0.00919		

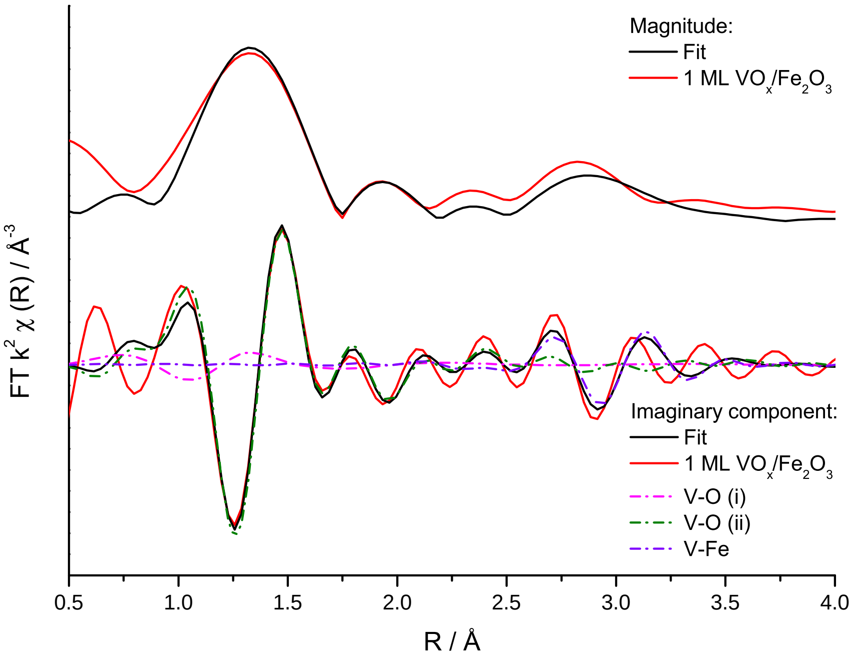

Figure 3.29: Magnitude and imaginary component of the k_2 weighted Fourier transformed fit for the EXAFS data of 1 ML VO_x/Fe_2O_3. Individual scattering paths are displayed in the imaginary component.

three V−O bonds pointing downwards, towards the Fe_2O_3 surface: correspondingly, one V−O will protrude upwards, away from the surface. The three V−O bonded oxygens directed towards the Fe_2O_3 surface will themselves bond with Fe cations at the surface of the Fe_2O_3, drawing themselves closer to the Fe_2O_3 surface, and in doing so, extending the V−O distances in comparison to the single, upwardly-facing V−O bond. This structural behaviour is manifested in the EXAFS fit of 1 ML VO_x/Fe_2O_3 by fixing the coordination numbers during fitting: if the fit is of high quality when coordination numbers are fixed, it signifies that the coordination numbers are fixed correctly. In the 1 ML VO_x/Fe_2O_3 fit, the longer (i.e. bridging) V−O scattering path has coordination number 3, while the shorter (i.e. terminal) V−O path has coordination number 1. Moreover, since there are three V−O−Fe bridging oxygens per VO_4 unit, there will duly be three V−Fe distances of the same value: this too is reflected in the fit, where the coordination number for the V−Fe path is 3. The statistical soundness of the fit arising from these scattering paths and coordination numbers is a testament to their validity at representing the 1 ML VO_x structure. The sanity of the fit is enhanced further by the sensible values calculated for the EXAFS parameters. For instance, the low $2\sigma^2$ (mean-squared disorder) values denote that the scattering paths used in fitting are appropriate and fairly represent the actual data.

Little vanadium EXAFS has been reported in the literature, though one study by Feng et al. examined vanadia placed on single-crystal iron oxide supports by atomic layer deposition.[14] They similarly suggested the existence of distorted tetrahedral VO_4 units on the iron oxide support, with similar XANES behaviour to that discussed above, but they differed in their assessments of bonding distances and coordination numbers. Their EXAFS fits were reported with two V−O distances of 1.62 Å and 1.82 Å respectively: these distances were trialled in the EXAFS fitting of 1 ML VO_x/Fe_2O_3 and found to be markedly inferior to the distances detailed above. While the XANES data reported by Feng et al. correspond well to that of 1 ML VO_x/Fe_2O_3, the EXAFS data do not; however, no R-factor—a parameter essential to gauge the fundamental validity or reliability of a fit, irrespective of the otherwise apparent suitability of other parameters—was reported for their EXAFS fits. EXAFS data reported without an R-factor cannot be considered trustworthy. Consequently, while the XANES data in the literature corroborate the discussion of VO_x/Fe_2O_3 catalysts above, no dependable EXAFS data of vanadia on iron oxide exist in the literature for comparison.

Assessed in concert with the earlier XANES data, the EXAFS fits from 1 ML VO_x/Fe_2O_3

strongly imply that the active site at the surface of VO_x/Fe_2O_3 catalysts comprises distorted VO_4 units. The XANES data indicate that the structure is tetrahedral, suggesting a VO_4-like structure, and the EXAFS fits corroborate this suggestion. For the results reported here, all XANES data and EXAFS fits have been performed using primary data obtained from XAS measurements at B18, but further studies are warranted based on these encouraging findings. A future prospect might be to glean more precise understanding of the structure and speciation of the surface by computational modelling (as was undertaken for MoO_x/Fe_2O_3). Using DFT calculations can provide an exact model for the most thermodynamically favourable structure, whose bond distances and structural properties can then be used for more refined EXAFS fitting in place of $FeVO_4$-derived information.

In summary, higher ML coverage VO_x/Fe_2O_3 catalysts resemble $FeVO_4$, which is the behaviour expected from the shell-core catalyst model; the amount of $FeVO_4$ present in the sandwich layer between the outermost VO_x layer and the Fe_2O_3 core scales linearly with ML coverage. The selective outermost VO_x layer represented by 1 ML VO_x/Fe_2O_3 contains VO_4-like units, which are tetrahedral in structure. These tetrahedra are distorted by the Fe_2O_3 support, reducing the proximity of three oxygen atoms to the vanadium centre and thereby shifting the XANES pre-edge peak.

Having explored the structure of VO_x/Fe_2O_3 catalysts by *ex situ* measurements, a useful future study would be to undertake further EXAFS studies using *in situ* measurements to probe the structural changes during reaction, and the properties of the reduced form of the catalyst. As mentioned before, however, *in situ* measurement of vanadium compounds can be problematic due to its soft X-ray absorption energy restricting the choice of *in situ* cell window materials.

3.3.7 *In situ* XAS investigations of VO_x/Fe_2O_3 shell-core catalysts

Having explored fully oxidised VO_x/Fe_2O_3 catalysts in detail, the opportunity to investigate VO_x/Fe_2O_3 catalysts under working conditions was pursued. By virtue of the shell-core model in which vanadium is isolated at the surface, *in situ* XAS analysis of VO_x/Fe_2O_3 catalysts can supply a wealth of information regarding surface species present during catalysis, active sites and intermediates formed. One of the original intentions behind the production of a VO_x/Fe_2O_3 shell-core catalyst was to investigate its potential as a propane or propylene oxidation catalyst, due to the significant pedigree vanadium catalysts have in that regard. An *in situ* XAS experiment was applied for at the XMaS beamline at the ESRF to investigate propylene oxidation to acrolein using various ML coverages of VO_x/Fe_2O_3 catalysts, and successfully granted. It was intended to perform the reaction at high temperatures, in excess of the maximum safe temperature for Kapton® tape. The XMaS beamline had been constructing a custom *in situ* sample cell with diamond windows, capable of high temperature operation while still retaining sufficient X-ray transmissivity: this cell was thought to be promising. In actuality, however, the cell remained a prototype and possessed several deficiencies, most notably the inability to maintain a gastight seal around the sample. This does not unduly perturb the sample environment *per se*, as a positive pressure gas flow can be applied to the system to prevent the ingress of air, but instead a significant safety issue arises when operating with flammable gases like propane and propylene. Due to the inability to remedy the continuous leakage of gas from the *in situ* cell, the propylene experiment could not be continued for safety reasons: instead, methanol was substituted as reactant for propylene. Two experiments were prepared on the XMaS beamline, namely a study of the redox properties of VO_x/Fe_2O_3 catalysts during methanol oxidation and an examination of structural changes during calcination. For both experiments, only XANES data were obtainable: the limitations of the equipment available at XMaS preclude the collection of meaningful EXAFS data. The author expresses his thanks to the XMaS beamline and Paul Thompson in particular, for their assistance with and provision of beamtime.

Probing the reduction of VO_x/Fe_2O_3

Using the *in situ* cell constructed specifically for the XMaS beamline, a reduction experiment was performed in concert with an online mass spectrometer. A range of vanadium standards were also measured prior to the reduction experiment, viz. V_2O_3, V_2O_4, $FeVO_4$ and V_2O_5. A 3 ML VO_x/Fe_2O_3 was placed in the sample cell, which was then connected to the gas flow system. The temperature at which the reaction was to be performed was 320°C, since this temperature is similar to the operating temperature of similar bulk industrial catalysts: by 320°C, the catalyst is highly active, meaning no VO_x will be left unreduced. The cell was then heated to 320°C and held there, and three XAS measurements were made. Unlike the QEXAFS facility at B18, Diamond Light Source, the measurement equipment at XAS was significantly slower, with each measurement lasting approximately 30 minutes. This was satisfactory for measurements where no reaction was taking place, and hence there were no fleeting changes to miss. During reaction, however, a scan duration of 30 minutes would fail to capture the expected changes. Based on literature vanadium XANES analysis, upon reduction of 3 ML VO_x/Fe_2O_3 the pre-edge region was expected to be affected to the greatest degree through changes in pre-edge peak intensity and position. Consequently, to expedite the progress of each measurement scan, and thereby attain superior time resolution, it was decided to focus solely on the pre-edge peak for scans taken during the reaction.

After the initial three scans at 320°C, continuous scanning was initiated, measuring only the pre-edge peak (Figure 3.30). Ten minutes passed, after which a methanol flow (obtained by piping helium through a Drechsel bottle of liquid methanol) was introduced; however, due to the piping distance and bubbler setup, methanol arrived in the sample cell approximately one minute after the MFCs were switched. Complete reduction of the catalyst was achieved in short order. Throughout this period, formaldehyde was visible by mass spectrometry, though at this temperature CO is the major product. After a further 30 minute period, during which no other significant changes were seen, the methanol flow was halted, along with sample heating. A continuous flow of helium was maintained throughout the cooling period until 80°C, during which time normal, full-spectrum XAS measurements were made (Figure 3.31). Once these scans were complete, the gas flow was switched to 10% O_2 in He and the sample was slowly heated to 160°C, with prolonged dwell periods at intermediate temperatures to compensate for the duration of each XAS measurement. No evidence of catalyst reoxidation was observed in the sample at 80°C, nor 160°C; however, by 250 °C, partial reoxidation has occurred. Interestingly, no further reoxidation was apparent, even by 320°C, and the intensity of the pre-edge peak never recovers to its pre-reaction zenith (Figure 3.31). This is attributed to a degree of passivation: at 320°C, the outer layer of the 3 ML VO_x/Fe_2O_3 catalyst is oxidised, shielding the inner layers from reoxidation. Further treatment with oxygenic atmospheres at higher temperatures, however, would fully reoxidise the catalyst (indeed, for this reason a pre-treatment under oxygen at 500°C was performed ahead of each TPD study of VO_x/Fe_2O_3 catalysts). In this instance, the electrical heating system of the sample cell in use could not achieve temperatures greater than 320°C, denying any opportunity to drive greater reoxidation.

The significant difference between the pre- and post-reaction 3 ML VO_x/Fe_2O_3 XANES spectra is the effective disappearance of the pre-edge peak upon reduction, to leave a small pre-edge shoulder, and a notable modification of the main absorption edge shape. Assessed visually, the reduced form of the 3 ML VO_x/Fe_2O_3 catalyst most resembles the V_2O_3 standard, signifying a reduction from V(V) to V(III) (Figure 3.32). This is highly encouraging, as a reduction of two oxidation states is a key part of the MVK mechanism for

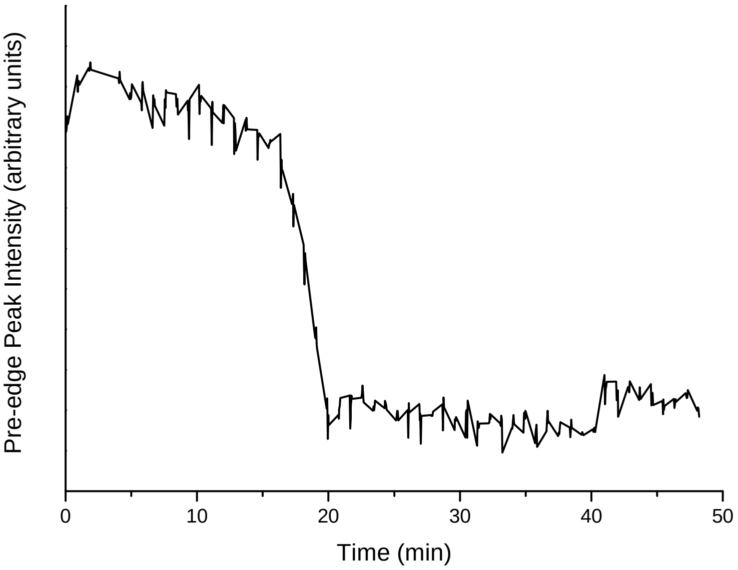

Figure 3.30: Vanadium pre-edge intensity for 3 ML VO_x/Fe_2O_3 as a function of time during reaction with methanol. The beamline equipment and scanning method generated regular oscillations in the signal throughout the experiment: the resulting noise is not indicative of any genuine changes.

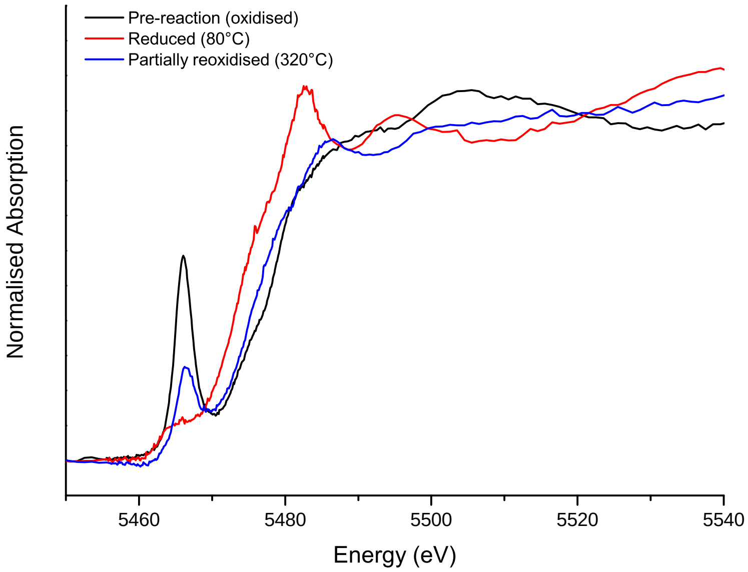

Figure 3.31: A comparison of *in situ* XANES data for the pre-reaction, reduced and partially reoxidised forms of 3 ML VO_x/Fe_2O_3.

selective oxidation. V_2O_3 possesses a trigonal crystal structure, with space group R$\overline{3}$c (the corundum structure). More precisely, this structure is known as ditrigonal scalenohedral: crucially, it is centrosymmetric. Since the intensities of XANES pre-edge features decrease with greater structural centrosymmetry, the pre-edge feature intensity for V_2O_3 is weak. The shape of the absorption edge for 3 ML VO_x/Fe_2O_3 correlates well with V_2O_3, and importantly shares a similarly small pre-edge feature: accordingly, the structure of reduced 3 ML VO_x must exhibit significantly greater centrosymmetry than fully oxidised 3 ML VO_x/Fe_2O_3.

The identity of the structure cannot be definitively ascertained by XANES alone, but reliable inferences can be drawn. Within the V_2O_3 structure, the existence of VO_6 octahedra has been reported, particularly when confined to thin layers atop support structures.[15] The pre-edge feature is therefore weak, due to its high centrosymmetry. Considering that the reduced 3 ML VO_x catalyst spectrum is so similar, it is reasonable to suggest that its vanadium coordination environment is octahedral also. This raises a quandary, however, as the studies of the fully oxidised catalyst indicated VO_4 tetrahedra: in general, oxygen is removed during reduction, not gained. It is not unfeasible that changes could occur elsewhere in the catalyst during reduction, and were this the case, then the generation of octahedral VO_6 would be possible. For example, portions of the Fe_2O_3 structure near the surface could be reduced during the reaction of methanol at the surface to leave oxygen deficiencies in the Fe_2O_3. Considering the MVK mechanism, and its preference to fill oxygen vacancies with lattice oxygen over gaseous oxygen, the “excess” oxygens present in the reduced VO_x octahedra could be donated to the reduced Fe_2O_3 upon reoxidation, filling the vacancies and restoring the catalyst. Alternatively, the centrosymmetry could arise from the adoption of another centrosymmetric coordination environment. Nonetheless, based on the measurements reported here, the resemblance of V_2O_3 and reduced 3 ML VO_x is strong, hence it is likely that they share structural properties.

After treatment with oxygen at moderate temperatures, it is clear that the catalyst has been partially reoxidised (Figure 3.33). The pre-edge peak, the marker of deviation from centrosymmetry, has returned, though with a lower intensity than seen for the original pre-reaction catalyst. At this stage, the greatest visual similarity to the reoxidised catalyst is displayed by V_2O_4: this could indicate that partial reoxidation from V(III) to V(IV) has been achieved. When LCF analysis is conducted on the *in situ* 3 ML VO_x/Fe_2O_3 data, however, the reoxidised sample is revealed to be a poor likeness of V_2O_4 (Table 3.8). At this juncture, one must recall that XAS is a bulk averaging technique: the

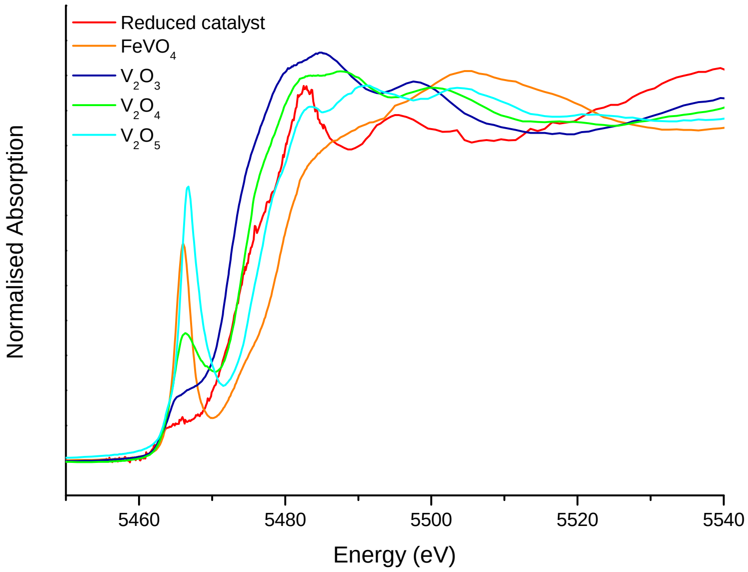

Figure 3.32: A comparison of *in situ* XANES spectra from the reduced 3 ML VO_x/Fe_2O_3 catalyst and vanadium reference compounds.

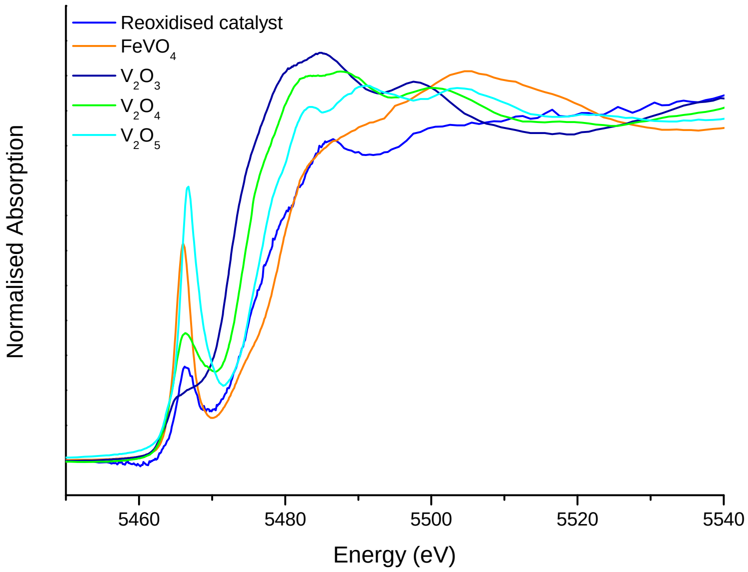

Figure 3.33: A comparison of *in situ* XANES spectra from the reoxidised 3 ML VO_x/Fe_2O_3 catalyst and vanadium reference compounds.

XANES spectrum resulting from an even mix of two extremes will appear centrally between them. In this instance, the reoxidised sample demonstrates this behaviour: after partial reoxidation, LCF analysis indicates that the sample is a mixture of unoxidised V(III) V_2O_3 and reoxidised V(V) $FeVO_4$. This supports the suggestion that the sample undergoes a type of passivation and remains in a stable partially-reduced state, wherein the outermost surface VO_x are reoxidised but not those VO_x species below. Greater thermal energy is required to proceed beyond this stage, which is provided either by high temperature calcination (e.g. at 500°C) or through the localised exotherms produced at the surface by the oxidation of methanol under an oxygenic atmosphere (i.e. when operating as a catalyst).

Table 3.8: LCF statistical fitting data from *in situ* XANES measurements of 3 ML VO_x/Fe_2O_3.

	Similarity to standards (%)			
Species	V_2O_3	V_2O_4	$FeVO_4$	R-factor
Pre-reaction	2.5	0	97.5	3.90×10^{-3}
Reduced	88.3	0	11.7	3.65×10^{-2}
Reoxidised	18.9	5.3	75.8	5.22×10^{-2}

In contrast to the partially reoxidised sample, the LCF data for the fully reduced sample are highly promising. The fit indicates that the vast majority of the sample comprises V_2O_3 or a V_2O_3-like analogue. This corroborates the earlier discussion of the reduced 3 ML VO_x/Fe_2O_3 catalyst, buttressing confidence in the structure and octahedral/centrosymmetric coordination environment proposed for reduced VO_x/Fe_2O_3.

A similar experiment was conducted using a 12 ML VO_x/Fe_2O_3 catalyst to assess by XAS whether the quantity of VO_x present in the shell influences the reduction process of the catalyst. Using the same *in situ* cell and initial experimental method, a 12 ML VO_x/Fe_2O_3 catalyst was loaded and heated to 320°C. For the 12 ML VO_x experiment, continuous scanning of the pre-edge feature was not initiated before release of methanol to the sample, hence there is no dwell period before reduction, and full reduction of the sample occurs speedily (Figure 3.34). Unlike the 3 ML VO_x experiment, however, no reoxidation was performed on this sample: instead, a continuous flow of methanol in helium remained during sample cooling.

Similarly to 3 ML VO_x/Fe_2O_3, after the addition of methanol the 12 ML VO_x/Fe_2O_3 catalyst has been reduced from V(V) to V(III), shown by the almost disappearance of the pre-edge peak (Figure 3.35). This signifies the adoption of a more centrosymmetric

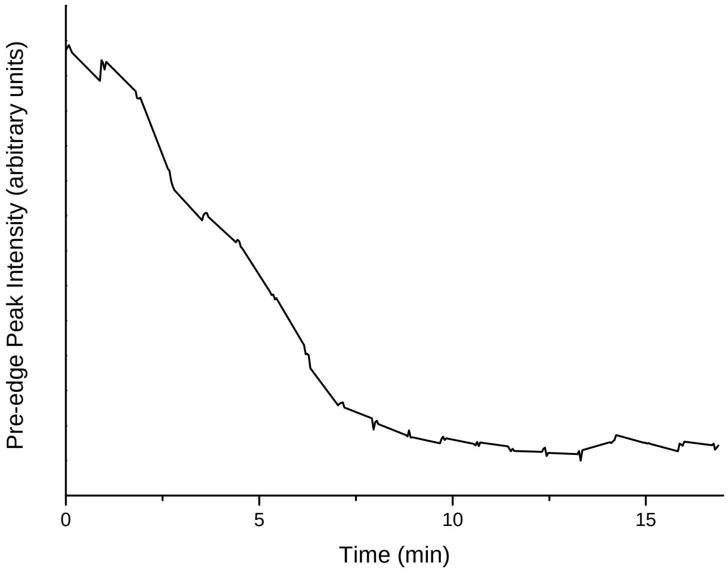

Figure 3.34: Vanadium pre-edge intensity for 12 ML VO_x/Fe_2O_3 as a function of time during reaction with methanol. The beamline equipment and scanning method generated regular oscillations in the signal throughout the experiment: the resulting noise is not indicative of any genuine changes.

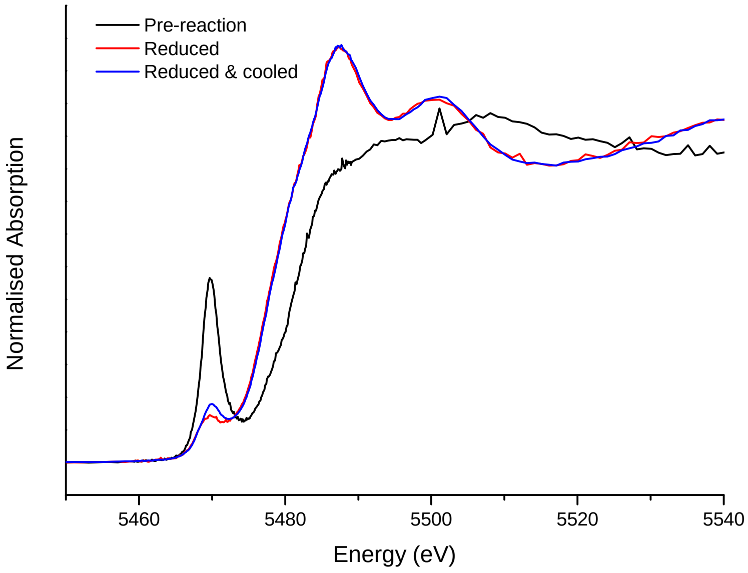

Figure 3.35: A comparison of XANES data for the pre-reaction, reduced and cooled forms of 12 ML VO_x/Fe_2O_3.

coordination environment, and is in agreement with the behaviour witnessed for 3 ML VO_x/Fe_2O_3. No significant differences were observed between the respective behaviours of the 3 and 12 ML VO_x/Fe_2O_3 catalysts, which is encouraging: the shell-core model does not predict, nor have prior experiments demonstrated, disparities between the behaviours of ≥ 1 ML VO_x/Fe_2O_3 catalysts.

In situ **examination of VO_x/Fe_2O_3 formation**

Alongside the investigation of the properties of the catalyst during reaction, an ongoing interest has been directed towards the formation process of VO_x/Fe_2O_3 and similar shell-core catalysts in general. An experiment to explore the formation process of VO_x/Fe_2O_3 catalysts in greater detail was therefore proposed to accompany the reduction experiment performed at XMaS.

A 3 ML VO_x/Fe_2O_3 catalyst was prepared normally by incipient wetness impregnation and dried, but not calcined. This sample was then mounted in the same *in situ* cell used in the reduction experiment. Since calcination is performed in air, there were no requirements for gas mixtures from a chemical perspective; however, for safety reasons and to ensure efficient exhaust of any fumes generated during calcination, the cell was connected to a constant feed of oxygen in helium to replicate the effects of an air atmosphere and assuage safety fears. It was decided to perform two measurements at each temperature stage throughout the experiment, as this offered the greatest compromise between sample quality—multiple scans can be merged to remove error—and time constraints. Two XAS scans were performed on the dried 3 ML VO_x/Fe_2O_3 catalyst at room temperature, before increasing the temperature to 140°C initially and then in 40°C increments to 300°C: thereafter, increments of 20°C were used to 500°C. Upon reaching 480°C, however, an electrical component in a heating cartridge failed, fusing the entire heating system. This fault also impacted the sample environment at the moment of failure, shifting the sample physically away from the optimal position for measurement, but this was not observed until XAS measurement was complete. Due to the suboptimal positioning, the data from 480°C and 500°C were of notably poorer quality than prior scans, and were deemed untrustworthy. Attempts were made to remedy the electrical issues, but to no avail: indeed gremlins in the heating system plagued the entire beamtime (including the *in situ* reduction experiment). Nonetheless, the data obtained prior to the electrical failure are of high quality. Clear differences can be seen between the XANES spectra of the room temperature and the 460°C calcined catalysts, with a clear progression visible as a function of temperature

(Figure 3.36).

As before, the vanadium pre-edge feature warrants particular scrutiny, since it imparts significant information regarding the structure of the VO_x catalyst: assessing differences in the pre-edge feature is an excellent means by which to observe changes in the catalyst. Before heating commences, the pre-edge feature is visible along with a slight shoulder in the main absorption edge. As the temperature of calcination increases, so does the intensity of the pre-edge feature, achieving its acme between 400 and 440°C. The main absorption edge is also affected, with the highest point of the absorption edge climbing higher at elevated temperatures (navy blue in Figure 3.36): in concert, a post-edge depression develops approximately 40 eV beyond the absorption edge. Importantly, by 460°C the pre-edge feature has moved to slightly lower energy. To understand the significance of this shift, it is useful to compare spectra from key points throughout calcination with two relevant vanadium references, namely $FeVO_4$ and V_2O_5 (Figures 3.37 and 3.38).

The pre-edge position and absorption edge shape for the 400°C calcined catalyst correlate well to the pre-edge feature and edge shape of V_2O_5. This is an auspicious result, since the schematic model devised to explain VO_x/Fe_2O_3 shell-core catalyst formation includes a stage at 400°C wherein the vanadium present exists as aggregates of V_2O_5 on the haematite surface (see Section 3.3.3). The model arose from interpretation of Raman spectra of samples from different points during calcination: confidence in the model is greatly bolstered by this encouraging XAS result. Recall that the model states that, after V_2O_5 has formed at 400°C, further calcination removes the V_2O_5 aggregates and by 500°C produces the desired catalyst structure (which at 3 ML, will contain the sandwich $FeVO_4$ layer). Accordingly, if the model is accurate, increasing differences from V_2O_5—and greater similarity to $FeVO_4$—should be seen as the calcination temperature approaches 500°C: hearteningly, such differences are indeed observed. The pre-edge peak of the 460°C calcined catalyst has shifted lower in energy, thereby resembling $FeVO_4$ to a greater extent. This clearly supports the assertion that the V_2O_5 aggregates formed at 400°C begin to decompose when calcination nears 500°C, to form the intended VO_x/Fe_2O_3 catalyst.

3.3.8 Summary of VO_x/Fe_2O_3 catalysts

The abilities of VO_x/Fe_2O_3 catalysts as methanol selective oxidation catalysts have been clearly demonstrated, alongside verification of the ability to incorporate new metal oxides into the metal oxide shell/haematite core architecture. High selectivity to formaldehyde is

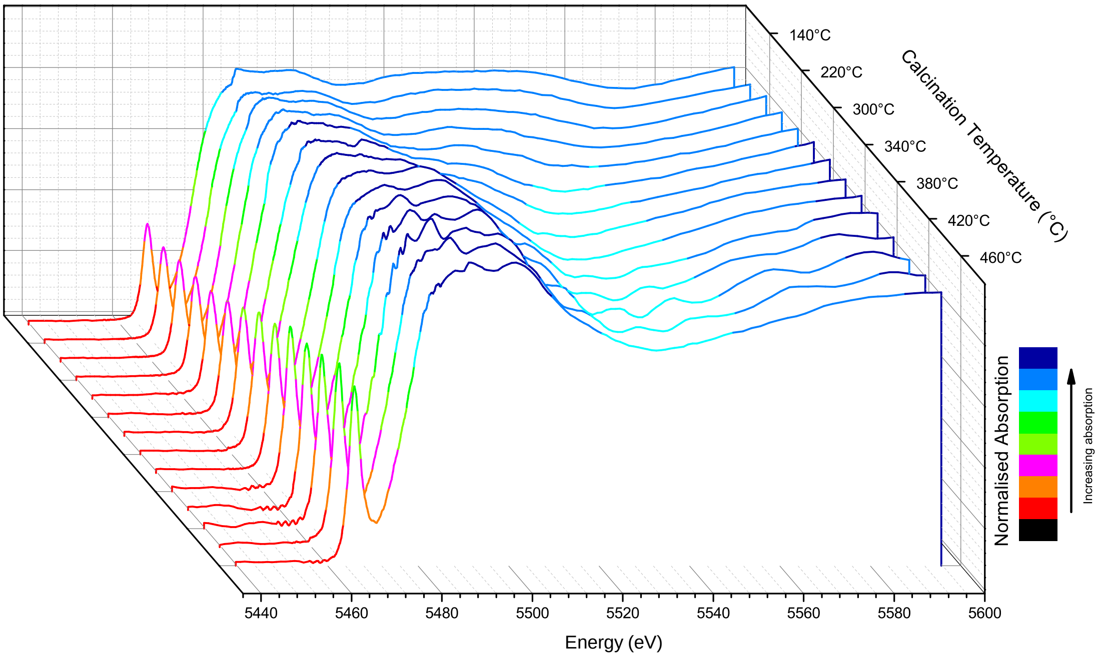

Figure 3.36: A study of 3 ML VO_x/Fe_2O_3 XANES spectra as a function of calcination temperature. Differences in normalised absorption are specified by the colour scale on the ordinate axis.

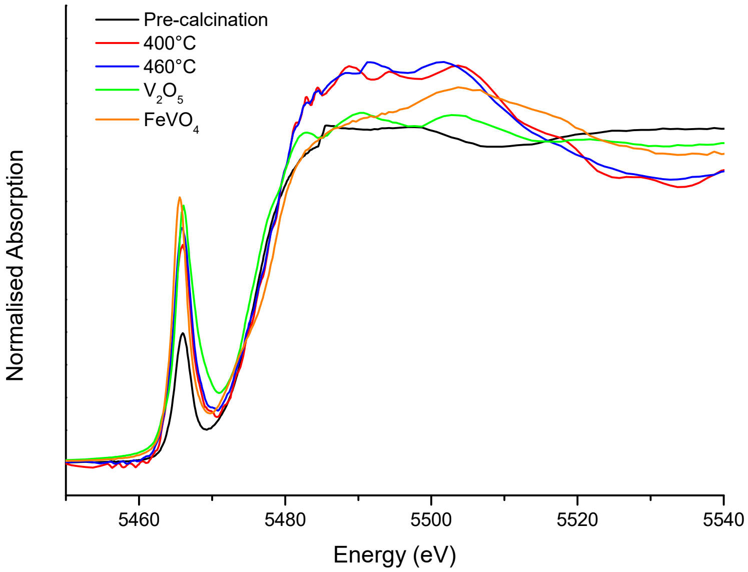

Figure 3.37: A comparison of select *in situ* XANES spectra from the calcination of 3 ML VO_x/Fe_2O_3 with $FeVO_4$ and V_2O_5 reference spectra.

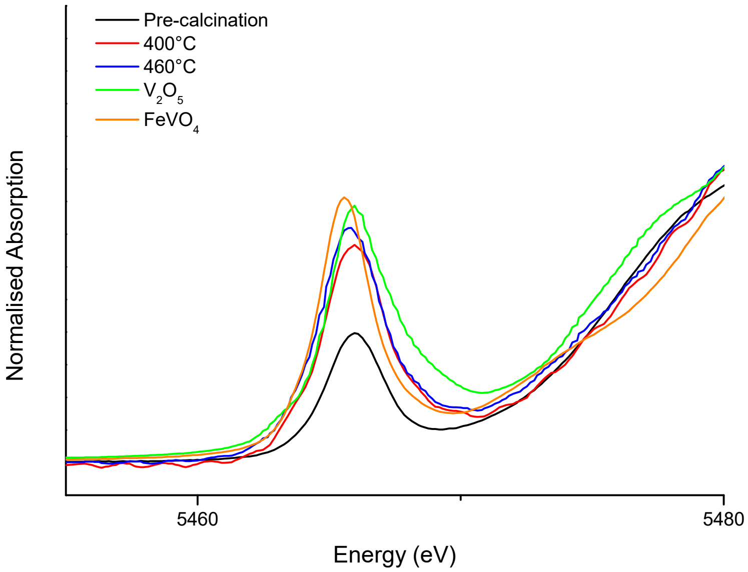

Figure 3.38: An expanded view of the pre-edge features in *in situ* XANES spectra from the calcination of 3 ML VO_x/Fe_2O_3.

achieved for all catalysts with one or more ML coverage of VO_x atop the Fe_2O_3 core. This fully agrees with the suggested shell-core model, and corresponds well with earlier work on MoO_x/Fe_2O_3 equivalent catalysts. The effects of shell loading have been explored; while shell loadings greater than 1 ML provide no additional advantages for catalysis, sub-ML loadings are detrimental to catalytic properties (as expected due to the presence of naked haematite). The mechanisms by which undesired products are formed are corroborated by the sub-ML behaviour. Where the VO_x shell occupies $^3/_4$ of the surface, CO production is strong, due to the large numbers of exposed isolated Fe sites. In contrast, where VO_x represents a minority of species at the surface, an abundance of exposed Fe sites, capable of interacting, is exposed at the surface. This stabilises a formate intermediate which then forms CO_2 (the most thermodynamically favourable product of methanol oxidation). Up to three main constituents are present in a VO_x/Fe_2O_3 catalyst: the selective outermost layer VO_x units; a sandwich layer of $FeVO_4$ for catalysts with ≥ 1 ML; and the haematite core.

The formation process of VO_x/Fe_2O_3 catalysts has been examined, and discovered to be essentially analogous to the formation of the equivalent MoO_x/Fe_2O_3 catalysts. Several key structural stages reached during calcination of the catalysts have been explored by Raman spectroscopy and XAS, indicating that distinct quantities of V_2O_5 are formed by 400°C, which are then replaced by $FeVO_4$ where applicable. Based on XANES and EXAFS data of fully-formed catalysts, the selective VO_x layer is believed to contain distorted tetrahedra of VO_4, while successive ML coverages increase the quantity of (and hence spectral resemblance to) $FeVO_4$. The redox behaviour of VO_x/Fe_2O_3 catalysts is similar in principle to that of MoO_x/Fe_2O_3. Upon contact with methanol, the VO_x/Fe_2O_3 is reduced from V(V) to V(III). This process can be monitored by XAS, in which the crucially important vanadium pre-edge feature decreases markedly upon reduction due to the adoption of a centrosymmetric structure (similar to V_2O_3). It was also determined that reoxidation does not occur fully at 320°C: higher temperatures are necessary to completely restore the catalyst.

Ultimately, VO_x/Fe_2O_3 catalysts have been excellent materials to showcase the wider applicability of the shell-core model. These model systems possess a multitude of analytical advantages: chief among them is the ability to perform simple XAS measurements and obtain quasi-surface-sensitive information in return.

3.4 NbO_x/Fe_2O_3 shell-core catalysts

While selective oxidation catalysts based on oxides of molybdenum and vanadium have traditionally induced the greatest research efforts, niobium-containing materials have been the subject of significant research. Whether as the primary material in the catalyst or merely a dopant, niobium compounds possess a multitude of properties useful for catalytic purposes. Niobium-based catalysts have historically been studied as oxidation catalysts for numerous industrial processes, but more recently they have mustered increasing interest as an electrochemical catalyst added to novel batteries.[16–18]

This section will detail the explorations of niobium-containing catalysts (NbO_x) conducted after the studies of VO_x/Fe_2O_3. With the efficacy of MoO_x and VO_x shells soundly demonstrated, the primary aim of NbO_x experiments was to probe whether the same shell-core catalyst system could be exported yet further to a new metal oxide shell material. Like MoO_x and VO_x, oxides of niobium generate selective products during the oxidation of methanol; however, unlike earlier catalysts, the significant selective product is DME, not formaldehyde. Nonetheless, the validity of the mechanisms by which shell-core segregation is assessed (i.e. differential reactivity from TPD) remains. A secondary aim, should NbO_x/Fe_2O_3 catalysts have been attainable, was to examine their efficacy in alternative catalytic processes. Significant portions of this section were accepted for publication in the *Chinese Journal of Catalysis* in 2019.[19]

3.4.1 Assessing the viability of NbO_x/Fe_2O_3 shell-core catalysts

Unlike Mo and V, both of which boast significant pedigree in formaldehyde-selective methanol oxidation catalysts, Nb-based catalysts are rarely mentioned in the context of methanol oxidation. To assess the behaviour of NbO_x/Fe_2O_3 shell-core catalysts during methanol oxidation, one must first understand the catalytic behaviour of the "free" equivalent metal oxide, niobia (Nb_2O_5). Using a calcined sample of Nb_2O_5, a methanol TPD experiment was performed in the same way as for MoO_x and VO_x/Fe_2O_3 catalysts (Figure 3.39).

The contrast to MoO_x and VO_x catalysts, namely the low selectivity to formaldehyde, is immediately apparent. Instead, moderate selectivity to DME is observed alongside moderate selectivity to CO. The former product, while not formaldehyde, is nonetheless a selective product from methanol dehydration. Most importantly, no CO_2 production is observed at all. This is the vital condition of metal oxide shell-haematite core catalysts, that the combustion elicited by the core haematite when exposed is not masked by

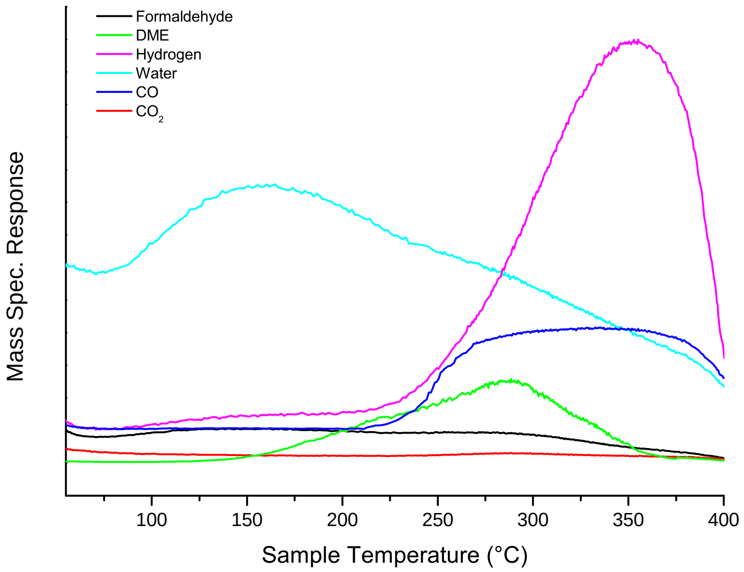

Figure 3.39: TPD data for Nb_2O_5 calcined to 500°C. The major products are DME and CO: crucially no CO_2 is observed.

combustion products produced by the shell material.

With the selectivity of Nb_2O_5 known, investigations of NbO_x/Fe_2O_3 catalysts can commence. Similarly to the precursor of MoO_x/Fe_2O_3 catalysts, the precursor compound used to produce NbO_x (ammonium niobate oxalate hydrate, $C_{10}H_5NbO_{20} \cdot xH_2O$) is water soluble, enabling a simpler incipient wetness impregnation process than that performed for VO_x/Fe_2O_3 which uses viscous ethanolamine as the solvent. Two NbO_x catalysts, 1 and 3 ML NbO_x/Fe_2O_3, were prepared in an analogous manner to MoO_x/Fe_2O_3, dried and finally calcined at 500°C for 24 hours. The specific surface area values of 1 and 3 ML NbO_x/Fe_2O_3 were calculated by BET to be 19.1 $m^2\,g^{-1}$ in both cases. Since the haematite support dictates the overall catalyst surface area, no meaningful discrepancies between ML loadings are expected. 1 and 3 ML coverages of NbO_x were selected from consideration of the shell-core model demonstrated by MoO_x and VO_x catalysts: at 1 ML, the catalyst surface will contain solely the selective layer, while at 3 ML a sandwich layer of the relevant iron-metal compound will be formed (which, for NbO_x, is assumed to be iron niobate). This validity of these structural predictions does, however, rely on the feasibility of NbO_x shell-core catalysts. XRD measurements of 1 and 3 ML NbO_x/Fe_2O_3 produce patterns containing only haematite peaks, as anticipated (Figure 3.40): the NbO_x is present only in small quantities with little crystallinity. This confirms that the synthetic method for NbO_x/Fe_2O_3 does not unintentionally produce an iron niobate, which would be visible by XRD. Additionally, XPS confirms that Nb is present in the sample near the surface, and that it exists in its highest oxidation state as Nb(V).

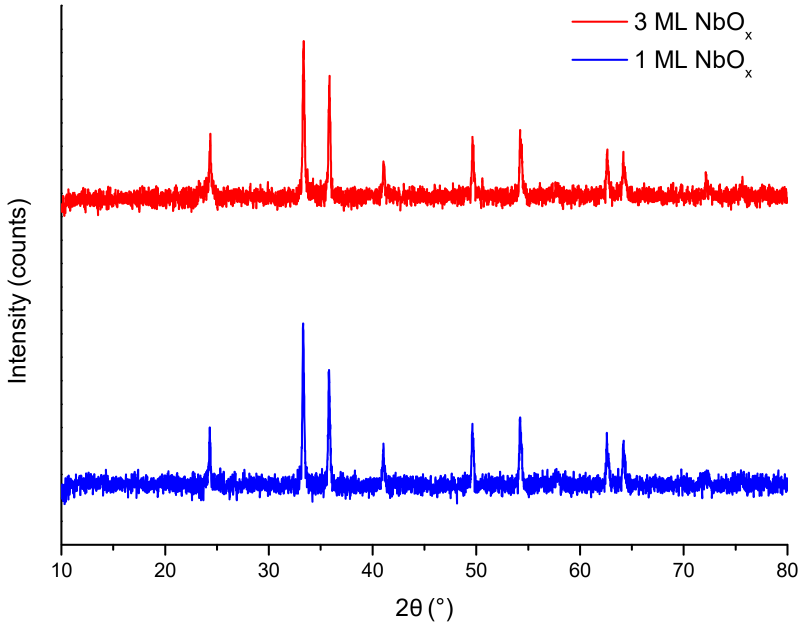

Figure 3.40: XRD patterns for 1 and 3 ML NbO_x/Fe_2O_3.

The utility of TPD measurements as a means to gauge the degree of shell-core formation has been consistently demonstrated throughout the investigations of MoO_x and VO_x shell-core catalysts. To assess the success of NbO_x/Fe_2O_3 segregation, TPD measurements were performed on two samples, namely 1 and 3 ML NbO_x/Fe_2O_3 (Figures 3.41 and 3.42).

The most significant contrast between the TPD data of Nb_2O_5 and 1 and 3 ML NbO_x/Fe_2O_3 is the appearance of significant CO_2 above 300°C for the monolayer catalysts. This unquestionably indicates that haematite is directly participating in catalysis for both 1 and 3 ML NbO_x/Fe_2O_3, and is a significant departure from the trend seen for MoO_x and VO_x/Fe_2O_3 catalysts. One might assume therefore that the synthetic method has not deposited the NbO_x on the Fe_2O_3 support, but this is not the case; it is clear that NbO_x is present in the catalyst, as significant quantities of DME (the preferred product of Nb_2O_5) are produced alongside other selective, though undesired, products like CO and H_2. Small differences in product distribution are seen between 1 and 3 ML NbO_x/Fe_2O_3—e.g. slightly greater DME generation and small, but significant formaldehyde production—which are attributed to the greater quantity of NbO_x present at 3 ML. No major disparities between the quantity of CO_2 produced by each catalyst are

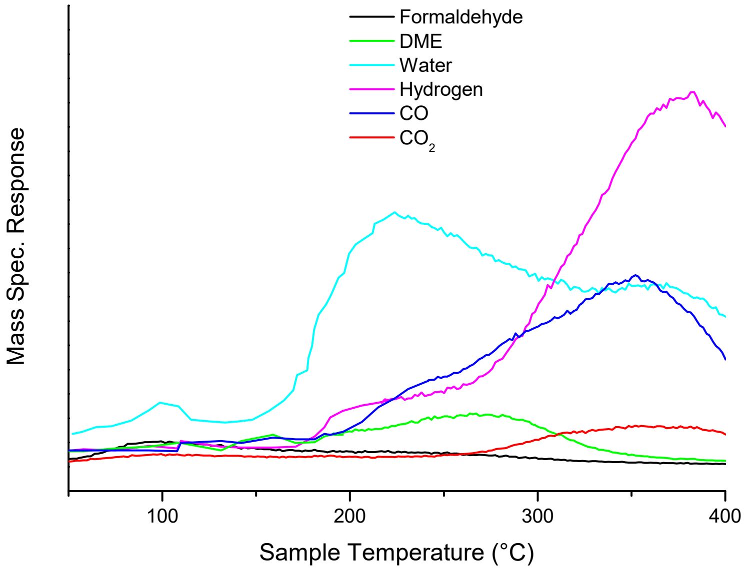

Figure 3.41: TPD data for 1 ML NbO_x/Fe_2O_3 calcined to 500°C. Gas flow: 30 mL/min He. Sample: 250 mg.

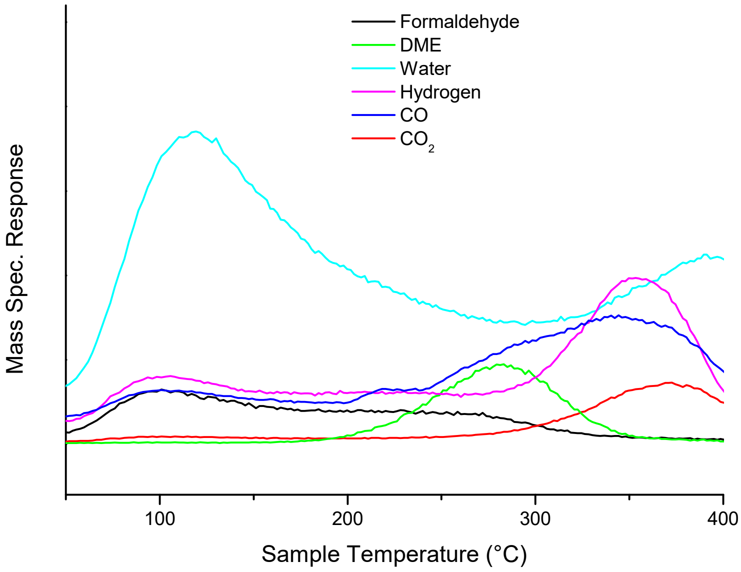

Figure 3.42: TPD data for 3 ML NbO_x/Fe_2O_3 calcined to 500°C. Gas flow: 30 mL/min He. Sample mass: 250 mg.

observed, implying that the degree of core haematite exposure is similar in both 1 and 3 ML NbO_x/Fe_2O_3. Importantly, however, the amount of CO_2 produced by 1 and 3 ML NbO_x/Fe_2O_3 in TPD is far smaller than the equivalent production of CO_2 by unfettered Fe_2O_3, indicating that direct combustion of methanol by the haematite core is at least partially inhibited. The profoundly different TPD findings raise serious questions, chief amongst which is why, despite selective products being observed, the shell layers of 1 and 3 ML NbO_x/Fe_2O_3 are unable to fully isolate the core Fe_2O_3 from reaction with methanol. This behaviour markedly conflicts with that predicted by the shell-core model: clearly a fundamental difference exists for NbO_x, detrimental to its prospects as a shell material.

PFR measurements are an important means by which to further assess the suitability of NbO_x/Fe_2O_3 catalysts. Unlike TPD experiments, CO_2 is observed in PFR studies in all cases (including for MoO_x and VO_x catalysts): it is not the presence of CO_2 which is relevant for PFR, but the temperature at which it appears. If significant CO_2 production commences at high temperatures (above 290°C), this signifies that the haematite is not participating directly at the surface, and instead that the CO_2 is produced from the combustion of selective products upon their formation. Should CO_2 production begin in earnest at lower temperatures (above 190°C), however, this is typically indicative of an improperly-formed shell layer and hence exposed haematite.

The catalytic properties of 1 and 3 ML NbO_x/Fe_2O_3 were explored by PFR investigations under oxygenic atmospheres (Figures 3.43 and 3.44). As for prior PFR experiments, the samples were heated at a constant rate to 500°C with regular microlitre injections of methanol. Small differences in selectivities between the samples were seen, though these broadly fall within the tolerances of the experimental setup. Tellingly, in both cases significant quantities of CO_2 were generated above approximately 160°C. This corroborates the behaviour witnessed by TPD, and moreover strongly reinforces the suggestion that the shell layers of NbO_x/Fe_2O_3 catalysts are improperly formed and unable to inhibit direct core participation in catalysis.

3.4.2 Understanding the inefficacy of NbO_x/Fe_2O_3 catalysts

A considerable volume of spectroscopic information has been gathered on MoO_x and VO_x/Fe_2O_3 catalysts, particularly by Raman spectroscopy. Analysis of Raman features facilitates the assessment of catalyst speciation in its fully-calcined state, while also providing a means to monitor the progress of calcination and to explore the speciation of intermediates formed during calcination. It had been anticipated that Raman spectroscopy

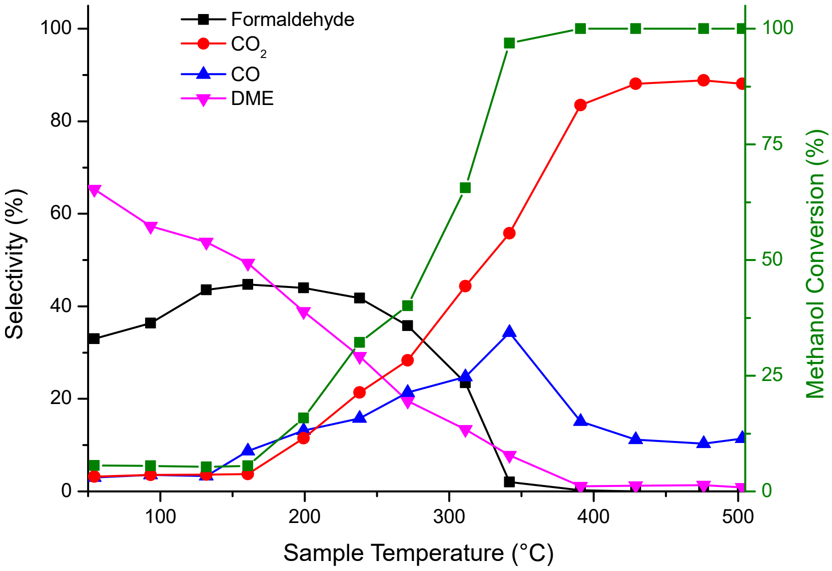

Figure 3.43: Pulsed-flow reaction data for 1 ML NbO_x/Fe_2O_3. Methanol conversion is shown in green on the right-hand y-axis. Gas flow: 30 mL/min 10% O_2 in He. Sample mass: 250 mg.

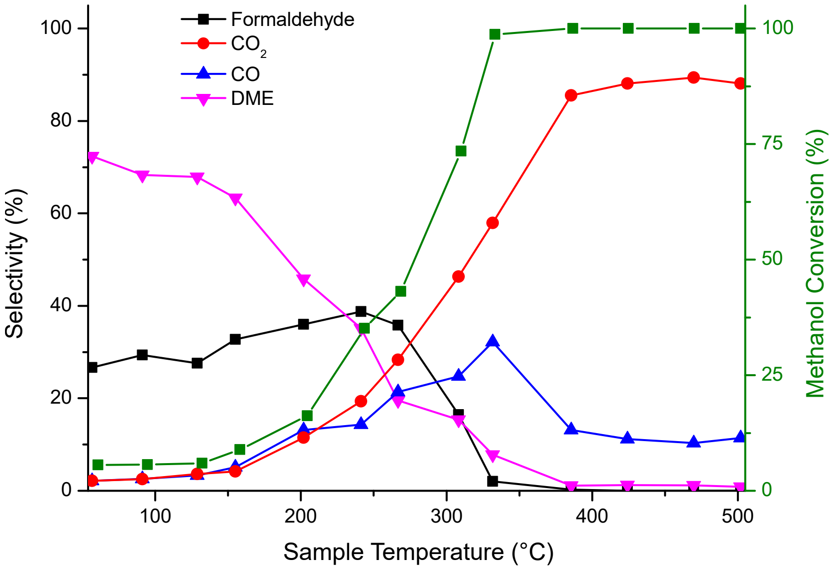

Figure 3.44: Pulsed-flow reaction data for 3 ML NbO_x/Fe_2O_3. Methanol conversion is shown in green on the right-hand y-axis. Gas flow: 30 mL/min 10% O_2 in He. Sample mass: 250 mg.

would assist the characterisation of NbO_x/Fe_2O_3 catalysts. Considering the results of TPD and PFR measurements, however, significant differences to the trends demonstrated by Raman spectroscopy for MoO_x and VO_x catalysts were envisaged.

When 1 and 3 ML NbO_x/Fe_2O_3 were analysed by Raman spectroscopy in the same manner as MoO_x and VO_x/Fe_2O_3 catalysts, further evidence of the deviation of NbO_x from the expected shell-core model was obtained. The spectra lack any distinguishing features apart from those Raman peaks arising from the haematite component (Figure 3.45); importantly, Raman signals from 1 ML NbO_x/Fe_2O_3 are not predicted to be visible due to their limited dimensionality (as for other shell-core catalysts). To verify that Raman information can be acquired from niobium compounds with the experimental setup available, a sample of Nb_2O_5 was also measured (Figure 3.45). Clear peaks were visible in the Raman spectrum of Nb_2O_5, though not all of the assignments detailed below (Table 3.9) are visible in the spectrum.

Table 3.9: Raman assignments for peaks relevant to Nb_2O_5.[20,21]

Wavenumber (cm^{-1})	Raman assignment	Strength
988	Nb=O bond stretching	Strong
904	Nb−O stretching	Weak
664-700	O−Nb−O vibrations	Strong
632	Nb−O stretching	Strong

None of the literature-reported Raman peaks were observed for either 1 or 3 ML NbO_x/Fe_2O_3: from experience, this is expected of 1 ML NbO_x/Fe_2O_3, but for the Raman spectrum of a 3 ML NbO_x/Fe_2O_3 catalyst to be devoid of peaks indicates that the catalyst is fundamentally different. Since niobium oxides are Raman active, and exhibit a wide range of peaks, it can be concluded here that even at 3 ML, the NbO_x present lack any long range order, masking them from observation by Raman.

It is helpful to contrast the Raman spectra of NbO_x/Fe_2O_3 catalysts with the Raman spectra of the equivalent MoO_x and VO_x catalysts (Figures 3.46 and 3.47). Due to the limited dimensionality imparted by the tenuity of the shell layer present in 1 ML MoO_x and VO_x/Fe_2O_3 catalysts, no features are identifiable in their respective Raman spectra; however, the 3 ML MoO_x and VO_x/Fe_2O_3 spectra are more rewarding. For the 3 ML MoO_x/Fe_2O_3 catalyst, signals corresponding to iron molybdate can be seen, although these are partially obscured at 3 ML (Figure 3.46): this parallels the previous studies of MoO_x/Fe_2O_3 systems.[2,3,22] The iron molybdate peaks originate from the two monolayers

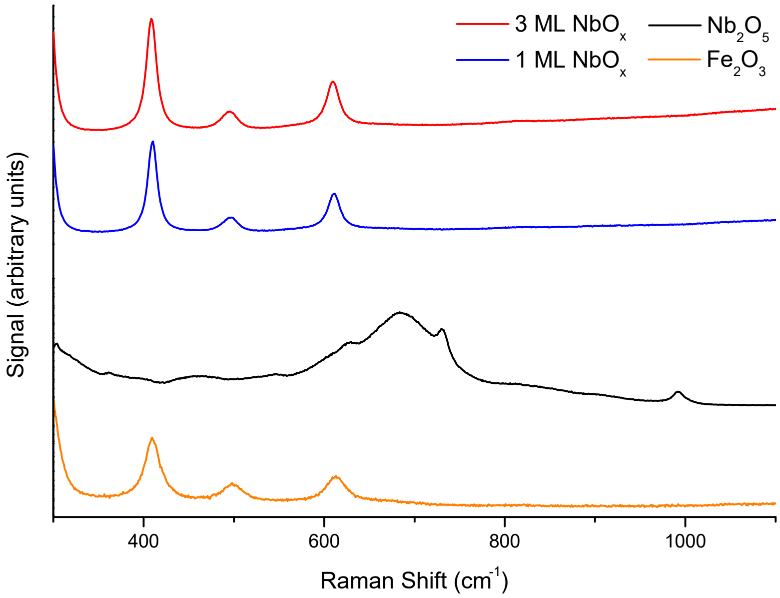

Figure 3.45: Raman spectra of 1 and 3 ML NbO_x/Fe_2O_3 with Nb_2O_5 and Fe_2O_3 for comparison. Three accumulations, each of 1% laser power and duration 20 seconds, were collected per sample.

of iron molybdate in the sandwich layer of a 3 ML MoO_x/Fe_2O_3 catalyst. For the analogous 3 ML VO_x/Fe_2O_3 catalyst, peaks arising from the iron vanadate sandwich layer are plainly visible, though unlike the 3 ML MoO_x/Fe_2O_3 iron molybdate peaks they are markedly less obscured (Figure 3.47). Both MoO_x and VO_x adhere to the postulated shell-core behaviour, and hence yield useful Raman spectra: since NbO_x does not conform as well to the shell-core model, Raman is notably less useful.

While the Raman spectra of the fully-calcined NbO_x/Fe_2O_3 samples are bereft of sample peaks, it was decided to investigate the calcination process of NbO_x/Fe_2O_3 catalysts with Raman spectroscopy. For MoO_x and VO_x, a rich seam of structural information is obtainable by analysing the species formed during calcination with Raman spectroscopy: e.g. by 400 °C, both MoO_x and VO_x display the presence of significant quantities of their respective oxides (MoO_3 and V_2O_5). It was hoped that similar findings might be made for NbO_x catalysts. A series of 3 ML NbO_x/Fe_2O_3 samples was prepared with a range of calcination temperatures, viz. 300, 400 and 500°C, together with an uncalcined sample. These were subsequently analysed by Raman spectroscopy (Figure 3.48). No differences between any NbO_x/Fe_2O_3 spectra can be discerned: this is wholly unlike the trends seen for MoO_x and VO_x/Fe_2O_3. It is not apparent that anything occurs during the calcination of NbO_x/Fe_2O_3 catalysts, certainly not the development of the structural features thought to be necessary for selectivity in shell-core catalysts.

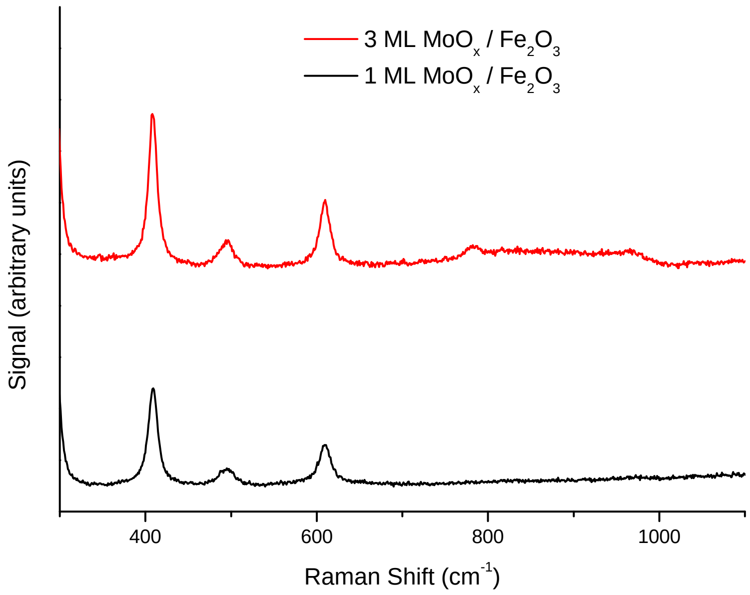

Figure 3.46: Raman spectra of 1 and 3 ML MoO$_x$/Fe$_2$O$_3$. Three accumulations, each of 0.5% laser power and duration 25 seconds, were collected per sample.

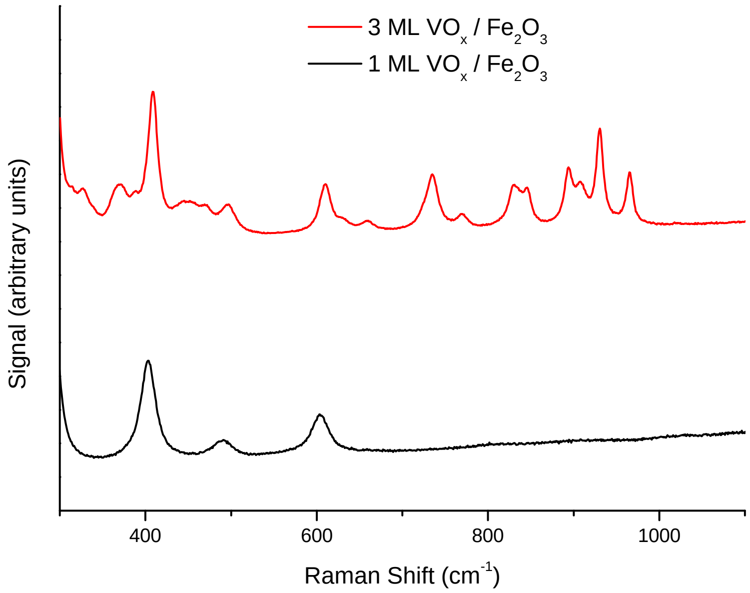

Figure 3.47: Raman spectra of 1 and 3 ML VO$_x$/Fe$_2$O$_3$. Three accumulations, each of 0.5% laser power and duration 25 seconds, were collected per sample.

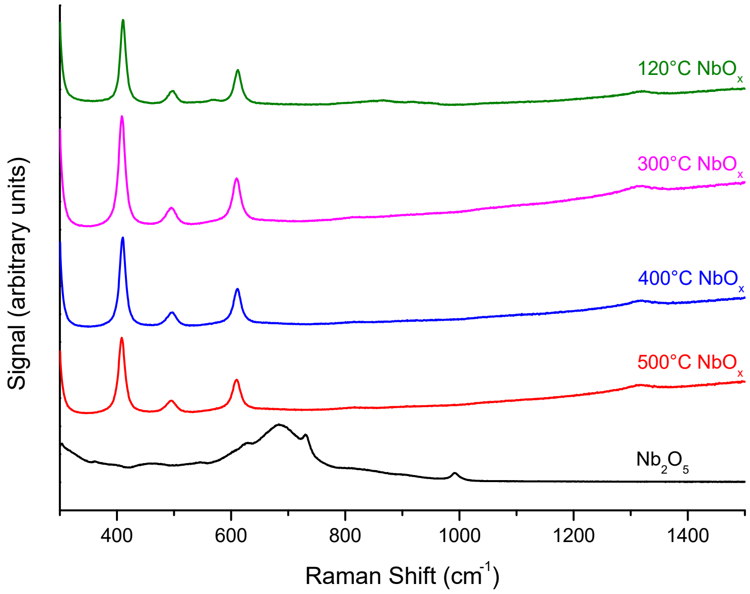

Figure 3.48: Comparison of Raman spectra from different points during the calcination of 3 ML NbO_x/Fe_2O_3. Three accumulations, each of 0.5% laser power and duration 25 seconds, were collected per sample.

For MoO_x and VO_x/Fe_2O_3 catalysts, a clear development of the shell-core structure is witnessed in Raman spectra from different stages during calcination (Figures 3.49 and 3.50). The dried, pre-calcination MoO_x/Fe_2O_3 catalyst exhibits broad, poorly defined Raman peaks, symptomatic of poorly-ordered amorphous MoO_x structures. By 300°C, clear signs of crystalline MoO_3 can be seen, which are greatly enhanced by 400°C. By 500°C, MoO_3 peaks have disappeared to be replaced by those of $Fe_2(MoO_4)_3$. Similarly, dried VO_x/Fe_2O_3 catalysts exhibit weak and indistinguishable peaks, suggesting the presence of amorphous VO_x units. Crystalline V_2O_5 can be seen from 300°C, though the V_2O_5 peaks are notably clearer at 400°C. By 500°C, the V_2O_5 peaks have been supplanted by $FeVO_4$ peaks. This progression from amorphous precursor, through intermediate crystalline metal oxides which then spread across the surface (a thermodynamically favourable process) to produce the final catalyst, is essential to attain the benefits of shell-core catalysts. A key marker of high selectivity in the final catalyst is the appearance of the metal oxide band below 1000 cm^{-1} in Raman spectra taken during catalyst formation: where it is not seen, neither is selectivity.

In view of the significant differences encountered in NbO_x/Fe_2O_3 catalysts, namely the notably poorer performance in TPD and PFR studies than MoO_x and VO_x/Fe_2O_3 catalysts, it is highly probable that NbO_x/Fe_2O_3 catalysts are unable to properly seg-

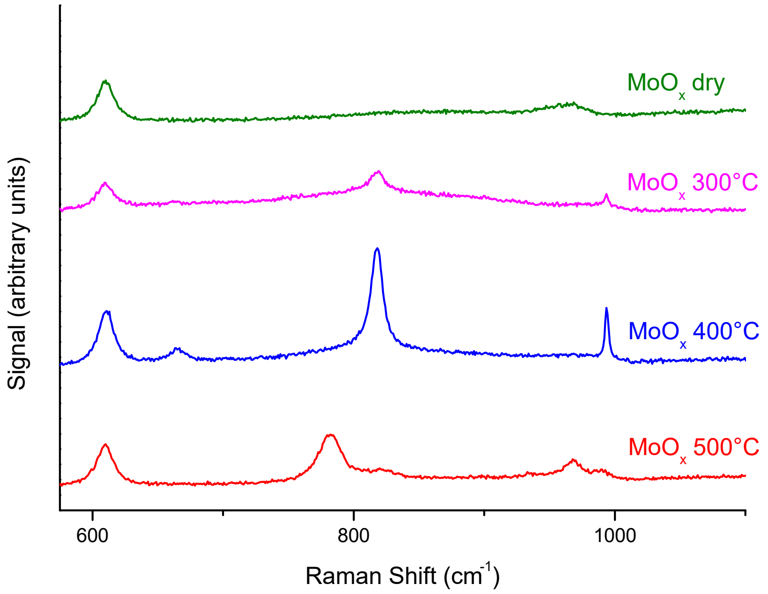

Figure 3.49: Comparison of Raman spectra from different points during the calcination of 3 ML MoO$_x$/Fe$_2$O$_3$. Three accumulations, each of 1% laser power and duration 25 seconds, were collected per sample.

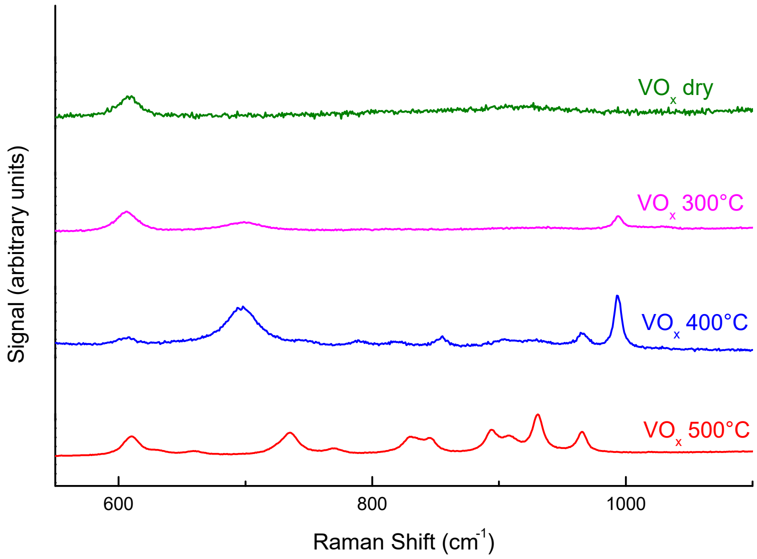

Figure 3.50: Comparison of Raman spectra from different points during the calcination of 3 ML VO$_x$/Fe$_2$O$_3$. Three accumulations, each of 1% laser power and duration 25 seconds, were collected per sample.

regate the haematite core, resulting in a severely perforated shell, with large areas of exposed haematite able to participate directly in catalysis. The Tamman temperature, the temperature at which the mobility of a species in a solid becomes significant, could provide the explanation for this divergence from the expected shell-core behaviour. It is believed that the final stage of shell-core catalyst development for MoO_x and VO_x/Fe_2O_3 is the spreading of the respective shell material from the aggregated crystalline oxides to the final MoO_x and VO_x surfaces across the Fe_2O_3 moiety. The Tamman temperatures for MoO_3 and V_2O_5 (the closest analogues to the systems described here) are 261°C and 209°C respectively.[23] Accordingly, since the calcination temperatures used to produce MoO_x and VO_x shell-core catalysts exceed these Tamman temperatures, diffusion of Mo and V around the surface is facile. The Tamman temperature of Nb_2O_5, however, is 620°C, significantly higher than the maximum calcination temperature of 500°C used for catalyst calcination.[24] Consequently, at no point does the mixture of Nb and haematite exceed the temperature at which NbO_x would become fully mobile and able to diffuse across the surface. This may prevent the formation of aggregates of Nb_2O_5 (akin to the midstage MoO_3 and V_2O_5 products), which must exist at the surface in order for the spreading process to generate a full shell around the haematite.

In essence, calcination of MoO_x and VO_x completes the development of the catalyst, affording properly formed shell-core catalysts; however, NbO_x is unable to complete its formation process at 500°C, instead remaining improperly formed. This state likely involves clusters of NbO_x dispersed throughout the Fe_2O_3, which lack the order or size necessary to be observed by XRD or to be seen by Raman spectroscopy. It is possible that a shell of NbO_x might be formed through calcination at temperatures in excess of 620°C, but at the cost of inexorably undermining the efficacy of the catalyst. Such high temperatures during calcination invariably effect deleterious changes in the particle size properties of Fe_2O_3 by destroying small particles and impelling the agglomeration of particles. This will hugely reduce the surface area of the Fe_2O_3 support, and hence the activity of the final catalyst also.

3.5 Further XAS investigations of MoO_x/Fe_2O_3 catalysts

MoO_x/Fe_2O_3 catalysts were the first examples of shell-core catalysts based on haematite to be developed, and a large body of work exists already detailing their reactivity, structural properties, and formation processes.[1–3] As for the VO_x/Fe_2O_3 catalysts explored above, the contribution from XAS analysis has been large. This section will not revisit the reactivity of MoO_x/Fe_2O_3 catalysts, but instead will focus on the structure of MoO_x shell layers as determined by XAS.

3.5.1 Background information

The sizeable existing EXAFS studies notwithstanding, the identity of the fundamental active site in the selective MoO_x monolayer remains to be definitively determined.[2,3] The EXAFS studies reported suggest that the MoO_x layer in effect resembles a series of MoO_3 units sitting on the Fe_2O_3 surface, which constitute the active sites, but this is not conclusive by itself.[2] Moreover, the reported EXAFS fitting values for MoO_x/Fe_2O_3 cannot be entirely replicated, despite the use of the original data file and identical fitting parameters. Attempts to recreate the reported fit have succeeded only in recreating certain parameters, but have always failed to achieve an R-factor as good as that reported in the publication (0.005 reported vs. 0.15 calculated anew). Given the nature of EXAFS fitting software, it is possible that an older version of Demeter generated the reported fit where the recent version will not: nonetheless, the freshly-calculated version of the reported fit is a reasonable fit, but is not as compelling as was originally reported.

Scanning tunnelling microscopy (STM), a technique well-suited to atomic level imaging, has not been employed to examine either MoO_x/Fe_2O_3 or VO_x/Fe_2O_3 catalysts *per se*; however, some STM imaging has been previously performed in the Bowker group on comparable systems, namely molybdena supported on single crystals of Fe_2O_3 (Figure 3.51).[25] These images strongly implied the presence of triangular clusters of MoO_x, each containing three molybdenum atoms. At the time the imaging was performed, the investigation of MoO_x/Fe_2O_3 catalysts was in its infancy, and the possibility of a multimeric Mo species was overlooked. With a wealth of information on MoO_x/Fe_2O_3 catalysts now available, and ever easier access to XAS facilities, it was decided to revisit MoO_x/Fe_2O_3 catalysts with the intention of ascertaining whether the multimeric Mo species existed on non-single crystal MoO_x/Fe_2O_3, and whether such a structure, if present, could represent the active site for methanol oxidation (and hence improve mechanistic knowledge of methanol oxidation).

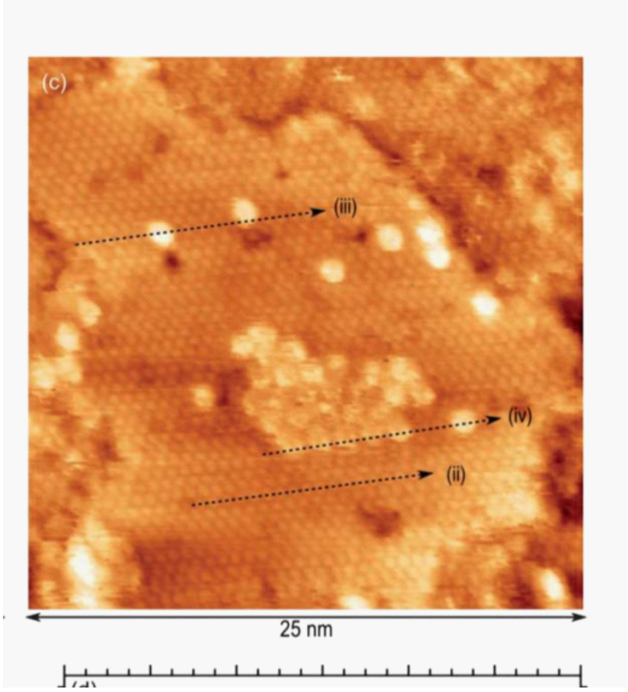

Figure 3.51: STM image after exposure of single crystal iron oxide to molybdenum oxide, adapted from Bamroongwongdee et al.[25]

3.5.2 Mo_3O_9: the active site for methanol oxidation?

Based on the results of the STM images, consideration was given to the possible structures of MoO_x which contained multiple molybdenum atoms with a triangular structure with respect to molybdenum. It is known that a wide range of molybdenum oxide compounds beyond standard MoO_3 is accessible depending on synthetic conditions. One of the better researched molybdenum oxides is Mo_3O_9, encountered initially as a gas phase compound produced during high temperature decomposition of other molybdenum compounds, though subsequently it has been of interest for its electronic structure on thin-films.[26–28] From the STM images, it was suggested that Mo_3O_9 was present on the iron oxide surface.[25] An indicative structure for Mo_3O_9 was obtained, from which bonding information was obtained (Figure 3.52). In light of the triangular multi-Mo structures witnessed by STM, Mo_3O_9 was identified as a candidate for the species seen by STM. Additionally, more recent *in situ* XAS studies of MoO_x/Fe_2O_3 catalysts have implied that effective cooperation between multiple Mo atoms is essential for high selectivity.[22] Since this is achievable only with sufficient inter-Mo proximity, this raised the possibility of a multi-Mo candidate as the active species. After reduction with methanol, clear evidence by EXAFS of Mo−Mo direct bonding (of length 2.6 Å) was seen, corresponding to a Mo(IV)−Mo(IV) multimer (most likely a trimer).[22] The full assembly of such a multimeric structure from individual MoO_3-like units upon reduction is unlikely. Rather, it is more plausible that the multimeric Mo reduced species forms from an oxidised structure suited to the adoption of a multimer: in other words, the structure of the oxidised species can be imagined as a proto-multimer. A structure like Mo_3O_9 could fulfil such a role. No direct bonding is thought to exist between the Mo atoms in Mo_3O_9, but the interatomic distances are small enough that minor structural alterations upon reduction—combined with electronic factors—would elicit direct Mo−Mo bonding.

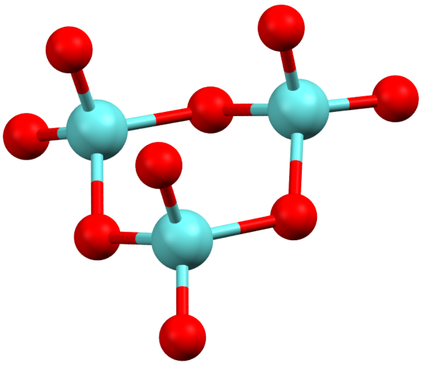

Figure 3.52: The proposed structure of Mo_3O_9 as a free Mo_3O_9 structure: Mo atoms are blue, oxygen atoms are red. When supported on a Fe_2O_3 surface, some structural distortions could occur. Bonding information can be obtained directly by measurement and computed by trigonometry where required.

XAS analysis, in particular through EXAFS fitting, is an extremely effective means of determining structural properties, bonding distances and coordination numbers. Consequently, if a structure like Mo_3O_9 is present in a catalyst, EXAFS fitting will reveal it (subject to sufficient data quality). MoO_x/Fe_2O_3 catalysts, while not identical to the molybdena on single-crystal case seen by STM, are sufficiently similar that it was thought reasonable that Mo_3O_9 would form in the MoO_x layer atop MoO_x/Fe_2O_3 catalysts, if it can form at all. The choice of ML coverage, however, is limited due to the behaviour of > 1 ML catalysts. The 3, 6 and 12 ML MoO_x/Fe_2O_3 catalysts clearly resemble $Fe_2(MoO_4)_3$ when assessed by XAS, as they have 2, 5 and 11 ML respectively of $Fe_2(MoO_4)_3$ in the sandwich layer beneath the outermost MoO_x layer. In such circumstances, the EXAFS contribution from the $Fe_2(MoO_4)_3$ will greatly outweigh the contribution from the surface layer, hindering attempts to assess surface alone. The choice of ML coverage for effective EXAFS analysis of only the surface layer is therefore limited to catalysts of ≤ 1 ML MoO_x.

The formation of a structure like Mo_3O_9 is thought to be thermodynamically favourable, especially so when molybdenum is scarce. For this reason, and given the upper bound of

1 ML MoO_x, it was decided to analyse a sub-ML sample, namely 0.25 MoO_x/Fe_2O_3. At this loading, the absence of $Fe_2(MoO_4)_3$ can be assured, as no sandwich layer forms without a full layer already in place. This sample was analysed at B18, Diamond Light Source, using the QEXAFS functionality. Three scans of three minutes' duration were taken, aligned, calibrated and merged to produce one reliable dataset on which to base EXAFS fitting.

The XANES data are an important confirmation that the intended sub-ML loading has been achieved, and that no $Fe_2(MoO_4)_3$ is present (Figure 3.53). Two molybdenum reference compounds—MoO_3 and $Fe_2(MoO_4)_3$—were also measured (Figure 3.54); when 0.25 ML MoO_x/Fe_2O_3 is compared to these references, strong resemblance to MoO_3 is seen, further evincing the absence of $Fe_2(MoO_4)_3$. Consequently, EXAFS fitting of this XAS data is not complicated by contributions to the signal from $Fe_2(MoO_4)_3$, facilitating the search for the theorised Mo_3O_9 active site.

The principal bond distances for EXAFS fitting were obtained from the model of the Mo_3O_9 unit (Figure 3.55): two Mo−O distances at 1.74 and 2.01 Å respectively and a Mo−Mo distance of 3.35 Å. For a Mo_3O_9 unit, the coordination number for each oxygen distance would be two—two ring oxygen scattering paths, and two terminal oxygen paths—and the Mo−Mo scattering path coordination number would also be two. The Mo−Fe distances derived from a computationally-generated model of MoO_3 on a Fe_2O_3 surface. This model provided the O−Fe distance: using the Mo_3O_9 bond angles and elementary trigonometry, two Mo−Fe distances for Mo_3O_9 were produced, 2.80 and 3.03 Å respectively. The coordination numbers of the two Mo−Fe paths would differ, as while both ring oxygens are able to interact with the Fe_2O_3 surface, only one of the terminal oxygens at each Mo is oriented correctly to bond with the Fe_2O_3. Using these scattering paths and coordination numbers generates a high quality EXAFS fit with excellent visual similarity to the sample Fourier transformed data (Figure 3.56). The calculated statistical parameters strongly support the reliability of the fit, with an R-factor of 0.013 (Table 3.10).

The reliable fit obtained using a model of Mo_3O_9 considerably increases the credibility of the possibility that the oxidised catalyst comprises Mo_3O_9 units at the outermost surface: a highly promising result. The low mean-squared disorder values for each scattering path further testify to the soundness of the fit. Compared to previous EXAFS fits for a MoO_3 structure at the surface, the new fit with Mo_3O_9 is an improvement in terms of R-factor (note the earlier discussion regarding the reproducibility of earlier MoO_x EXAFS

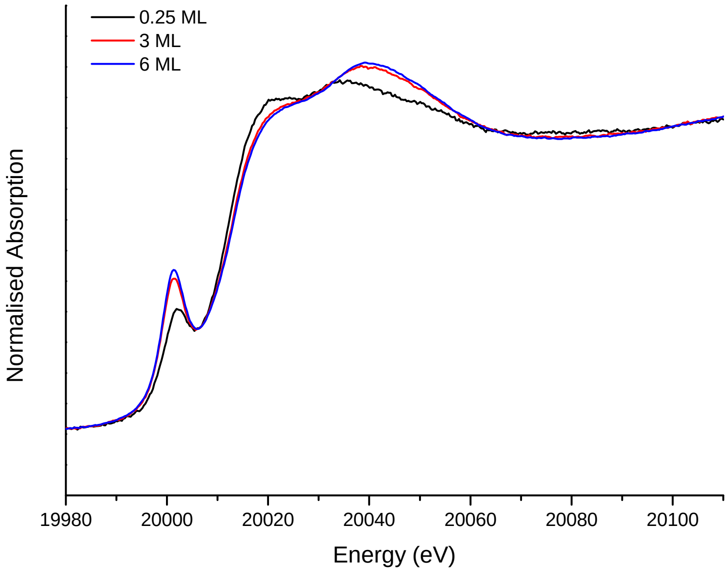

Figure 3.53: XANES spectra of 0.25, 3 and 6 ML MoO_x/Fe_2O_3. 0.25 ML MoO_x/Fe_2O_3 is markedly different in edge shape and pre-edge intensity, indicating its dissimilarity from the higher ML catalysts (and hence iron molybdate).

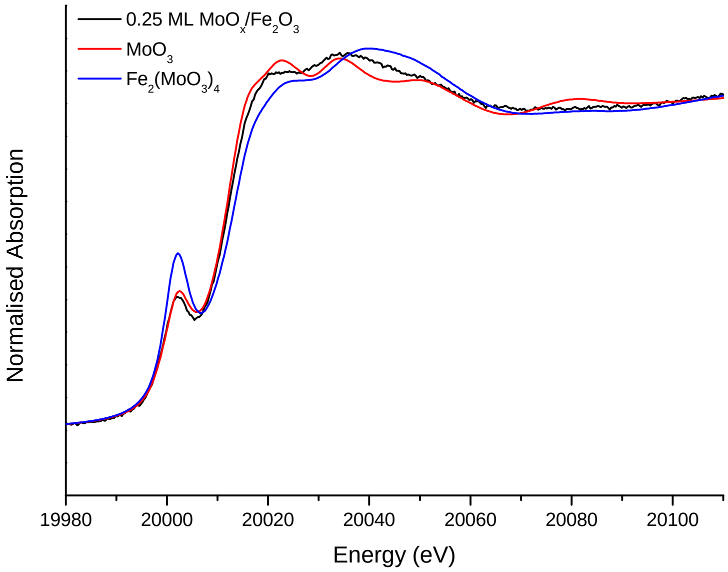

Figure 3.54: XANES spectrum of 0.25 ML MoO_x/Fe_2O_3 compared with molybdenum references.

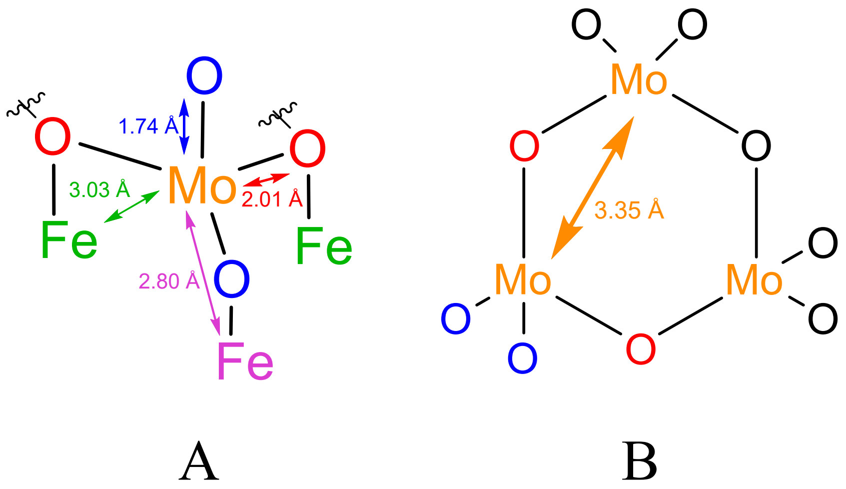

Figure 3.55: A schematic of Mo_3O_9 scattering distances wherein equivalent scattering paths are indicated by shared colours: A) an expanded view in the ring plane of one tetrahedral Mo unit in Mo_3O_9, showing the two Mo−O distances and the two Mo−Fe distances; B) an overview of the whole Mo_3O_9 ring displaying the Mo−Mo distance between each Mo tetrahedral unit.

experiments), and is therefore highly promising. At this point it must be remembered that increasing the number of fitting paths will inevitably produce superior fits; however, in this instance the difference between the earlier EXAFS fitting and the studies reported here is a new Mo−Mo scattering path, not simply a change in coordination number or distance. If a better fit is achieved after the addition of an entirely new and more detailed scattering path, it is achieved not as a function of the number of fitting parameters but as a result of a more appropriate representation of the structure of the sample.

Due to the small quantity of molybdenum present in a 0.25 ML MoO_x/Fe_2O_3 catalyst, the signal-to-noise ratio of the resulting data is poorer than for multi-ML catalysts. This is compounded by the typical method of operation at B18, which performs quick measurements. To bolster confidence in the proposed Mo_3O_9 structure, further studies of sub-ML MoO_x catalysts were applied for at B18, but with modifications to the experimental technique in order to increase the duration of data acquisition (and hence to improve data quality). Three 30 minute measurements of 0.25 ML MoO_x/Fe_2O_3 were made, and subsequently processed similarly to the previous data. The reliability and validity of an EXAFS fit depend on the quality of the underlying sample data, which is best assessed by examination of k-space data (i.e. un-Fourier transformed EXAFS data): the greater the k-range to which the sample signal is stable, the better the quality of the data. Measurement of 0.25 ML MoO_x/Fe_2O_3 over a longer period imparts a significant improvement in EXAFS data quality. By comparing the k-space data of the samples measured by QEXAFS and by long-duration techniques, it is apparent that slower measurements afford significantly

Table 3.10: EXAFS fitting parameters for 0.25 ML MoO_x/Fe_2O_3 calcined to 500°C. Preset fitting parameters: $S_0^2 = 0.82$ as calculated from the MoO_3 standard; range $2.0 > k > 10.2$, $1 > R > 3.8$; no. of independent points = 17.

Abs - Sc	N	R/Å	$2\sigma^2$ / Å^2	E_f/eV	R-factor
Mo−O (i)	2	1.74	0.001		
Mo−O (ii)	2	2.01	0.012		
Mo−Mo	2	3.35	0.013	-1.4	0.013
Mo−Fe (i)	1	2.80	0.006		
Mo−Fe (ii)	2	3.03	0.008		

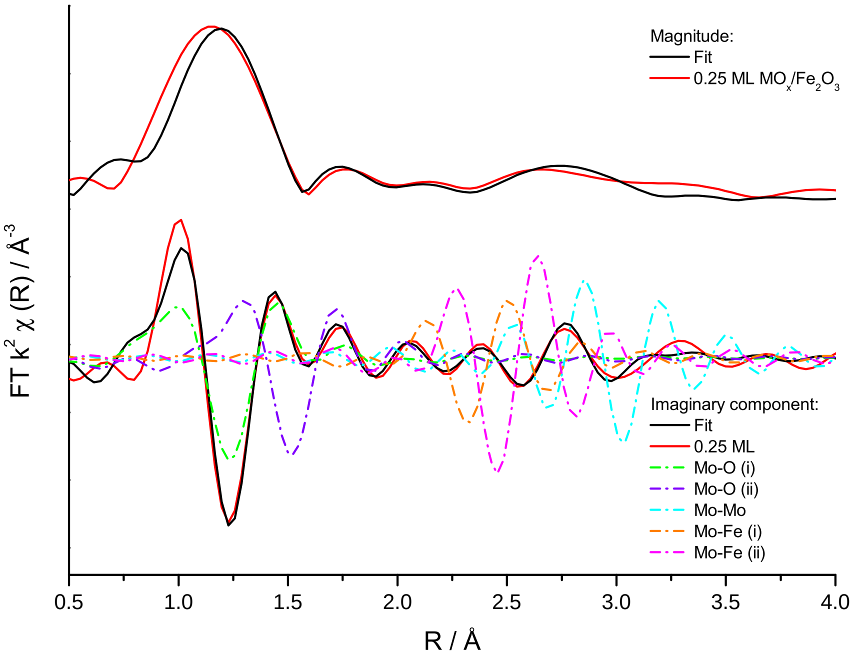

Figure 3.56: Magnitude and imaginary component of the k_3 weighted Fourier transformed fit for the EXAFS data of 0.25 ML VO_x/Fe_2O_3. Individual scattering paths are displayed in the imaginary component.

greater signal-to-noise ratio to considerably a greater k-range (Figures 3.57 and 3.58).

While the k-range of the QEXAFS-measured sample of 0.25 ML MoO_x/Fe_2O_3 is limited to approximately $k = 10.5$, the k-range of the sample measured for a longer duration extends to $k = 14$. This range extends beyond the scattering path distances included in EXAFS fitting for Mo_3O_9, greatly exceeding the range required for EXAFS analysis of the sample. With plenty of reliable sample data points available during fitting, the overall quality of the EXAFS fit can increase. A fit using scattering paths representing the sample environment well will increase in quality; however, a fit based on poorly representative scattering paths will suffer. Accordingly, should a set of scattering paths continue to produce reliable fits with additional higher k-range datasets, the credibility of those paths increases.

Using the same scattering paths as the initial 0.25 MoO_x/Fe_2O_3 EXAFS fits, a reliable fit to Mo_3O_9 is generated from the sample measured for a longer duration (Figure 3.59). The calculated fitting parameters indicate strong fit reliability, with an overall R-factor of 0.018 (Table 3.11). Encouragingly, mean-squared disorder values for the Mo−O scattering paths are lower than for the QEXAFS-measured sample, indicating that the Mo_3O_9 distances correlate with the sample to a greater degree with greater data quality.

From both sets of EXAFS fits, it is clear that a model of Mo_3O_9 reliably represents the actual surface structure of the catalyst. In particular, quality EXAFS fits are obtained using coordination numbers from the ring structure of Mo_3O_9, greatly supporting the suggestion that MoO_x at the surface adopts an effectively cyclic structure. Crucially, the Mo−Mo scattering paths correspond well to the underlying data in the fit: this is highly promising, considering that such Mo−Mo scattering paths have never before been considered for MoO_x/Fe_2O_3. Examined in concert with the earlier STM images, which displayed triangular arrangements of Mo cations (where anions were not visible), the EXAFS data significantly enhance the validity of a suggested Mo_3O_9 structure at the surface of MoO_x. It is worth remembering, however, that while EXAFS analysis can yield promising evidence for a structure, absolute determination of a structure cannot be achieved by EXAFS alone. Further experimentation is required to more fully understand whether the surface does indeed consist of Mo_3O_9 units, or whether a mixture of molybdenum-containing species is present across the surface. Additional imaging techniques, either through more detailed STM or HR-TEM, warrant inclusion in future studies.

At this juncture, a discussion of the XANES features of the sample is pertinent, with a particular focus on the similarity of the sample to molybdenum references (Figure 3.54).

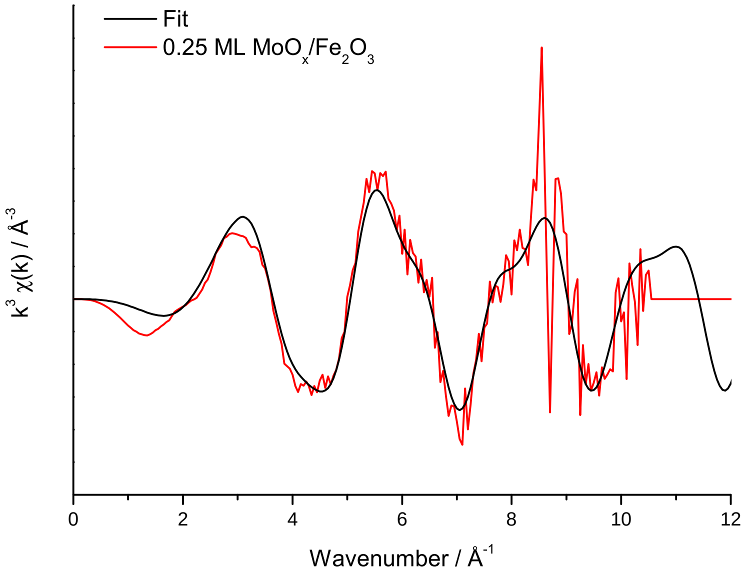

Figure 3.57: k_3 weighted data from 0.25 ML MoO_x/Fe_2O_3 measured in QEXAFS mode.

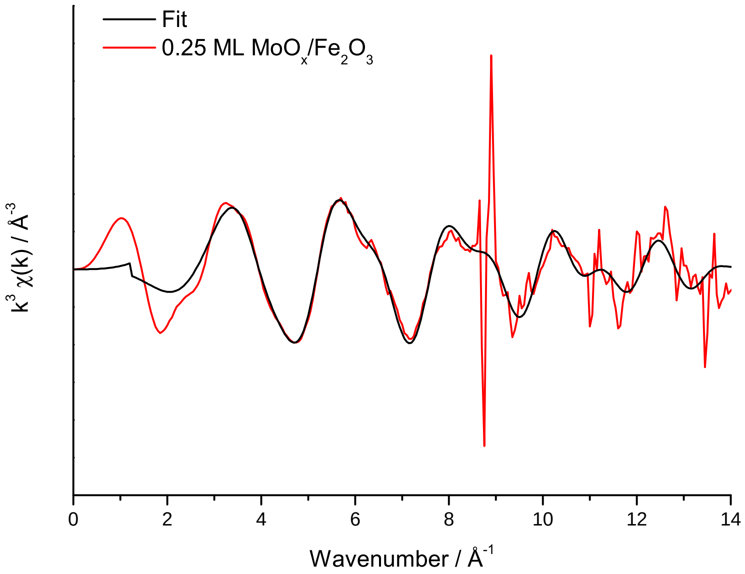

Figure 3.58: k_3 weighted data from 0.25 ML MoO_x/Fe_2O_3 with extended measurement duration.

Table 3.11: Calculated EXAFS fitting parameters for 0.25 ML MoO_x/Fe_2O_3 (extended measurement) calcined to 500°C. Preset fitting parameters: $S_0^2 = 0.82$ as calculated from the MoO_3 standard; range $3 > k > 13.5$, $1 > R > 3.5$; no. of independent points = 16.

Abs - Sc	N	R/Å	$2\sigma^2$ / Å^2	E_f/eV	R-factor
Mo−O (i)	2	1.74	0.003		
Mo−O (ii)	2	2.01	0.001		
Mo−Mo	2	3.35	0.019	5.526	0.018
Mo−Fe (i)	1	2.80	0.011		
Mo−Fe (ii)	2	3.03	0.005		

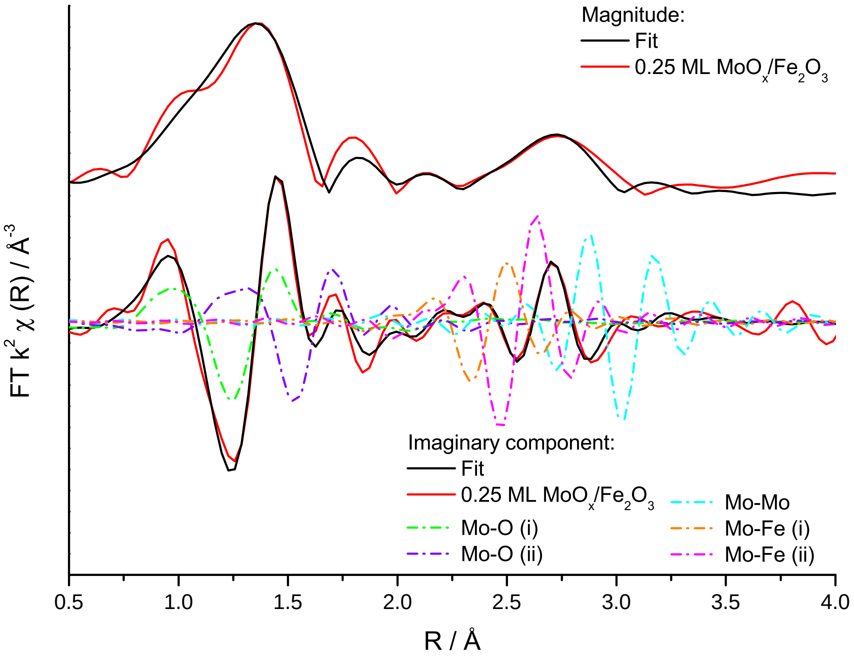

Figure 3.59: Magnitude and imaginary component of the k_3 weighted Fourier transformed fit of the EXAFS data of 0.25 ML MoO_x/Fe_2O_3 from longer duration measurement. Individual scattering paths are displayed in the imaginary component.

A perfunctory examination of the XANES features in relation to the fitting coordination numbers might induce the opinion that there is a mismatch between the XANES evidence and the coordination numbers: i.e. that, since the sample resembles MoO_3 by XANES, the coordination numbers for the Mo−O paths must be three apiece. This view would be at best unsubstantiated and at worst plainly mistaken. While MoO_3 is commonly referred to as octahedral, its true structure belies this epithet. In actuality, its structure is profoundly distorted, as manifested by its strong pre-edge feature. An octahedral structure is centrosymmetric, and thus produces no pre-edge. Since strong pre-edge features are seen for 0.25 ML MoO_x/Fe_2O_3 and MoO_3, they are patently not octahedral (see Chapter 1, Section 1.6 for further discussion). Hence, no reliable Mo_3O_9-disqualifying inferences can be drawn from the resemblance of 0.25 ML to MoO_3 in XANES spectra.

3.6 Conclusions

The primary purpose of the studies reported in this chapter was to examine the possibility of incorporating alternative metal oxides into the shell-core structure developed for MoO_x/Fe_2O_3 catalysts: vanadium oxide was selected as the alternative of choice. It has been soundly demonstrated that VO_x can be easily adapted into an analogous shell-core catalyst, forming monolayer VO_x/Fe_2O_3 catalysts comparable to MoO_x/Fe_2O_3. These catalysts are effective methanol selective oxidation catalysts, producing high quantities of formaldehyde in methanol TPD and during reaction with methanol under oxygen: this is the principal indicator of successful shell-core segregation. The quantity of vanadium present in these catalysts can be carefully controlled in a similar way to MoO_x/Fe_2O_3 catalysts, through careful control of the ratio of vanadium precursor to solvent. Similar trends are seen during the calcination of VO_x/Fe_2O_3 catalysts, wherein the fundamental structural changes during VO_x/Fe_2O_3 formation relate well to those of MoO_x/Fe_2O_3. Additionally, the presence of the sandwich layer of $FeVO_4$ has clearly been seen (and mimics that of the $Fe_2(MoO_4)_3$ layer in MoO_x/Fe_2O_3): crucially, its thickness scales linearly with every ML beyond 1 ML, validating the shell-core theory.

With the help of XAS studies, greater understanding of the structures present at the surface of VO_x/Fe_2O_3 catalysts has been obtained. The oxidised catalyst resembles $FeVO_4$, existing as distorted VO_4 tetrahedral units with three V−O−Fe linkages and one terminal V=O bond projecting outwards from the catalyst surface per unit. When reduced with methanol, the VO_x shell appears to resemble octahedral V_2O_3 by XANES, most notably by the disappearance of the strong vanadium pre-edge feature (the presence of the peak indicating a non-centrosymmetric environment). It is possible that VO_6 octahedra are indeed formed, but this would necessitate the modification of additional portions of the catalyst: for example, parts of the Fe_2O_3 support beneath the VO_x shell may be reduced simultaneously. Whether the reduced catalyst is genuinely octahedral, or an alternative centrosymmetric structure cannot be ascertained from the XANES data alone. *In situ* EXAFS analysis would be an excellent answer to this question, but given the soft X-ray energy of the vanadium K-edge, such an experiment would need to be performed at a beamline with experience with soft energy *in situ* measurements.

Given the significant prior corpus available on MoO_x/Fe_2O_3 catalysts, one aspect of MoO_x/Fe_2O_3 catalysts was investigated in greater detail, namely the identity of the active site at the surface. EXAFS fitting is a vital method for determining the structural parameters of a material; thanks to the shell-core structure ensuring that MoO_x exists only at the surface, all EXAFS information pertains to the surface layers. Based on previous studies of similar systems of molybdenum oxides on iron oxide (albeit single crystal iron oxide), the possibility of the existence of a cyclic Mo_3O_9 structure was raised. It was thought that such a cyclic structure would form in instances of Mo scarcity, e.g. when less than one monolayer of MoO_x is present at the surface. Consequently, XAS measurements of sub-ML MoO_x/Fe_2O_3 catalysts were performed, initially with a standard QEXAFS collection mode and subsequently with a longer duration measurement. In both cases, EXAFS fitting using a model Mo_3O_9 system produced high quality fits. EXAFS as a technique is unable to definitively guarantee that a structure is what a fit indicates it to be; however, in concert with the earlier STM imaging of suspected Mo_3O_9, the EXAFS fitting bolsters the credibility of the proposed Mo_3O_9 structure at the surface.

The shell-core model has been proven to be valid for MoO_x and VO_x/Fe_2O_3 catalysts, but significant discrepancies have been found when attempting to incorporate Nb into a counterpart NbO_x/Fe_2O_3 shell-core catalyst (an overview schematic of MoO_x, VO_x and NbO_x shell-core catalysts is provided below in Figure 3.60). The fundamental methanol oxidation selectivity of Nb_2O_5—and hence NbO_x—is not to formaldehyde, but to DME: importantly, CO_2 is not selectively formed. This notwithstanding, significant CO_2 production is evident by TPD for NbO_x/Fe_2O_3—irrespective of NbO_x ML coverage—whereas this is not the case for MoO_x or VO_x. While some selective products are seen, the presence of CO_2 in TPD denotes an improperly-formed shell-core catalyst, as combustion is elicited only when the core Fe_2O_3 is able to directly participate in catalysis (and moreover when exposed Fe sites are plentiful, as CO_2 production requires the interaction of neighbouring Fe sites). The trends found by TPD are mirrored by PFR studies of NbO_x/Fe_2O_3, which generates CO_2 throughout the reaction and not solely at high temperatures. With some selective products formed alongside significant quantities of combustion products, the strong implication is that, while the NbO_x is at the surface, the shell has failed to completely cover the haematite core. Measurements of NbO_x/Fe_2O_3 catalysts by Raman spectroscopy are fruitless, both when analysing the fully-calcined catalyst and a range of samples from different points during catalyst formation. This is ascribed to a failure of the sample to proceed beyond its post-drying stage to form the intended catalyst. The rationale for this lies in the Tamman temperature, the temperature at which diffusion in solid materials becomes significant. Calcination at 500°C is sufficient for MoO_x/Fe_2O_3 and VO_x/Fe_2O_3, as 500°C is well in excess of their respective Tamman temperatures, enabling diffusion of the solid metal oxides and the ensuing spreading of the shell material. The Tamman temperature of NbO_x, however, is over 100°C greater than 500°C, hence no significant diffusion of the solid NbO_x can occur during normal calcination: consequently, the NbO_x is unable to diffuse across the surface to effectively isolate the haematite, producing the non-selective catalytic behaviour witnessed by TPD.

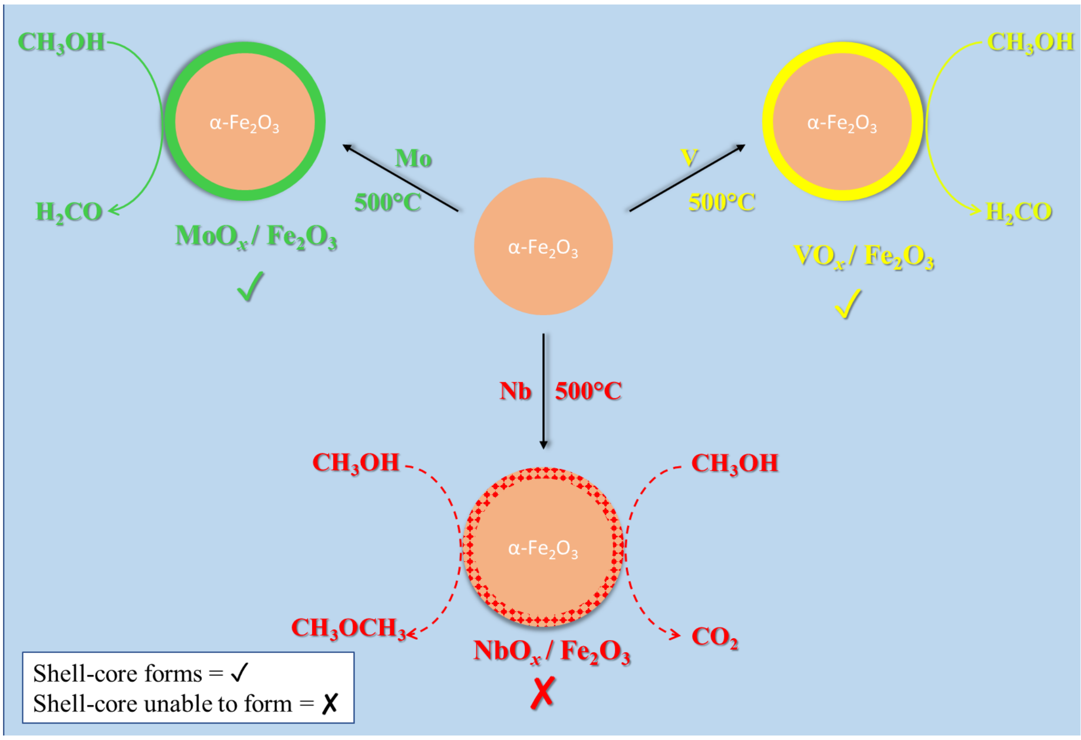

Figure 3.60: A graphical abstract of the catalytic properties of MoO_x/Fe_2O_3, VO_x/Fe_2O_3 and NbO_x/Fe_2O_3 catalysts, emphasising the markedly poorer performance of NbO_x/Fe_2O_3 due to its inability to fully isolate the core moiety.

Future work

Significant progress has been made in expanding the scope of metal oxide shell-haematite core selective oxidation catalysts, but further advances can yet be made, in both the existing catalysts and entirely novel systems. Further structural understanding of MoO_x and VO_x/Fe_2O_3 catalysts, and in particular the changes occurring during reaction, would greatly benefit the field of methanol oxidation catalysis. This could be achieved by further, more specialised XAS investigations, though as mentioned before, *in situ* analysis of vanadium can be problematic. While the formation processes occurring during calcination can be tracked relatively easily, little is known about the rationale behind the formation process: e.g. why does a body of crystalline metal oxide form at an intermediate temperature, only to disappear when the shell is properly formed? *In situ* measurements with imaging techniques like TEM would be deeply worthwhile in helping to answer such queries. In terms of new shell-core systems, it is now proposed that the Tamman temperature of the metal oxide in question is highly relevant to the success of a prospective shell-core catalyst. If a metal oxide intended for use as a shell component possesses a Tamman temperature considerably higher than 500°C, its prospects are limited. Nevertheless, several metal oxides have Tamman temperatures only slightly higher than the typical calcination temperatures (e.g. WO_3, approximately 590°C): these represent interesting future candidates for study, either for attempted incorporation into shell-core catalysts similar to MoO_x and VO_x/Fe_2O_3, or for inclusion in a mixed metal oxide shell layer. WO_3 in particular would be an interesting test case. In methanol oxidation, WO_3 is selective to formaldehyde; however, it converts methanol at markedly higher temperatures than MoO_x ($>$ 350°C vs. $>$180°C). Were it possible to combine the properties of MoO_x and WO_x in a single mixed shell-layer, greater overall yields of formaldehyde might be achievable. This may, however, be a step too far. Given the vastly different diffusion properties as a function of temperature between different metal oxides, it is far from certain that a mixed metal oxide shell layer is attainable: indeed, it is quite possible that two stacked heterogeneous layers of shell metal oxides would be obtained instead. Nonetheless, such systems may warrant wider exploration.

References

(1) M. Bowker, R. Holroyd, M. House, R. Bracey, C. Bamroongwongdee, M. Shannon and A. Carley, *Topics in Catalysis*, 2008, **48**, 158–165.

(2) C. Brookes, P. P. Wells, N. Dimitratos, W. Jones, E. K. Gibson, D. J. Morgan, G. Cibin, C. Nicklin, D. Mora-Fonz, D. O. Scanlon, C. R. A. Catlow and M. Bowker, *The Journal of Physical Chemistry C*, 2014, **118**, 26155–26161.

(3) C. Brookes, P. P. Wells, G. Cibin, N. Dimitratos, W. Jones, D. J. Morgan and M. Bowker, *ACS Catalysis*, 2014, **4**, 243–250.

(4) K. Routray, W. Zhou, C. J. Kiely, W. Grünert and I. E. Wachs, *Journal of Catalysis*, 2010, **275**, 84–98.

(5) M. Ai, *Journal of Catalysis*, 1978, **54**, 426–435.

(6) P. Hellier, P. P. Wells, D. Gianolio and M. Bowker, *Topics in Catalysis*, 2018, **61**, 357–364.

(7) G. Silversmit, D. Depla, H. Poelman, G. B. Marin and R. D. Gryse, *Journal of Electron Spectroscopy and Related Phenomena*, 2004, **135**, 167–175.

(8) S. Pak, C. E. Smith, M. P. Rosynek and J. H. Lunsford, *Journal of Catalysis*, 1997, **165**, 73–79.

(9) J. E. Sambeth, M. A. Centeno, A. Paúl, L. E. Briand, H. J. Thomas and J. A. Odriozola, *Journal of Molecular Catalysis A: Chemical*, 2000, **161**, 89–97.

(10) A. Š. Vuk, B. Orel, G. Dražič, F. Decker and P. Colomban, *Journal of Sol-Gel Science and Technology*, 2002, **23**, 165–181.

(11) R. Baddour-Hadjean, M. B. Smirnov, V. Y. Kazimirov, K. S. Smirnov and J.-P. Pereira-Ramos, *Journal of Raman Spectroscopy*, 2015, **46**, 406–412.

(12) J. Wong, F. Lytle, R. Messmer and D. Maylotte, *Physical Review B*, 1984, **30**, 5596.

(13) B. Robertson and E. Kostiner, *Journal of Solid State Chemistry*, 1972, **4**, 29–37.

(14) Z. Feng, Q. Ma, J. Lu, H. Feng, J. Elam, P. C. Stair and M. J. Bedzyk, *RSC Advances*, 2015, **5**, 103834–103840.

(15) S. Surnev, M. Ramsey and F. Netzer, *Progress in Surface Science*, 2003, **73**, 117–165.

(16) I. Wachs, J.-M. Jehng, G. Deo, H. Hu and N. Arora, *Catalysis Today*, 1996, **28**, Catalytic Properties of Niobium Materials and Related Subjects (Proceedings of the Second International Symposium on Niobium Compounds), 199–205.

(17) K. Tanabe, *Catalysis Today*, 1990, **8**, 1–11.

(18) B. Li, M. Gu, Z. Nie, X. Wei, C. Wang, V. Sprenkle and W. Wang, *Nano Letters*, 2014, **14**, 158–165.

(19) P. Hellier, P. P. Wells and M. Bowker, *Chinese Journal of Catalysis*, 2019, **40**, 1686–1692.

(20) J. M. Jehng and I. E. Wachs, *Chemistry of Materials*, 1991, **3**, 100–107.

(21) B. X. Huang, K. Wang, J. S. Church and Y.-S. Li, *Electrochimica Acta*, 1999, **44**, 2571–2577.

(22) C. Brookes, M. Bowker, E. K. Gibson, D. Gianolio, K. M. H. Mohammed, S. Parry, S. M. Rogers, I. P. Silverwood and P. P. Wells, *Catalysis Science & Technology*, 2016, **6**, 722–730.

(23) K. Chen, A. T. Bell and E. Iglesia, *The Journal of Physical Chemistry B*, 2000, **104**, 1292–1299.

(24) I. E. Wachs, Y. Chen, J.-M. Jehng, L. E. Briand and T. Tanaka, *Catalysis Today*, 2003, **78**, 4th International Symposium on Group Five Compounds Bicentennial Meeting, 13–24.

(25) C. Bamroongwongdee, M. Bowker, A. F. Carley, P. R. Davies, R. J. Davies and D. Edwards, *Faraday Discussions*, 2013, **162**, 201–212.

(26) J. I. Gu, J. Lee, C. K. Rhee and Y. Sohn, *Applied Surface Science*, 2019, **469**, 348–356.

(27) S. M. Shugurov, A. I. Panin, S. I. Lopatin and K. A. Emelyanova, *Rapid Communications in Mass Spectrometry*, 2015, **29**, 1427–1436.

(28) M. Xue, M. Nakayama, P. Liu and M. G. White, *The Journal of Physical Chemistry C*, 2017, **121**, 22234–22247.

Chapter 4

Surface area enhancements through haematite core modification

4.1 Introduction

While the previous chapter focussed on the shell layers of metal oxide shell-haematite core catalysts and the alterations made thereunto to vary the resulting catalytic properties, this chapter addresses the modifications which can be made to the core of the catalyst to influence catalysis. Specifically, the fundamental core modification of interest in this chapter is the incorporation of varying proportions of aluminium dopants in haematite. The inclusion of Al dopants in haematite, if substituted isomorphically throughout the whole structure, can greatly boost surface area.

The effects of doping haematite with small quantities of aluminium have been explored previously, primarily from a mineralogical perspective, although more recently from the viewpoint of MoO_x/Fe_2O_3 catalysts also.[1–5] Al-substitution into Fe_2O_3 is ubiquitous in terrestrial sources of haematite, but importantly the Al incorporates without significantly disrupting the overall haematite structure.[6] There are, however, small changes in structural properties arising from the presence of Al throughout the haematite structure: typically, structural lattice parameters decrease as a function of the lower atomic displacement of Al in comparison to Fe (0.535 Å and 0.645 Å respectively). This reduction in lattice spacing and the concomitant altering of electrostatic interactions induces a degree of lattice strain throughout the structure, encouraging the growth of smaller crystallites: this in turn affords a greater value of specific surface area.[5] Since catalytic activity depends on surface area, increases in surface area are hugely attractive to the catalysis chemist.

Initial studies have been conducted into the use of Al-doped haematites as support materials in shell-core selective oxidation catalysts.[5] It was found that the incorporation of 5 wt% Al into Fe_2O_3 doubled the surface area of the post-calcination material. Subsequently, after adding MoO_x shell layers to the Al-doped Fe_2O_3 and assessing the reactivity of the resulting catalysts, it was determined that the greater surface area of the catalyst lowered the effective operating temperature of the catalyst by approximately 20°C. This was a significant result, but one which was not pursued further at the time: this chapter continues the research into Al-doped haematites as core materials in shell-core oxidation catalysts.

With the knowledge gained from the preliminary studies in mind, four main areas of enquiry were identified:

(i) Can quantities of Al greater than 5 wt% be added to haematite without compromising structural composition or inducing phase separation?

(ii) Does surface area increase linearly with Al content, and will an upper bound be reached?

(iii) Is the catalytic behaviour of haematite influenced by increasing proportions of Al dopants?

(iv) How are the catalytic selectivities of MoO_x shell-core catalysts impacted through the use of Al-doped haematite core moieties?

There must logically be an upper limit to Al loading, beyond which the normal haematite structure is untenable: one of the primary objectives is to assess how much Al can be added before this limit is reached. It is also vital to confirm that further increases in specific surface area are achievable without drastically modifying the chemical behaviour of the haematite. It was thought possible that a compromise might ultimately be necessary, for example between boosting surface area and minimising undesirable structural or catalytic disruption; however, the potential returns—i.e. more active catalysts—warranted the effort invested.

4.2 Experimental

Al-doped haematite samples were prepared by co-precipitation of aluminium nitrate and iron nitrate, after which samples were dried and then calcined at 500°C for 24 hours.

MoO_x/Al-doped Fe_2O_3 catalysts were prepared analogously to MoO_x/Fe_2O_3 and VO_x/Fe_2O_3 by incipient wetness impregnation. It is essential to consider the additional surface area present in Al-doped Fe_2O_3 before synthesis, as the method used to calculate the quantity and concentration of Mo precursor must be adjusted to account for the greater absolute quantity of Mo required to produce the same relative ML coverage.

The characterisation methods employed to analyse Al-doped haematite catalysts were identical to those used in Chapter 3, with the only significant exception being the beamline used to gather Al XAS data. B18 at Diamond Light Source is unable to measure edges softer than 2.1 keV, precluding its use for Al XAS measurements (K-edge 1.5596 keV); instead, the PHOENIX beamline at the Swiss Light Source was used to gather Al K-edge XAS data. PHOENIX possesses two measurement ranges, namely 0.8 - 8.0 keV and 0.4 - 2.0 keV, which are ideally suited to measurements with tender X-rays.

4.3 High Surface Area Fe_2O_3

At this juncture, it is useful to detail the nomenclature used throughout this chapter for these materials. Since Al-doping boosts specific surface area, Al-doped samples of Fe_2O_3 are known as High Surface Area (HSA) Fe_2O_3: the weight proportion of Al in a sample is denoted in percentage terms, e.g. 5 wt% Al-doped Fe_2O_3 is labelled 5% HSA Fe_2O_3.

4.3.1 Initial characterisation

It had been found previously that post-calcination surface area could almost be doubled through the addition of 5 wt% Al to a sample of Fe_2O_3, without incurring any detrimental effects on reactivity, either when used *per se* or as a core support for a MoO_x shell. The obvious first experiment therefore was to assess whether further surface area enhancements were obtainable from greater quantities of Al in Fe_2O_3. To that end, several HSA Fe_2O_3 samples were prepared over a series of stages. Initially, a 10% HSA Fe_2O_3 sample was prepared alongside a fresh sample of 5% HSA Fe_2O_3, and analysed by BET and XRD. Having found 10% HSA to be attainable, two further samples were prepared, viz. 15 and 20% HSA Fe_2O_3, and similarly analysed. A clear trend is visible in surface area as a function of Al loading (Table 4.1), while no structural changes were perceptible by XRD (Figure 4.1): these were corroborated by further batches of HSA Fe_2O_3 materials.

The observed trend in surface area is highly encouraging. Considerable further gains in surface area can be achieved with greater proportions of Al dopants in Fe_2O_3, reaching a zenith at 98.3 $m^2\,g^{-1}$, almost a fivefold increase on un-doped post-calcination Fe_2O_3.

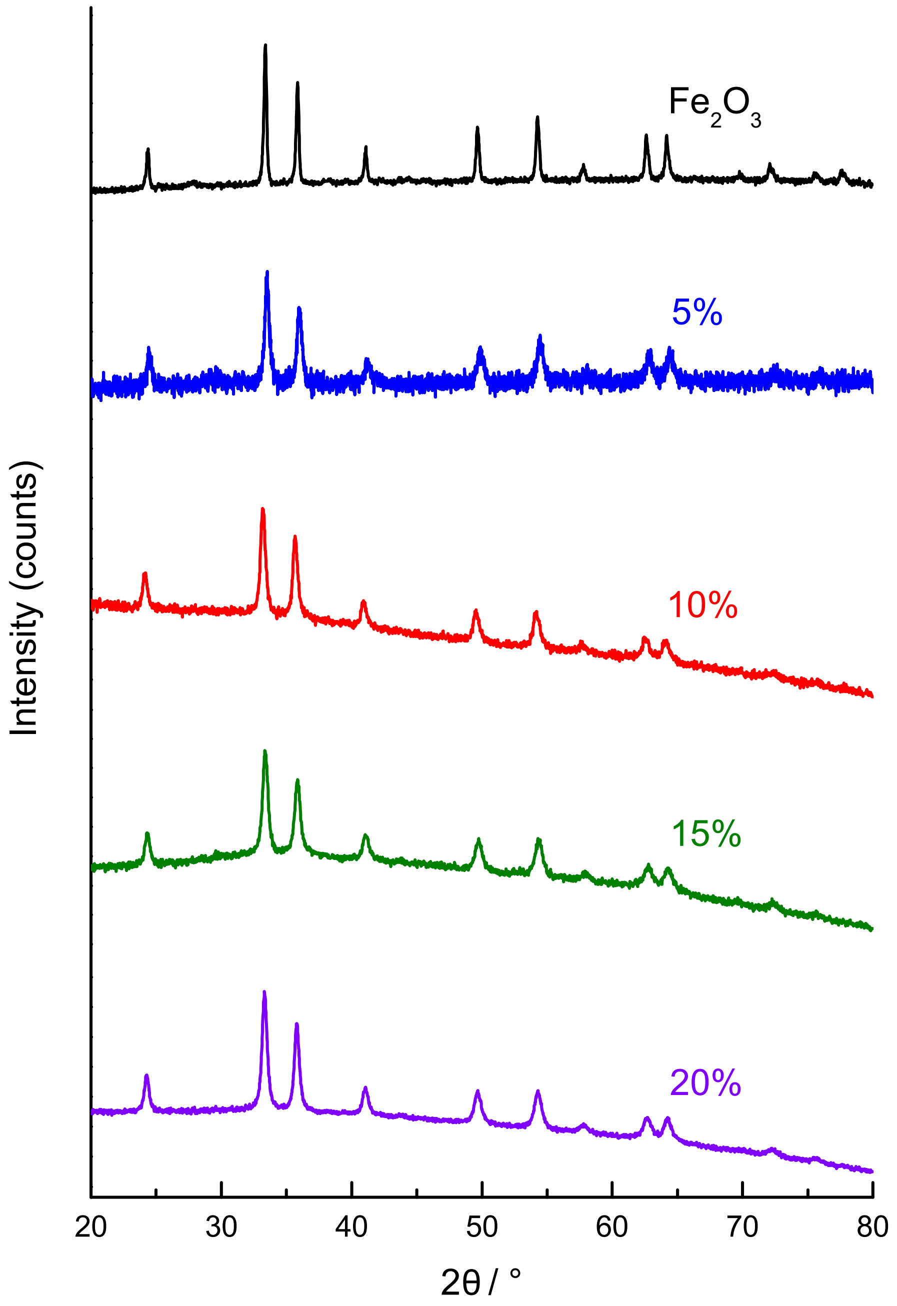

Figure 4.1: A comparison of XRD patterns for 5%, 10%, 15%, 20% HSA Fe_2O_3 with a pristine (i.e. 0% Al) Fe_2O_3 reference.

Table 4.1: A comparison of BET-derived specific surface area values as a function of Al loading in Fe_2O_3. Note: 0 wt% Fe_2O_3 is the standard Fe_2O_3 support used to produce shell-core catalysts, whose specific surface area was at greatest 22.0 $m^2\,g^{-1}$.

Al wt%	Specific surface area ($m^2\,g^{-1}$)
0	22.0
5	46.0
10	70.7
15	98.3
20	88.6

It was noted in subsequent batches of HSA Fe_2O_3 that the specific surface area values obtained for 15% and 20% HSA Fe_2O_3 varied within a region of 90 $m^2\,g^{-1}$ ± 10%, with 15% always possessing the greatest values (the 98.3 $m^2\,g^{-1}$ value being the highest recorded). This behaviour suggests that a plateau is reached by 15 wt% Al, after which no further significant increases are achieved with greater quantities of Al. The variations in the surface area of subsequent batches can be attributed to experimental differences between successive coprecipitations.

Having determined that yet greater surface area increases are attainable with quantities of Al greater than 5 wt%, it is essential to ensure that these gains are not obtained at the expense of structural homogeneity or speciation within the Fe_2O_3. Comparing the XRD data obtained from each HSA catalyst against a pristine Fe_2O_3 standard reveals no changes in peak distribution between pristine and Al-doped Fe_2O_3, although small differences in peak position and peak width are seen. According to Bragg's law, when the d-spacing of a material is reduced, its diffraction peaks will shift slightly to higher angles of 2θ. Since it is believed that the introduction of Al into the Fe_2O_3 structure reduces d-spacing by causing lattice strain, small increases in peak angles should be observed: this is indeed the case. The haematite peaks are shifted slightly higher in angle, and are notably broadened compared to pristine Fe_2O_3. This broadening is attributed to the smaller particle size and constrained unit cell growth throughout the Al-doped Fe_2O_3 structures. Considering the XRD patterns together, the structural differences between pristine Fe_2O_3 and the HSA Fe_2O_3 catalysts are significant enough to appear, but those between different Al loading HSA Fe_2O_3 samples—if present—are not.

The Scherrer equation, which permits the determination of a lower bound on particle size in a material from its XRD pattern, reveals that the lower bound for post-calcination HSA Fe_2O_3 is at its lowest 21.7 nm at 15 wt% Al. In contrast, the equation yields a value

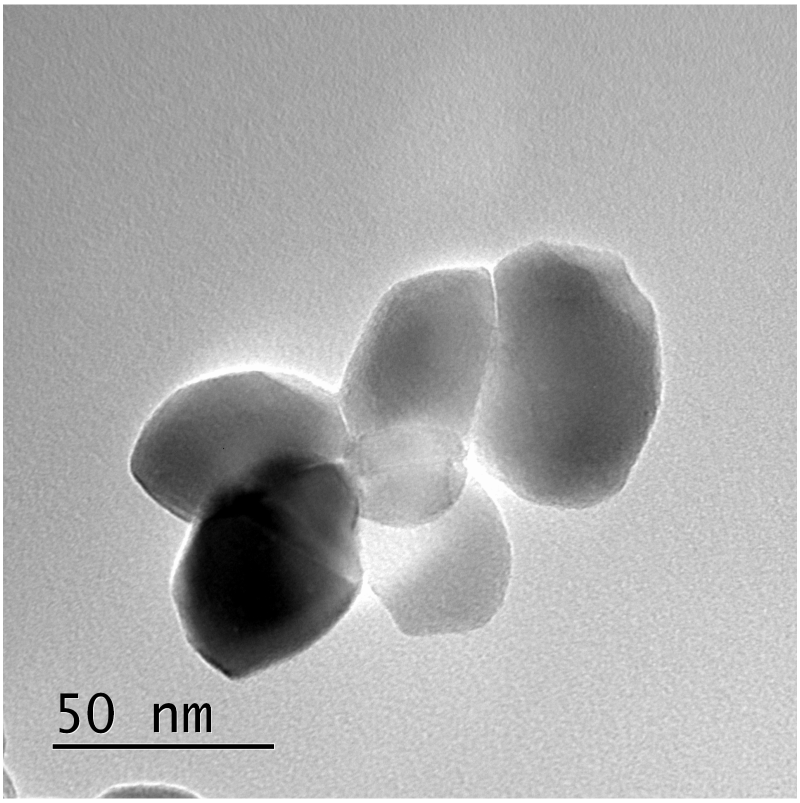

Figure 4.2: An example TEM image of 10% HSA Fe_2O_3: average particle diameter is approximately 45 nm.

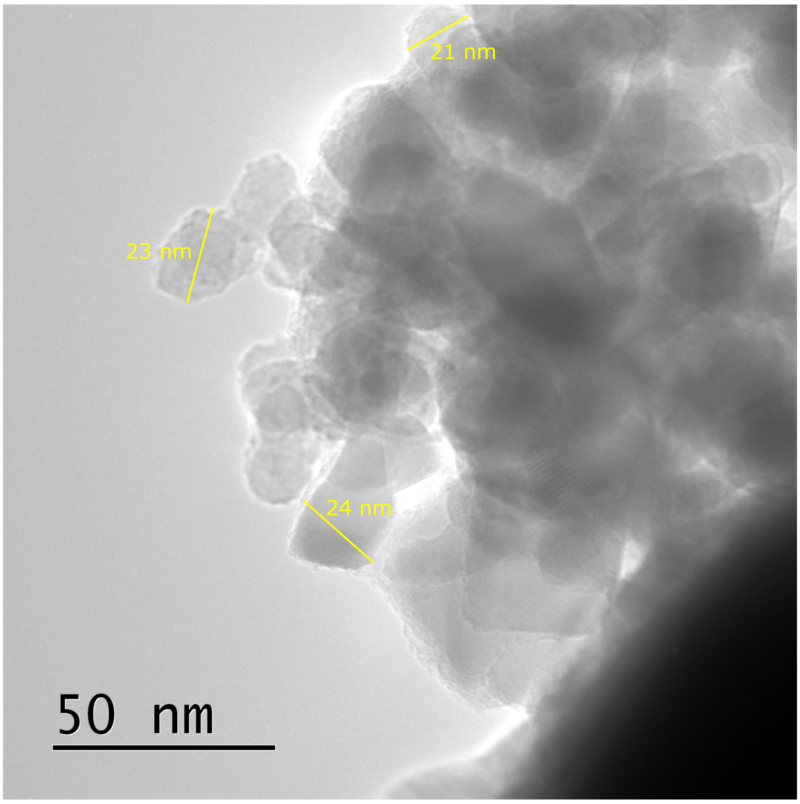

Figure 4.3: An example TEM image of 15% HSA Fe_2O_3. While most of the sample has formed a stack, and hence cannot be imaged successfully, particles at the surface are in focus: three diameters are labelled as examples.

of 66 nm for post-calcination unadulterated Fe_2O_3. This strongly reinforces the assertion that smaller particle sizes have been achieved in Al-doped Fe_2O_3. Crucially, however, one must not forget that the Scherrer equation does not define particle size, but rather delimits it. An additional means to determine particle size is by direct imaging, e.g. by electron microscopy. Two example images are displayed, of 10% and 15% HSA Fe_2O_3 (Figure 4.2 and 4.3), which show particles of approximate diameter 45 - 50 nm and 25 nm respectively, considerably less than the calculated lower bound size for standard Fe_2O_3.

The reduction in particle size as a function of increased Al loading can also be monitored by Raman spectroscopy. To demonstrate this, Raman spectra from all four HSA Fe_2O_3 materials were obtained and compared against a reference spectrum of standard Fe_2O_3 (Figure 4.4). Major disparities were neither anticipated nor observed in the Raman spectra between the different Al loading HSA Fe_2O_3 samples, nor between the four samples together and the standard Fe_2O_3 reference. All of the Raman peaks visible can be attributed to Fe_2O_3, with no evidence of the formation of separate species in the HSA Fe_2O_3 materials from the incorporation of Al. There are, however, noteworthy differences in the positions of the Fe_2O_3 Raman peaks depending on Al content: namely, the peaks are blueshifted to a greater degree with higher quantities of Al present in the Fe_2O_3. This is attributed to two main factors: firstly, from energetic quantum confinement effects caused by smaller particle sizes;[7] and secondly, from the replacement of large numbers of Fe^{3+} cations by smaller Al^{3+} cations, decreasing the separation between cations and therefore boosting the strength of the interconnecting bonds.[3,8] As for surface area, the behaviour beyond 15% diverges from the trend: peaks for the 20% HSA Fe_2O_3 sample are less blueshifted than those for 15% HSA Fe_2O_3. This supports the implication that a plateau is reached by 15% Al, after which further increases in surface area—i.e. by reducing particle size—are not feasible. A full list of the peaks, their assignments and their positions is given below (Table 4.2).

Table 4.2: Haematite Raman peak positions in standard and HSA Fe_2O_3. Peak identity/Mulliken notations have been obtained from literature.[9]

	Raman Shift (cm^{-1})				
Assignment	Fe_2O_3	5% HSA	10% HSA	15% HSA	20% HSA
e_g	405	410	412	413	409
a_{1g}	492	498	501	503	499
e_g	604	609	612	615	612

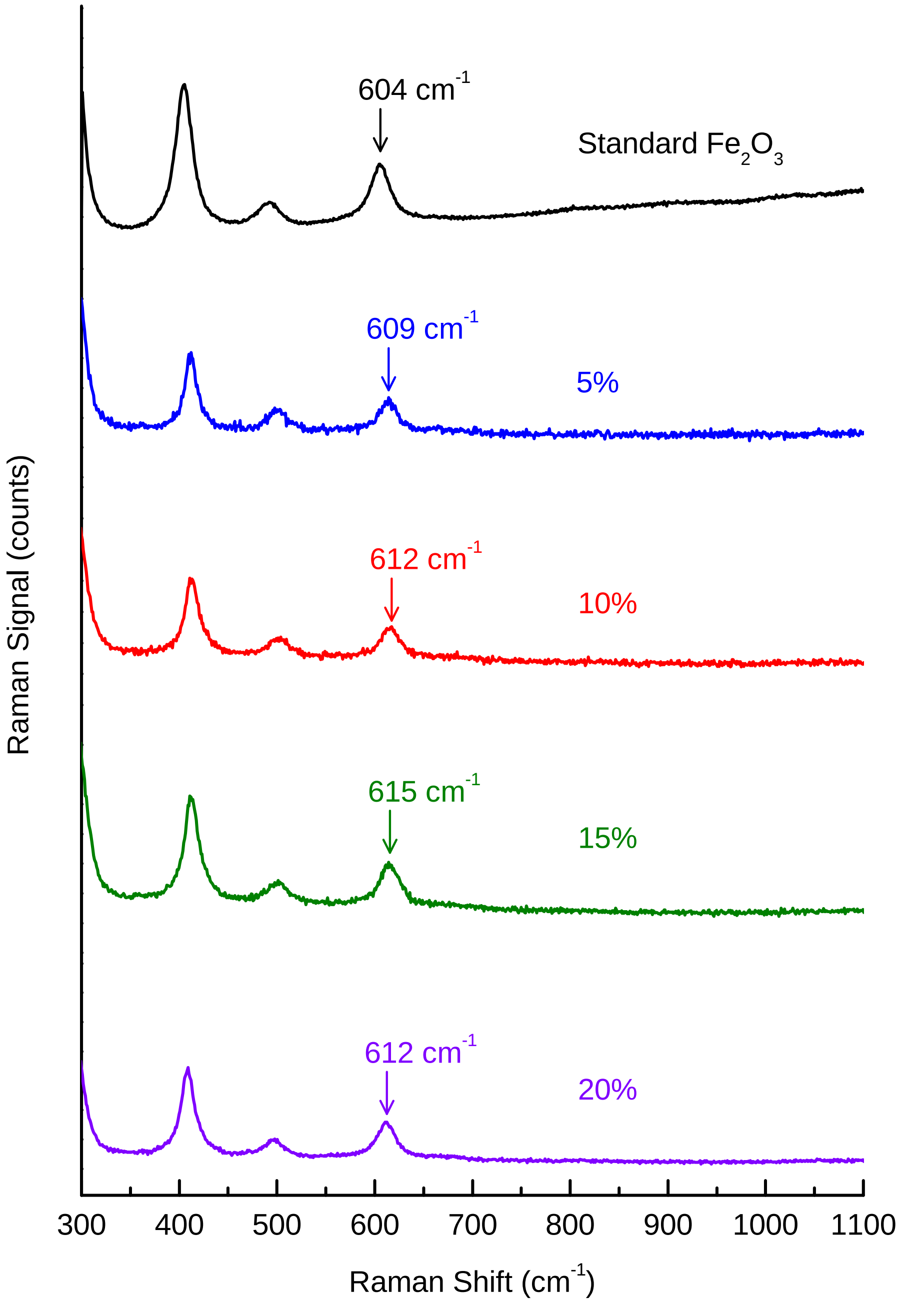

Figure 4.4: A comparison of Raman spectra for 5%, 10%, 15%, 20% HSA Fe_2O_3 with a pristine Fe_2O_3 reference.

4.3.2 Reactivity studies of HSA Fe_2O_3

The lack of any major structural or phase disparities detectable by XRD or TEM between the four loadings of HSA Fe_2O_3, notwithstanding the vastly different surface areas and particle sizes, is a testament to the soundness of Al doping. It is equally important to assess, however, whether the reactivity of haematite is significantly altered by the introduction of Al dopants, and if so, whether the effects of such alterations correspond linearly with the quantity of Al present.

In order to assess shell-core segregation by TPD and similar methods, it is essential that shell and core moieties display fundamentally different reactivities, and thus that the catalytic selectivity of the Fe_2O_3 core be unaffected by Al doping. Ideally, the reactivities of HSA Fe_2O_3 samples would not differ from normal Fe_2O_3. To determine whether this was the case, standard Fe_2O_3 was analysed by methanol TPD (Figure 4.5) along with samples of 5%, 10%, 15% and 20% HSA Fe_2O_3 (Figures 4.6, 4.7, 4.8 and 4.9).

Combustion is the dominant process for all four HSA Fe_2O_3 samples as it is for normal Fe_2O_3. This resemblance of reactivity permits HSA Fe_2O_3 to be used as the support in a MoO_x-shell/HSA Fe_2O_3 shell-core catalyst, as the inferences drawn from TPD regarding shell-core formation would remain valid. While no major modifications to product distribution are seen by TPD, there are significant differences in the peak positions of the HSA Fe_2O_3 samples relative to the standard Fe_2O_3. The zenith of the CO_2 in the TPD of standard Fe_2O_3 lies at approximately 315°C, while the CO_2 peak position for 5% HSA Fe_2O_3 is shifted to higher temperature, occurring at approximately 325°C. This trend appears to continue, with higher Al loadings affording higher temperature CO_2 peaks; these peak positions are tabulated below (Table 4.3).

Table 4.3: CO_2 TPD peak position as a function of Al loading in Fe_2O_3.

Al wt%	Approximate CO_2 TPD peak position (°C)
0	315
5	325
10	335
15	350
20	345

Interestingly, the shift in CO_2 peak position as a function of Al loading effectively mirrors the increase in specific surface area with increasing Al content. The CO_2 peak position for 20% HSA Fe_2O_3 is slightly lower than that of 15% HSA Fe_2O_3, which echoes

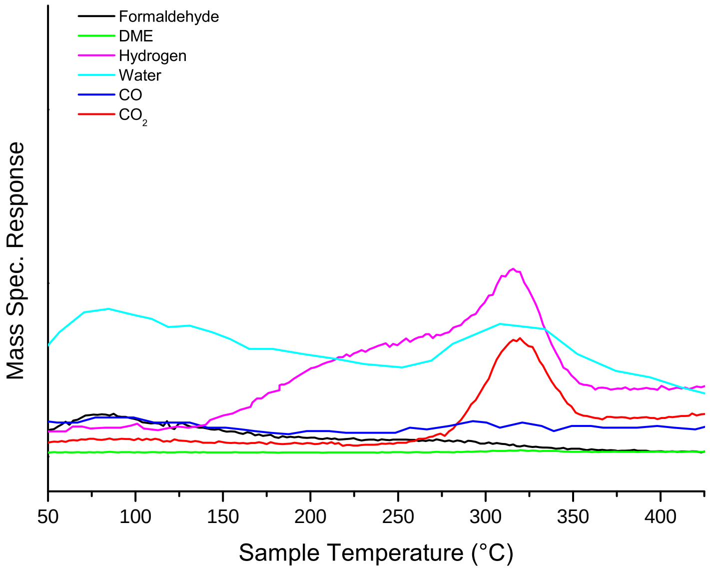

Figure 4.5: TPD data from pristine Fe_2O_3. Gas flow: 30 mL/min He. Sample mass: 200 mg.

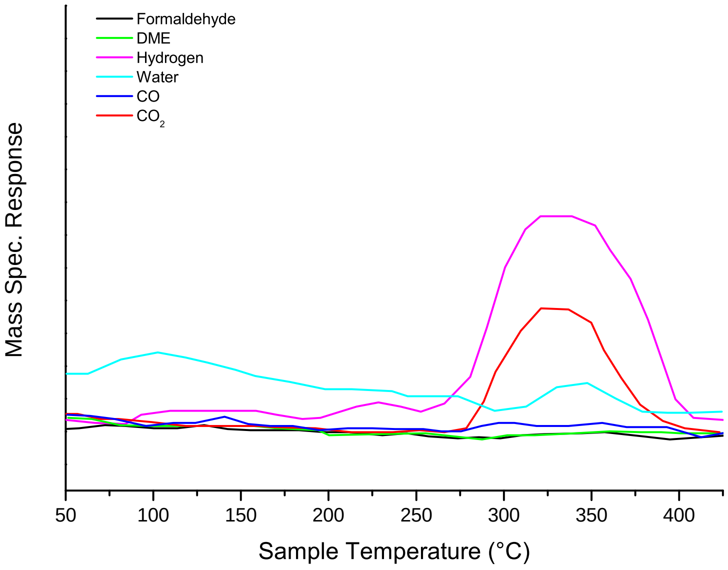

Figure 4.6: TPD data from 5% HSA Fe_2O_3. Gas flow: 30 mL/min He. Sample mass: 200 mg.

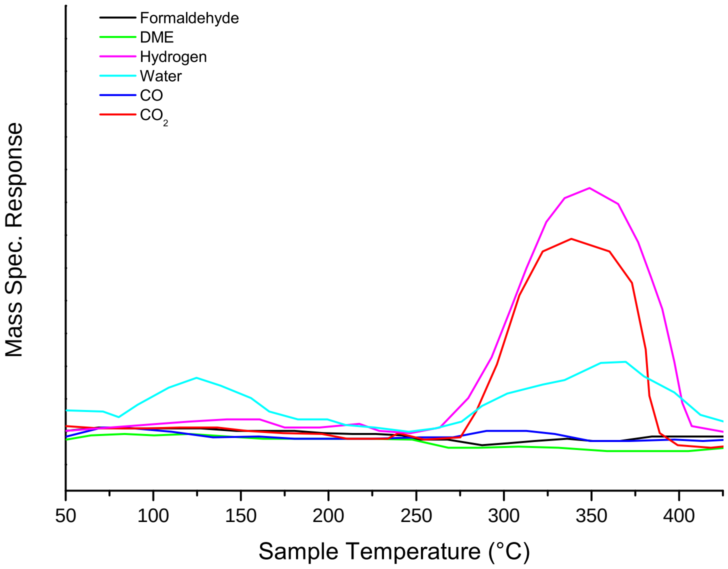

Figure 4.7: TPD data from 10% HSA Fe_2O_3. Gas flow: 30 mL/min He. Sample mass: 200 mg.

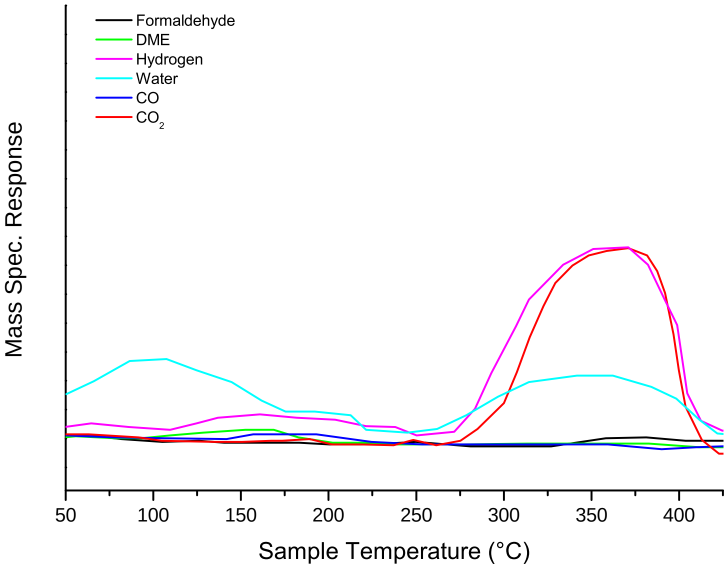

Figure 4.8: TPD data from 15% HSA Fe_2O_3. Gas flow: 30 mL/min He. Sample mass: 200 mg.

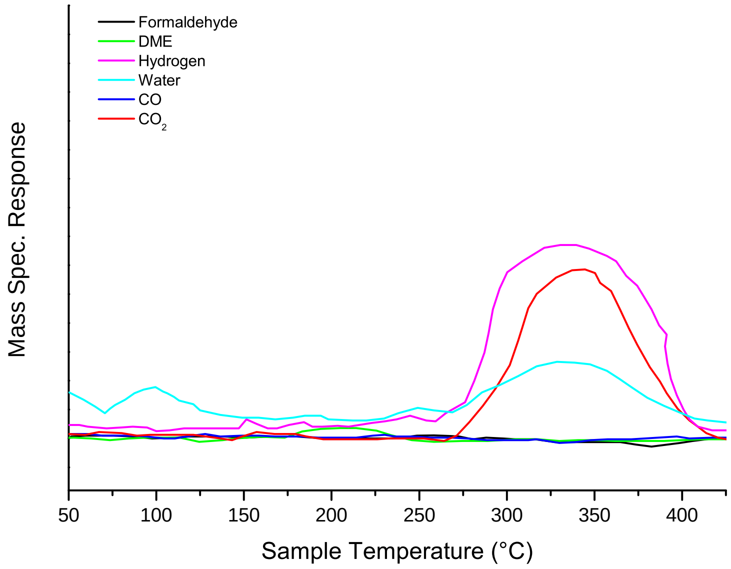

Figure 4.9: TPD data from 20% HSA Fe_2O_3. Gas flow: 30 mL/min He. Sample mass: 200 mg.

the slight reduction in surface area observed for 20% HSA Fe_2O_3 relative to 15% HSA Fe_2O_3. This is to be expected, as specific surface area strongly influences the chemical processes occurring during TPD. Increases in specific surface area arise from the formation of smaller particle sizes in a material; it is this decrease in particle size which increases the CO_2 production temperature during TPD of HSA Fe_2O_3 samples. By reducing particle size, surface free energy is accordingly increased due to the more severe curvature at the surface of a smaller particle. This greater curvature additionally boosts the number of low-coordinate surface sites, which can better stabilise any species adsorbed at the surface. The generation of CO_2 by combustion is known to proceed *via* a bidentate formate intermediate, which adsorbs at the surface. If this intermediate is adsorbed more strongly by interaction with the greater quantity of low-coordinate sites present on smaller particles, then correspondingly greater energy is required to initiate the reaction of formate to CO_2. This larger energy barrier is manifested in TPD by the shift of CO_2 production to higher temperatures.

Another noticeable difference between HSA and standard Fe_2O_3 in TPD is the quantity of CO_2 produced in relation to the hydrogen generated. For unmodified Fe_2O_3, the production of hydrogen outstrips that of CO_2; with each increment of Al added, however, the gap between the quantities of each TPD feature minimises. This implies a greater efficacy of combustion with increasing Al loading: as the temperature at which combustion occurs shifts higher, the efficiency of combustion increases. As was insinuated by the trends observed in specific surface areas and TPD peak positions, comparison of the 15 and 20% HSA Fe_2O_3 TPD analyses further supports the suggestion that an upper bound on beneficial effects is attained at 15%, for the quantity of CO_2 produced relative to the hydrogen decreases, resembling 10% HSA Fe_2O_3 more than 15% HSA Fe_2O_3.

Importantly, the amount of DME produced by each catalyst differs. Alumina, Al_2O_3, is a known dehydrator of methanol, selectively producing DME during reaction with methanol: correspondingly, the appearance of DME in TPD suggests that alumina (or an alumina-like substance) is participating in the reaction process. 5% and 10% HSA Fe_2O_3 do not produce any significant DME, but crucially 15% and 20% HSA Fe_2O_3 do. This signifies that the normal Fe_2O_3 behaviour is disrupted by the levels of Al present, and strongly suggests that Al phase separation has occurred; however, phase separation is not indicated by the XRD patterns, which display only Fe_2O_3 peaks. Accordingly, if alumina phases have indeed formed by 15% and 20%, they must be small, for otherwise they would be observed by XRD.

While TPD is the most important technique for assessing the reactivity of HSA Fe_2O_3, PFR studies can further corroborate the evidence obtained by TPD. Due to the fungibility of the four HSA loadings, as demonstrated by TPD, a PFR study was conducted on only one sample. In view of its status as the sample with greatest specific surface area, 15% HSA Fe_2O_3 was selected for analysis (Figures 4.10 and 4.11).

In terms of selectivity, nothing untoward is revealed by the PFR measurement. CO_2 is the dominant product once methanol conversion has begun in earnest, while CO is a major product until approximately 20% conversion. Importantly, no formaldehyde or DME—i.e. selective products—are seen. This behaviour is strongly reminiscent of normal Fe_2O_3.[10] The significant difference lies not in the mass spectra, but instead in the temperature monitoring. For the duration of each CATLAB experiment, a thermocouple inserted in the catalyst bed continuously reports the actual temperature in the catalyst, alongside the furnace temperature and the planned temperature. The thermal profile chosen for this experiment consists of a constant temperature ramp rate for the duration of mass spectral measurement, but in this instance the thermocouple reports severe disruption to the thermal profile (Figure 4.10). These perturbations appear at the point at which methanol conversion begins to become significant. Below 325°C, their effect on the overall temperature ramp is not overly problematic, and the temperature controller is able to mitigate these exotherms. Above 325°C, however, the exotherms are strong enough to destabilise the temperature controller, causing significant oscillations in temperature and

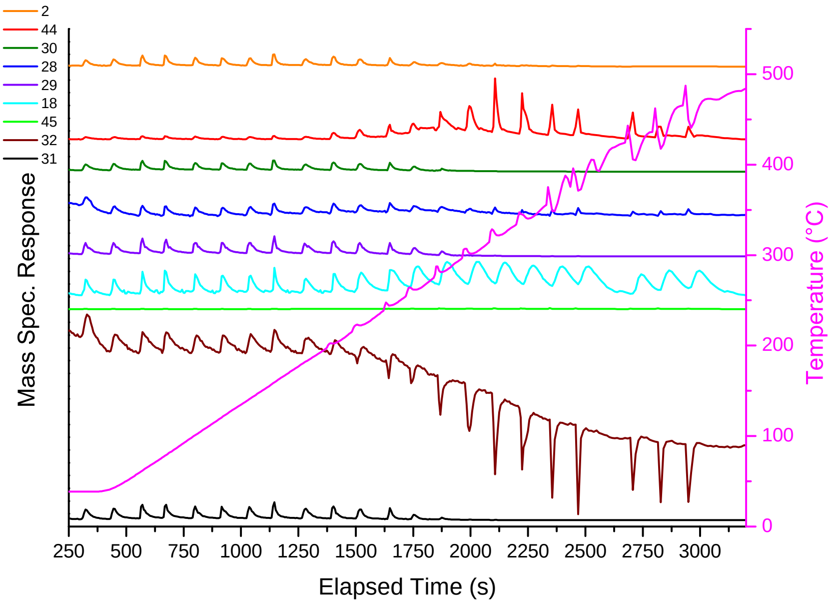

Figure 4.10: Unprocessed PFR mass spectra from 15% HSA Fe_2O_3. Mass 31 corresponds to methanol, mass 44 to CO_2, mass 32 to O_2: consult Table 2.3 for greater detail of spectral overlaps. Note the strong temperature fluctuations upon each injection beyond 250°C induced by strong exotherms from methanol combustion (as a consequence of which injections of methanol could not be made every two minutes, but instead once temperature stability had been regained).

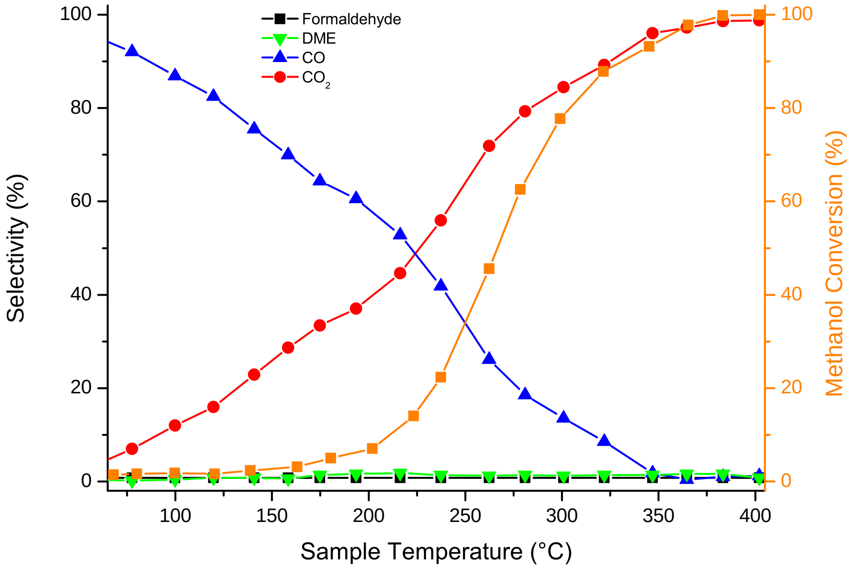

Figure 4.11: Processed PFR data from 15% HSA Fe_2O_3: the data have been processed and all spectral overlaps resolved. Gas flow: 30 mL/min 10% O_2 in He. Sample mass: 200 mg.

necessitating a longer period between injections to permit the oscillations to decay. This loss of control is caused initially by the sudden but large increase in temperature from the combustion exotherm. Since the controller reads not only the current sample temperature but also its rate of change to program the heating and cooling properties of the reactor, the extremely high rate of temperature change at the point of the combustion exotherm prompts the controller to deliver maximum cooling power to the reactor. This cools the sample; however, the response time of the instrument is insufficient to arrest the cooling before overcooling occurs, which initiates the opposite procedure, namely maximum heating followed by overheating. At least five minutes is required for the temperature to regain equilibrium in the absence of any further temperature perturbations. Consequently, the standard frequency of methanol injections—every two minutes—cannot be maintained. This issue has not been seen with standard Fe_2O_3; while Fe_2O_3 does produce visible combustion exotherms, they are markedly less destabilising to the temperature profile in the experiment. Only the HSA Fe_2O_3 samples, and particularly 15% HSA Fe_2O_3, produce the violent exotherms capable of confusing the reactor software. This can be attributed not to the overall energy of the exotherm (as 100% combustion will produce the same energy for pristine Fe_2O_3 and HSA Fe_2O_3), but instead to the rapidity with which the energy is released. Due to their greater surface areas and hence catalytic activities, HSA Fe_2O_3 materials will combust more methanol earlier in the catalyst bed. Since the thermocouple is inserted into the top of the sample—i.e. the beginning of the catalyst bed—a strong exotherm will generate a more pronounced response from the thermocouple (and hence the temperature controller) if generated directly adjacent to it, at the beginning of the bed. In contrast, an exotherm produced more evenly throughout the catalyst bed and not in the vicinity of the thermocouple—as would be the case for less active pristine Fe_2O_3—will not destabilise the temperature profile.

4.4 MoO_x/HSA Fe_2O_3 catalysts

It has been demonstrated that HSA Fe_2O_3 is a viable substitute for normal Fe_2O_3. Enhancements in surface area, and accordingly catalytic activity, are achievable seemingly without detriment. Importantly, however, the studies of reactivity discussed above considered only the catalytic abilities of HSA Fe_2O_3 *per se*; having determined its suitability in this regard, the experimental focus shifted to its use as a core moiety encapsulated by MoO_x, to form a shell-core catalyst of the familiar type.

As with all metal oxide shell-haematite core catalysts, the core component of the resulting catalysts must be adequately sequestered, lest it directly react with and combust methanol. Considerable structural and speciational information is already known for MoO_x/Fe_2O_3 catalysts employing standard Fe_2O_3 as the core material, but little is known of the applicability of HSA Fe_2O_3 as a support for a MoO_x shell. In theory, if the Al occupies Fe spaces in the Fe_2O_3 structure as proposed, then few differences from MoO_x/Fe_2O_3 catalysts are expected with MoO_x/HSA Fe_2O_3 catalysts. Nonetheless, especially at larger Al proportions, the difference in support speciation could impact the ability of the core to support a complete MoO_x shell.

A series of 3 ML MoO_x/HSA Fe_2O_3 catalysts based on 5%, 10%, 15% and 20% HSA Fe_2O_3 was produced by the standard incipient wetness impregnation route (considering the impact of greater surface areas on the monolayer calculations) and calcined at 500°C. In all cases, the HSA Fe_2O_3 supports had previously been calcined at 500°C for long periods: further calcination at 500°C after incipient wetness is therefore unlikely to modify the properties of the HSA Fe_2O_3 any further.

4.4.1 Reactivity studies

TPD measurements have consistently been the most immediately useful for exploring shell-core MoO_x/Fe_2O_3 catalysts, and catalysts using HSA Fe_2O_3 cores instead are no exception. If the shell-core formation process has occurred correctly, formaldehyde will be a major product, and significant CO_2 will not be observed. On the contrary, if CO_2 is seen, then the core remains at least partially exposed at the surface. The degree to which the core is exposed is ascertained by comparing the quantities of selective products and CO_2 from TPD, and considering the strong thermodynamic favourability of combustion over selective oxidation. If little CO_2 is produced alongside significant formaldehyde, for example, this would indicate that only a small portion of the core is exposed, as most of the methanol is being converted to the selective product in spite of its lesser thermodynamic favourability; conversely, if no formaldehyde is produced with the CO_2, then the core is entirely exposed. TPD analysis was performed to compare standard 3 ML MoO_x/Fe_2O_3 (Figure 4.12) with the four HSA catalysts each with a shell of 3 ML MoO_x across their surfaces (Figures 4.13, 4.14, 4.15 and 4.16).

It is clear that, in general, the 3 ML MoO_x/HSA Fe_2O_3 catalysts strongly resemble the 3 ML MoO_x/Fe_2O_3 catalyst in TPD. Formaldehyde is produced in high quantities for all samples, indicating that shell-core formation has been successfully achieved with HSA Fe_2O_3 employed as the core support. There are, however, differences between the

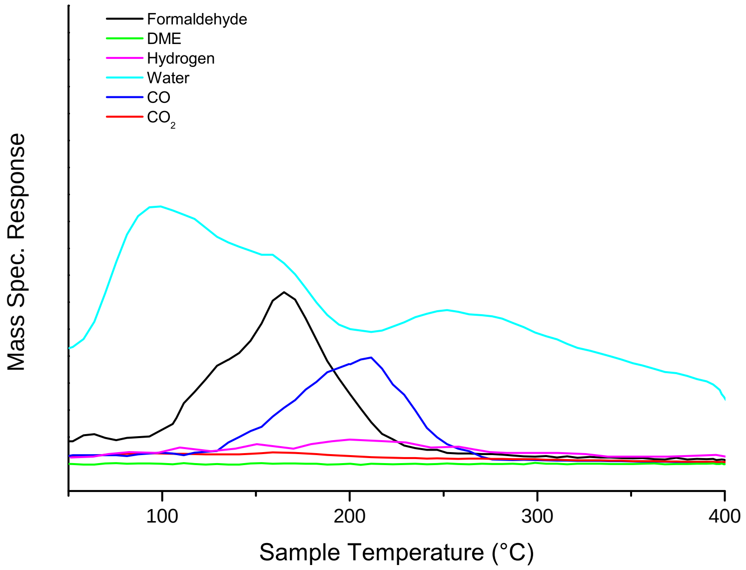

Figure 4.12: TPD data from 3 ML MoO_x/Fe_2O_3.

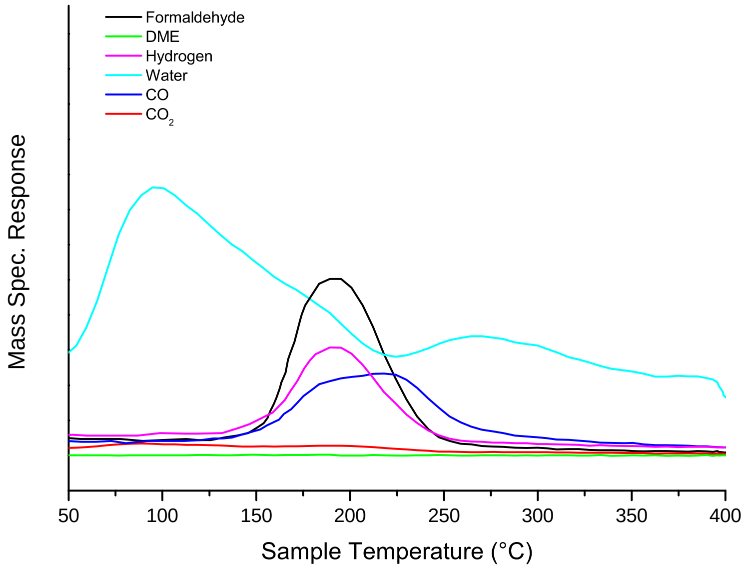

Figure 4.13: TPD data from 3 ML MoO_x/5% HSA Fe_2O_3. Gas flow: 30 mL/min He. Sample mass: 200 mg.

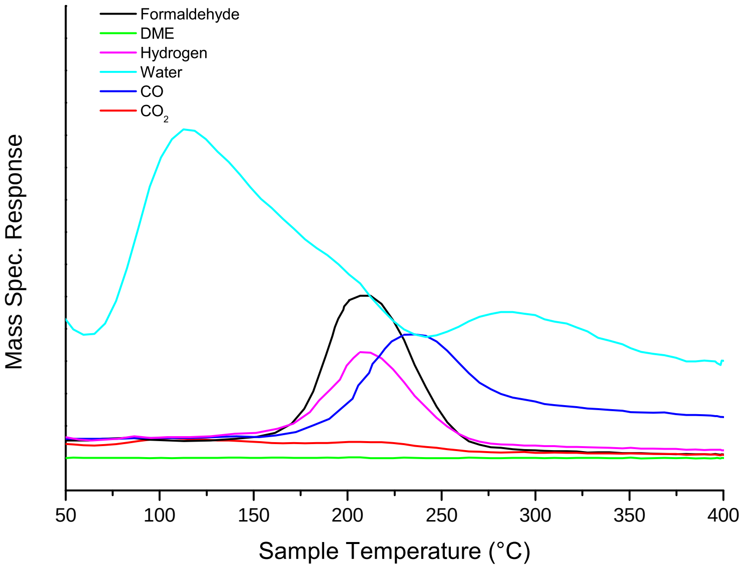

Figure 4.14: TPD data from 3 ML MoO_x/10% HSA Fe_2O_3. Gas flow: 30 mL/min He. Sample mass: 200 mg.

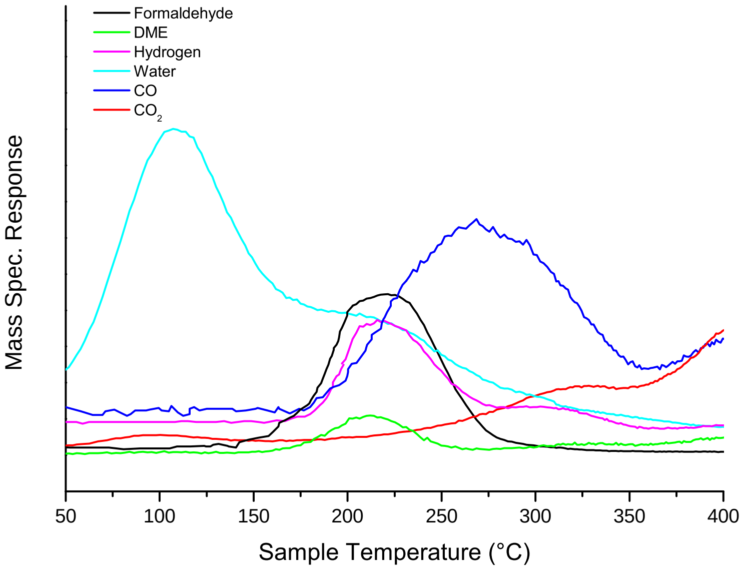

Figure 4.15: TPD data from 3 ML MoO_x/15% HSA Fe_2O_3. Gas flow: 30 mL/min He. Sample mass: 200 mg.

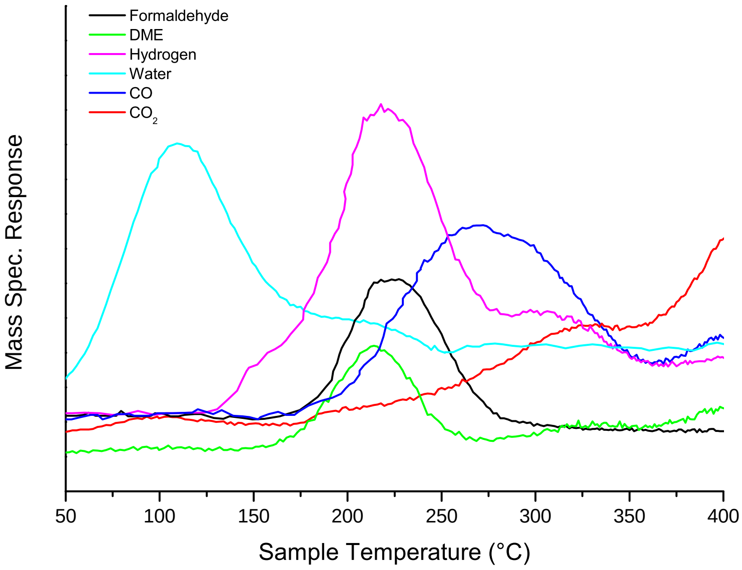

Figure 4.16: TPD data from 3 ML MoO_x/20% HSA Fe_2O_3. Gas flow: 30 mL/min He. Sample mass: 200 mg.

catalysts based on HSA and normal Fe_2O_3, and also significant differences between the different Al loading HSA-based catalysts.

For the 3 ML MoO_x/Fe_2O_3 catalyst, formaldehyde evolution commences at approximately 130°C in significant quantity, reaching its zenith at 160°C. Contrarily, for the catalysts using HSA Fe_2O_3 materials as core supports, the onset of worthwhile formaldehyde production is delayed to approximately 150°C, and moreover, this shift to higher temperature appears to increase with Al loading. This echoes the TPD behaviour demonstrated previously for naked HSA Fe_2O_3 materials, wherein the CO_2 peak from combustion was shifted to higher energy due to a greater energetic barrier from the stronger adsorption of the formate intermediate. For the MoO_x-covered catalysts, a similar phenomenon exists: the smaller particle sizes of HSA Fe_2O_3 induce greater surface curvature and stronger adsorption of reactants to the catalyst surface, necessitating a greater energy input to elicit reaction.

The selectivities displayed by 3 ML MoO_x/5% and 3 ML MoO_x/10% HSA Fe_2O_3 resemble those of 3 ML MoO_x/Fe_2O_3: formaldehyde is the major product, alongside a CO by-product. Crucially, in neither case is any significant CO_2 observed: accordingly, these catalysts are effective, and the requisite shell-core segregation has been fully achieved. The 3 ML MoO_x/15% and 3 ML MoO_x/20% HSA Fe_2O_3 catalysts, however, diverge from the behaviour expected in TPD. The 3 ML MoO_x/15% HSA Fe_2O_3 catalyst produces mostly formaldehyde, albeit with markedly more CO and some DME; in addition—and more concerningly—a quantity of CO_2 is observed. For this catalyst, the amount produced is still relatively small compared to the formaldehyde produced, implying that the shell is still mostly in place, and isolating a large portion of the core. This is not the case for 3 ML MoO_x/20% HSA Fe_2O_3. Instead, although formaldehyde is still generated in appreciable quantity, there is now considerably more CO_2 in relation, with correspondingly larger H_2 production. This implies that shell-core formation is incomplete, and that the 20% HSA Fe_2O_3 core is participating directly in the catalysis. The rationale for this cannot be conclusively determined by TPD alone. Several possibilities were considered: that the MoO_x shell is unable to spread as easily across Al cations, which by 20 wt% Al constitute a significant component of the support; that an additional bulk aluminium molybdate phase is formed, which is either unselective or fails to impede direct core participation; or alternatively that phase separation into a mixture of Fe_2O_3 and Al_2O_3 particles has occurred. The evidence from TPD is strongest for the latter case. Similarly to the naked HSA Fe_2O_3 materials, there is an important difference in the quantities of DME produced by each MoO_x/HSA Fe_2O_3 catalyst: again, the 15% and 20% cases produce markedly more DME. This can be attributed to the formation of alumina portions within the catalyst, which are selective to DME during reaction with methanol. Crucially, the size of the alumina particles cannot be large, since they are not observed by XRD (*vide infra*).

While TPD is the quickest means to detect divergences from the expected shell-core catalyst behaviour, it is equally useful to appraise the behaviour under an oxygenic atmosphere more akin to working conditions. This is achieved through PFR studies of the catalysts, wherein microlitre pulses of methanol are introduced to the catalyst at regular intervals. There are some crucial differences in the products observed by PFR measurements as opposed to TPD: for example, CO_2 is expected to be observed in all PFR measurements. Unlike TPD, where the presence or absence of CO_2 is significant, here it is the position of the CO_2 production which is important. Where significant evolution of CO_2 is first observed at high temperatures (beyond 260°C), the CO_2 arises not from direct combustion of methanol by the catalyst, but from the formation and subsequent combustion of selective products due to the elevated temperatures. In contrast, should significant CO_2 be produced at lower temperatures, it is strongly indicative of an improperly formed shell-core catalyst: i.e. the (HSA) Fe_2O_3 core is exposed.

Similarly to the TPD measurements, PFR measurements were undertaken to compare standard 3 ML MoO_x Fe_2O_3 (Figure 4.17) with the four different loadings of 3 ML

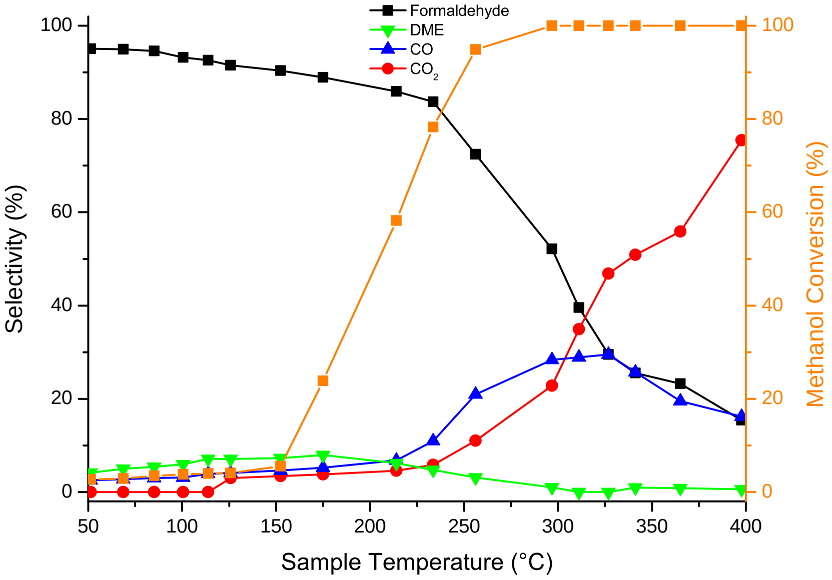

Figure 4.17: PFR data from 3 ML MoO_x/Fe_2O_3. Methanol conversion is shown in orange on the right-hand y-axis. Gas flow: 30 mL/min 10% O_2 in He. Sample mass: 200 mg.

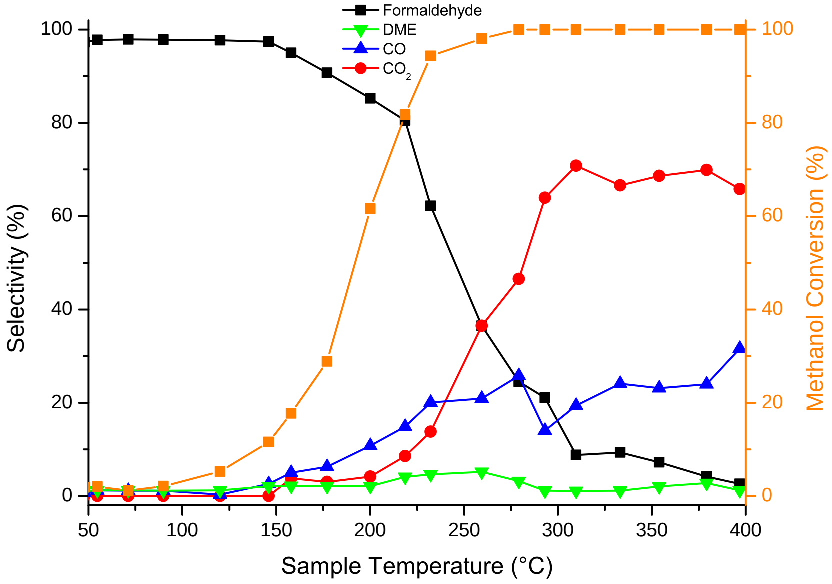

Figure 4.18: PFR data from 3 ML MoO_x/5% HSA Fe_2O_3. Methanol conversion is shown in orange on the right-hand y-axis. Gas flow: 30 mL/min 10% O_2 in He. Sample mass: 200 mg.

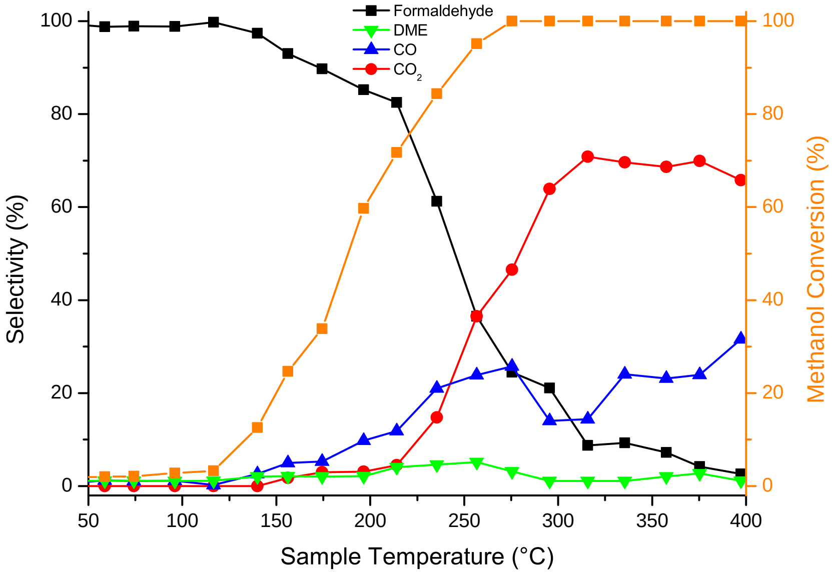

Figure 4.19: PFR data from 3 ML MoO$_x$/10% HSA Fe$_2$O$_3$. Methanol conversion is shown in orange on the right-hand y-axis. Gas flow: 30 mL/min 10% O$_2$ in He. Sample mass: 200 mg.

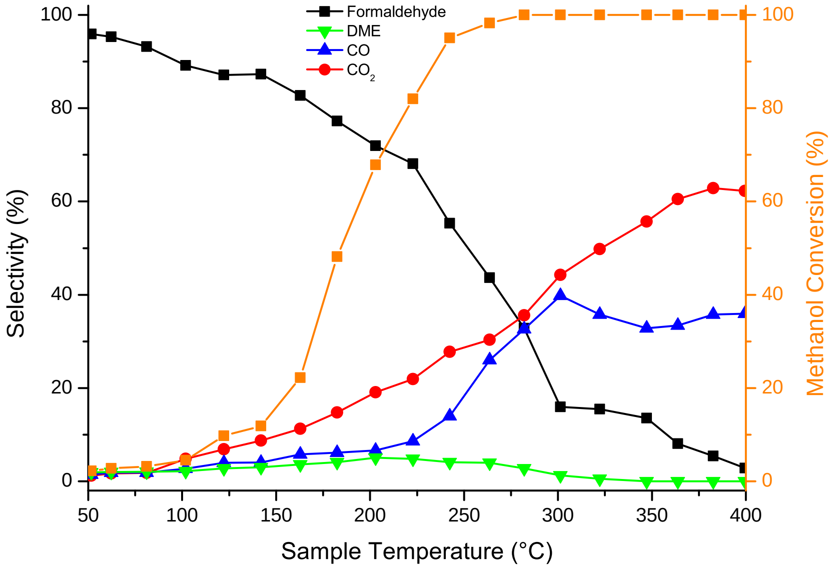

Figure 4.20: PFR data from 3 ML MoO$_x$/15% HSA Fe$_2$O$_3$. Methanol conversion is shown in orange on the right-hand y-axis. Gas flow: 30 mL/min 10% O$_2$ in He. Sample mass: 200 mg.

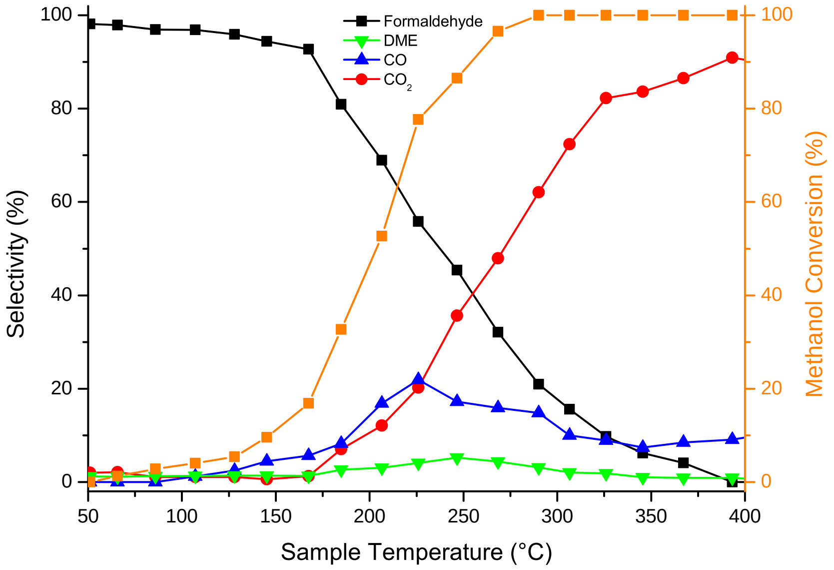

Figure 4.21: PFR data from 3 ML MoO_x/20% HSA Fe_2O_3. Methanol conversion is shown in orange on the right-hand y-axis. Gas flow: 30 mL/min 10% O_2 in He. Sample mass: 200 mg.

MoO_x/HSA Fe_2O_3 catalysts (Figures 4.18, 4.19, 4.20 and 4.21). In general, all four HSA catalysts are selective to formaldehyde, indicating that the core is being sufficiently inhibited from direct participation in each sample (with varying degrees of inhibition): due to the thermodynamic favourability of combustion, if any formaldehyde is seen, it can be assumed that the core Fe_2O_3 is at least partially isolated. The activities of the HSA Fe_2O_3-based catalysts are improved relative to the 3 ML MoO_x/standard Fe_2O_3 catalyst, with equivalent methanol conversions occurring at lower temperatures (Table 4.4): this is attributed to the smaller particle size and hence greater specific surface areas of the catalysts whose core components comprise HSA Fe_2O_3.

In TPD, smaller particle size induces an increase in product evolution temperature; under working conditions in PFR, the opposite is true, with greater surface area affording greater catalytic activity. A correlation is seen between the Al content in the catalyst and the resulting reduction in onset, half, and full conversion temperatures; however, as for the BET-derived surface areas and the Raman peak shifting, the 20% HSA Fe_2O_3 sample appears to reverse the trend.

There are also significant differences in the selectivities exhibited by the four HSA Fe_2O_3-based catalysts. Two of the 3 ML MoO_x/HSA Fe_2O_3 catalysts, viz. 3 ML MoO_x/5% and 10% HSA Fe_2O_3, display high selectivities to formaldehyde throughout the reaction and overall yields similar to the standard 3 ML MoO_x/Fe_2O_3 catalyst: crucially, this similarity in selectivity is accompanied by an improvement in activity, with the reaction occurring at slightly lower temperatures. Additionally, the 3 ML MoO_x/5% and 10% HSA Fe_2O_3 catalysts display a secondary increase in CO production above 300°C coincident with plateaus in CO_2 production, which is not observed for the standard 3 ML MoO_x/Fe_2O_3 catalyst. This is due to the higher catalytic activity of the HSA Fe_2O_3-based catalysts, rapidly depleting the oxygen available to the catalyst. Consequently, insufficient oxygen is available at high temperatures to fulfil the requirements of complete combustion to CO_2, promoting incomplete combustion to CO instead.

In contrast, the selectivities and overall yields of the 15% and 20% HSA Fe_2O_3-based catalysts are worse, and for the latter decidedly so. For both catalysts CO_2 is produced at lower temperatures, signifying that their shells are improperly formed and unable to sequester the HSA Fe_2O_3 core. 3 ML MoO_x/15% HSA Fe_2O_3 displays formaldehyde selectivity slightly worse than for lower HSA loadings, and while CO_2 is produced at low temperatures, the quantity is small. This cannot be said of 3 ML MoO_x/20% HSA Fe_2O_3. The overall formaldehyde yield has been markedly reduced compared to the other catalysts, and significantly more CO_2 is produced from low temperatures, indicating direct combustion of reactant methanol by the 20% HSA Fe_2O_3 core and therefore that the requisite shell-core segregation is absent. In contrast to TPD, no significant DME production is observed for any catalyst during PFR studies, since the oxygenic atmosphere promotes the rapid combustion of any DME formed.

The behaviour witnessed in PFR measurements echoes that seen by TPD. 3 ML MoO_x catalysts with lower loading HSA Fe_2O_3 cores perform well, with few selectivity differences to normal 3 ML MoO_x/Fe_2O_3. By 15% loading, a small degree of undesired selectivity has appeared; by 20% the detrimental selectivity changes are large enough to negate the

Table 4.4: A comparison of the positions of significant stages of methanol conversion as a function of Al loading in 3 ML MoO_x/HSA Fe_2O_3 catalysts: T_o = onset temperature; T_{50} = 50% conversion; and T_{100} = full conversion.

	Temperature (°C)		
Catalyst	T_o	T_{50}	T_{100}
3 ML MoO_x/Standard Fe_2O_3	155	205	300
3 ML MoO_x/5% HSA Fe_2O_3	135	195	280
3 ML MoO_x/10% HSA Fe_2O_3	130	190	275
3 ML MoO_x/15% HSA Fe_2O_3	125	185	275
3 ML MoO_x/20% HSA Fe_2O_3	135	200	300

benefits of increased catalytic activity. Moreover, the trend of increasing surface area and activity seen for 5%, 10% and 15% HSA Fe_2O_3 goes awry beyond 15%, with 20% HSA Fe_2O_3 noticeably worse in all aspects. The reason behind this cannot be ascertained at this stage: by XRD and Raman, the samples appear alike. This suggests that the deleterious structural and speciational changes—i.e. suspected phase separation of Al_2O_3—which occur at and beyond 15% Al are ubiquitous enough to disrupt the overall catalytic behaviour, but too diminutive to be observed by such techniques. More specialised techniques—for example XAS—are required to understand the HSA Fe_2O_3 system in greater detail.

4.4.2 Structural characterisation

In spite of detecting no significant structural discrepancies between the naked HSA Fe_2O_3 supports, it is clear that something is amiss with the higher Al loading HSA Fe_2O_3 samples, most notably when used in shell-core catalysts. 3 ML MoO_x/15% HSA Fe_2O_3 is a formaldehyde-selective catalyst, though unlike the equivalent catalysts containing lower Al loading supports, it generates small quantities of CO_2 in TPD; 3 ML MoO_x/20% HSA Fe_2O_3, however, is markedly worse, with significant CO_2 production in TPD. Since these detrimental effects occur for higher Al loadings, it is logical to assume that they result from structural changes elicited by the introduction of too great a quantity of Al. To attempt to elucidate the cause of such structural disruption, the MoO_x shell-core catalysts containing 5%, 10%, 15% and 20% HSA Fe_2O_3 were assessed by XRD (Figure 4.22).

Notwithstanding the manifest differences in reactivity discussed above, no significant distinctions can be made by XRD beyond the changes common to all HSA Fe_2O_3 materials (viz. a slight shift to higher 2θ and peak broadening). This implies that the structural distortion which impairs the formation of a full shell-core catalyst, and hence the selectivity of the catalyst also, does not exhibit long-range structure. XRD measurements of this type are unable to detect structural phases which are present only in small units with poor long-range order: their signals in the resulting pattern are overwhelmed by experimental noise, rendering them meaningless. It was always considered possible that the addition of Al dopants to Fe_2O_3 might prompt phase separation—particularly at higher Al loadings—into Fe_2O_3 and Al_2O_3 phases; however, if this has indeed occurred by 15% and 20% HSA Fe_2O_3, the Al_2O_3 must exist in isolated, amorphous units, since it is not observed by XRD. Alternatively, a mixed aluminium molybdate phase could be formed upon coating with MoO_x. Again, were this phase present, it must exist in small independent units, since it is not seen by XRD either.

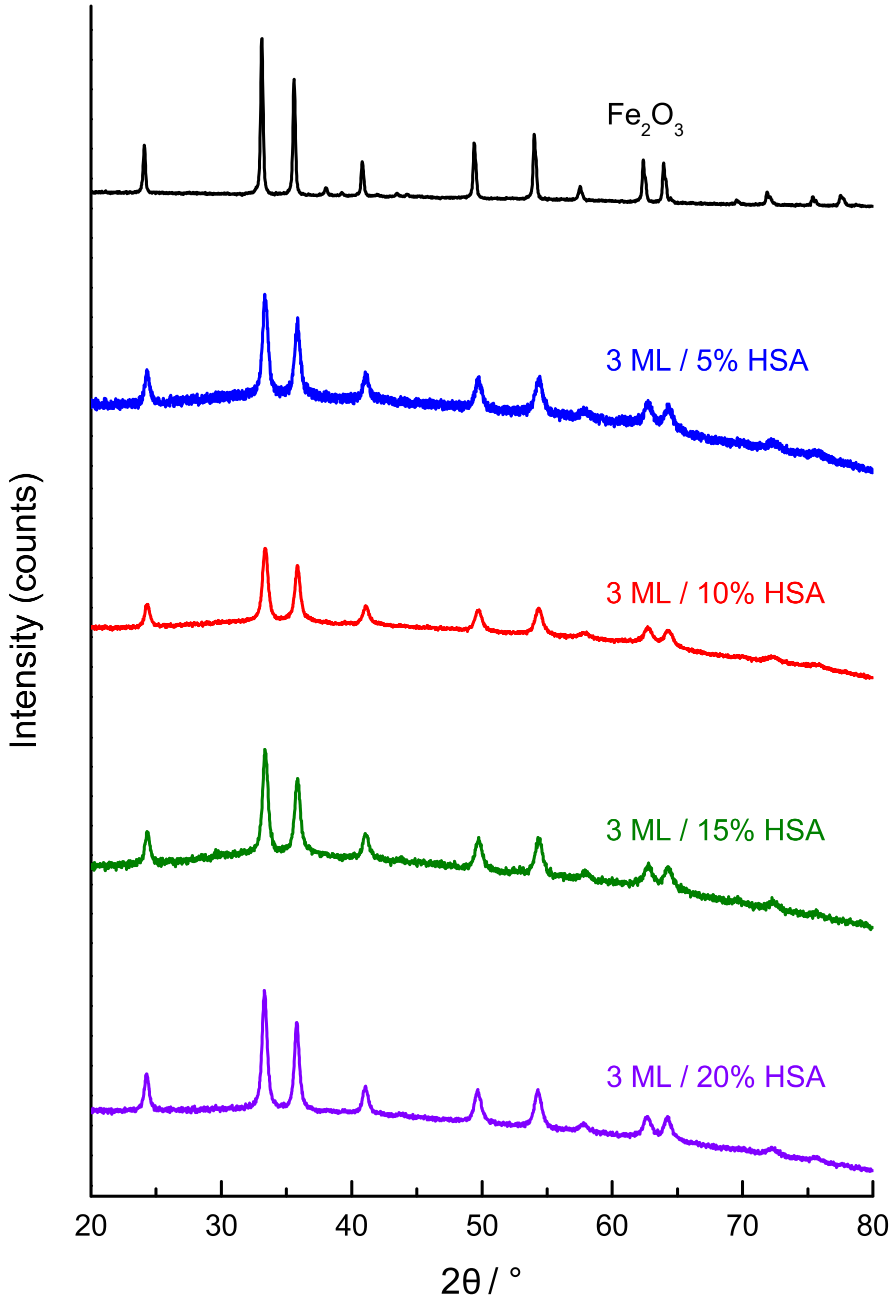

Figure 4.22: A comparison of XRD patterns for 3 ML MoO_x/HSA Fe_2O_3 catalysts with standard Fe_2O_3.

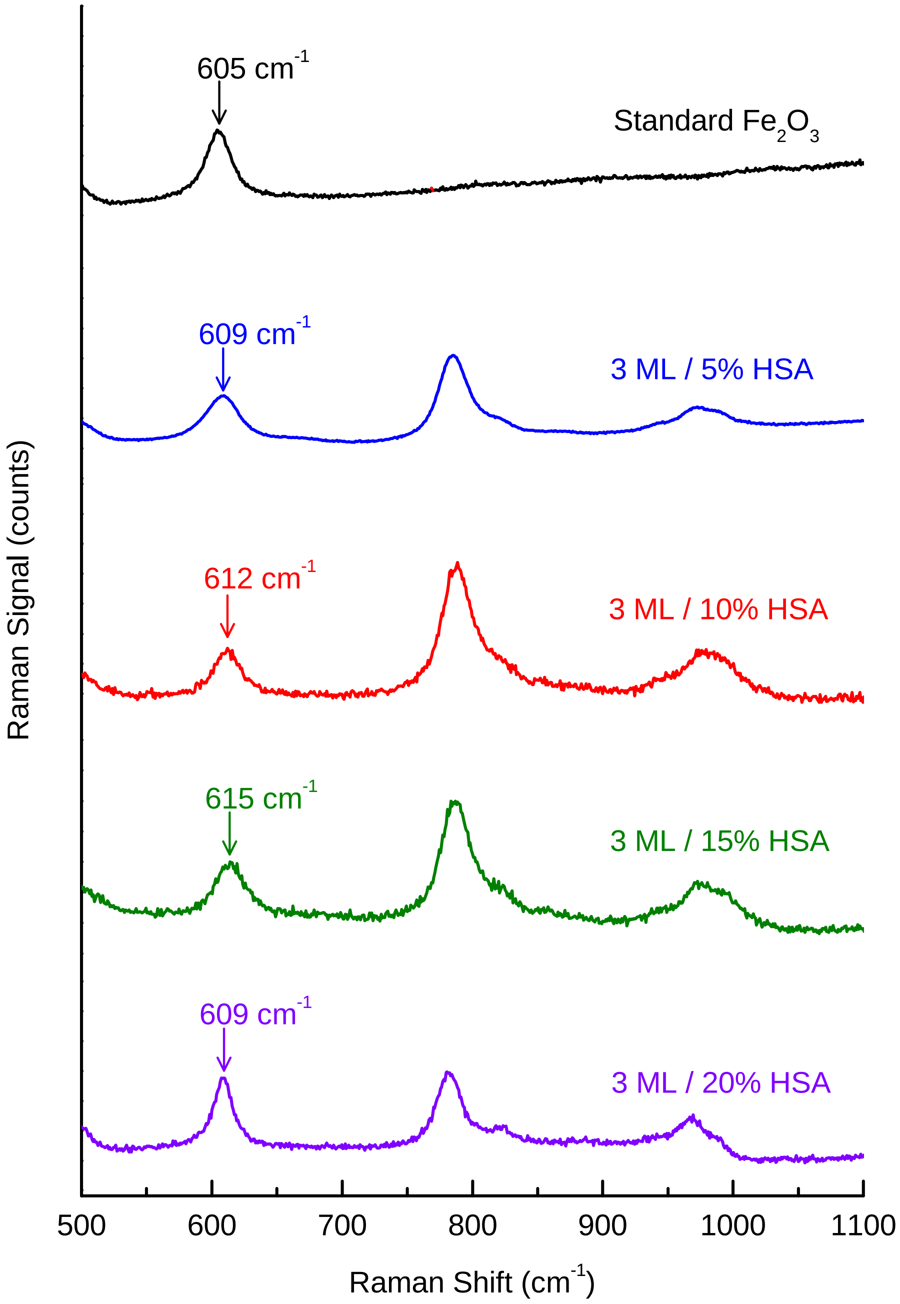

Figure 4.23: A comparison of Raman spectra for 3 ML MoO_x/x HSA Fe_2O_3 catalysts, where x = 5%, 10% or 15 % HSA Fe_2O_3 with a standard Fe_2O_3 reference. The haematite peak is marked in each spectrum to gauge its position as a function of Al loading.

Raman spectroscopy was also employed to assist in understanding the lack of selectivity demonstrated by the catalysts based on higher Al loadings. The catalysts were assessed alongside plain Fe_2O_3 as a reference material (Figure 4.23). For all four catalysts, the presence of iron molybdate is denoted by the broad peaks at approximately 790 and 980 cm^{-1}, while Fe_2O_3 provides the leftmost peak in each spectrum. Interestingly, the shift in the haematite peak position (above 600 cm^{-1}) to higher wavenumber with greater Al content is observed here also. This is attributed to greater substitution of Al^{3+} for Fe^{3+} in the Fe_2O_3 structure with higher Al loadings. This reduces the atomic separation throughout the material, thereby increasing the effective bond strength in the structure: this induces a blueshift in the Raman signals, the magnitude of which depends on the Al loading, and a slight broadening of the peaks.[3,8] In this instance, the peak is shifted more at higher Al loadings, corroborating the suggested decrease in atomic separation. The positions of the iron molybdate peaks are unaffected, since they neither contain Al nor experience the concomitant reduction in atomic distances and increase in bond force constants.

4.5 Understanding Al-doped Fe_2O_3 by XAS

XAS can provide huge insights into the speciation, environment and bonding present within a material, undeterred by the size limitations afflicting other spectroscopic techniques. While the Mo K-edge explored in other chapters requires hard X-rays, measurements at the Al K-edge—1.559 keV—use markedly softer X-rays. The experimental setup on B18, Diamond Light Source, is optimised to measure energies higher than 3 keV, hence an application for beamtime was made to an alternative beamline specialising in tender X-ray measurements: namely, PHOENIX at the Swiss Light Source. Based on the characterisation and reactivity measurements discussed earlier, it was hoped that XAS would answer three main questions:

(i) Can evidence for Al structural substitution in Fe_2O_3 be obtained?

(ii) What impact is made by the addition of a MoO_x shell?

(iii) Are the changes in selectivity as a function of Al loading reflected by differences in Al speciation?

Four Al loadings were investigated during the experiment at PHOENIX in May/June 2019, namely 5%, 10%, 15% and 20% HSA Fe_2O_3. For each loading, three samples were analysed: one naked HSA Fe_2O_3 support; one 1 ML MoO_x/HSA Fe_2O_3 catalyst; and one 3 ML MoO_x/HSA Fe_2O_3 catalyst. Each sample was measured simultaneously in two modes, fluorescence and total electron yield (TEY): fluorescence spectra are akin to normal, bulk XAS spectra, while TEY spectra are collected not from the entire sample, but solely from regions closer to the surface. Both are prone to—and did indeed suffer from—complications from self-absorption. Since the Al K-edge is low in energy, self-absorption is correspondingly greater, decreasing the signal quality compared to higher energy XAS transmission measurements (e.g. Mo). Caution must be taken when assessing the data: direct comparisons between TEY and fluorescence spectra are not valid, so comparisons should be limited to TEY with other TEY and fluorescence with other fluorescence.

4.5.1 XANES measurements of HSA Fe_2O_3 supports

Initial measurements were conducted on samples of naked HSA Fe_2O_3, i.e. the supports without MoO_x monolayers at the surface (Figures 4.24, 4.25, 4.26 and 4.27). In doing so, the differences resulting solely from differences in Al loading could be examined independently of any changes caused by the addition of MoO_x shells. There are noticeable differences in peak heights between the two spectral acquisition methods, which were not resolvable during sample measurement, arising mainly from self-absorption effects. Nonetheless, general trends are observed from both methods.

Generally, the XANES features for 10%, 15% and 20% HSA Fe_2O_3 (though the TEY spectrum of 20% is distorted) exhibit good resemblance to each other: the pre-edge features are similar as is the overall edge shape. The single broad pre-edge feature at 1557 eV displayed by each of these three loadings resembles the pre-edge feature found in Al_2O_3, which is attributed to forbidden 1s → 3s transitions facilitated by atomic vibrations.[11,12] Crucially, this transition can only occur with a degree of hybridisation between 3s and 3p orbitals, which itself is only possible if the Al absorber does not occupy an inversion centre. While α-Al_2O_3 and γ-Al_2O_3 are deemed octahedral with respect to Al, in reality neither is centrosymmetric, enabling mixing by atomic vibration of the s and p orbitals necessary to produce the pre-edge peak.[11,12] The source of the transitions aside, it is clear that higher Al loadings boost resemblance to γ-Al_2O_3.

The 5% HSA Fe_2O_3 sample, however, is noticeably different. Its overall shape is dissimilar, but more significantly, there are two small pre-edge features present for 5% HSA Fe_2O_3 at 1556 and 1558 eV, which are absent in the higher Al loadings (Figure 4.28). Importantly, these do not arise from Al orbital mixing like the pre-edge feature of

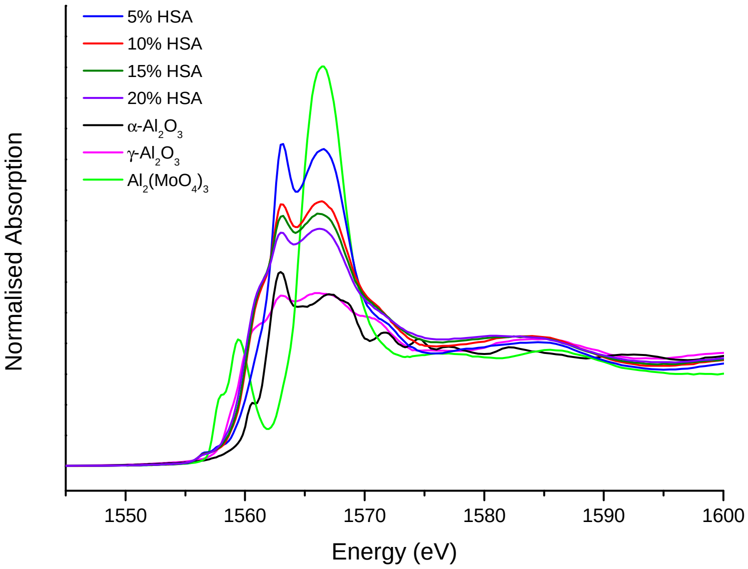

Figure 4.24: Normalised fluorescence XANES spectra of 5%, 10%, 15% and 20% HSA Fe_2O_3 with reference compounds α-Al_2O_3, γ-Al_2O_3 and $Al_2(MoO_4)_3$.

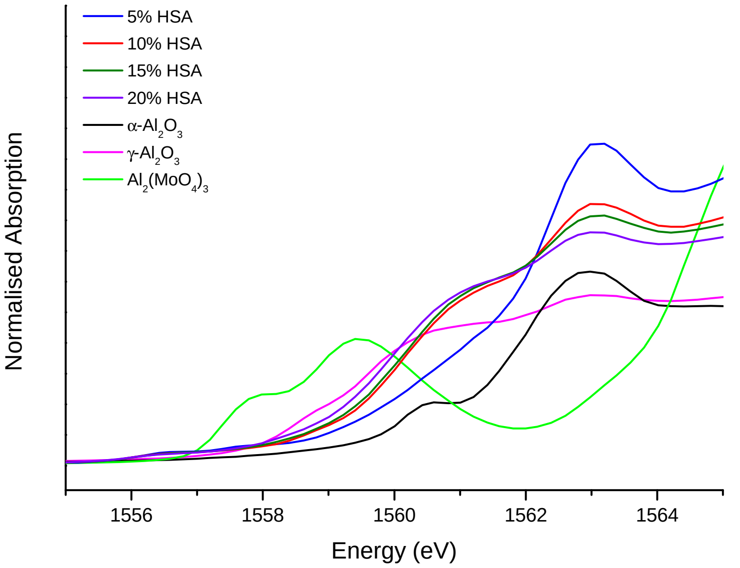

Figure 4.25: Expanded fluorescence XANES pre-edge region of 5%, 10%, 15% and 20% HSA Fe_2O_3 with reference compounds α-Al_2O_3, γ-Al_2O_3 and $Al_2(MoO_4)_3$.

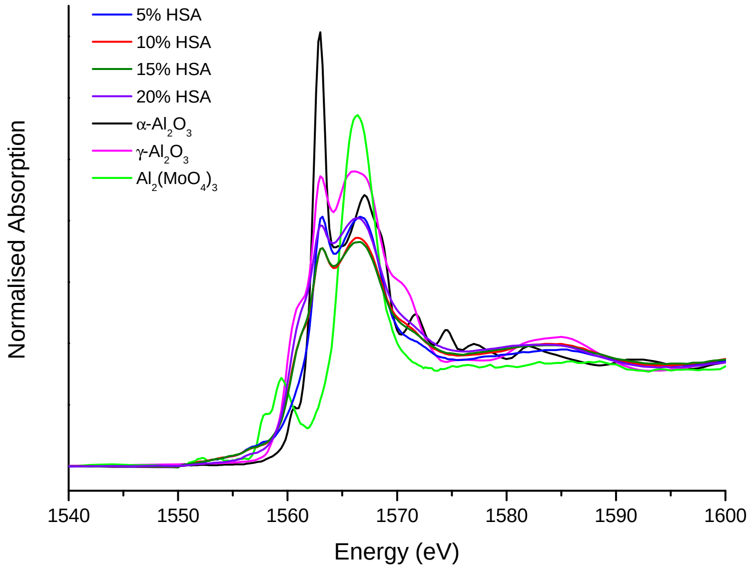

Figure 4.26: Normalised TEY XANES spectra of 5%, 10%, 15% and 20% HSA Fe_2O_3 with reference compounds α-Al_2O_3, γ-Al_2O_3 and $Al_2(MoO_4)_3$.

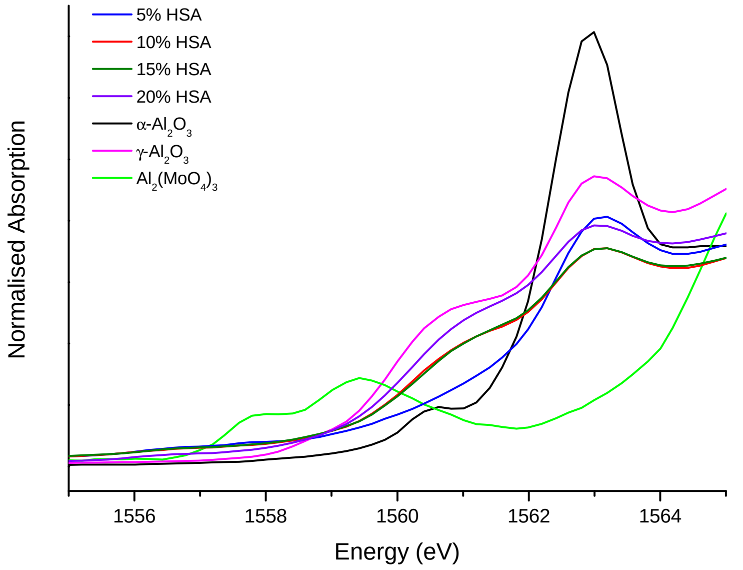

Figure 4.27: Expanded TEY XANES pre-edge region of 5%, 10%, 15% and 20% HSA Fe_2O_3 with reference compounds α-Al_2O_3, γ-Al_2O_3 and $Al_2(MoO_4)_3$.

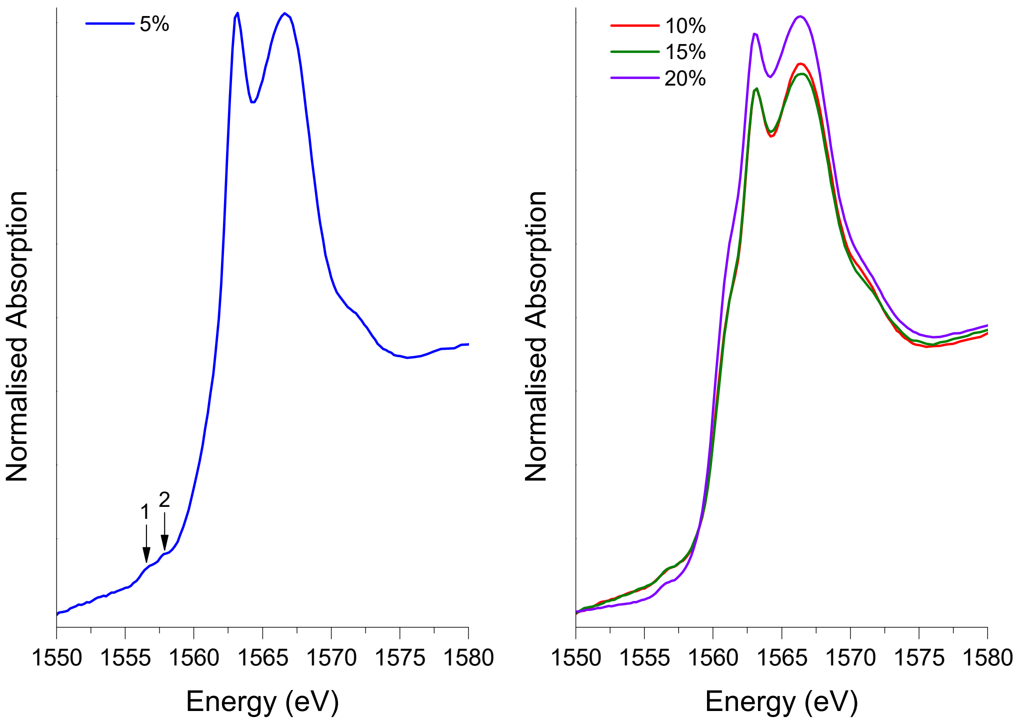

Figure 4.28: XANES pre-edge features of 5%, 10%, 15% and 20% HSA Fe_2O_3. The non-local Fe 3d excitations are marked 1 and 2 respectively for 5% HSA Fe_2O_3: note the replacement of these two pre-edge peaks by one broader alumina-like peak at higher Al loadings.

Al_2O_3, but instead from non-local interactions between the Al absorber and neighbouring Fe. The energy used to probe the Al K-edge has been shown in similar materials, e.g. by Ducher et al. for Al-doped goethite (FeO(OH)), to indirectly probe Fe 3d orbitals.[13] In Fe_2O_3 and goethite, each Fe atom inhabits an octahedral environment. The density of states (DOS) calculations conducted by Ducher et al. confirmed that the 3d orbitals in octahedral Fe are split into t_{2g} and e_g orbitals, with occupied majority-spin states and unoccupied minority-spin states. Similarly to 5% HSA Fe_2O_3, they reported two small pre-edge features in the same location for goethite, which they assigned to indirect probing of the empty Fe 3d t_{2g} and e_g orbitals respectively. In aluminous goethite, the difference between these two pre-edge peaks is measured at 1.5 eV. Encouragingly, in the XANES of 5% HSA Fe_2O_3, the difference in energy between the pre-edge peaks is also 1.5 eV. This figure can be used to accurately approximate the octahedral crystal field splitting parameter (Δ_o), which for octahedral Fe has separately been confirmed as 1.5 eV.[14] The pivotal requirement for these non-local excitations to occur is the ability for Al orbitals to hybridise with neighbouring orbitals, which is possible only with proximity of Al to octahedral Fe. In other words, this can only occur where the Al has inserted into the

Fe_2O_3 structure. Since the intention behind using Al dopants was that they would adopt positions within the Fe_2O_3 structure and thereby induce particle size reductions, this is an extremely encouraging result.

It must be remembered that XAS is an averaging technique, even when measured in a more surface-sensitive mode (where the average will be taken across the surface). Consequently, if the quantity of one species increases relative to another, it may not be possible to see the other species in the resulting spectrum. For HSA Fe_2O_3, only the Al which is incorporated into the Fe_2O_3 structure will generate the two pre-edge features in XANES spectra. At 5% Al, most of the Al is occupying Fe sites in the Fe_2O_3 structure; by 10%, however, this is clearly not the case. The two features have been replaced by one, with significantly greater resemblance to γ-Al_2O_3. It is not possible to definitively state that no Al has been substituted for Fe in the Fe_2O_3 structure by XANES alone; however, due to the relative abundance of Al_2O_3-like material, the two pre-edge features from Al structural incorporation are not seen. LCF is an effective means of quantitatively measuring the similarity of XANES spectra against chosen standards, and is ideal for ascertaining to what degree the Al content increasingly resembles γ-Al_2O_3 with increasing Al loading. To answer this, fitting was performed on 10%, 15% and 20% HSA Fe_2O_3 using 5% HSA Fe_2O_3—where Al has substituted into the Fe_2O_3 structure—and γ-Al_2O_3 as standards. It can be seen that greater Al loading elicits greater resemblance to γ-Al_2O_3, signifying that the Al content of the material is indeed phase separating (Table 4.5, Figure 4.29). The particles of Al_2O_3 which are formed at 10%, 15% and 20% Al must nonetheless be small, since they are not observed by XRD. While similar, the fits do not entirely match free γ-Al_2O_3; this is likely due to the structural distortion arising from the limited particle sizes of the Al_2O_3 present in the higher loading HSA materials, or alternatively due to the development of further Al phases beyond γ-Al_2O_3 by 20% HSA Fe_2O_3.

Table 4.5: LCF statistical fitting data from Al XANES measurements of 10%, 15% and 20% HSA Fe_2O_3 supports.

	Similarity to standards (%)		
Species	5% HSA Fe_2O_3	γ-Al_2O_3	R-factor
10% HSA Fe_2O_3	64.3	35.7	1.27×10^{-2}
15% HSA Fe_2O_3	46.6	63.4	1.66×10^{-2}
20% HSA Fe_2O_3	25.5	74.5	2.11×10^{-2}

The formation of phase separated Al as Al loading increases is not unexpected, but

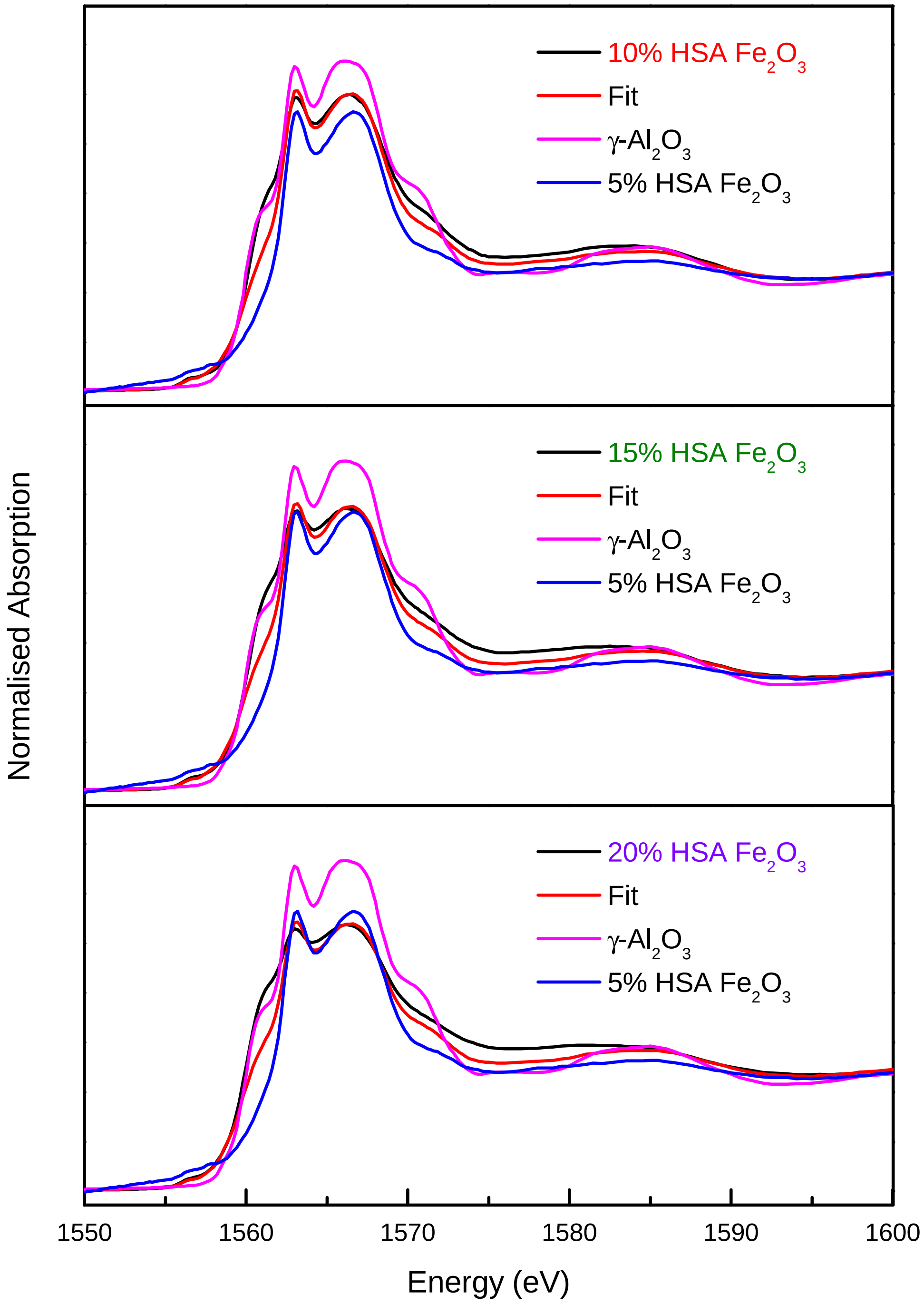

Figure 4.29: A comparison of LCF results for 10%, 15% and 20% HSA Fe_2O_3 supports using γ-Al_2O_3 and 5% HSA Fe_2O_3 as standards.

that it happens as low as 10% Al loading was not expected based on the selectivity and activity trends explored earlier. A possible explanation is that 5% HSA Fe_2O_3 is a Goldilocks case: there is enough Al present to significantly modify the Fe_2O_3 structure, but it is insufficiently ubiquitous at 5% loading to enable Al clustering. In contrast, at higher Al loadings, the Al readily encounters other Al particles, producing small clusters of phase separated alumina. If considered thermodynamically, the inclusion of Al in the Fe_2O_3 structure could be imagined as a local energy minimum, while phase separation is the overall energy minimum; the former is promoted by a relative structural paucity of Al, while the latter is attained with a relative plenitude of Al throughout the material. The spectral manifestations of the appearance of Al clusters at higher Al loadings in Fe_2O_3 mirror those of aluminous goethite materials, where the two pre-edge non-local Fe excitations also disappear with increasing Al loading in the goethite.[13] Considering the XANES features, it can be reliably surmised that successful substitution of Al dopants into the Fe_2O_3 structure has been accomplished at low Al loadings.

4.5.2 XANES measurements of 3 ML MoO_x/HSA Fe_2O_3 catalysts

Having surveyed the structural properties of HSA Fe_2O_3 supports in isolation, the focus then shifted to systems wherein HSA Fe_2O_3 is used as the core in shell-core catalysts. The structural behaviour of MoO_x shells has been extensively examined previously for MoO_x/Fe_2O_3 catalysts, and this knowledge greatly assists these XAS studies of HSA Fe_2O_3. 3 ML MoO_x/HSA Fe_2O_3 shell-core catalysts of each Al loading were prepared for analysis at the Al K-edge, and compared with Al reference compounds in fluorescence (Figure 4.30) and TEY modes (Figure 4.31).

Bearing in mind that the higher Al loading naked HSA Fe_2O_3 materials displayed increasing similarity to γ-Al_2O_3, a similar trend was anticipated for the higher Al loading 3 ML MoO_x/HSA Fe_2O_3 catalysts. Encouragingly, this is the case, with strong similarities to γ-Al_2O_3 seen for the catalysts based on 10%, 15% and 20% HSA Fe_2O_3: higher Al loadings display greater agreement with γ-Al_2O_3. This can be seen visually in the spectra, but is also confirmed quantitatively by LCF (Table 4.6, Figure 4.32). No significant structural changes in the core moiety are expected to result from the calcination used for shell-core catalyst synthesis, and this is supported by the presence of the same trend in the XAS as was seen for naked HSA Fe_2O_3. The 3 ML MoO_x/5% HSA Fe_2O_3 catalyst, however, exhibits many interesting differences. The two pre-edge peaks arising from the excitation of empty Fe 3d orbitals (labelled 1 and 2) are still present, although partially

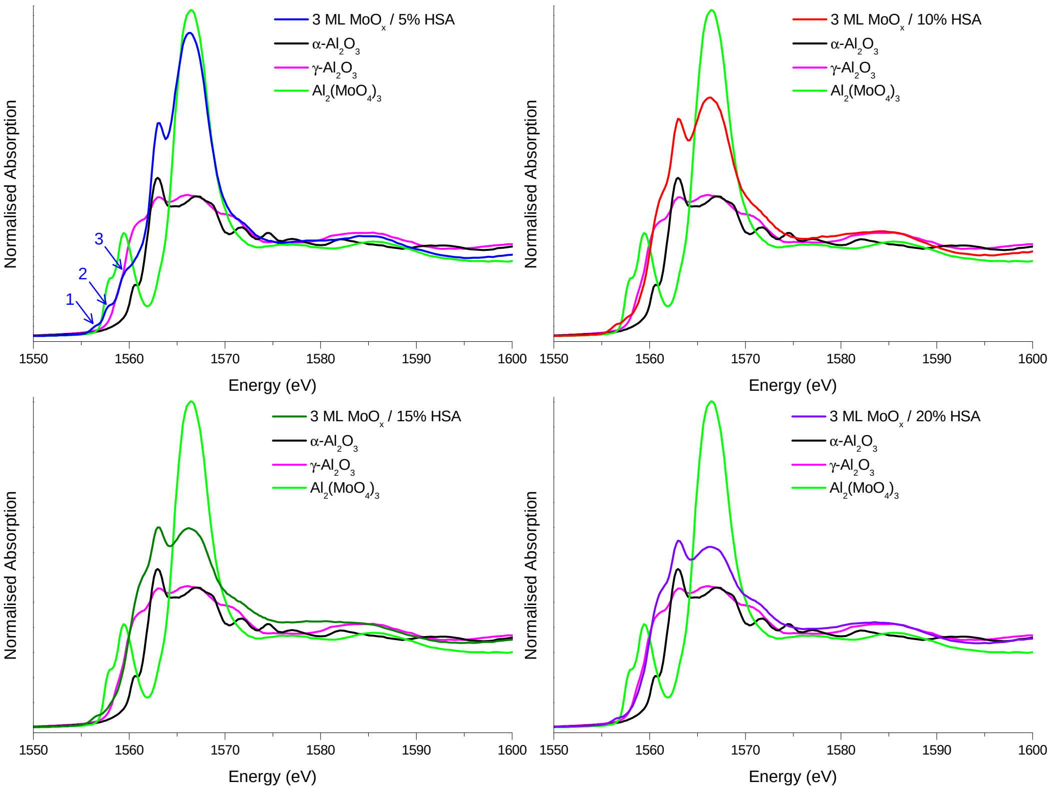

Figure 4.30: A comparison of fluorescence XANES features for 3 ML MoO$_x$/HSA Fe$_2$O$_3$ catalysts against reference compounds. Peaks 1 and 2 correspond to Fe 3d excitations, while peak 3 corresponds to an aluminium molybdate-like interaction.

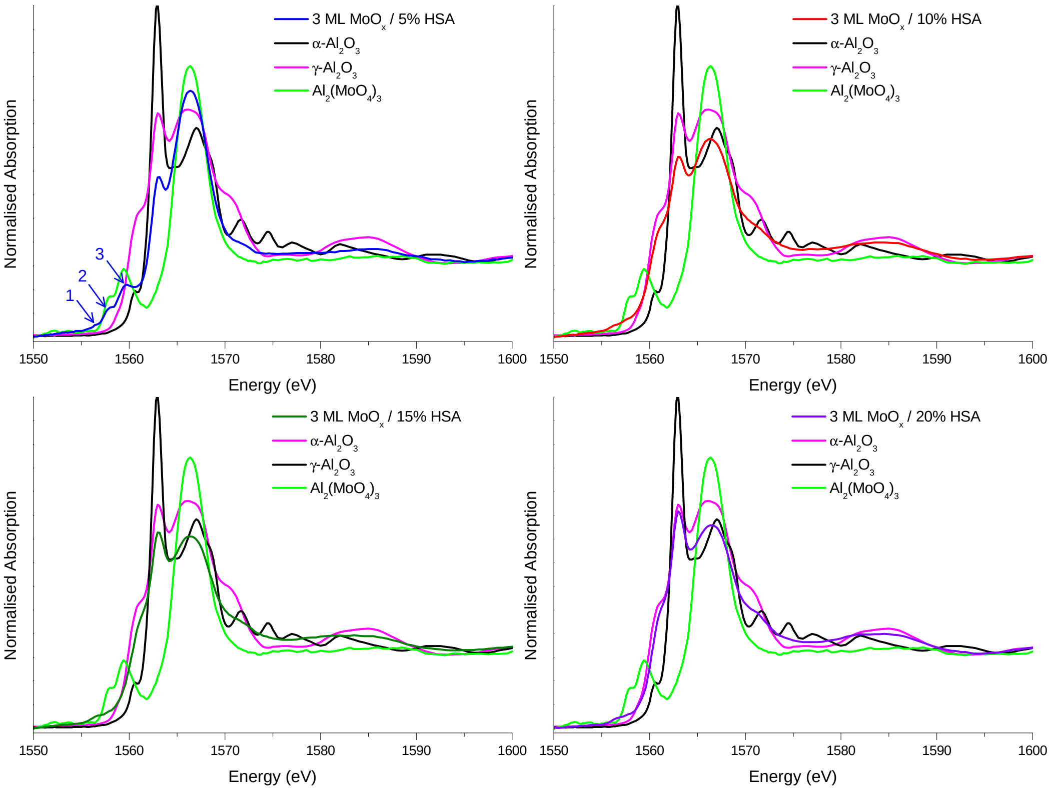

Figure 4.31: A comparison of TEY XANES features for 3 ML MoO$_x$/HSA Fe$_2$O$_3$ catalysts against reference compounds. Peaks 1 and 2 correspond to Fe 3d excitations, while peak 3 corresponds to an aluminium molybdate-like interaction.

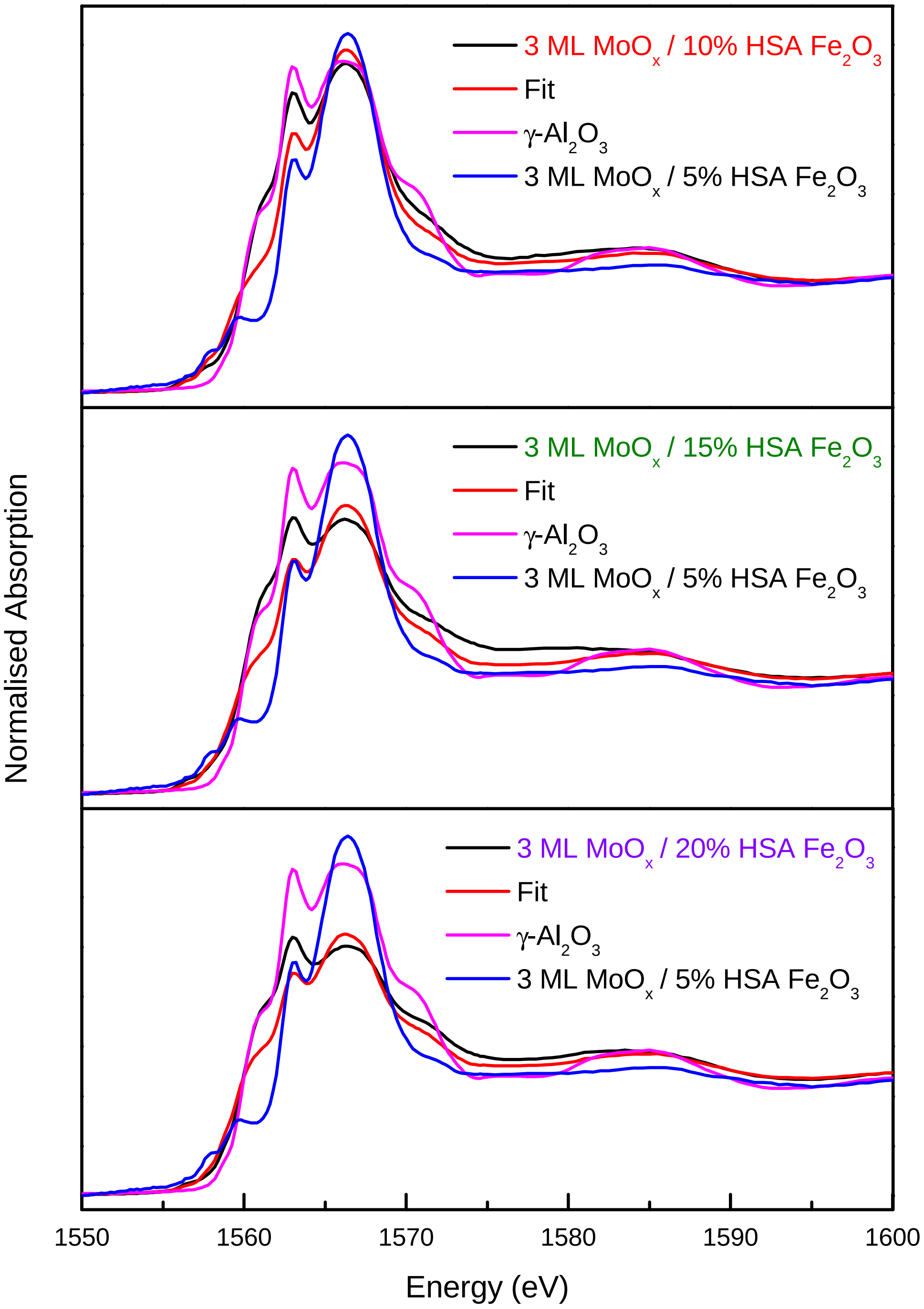

Figure 4.32: A comparison of LCF results for 3 ML MoO_x/10%, 15% and 20% HSA Fe_2O_3 catalysts using γ-Al_2O_3 and 3 ML MoO_x/5% HSA Fe_2O_3 as standards.

obscured by a third pre-edge peak (labelled 3). Significantly, this third pre-edge peak is coincident with the pre-edge peak of aluminium molybdate, thus it is likely from an Al → Mo non-local excitation. This strongly implies that either Al molybdate has been formed, or that some Al absorbers are in close proximity—either vicinal or incorporated in the structure—to iron molybdate.

Table 4.6: LCF statistical fitting data from Al XANES measurements of 3 ML MoO_x/10%, 15% and 20% HSA Fe_2O_3 catalysts.

	Similarity to standards (%)		
Species	3 ML/5% HSA	γ-Al_2O_3	R-factor
3 ML MoO_x/10% HSA Fe_2O_3	66.2	33.8	2.90×10^{-2}
3 ML MoO_x/15% HSA Fe_2O_3	42.1	57.9	4.00×10^{-2}
3 ML MoO_x/20% HSA Fe_2O_3	29.7	70.3	2.41×10^{-2}

For the catalysts based on 10%, 15% and 20% HSA Fe_2O_3, the aluminium molybdate-like pre-edge peak is not observed, with each peak instead having a continuous edge without a significant pre-edge shoulder feature. At first, this may seem discouraging, as each of the catalysts possesses the same relative quantity of MoO_x at the surface. Upon reflection, however, the absence of an aluminium molybdate-like pre-edge feature is understandable, if one again recalls that XAS spectra are averages. For the 5% HSA Fe_2O_3 support, the Al appears to inhabit the Fe_2O_3 structure in an orderly manner, but for 10%, 15% and 20% HSA Fe_2O_3, the Al displays markedly greater similarity to γ-Al_2O_3, indicating that a significant portion of the Al has phase separated (though to small particles). This fundamentally impacts the resultant catalyst structure following the addition of MoO_x to the support. Recall that in a normal 3 ML MoO_x/Fe_2O_3 catalyst, after calcination at 500°C, there are three main components, viz. the Fe_2O_3 core, the MoO_x surface layer and the iron molybdate sandwich layer in between. With Al-induced phase separation, however, a shell-core structure cannot be formed throughout the material as for pristine Fe_2O_3.

The origins of the aluminium molybdate-like pre-edge peak must be established in order to explain the differences in the pre-edge between the catalysts. Based on the similarity to aluminium molybdate, one might assume it to be a marker of aluminium molybdate present in the catalyst. As the synthesis method achieves a uniform distribution of MoO_x precursor, it seems feasible that aluminium molybdate might form at the boundary between MoO_x precursor and Al_2O_3 particles; however, this would be mistaken.

Unlike iron molybdate, which forms below 500°C, the production of aluminium molybdate requires long periods at temperatures in excess of 700°C: these are never attained during calcination. Consequently, the pre-edge shoulder, though visually similar to aluminium molybdate, must originate elsewhere: for the 3 ML MoO_x/5% HSA Fe_2O_3 catalyst, it originates from the sandwich iron molybdate layer. The ability of Al to occupy sites in the Fe_2O_3 structure is attributed to the shared structures of α-Al_2O_3 and Fe_2O_3; as iron molybdate and aluminium molybdate are also isostructural, it is reasonable to expect that Al can be substituted for Fe in iron molybdate too. Since the sandwich layer of iron molybdate forms during calcination from the mixing of both the MoO_x precursors at the surface (to provide the Mo) and the Fe_2O_3 core (to provide the Fe), where Al is already present in the Fe_2O_3, this aluminous Fe_2O_3 will be therefore used to form the sandwich layer. In consequence, some Al is transported into the iron molybdate layer and remains there, substituted into the iron molybdate structure. It is the formation of Al-doped iron molybdate which most likely accounts for the aluminium molybdate-like pre-edge shoulder in the XANES spectrum of 3 ML MoO_x/5% HSA Fe_2O_3.

The absence of the Al-doped iron molybdate pre-edge feature from the XANES spectra of higher Al loadings can be explained by considering the behaviour of Al within HSA Fe_2O_3 as a function of loading. It is apparent, both from the naked HSA Fe_2O_3 samples and the MoO_x covered catalysts, that an increased concentration of Al within the material impels greater phase separation and hence formation of Al_2O_3. This diminishes the pre-edge shoulder in two ways. Firstly, as Al content increases, the energetic impetus to phase separate increases due to the greater likelihood of Al encountering other Al. In other words, where Al might have occupied many Fe_2O_3 sites—and hence iron molybdate sites also—at 5% loading, by 10% and above fewer sites are occupied by Al due to the stronger lure of phase separated Al_2O_3. In effect, the amount of Al substitution in Fe_2O_3 per unit Al decreases with more Al. Secondly, the averaging effect of XAS will cause the higher Al_2O_3 content of higher Al loadings to dominate the XANES spectra, overwhelming the Al-doped iron molybdate signal at higher Al loadings. This spectral effect, combined with the reduction in Al structural substitution with increasing Al loading, explains why Al-doped iron molybdate cannot be seen beyond 3 ML MoO_x/5% HSA Fe_2O_3.

There is an important additional implication from the appearance of the aluminium molybdate-like pre-edge for 3 ML MoO_x/5% HSA Fe_2O_3. The MoO_x present in the material is known to be isolated at the surface, and therefore for Al to interact with the MoO_x, it must be close to the surface. In general, the averaging nature of XAS spectra would suggest that, as the aluminium molybdate-like pre-edge shoulder is clearly visible, a significant proportion of the Al present is located near the Mo, i.e. near the surface. This could imply that Al is not uniformly distributed throughout the Fe_2O_3 as desired, but concentrates in the surface regions of the Fe_2O_3 particles. Importantly, however, since the aluminium molybdate-like pre-edge is not coincident with any other XANES features observed in the whole dataset—and therefore is not in competition with those other features during XAS signal averaging—it is possible that the intensity of the Al → Mo pre-edge shoulder is exaggerated relative to the true quantity of Al close to Mo. Further study, ideally with computationally modelled XANES spectra, will be key to understanding whether Al is concentrated at the surface.

4.5.3 XANES measurements of 1 ML MoO_x/HSA Fe_2O_3 catalysts

While shell-core catalysts with 3 ML MoO_x shells have historically attracted the greatest research focus, it has been worthwhile to study the counterpart 1 ML MoO_x catalysts in addition. As a brief reminder, 3 ML MoO_x catalysts are effectively interchangeable with any ML catalyst greater than 1 ML in terms of structural design, but 1 ML MoO_x catalysts are different. To complement the XANES studies discussed above, XAS measurements were undertaken on a range of 1 ML MoO_x/HSA Fe_2O_3 catalysts, in both fluorescence (Figure 4.33) and TEY modes (Figure 4.34).

The overall trends displayed by 1 ML MoO_x/HSA Fe_2O_3 catalysts do not vary from those of 3 ML MoO_x/HSA Fe_2O_3 and indeed naked HSA Fe_2O_3: as expected, the 1 ML MoO_x/5% HSA Fe_2O_3 catalyst displays the greatest divergence from the trend due to greater Al structural substitution than phase separation. Unlike the higher loadings, the crucial two pre-edge peaks from non-local interactions with Fe 3d orbitals are present, indicating that for 1 ML MoO_x/5% HSA Fe_2O_3, the Al dopants have indeed inserted into the Fe_2O_3 structure. In contrast, the higher Al loadings do not display these two pre-edge peaks, but instead increasingly resemble γ-Al_2O_3. This can be determined by visual inspection of the XANES spectra, but also quantitatively by LCF (Table 4.7, Figure 4.35). Confidence in the theorised behaviour—that Al phase separation is driven more strongly as a function of Al loading to the detriment of Al substitution in Fe_2O_3—was already high from the earlier datasets and literature comparisons:[13] the 1 ML MoO_x dataset bolsters it further.

While 1 ML MoO_x/5% HSA Fe_2O_3 differs from 1 ML MoO_x/10%, 15% and 20% HSA Fe_2O_3 in overall edge shape, as is expected given the difference between the Al substituted

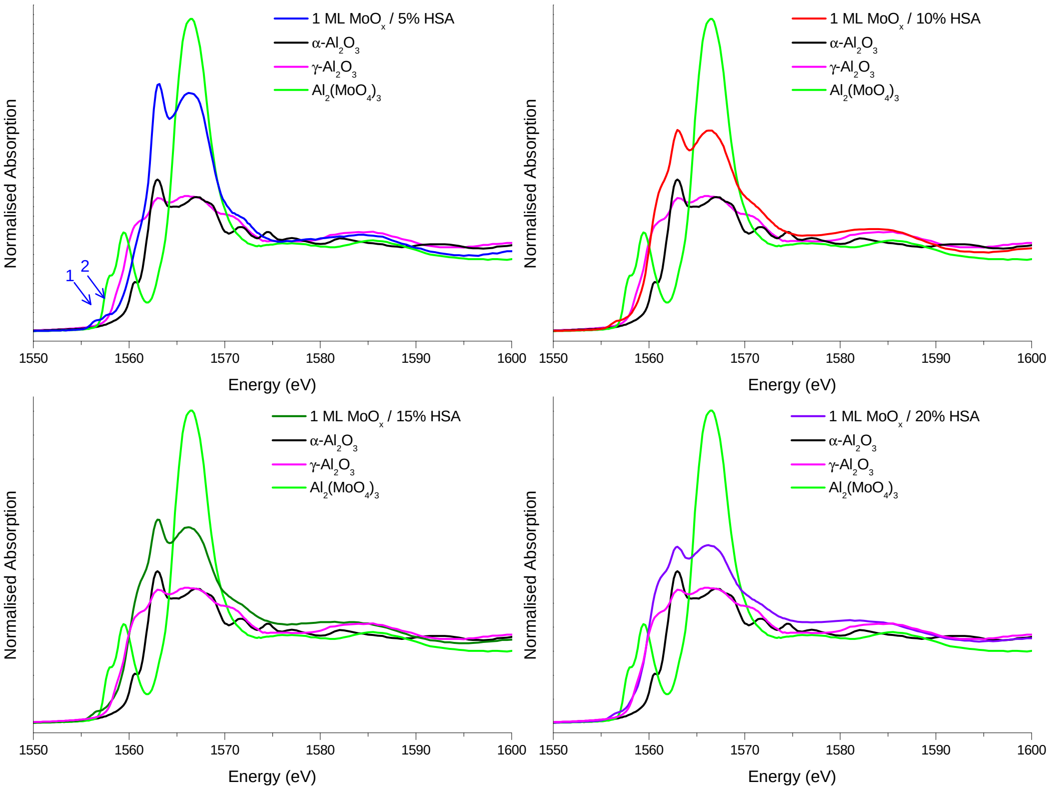

Figure 4.33: A comparison of fluorescence XANES features for 1 ML MoO$_x$/HSA Fe$_2$O$_3$ catalysts against reference compounds. Peaks 1 and 2 correspond to Fe 3d excitations.

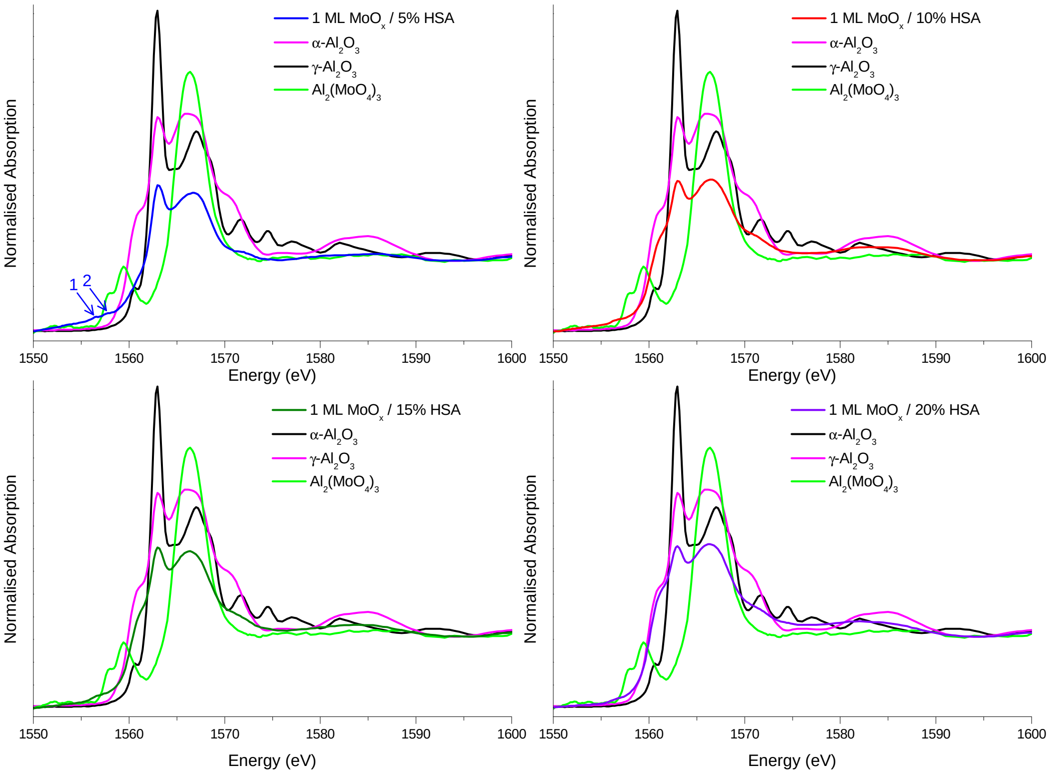

Figure 4.34: A comparison of TEY XANES features for 1 ML MoO$_x$/HSA Fe$_2$O$_3$ catalysts against reference compounds. Peaks 1 and 2 correspond to Fe 3d excitations.

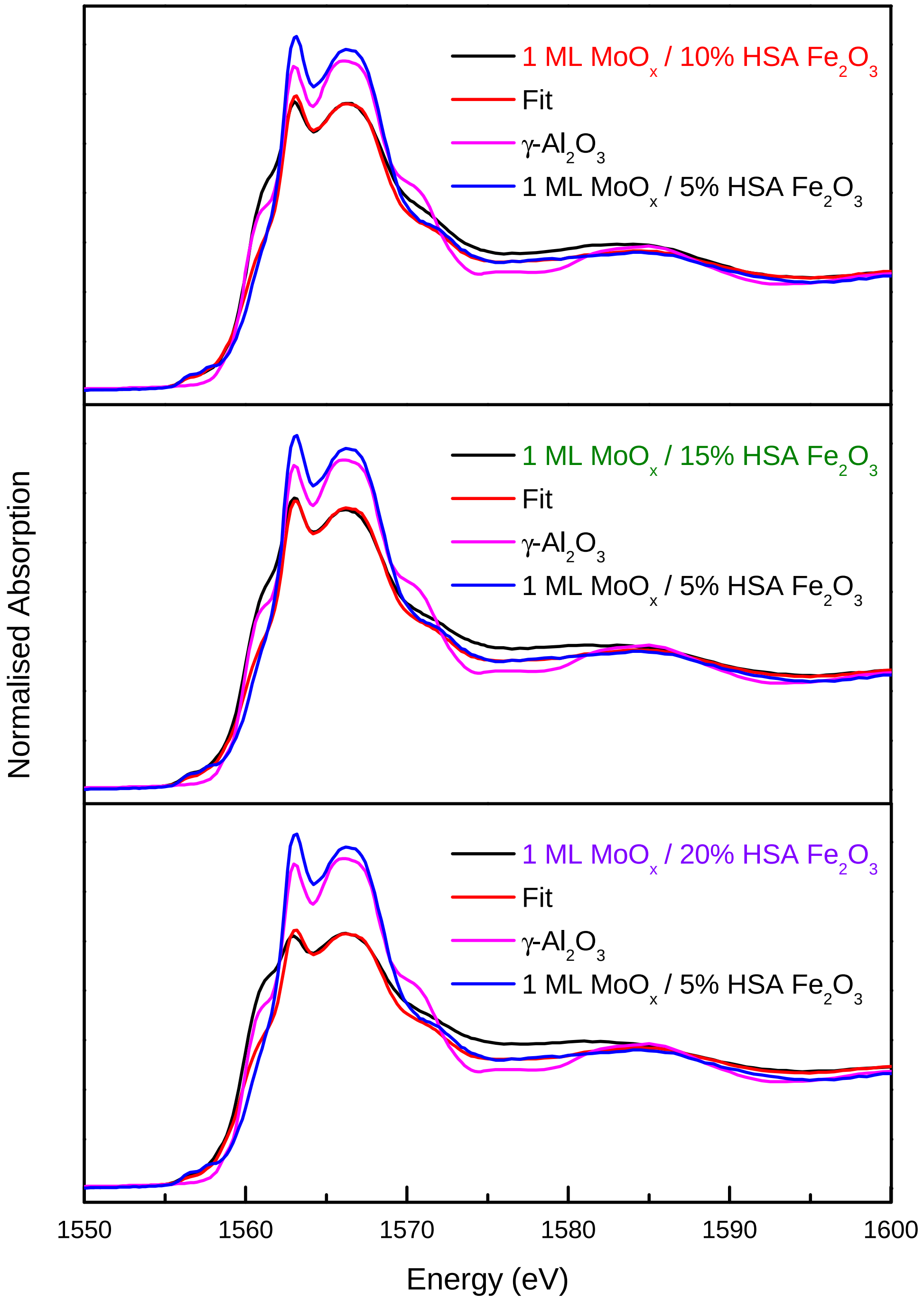

Figure 4.35: A comparison of LCF results for 1 ML MoO$_x$/10%, 15% and 20% HSA Fe$_2$O$_3$ catalysts using γ-Al$_2$O$_3$ and 1 ML MoO$_x$/5% HSA Fe$_2$O$_3$ as standards.

Table 4.7: LCF statistical fitting data from Al XANES measurements of 1 ML MoO_x/10%, 15% and 20% HSA Fe_2O_3 catalysts.

	Similarity to standards (%)		
Species	1 ML/5% HSA	γ-Al_2O_3	R-factor
1 ML MoO_x/10% HSA Fe_2O_3	63.2	36.8	1.78×10^{-2}
1 ML MoO_x/15% HSA Fe_2O_3	45.8	54.2	1.86×10^{-2}
1 ML MoO_x/20% HSA Fe_2O_3	31.2	68.8	2.64×10^{-2}

in Fe_2O_3 at 5% and the Al present as Al_2O_3 for the other loadings, the XANES spectra of the catalysts possess one important likeness: namely, the striking absence of any pre-edge features reminiscent of aluminium-molybdate. For the higher Al loadings, the aluminium molybdate-like pre-edge feature was not observed with the 3 ML MoO_x catalysts, and nor was its presence anticipated for 1 ML MoO_x equivalents: the rationale for this was discussed earlier. Yet the absence of any such pre-edge feature from 1 ML MoO_x/5% HSA Fe_2O_3 creates a marked discrepancy in comparison to the 3 ML MoO_x/5% HSA Fe_2O_3 catalyst. After all, in both cases, the Al has substituted into Fe sites within Fe_2O_3.

In actuality, the absence of an aluminium molybdate-like pre-edge feature for 1 ML MoO_x/5% HSA Fe_2O_3 provides further supporting evidence for the overall trends discussed earlier. Consider the example of a 1 ML MoO_x/Fe_2O_3 catalyst (i.e. non-HSA). 1 ML MoO_x/Fe_2O_3 comprises the Fe_2O_3 core and solely the outermost MoO_x layer, with no sandwich layer of iron molybdate; the sandwich layer can only form when more than one monolayer of MoO_x is present near the surface. Accordingly, for the analogous 1 ML MoO_x/5% HSA Fe_2O_3 catalyst, no iron molybdate sandwich layer is present either. Since the Al dopants cannot inhabit that which does not exist, no Al → Mo pre-edge feature from Al-doped iron molybdate is observed.

4.6 Conclusions

The conclusions obtained from the investigations of Al-doped Fe_2O_3 can be divided into two main portions based on the techniques used to obtain them. It had previously been determined that the inclusion of 5 wt% Al in Fe_2O_3 afforded significant boosts to post-calcination specific surface area. This afforded minor enhancements in reactivity terms without any observable detriment to catalytic selectivities, either when used as naked HSA Fe_2O_3 or when employed in a MoO_x/HSA Fe_2O_3 catalyst. The initial focus of the studies in this chapter was directed towards the attainment of further surface area enhancements through the use of greater quantities of Al: from a surface area perspective, this was successful. The post-calcination surface area could be increased almost fivefold through the incorporation of 15 wt% Al. When the higher loading HSA Fe_2O_3 supports were assessed by TPD and PFR studies, no divergence from the expected Fe_2O_3 behaviour was apparent. In structural terms, no obvious differences could be observed beyond the major difference shared by all HSA Fe_2O_3 materials, that the Fe_2O_3 XRD peaks were broadened and shifted to higher angles (a sign of reduced d-spacing), and the Fe_2O_3 Raman features were similarly affected. This was a highly encouraging start to the investigations.

When used in shell-core catalysts with MoO_x shells, XRD and Raman reveal no change in structural composition, even for the highest loading 20% HSA Fe_2O_3. During reactivity measurements, however, two significant discrepancies appear at higher Al loadings: viz. the production of CO_2 and the emergence of DME (the product of dehydration on alumina). Clearly by the higher loadings, MoO_x/HSA Fe_2O_3 catalysts do not fully resemble the planned shell-core structure of MoO_x/Fe_2O_3, and yet no structural changes could be observed by XRD. Accordingly, while phase separation disrupts the structure sufficiently to disrupt the reactivity, the size of the resulting phase separated aluminous regions must be small. Significant boosts in catalytic activity are obtained with the higher Al loading 3 ML MoO_x/HSA Fe_2O_3 catalysts, which convert more methanol at lower temperatures. This is due to the higher specific surface areas of the HSA Fe_2O_3 catalysts. Crucially, however, while more surface area is available for reaction (boosting activity), not all of it is formaldehyde-selective during reaction with methanol: e.g. the alumina particles are selective to DME.

To understand HSA Fe_2O_3 in more detail, XAS studies were undertaken at the Al K-edge. These were extremely beneficial in elucidating the structural behaviour of the Al-dopants as a function of their concentration. At 5% Al, the XANES data reveal that the Al dopants have indeed adopted positions within the Fe_2O_3 structure as intended, as determined by the presence of two crucial pre-edge features arising from Al-Fe non-local interactions. For 10%, 15% and 20%, however, vastly more Al exists as γ-Al_2O_3—with 20% HSA Fe_2O_3 displaying the strongest similarity to γ-Al_2O_3—and not within the Fe_2O_3 structure, shown by the disappearance of the two diagnostic pre-edge features. This is partially due to the averaging nature of XAS spectra, and the greater relative quantity of Al_2O_3 present at higher Al loadings, but also due to increasing suppression of Al substitution in Fe_2O_3 as more Al is present in the material. A similar phenomenon, wherein the likelihood of Al substitution decreases with increasing Al content, has been reported in the literature;[13] this bolsters confidence in the findings for HSA Fe_2O_3. The trends found for HSA Fe_2O_3 supports are echoed by the XANES data of the 1 ML MoO_x/HSA Fe_2O_3 and 3 ML MoO_x/HSA Fe_2O_3 catalysts, confirming that Al in excess of 5% is not incorporated into the Fe_2O_3 structure as would be desired, but instead phase separates, and that resemblance to Al_2O_3 increases with Al content. Importantly, it must be reiterated that in all cases, the results of phase separation are limited in size, since no phase separation is detectable by XRD.

Further evidence for Al substitution into the Fe_2O_3 structure was gathered from the XANES spectra of 1 ML MoO_x/5% HSA Fe_2O_3 and 3 ML MoO_x/5% HSA Fe_2O_3, where for the latter a third pre-edge peak/shoulder is observed in conjunction with the two pre-edge features from the excitation of the Fe 3d orbitals. The position of the third pre-edge peak corresponds approximately to the pre-edge peak of aluminium molybdate; however, aluminium molybdate cannot be present, since its production requires calcination at temperatures far in excess of those used to produce MoO_x/HSA Fe_2O_3 catalysts. Instead, the third pre-edge peak for 3 ML MoO_x/5% HSA Fe_2O_3 arises from Al incorporated within the iron molybdate sandwich layer, which can only be formed if the Al is evenly dispersed throughout the Fe_2O_3 which mixes with MoO_x to produce iron molybdate. Further proof is offered by the 1 ML MoO_x/5% HSA Fe_2O_3 spectrum. A 1 ML MoO_x catalyst contains no iron molybdate sandwich layer, hence there is nothing into which Al can incorporate: accordingly, the third pre-edge feature arising from Al-doped iron molybdate is not observed for 1 ML MoO_x/5% HSA Fe_2O_3.

In summary, a Goldilocks quantity of Al is now known to exist for Fe_2O_3, which permits Al incorporation into the Fe_2O_3 structure with a concomitant twofold increase in specific surface area. Attempts to produce shell-core catalysts with higher specific surface area values succeed in some cases, but in others at the cost of introducing considerable structural inhomogeneity, namely through the generation of Al_2O_3 particles. The precise quantity of Al required to produce phase separated alumina as opposed to substitution within the Fe_2O_3 structure is unknown, but it is known that it occurs between 5 wt% and 10 wt% Al.

A wide range of interesting future experiments could be undertaken to continue the exploration of this topic. With the knowledge gained from XAS, an extremely useful experiment would be to ascertain the effective maximum Al content possible in Fe_2O_3 while maintaining Al structural substitution and minimising structural irregularities. For example, if it is revealed that 8% or 9% HSA Fe_2O_3 is the maximum before phase separation occurs, the specific surface area of such a material would still be approximately double that of a 5% HSA Fe_2O_3—and fourfold greater than that of pristine Fe_2O_3—but without the structural disruptions deleterious to catalytic selectivities. The studies prior to and reported within this thesis and have focussed on increasing the Al content to maximise the benefit to specific surface area. It would be equally useful to investigate the structural environment of Al dopants in Fe_2O_3 in small quantities by techniques such as XAS. Some basic structural analysis has been performed on low Al content (e.g. 1.3%) Fe_2O_3 supports, but revealed little of interest. This is not due to the material under scrutiny, but rather the methods used to scrutinise. XAS, in contrast to more typical lab-bench analytical methods, can extract an abundance of structural, electronic and speciational information from the sample, and would be ideal for probing the structural behaviour present in low Al loading Fe_2O_3, where Al structural substitution can be guaranteed without the risk of phase separation to alumina. Essentially, there is much yet to explore concerning the use of Al-doped Fe_2O_3 materials for catalytic purposes.

References

(1) U. Schwertmann, *Soil Science*, 1979, **128**, 195–200.

(2) U. Schwertmann, R. Fitzpatrick, R. Taylor and D. Lewis, *Clay and Clay Minerals*, 1979, **27**, 105–112.

(3) A. Zoppi, C. Lofrumento, E. M. Castellucci and P. Sciau, *Journal of Raman Spectroscopy*, 2008, **39**, 40–46.

(4) U. Schwertmann and R. M. Cornell, in *Iron Oxides in the Laboratory*, John Wiley & Sons, Ltd, 2007, ch. 10, pp. 121–135.

(5) S. Chapman, C. Brookes, M. Bowker, E. K. Gibson and P. P. Wells, *Faraday Discussions*, 2016, **188**, 115–129.

(6) W. Li, X. Liang, P. An, X. Feng, W. Tan, G. Qiu, H. Yin and F. Liu, *Scientific Reports*, 2016, **6**, 35960.

(7) L. Truffault, B. Choquenet, K. Konstantinov, T. Devers, C. Couteau and L. J. M. Coiffard, *Journal of Nanoscience and Nanotechnology*, 2011, **11**, 2413–2420.

(8) H. Liu, T. Chen, X. Zou, C. Qing and R. L. Frost, *Journal of Raman Spectroscopy*, 2013, **44**, 1609–1614.

(9) A. M. Jubb and H. C. Allen, *ACS Applied Materials & Interfaces*, 2010, **2**, 2804–2812.

(10) M. Bowker, R. Holroyd, A. Elliott, P. Morrall, A. Alouche, C. Entwistle and A. Toerncrona, *Catalysis Letters*, 2002, **83**, 165–176.

(11) D. Cabaret and C. Brouder, *Journal of Physics: Conference Series*, 2009, **190**, 012003.

(12) D. Manuel, D. Cabaret, C. Brouder, P. Sainctavit, A. Bordage and N. Trcera, *Physical Review B*, 2012, **85**, 224108.

(13) M. Ducher, M. Blanchard, D. Vantelon, R. Nemausat and D. Cabaret, *Physics and Chemistry of Minerals*, 2015, **43**, 217–227.

(14) M.-A. Arrio, S. Rossano, C. Brouder, L. Galoisy and G. Calas, *Europhysics Letters*, 2000, **51**, 454–460.

Chapter 5

Exploring magnetocatalytic effects within a shell-core system

5.1 Introduction

This chapter details the investigations of magnetocatalytic effects displayed by new variants of the familiar shell-core catalyst design within the context of methanol selective oxidation. In particular, two main avenues of interest are addressed: firstly, the investigation of zinc-doped cobalt ferrites as a substitute for haematite as a core material, and the effects on key magnetic properties resulting from different proportions of Zn in the material; and secondly, whether or not, when encapsulated with a MoO_x shell, observable changes to catalytic properties occur with external magnetic influences. The studies reported in this chapter were conducted in concert with the Department of Chemical Engineering at the University of Cape Town, who provided the *in situ* magnetometer vital to the experiments herein. Given that the requisite background knowledge for this chapter is not required elsewhere, a specific detailed introduction to magnetism and magnetic properties is given here as opposed to the introductory chapter.

5.1.1 Magnetism

Before considering the world of magnetocatalysis, it is useful to explore the wider concept of magnetism and the various forms in which it can occur. All magnetism fundamentally originates from the contributions of two sources, namely electric current and the spin magnetic moments of elementary particles; however, to avoid straying unduly far into the realm of particle physics, for chemical purposes, only the spin magnetic moments of atomic electrons need be considered. While the particles within the nucleus (referred to as nucleons) also possess magnetic moments, they are several orders of magnitude smaller than the magnetic moments of electrons and hence negligible in terms of magnetisation. In contrast, in other contexts, e.g. nuclear magnetic resonance (NMR) analysis, the magnetic moments of nucleons are highly significant. In general, the electrons in a material arrange themselves in such a way that their magnetic moments cancel out throughout the entire structure. This is due to the electron configurations adopted by materials being dictated by the Pauli exclusion principle: electrons combine in pairs with opposing magnetic moments. Where unpaired electrons or unfilled orbitals are present in a material, the directions of the unbalanced magnetic moments will continuously vary at random, rendering the material effectively non-magnetic. Nonetheless, the unpaired magnetic moments of such materials can, either spontaneously or in response to an applied external field, line up. Consequently, a net magnetic field will be produced, and the material will appear magnetic.

While the electron configuration of a material exerts the greatest influence on the resultant magnetic properties, the temperature of the material is also relevant. At elevated temperatures, the random motion imparted by thermal vibrations increases, disrupting the ability of the electrons to maintain a unified alignment throughout the structure: this can in turn disrupt the net magnetic field, in some cases nullifying it altogether.

There are five main classifications of magnetism which describe the different arrangements of magnetic moments in a material and hence describe the magnetic behaviour perceived by an observer (Figure 5.1):

(i) Diamagnetism—upon exposure to an applied magnetic field, a diamagnetic material generates an induced magnetic field in the opposite direction, generating a repulsive force. This repulsion neutralises the effects of the applied field, rendering the substance apparently non-magnetic. Diamagnetism originates from the quantum mechanical behaviour of electrons in the presence of an applied field. When a field is applied, electrons orbiting a nucleus experience a Lorentz force from the field in addition to the Coulombic attraction to the nucleus. The Lorentz force can—depending on the orbital direction of the electrons—either increase or decrease the centripetal force acting on the electrons, drawing them into or away from the nucleus respectively. The result is that the magnetic moments aligned against the applied field are strengthened, while those aligned with the field are weakened, creating an overall magnetic moment in opposition to the applied field. These changes in moments are dictated by Lenz's law, which states that the direction of a current induced by a changing magnetic field is such that the induced magnetic field created by the induced current opposes the original changing magnetic field.[1] Alternatively, "*nature abhors a change in flux*".[2] Importantly, all materials, visibly magnetic or not, experience diamagnetism; however, diamagnetic effects are dwarfed by paramagnetic or ferromagnetic effects.

(ii) Paramagnetism—paramagnetic materials contain unpaired electrons unimpeded by the requirements of the Pauli exclusion principle, and therefore able to orient their magnetic moments in any direction. Upon the application of an external magnetic field, however, the magnetic moments of the unpaired electrons align with the field, strengthening it. Examples of paramagnetic materials include radical oxygen, many iron compounds and larger coordination complexes of d or f block metals.

(iii) Ferromagnetism—similarly to paramagnetic materials, ferromagnetic materials also contain unpaired electrons, which will align themselves with the direction of an applied external field. In the absence of such a field, however, the magnetic moments of the electrons in ferromagnetic materials orient themselves in a parallel direction to access a lower energy state, meaning that the material appears magnetic with or without an external field. With a field applied, the flux density is greatly enhanced by direct coupling interactions between the moments, facilitated by the crystalline structure. This form of magnetism is the most well known, with many examples including metallic iron, cobalt and rare earth metals.

(iv) Antiferromagnetism—in antiferromagnetic materials, the magnetic moments of neighbouring valence electrons are inclined to point in opposing directions. Across the wider structure, each pair of neighbours is anti-parallel, and consequently there is no net inherent magnetic moment. When an external field is applied to an antiferromagnet, a non-zero net magnetisation can be induced, but this is typically small. Antiferromagnetic behaviour is observed in many transition metal compounds, including *inter alia* haematite and nickel oxide; however, it can only be observed at low temperatures, below the Néel temperature. At or above this temperature, the thermal energy of the material is strong enough to destroy the microscopic ordering within the material responsible for antiferromagnetism. In general, the Néel temperatures of most materials occur at cold temperatures (e.g. 116 K for MnO), though examples of high Néel temperatures do exist (e.g. 948 K for Fe_2O_3).

(v) Ferrimagnetism—similarly to antiferromagnetic materials, there is a proclivity for neighbouring valence electrons in ferrimagnetic substances to point in opposite directions; however, the opposing magnetic moments in ferrimagnetic materials are uneven, yielding a net spontaneous magnetisation. This derives from the differences in the magnitudes of the magnetic moments of two or more separate sublattices within a structure, as is found for example in magnetite (iron(II,III) oxide). Magnetite contains both Fe^{2+} and Fe^{3+}, whose magnetic moments differ in magnitude: consequently, though aligned antipodally, a net magnetisation remains.

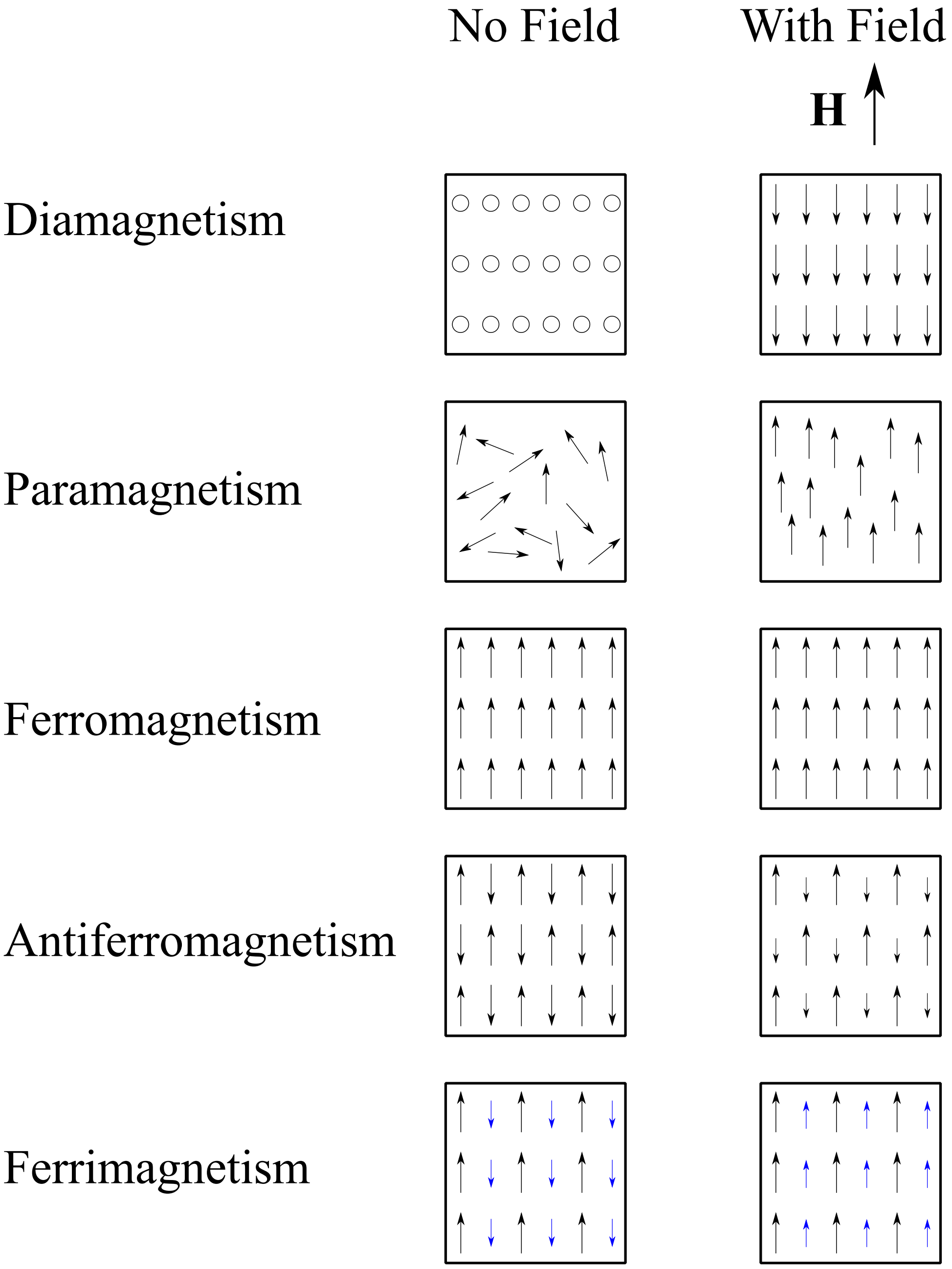

Figure 5.1: Schematic diagrams of the magnetic ordering in each class of magnetism.

There are additional forms of magnetism beyond the five main classes reported above, including metamagnetism and superparamagnetism. The former concerns dramatic increases in magnetisation with only a small change in external field properties, while the latter is found in small nanoparticles of ferromagnetic and ferrimagnetic materials. In the absence of an externally applied field, the magnetisation direction of a superparamagnetic material can invert due to the effects of temperature. The period of time between magnetic moment direction inversions is called the Néel relaxation time.[3] Since the sampling time resolution of techniques used to measure magnetisation is significantly greater than the Néel relaxation time, on average the magnetisation appears to be zero. This nominally zero magnetisation is the result of superparamagnetism. If an external field is applied to superparamagnetic nanoparticles, the nanoparticles will be magnetised akin to a normal paramagnet, but with vastly greater magnetic susceptibility than standard paramagnetic materials.

The magnetic properties of ferromagnetic, ferrimagnetic and antiferromagnetic materials—i.e. those with magnetic ordering—are not constant throughout their structures. Instead, each material is composed of magnetic domains, regions in which the magnetisation is uniform. Each region will not necessarily align its magnetisation with any other region, though the chance of alignment can be affected by the presence of an external influence or with certain internal magnetic properties. The spontaneous formation of magnetic domains in a material arises from the desire of a material to minimise its internal energy.[4] For a ferromagnetic material, for example, a large region of uniform magnetic moments creates a net magnetic field which extends beyond the boundaries of the particle, requiring significant magnetostatic energy (Figure 5.2A). To lessen this energetic demand, the material can divide to form two domains of opposite magnetisations, reducing the extra-material magnetic field to loops at the ends of the material (Figure 5.2B). These two domains can themselves divide, to form four domains with alternating magnetisations (Figure 5.2C). This process can continue until the magnetostatic energy of the material is satisfactorily minimised.

On a microscopic level, the magnetic moments in a ferromagnetic material are aligned with their neighbours in magnetic domains, producing large local magnetic fields; over the wider structure, however, structural energy minimisation weakens the large scale (i.e. non-local) magnetic field through the nullification of opposing field directions. Consequently, a ferromagnetic material existing in its lowest energy state is deemed unmagnetised. It is not always possible, however, for a ferromagnetic material to access its lowest energy state. Other configurations of magnetic domains can be adopted, for example those in which the magnetisation of the domains is aligned, producing a net external magnetic

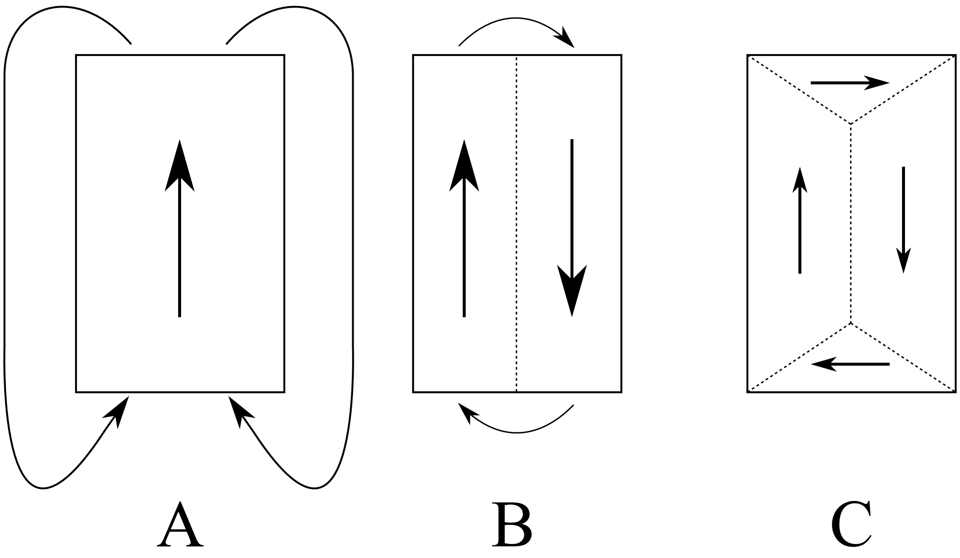

Figure 5.2: The origin of magnetic domains.

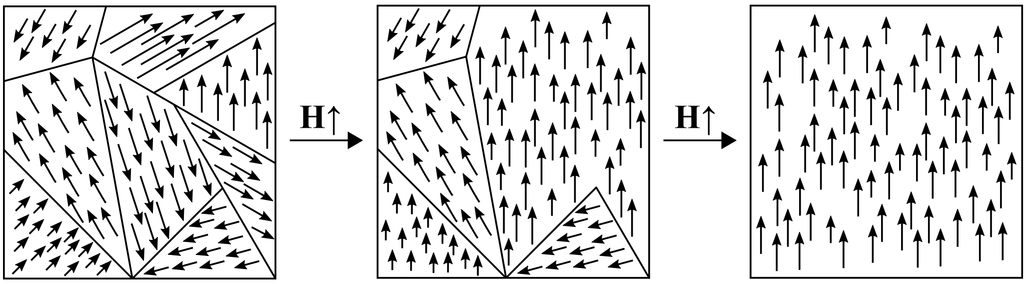

Figure 5.3: The effects of increasing external field strength upon magnetic domains. **H** ↑ indicates increasing external field strength in an upward direction.

field. Such configurations can be created by crystal defects fixing the domains in place and impeding attempts to minimise magnetostatic forces by the rotation of magnetic domains. These fixed configurations are not the lowest energy states, but represent local energy minima; moreover, they can be extremely stable depending on the environment around the material. The walls of each domain can be manipulated through the application of an external magnetic field: those aligned with the field will grow in size, while those oriented contrarily will shrink (Figure 5.3). When the applied field is removed, the domains are fixed in their new arrangements, aligned with the now-removed field, and thus an overall spontaneous magnetic field remains: this phenomenon is known as magnetic hysteresis. Without any further external influence, all ferromagnetic materials will return to their unaligned lowest energy state; however, the lifetime of this process is dependent on the material and its situation. Some materials will relapse relatively speedily, while some will remain magnetised for centuries if left undisturbed.

It is equally possible to demagnetise a ferromagnetic material, which is effectively the inverse of the procedure described above. By subjecting the magnetised material to physical vibration (e.g. by hammering), by heating it or by applying a rapidly oscillating external magnetic field (known as degaussing), the walls of the domains are released from their pinned states, allowing them to rotate to their favoured lower energy configurations with weaker overall spontaneous magnetic field.

5.1.2 Magnetocatalysis

The modern catalysis chemist has a wide variety of techniques at his disposal to tweak and influence the progress of a catalytic reaction, for example by modifying pressure, temperature and electrical properties. There are other means, however, to affect catalytic processes as they occur: one option is to apply a magnetic influence. The idea of imparting catalytic changes from the application of an external magnetic field existed throughout the 20th century, but attracted comparatively little research interest. This is due partially to the nascent nature of such studies, but also to the niche nature of magnetic investigations within chemistry and the corresponding scarcity of appropriate equipment.

Research into the relationship between magnetism and catalysis was first conducted by Hedvall et al. in the 1930s, who initially studied the changes occurring in catalytic activity concomitant with a change in crystal properties and subsequently with a change in magnetic properties.[5,6] They posited that, when a material passes its Curie temperature—the temperature at which permanent magnetism (in this instance ferromagnetism) is lost and replaced by paramagnetism—the state of the electrons in the material will change accordingly. Since these electrons may participate in catalytic reactions, modifying them in any way might in turn modify the activity of the catalyst.[6] The systems of interest to Hedvall et al. were the decomposition of nitrous oxide and carbon monoxide over nickel and cupronickel catalysts respectively and the hydrogenation of unsaturated oils over cupronickel/copper-palladium alloy catalysts. In all three cases, a marked increase in reaction yield occurs simultaneously with the loss of ferromagnetism at the Curie temperature.[7–9] Later, Hedvall studied the decomposition of formic acid over a cobalt-palladium alloy catalyst. In this instance, the activation energy of the decomposition is increased by approximately 30% when ferromagnetism is lost. They concluded that the greater electronic order afforded by a crystalline ferromagnetic material provides a stronger catalytic action, reducing the activation energy and thereby enhancing the catalysis.[6]

Subsequent studies attempted to replicate the magnetocatalytic effects observed by Hedvall (often referred to eponymously) in similar catalytic systems, albeit to varying degrees of success. In 1937, Forestier et al. reported a clear relationship between the catalytic properties of ferromagnetic oxides and the Curie temperature during the decomposition of acetic acid over various iron oxides.[10] This was manifested by a sudden—though fleeting—increase in catalytic activity at the Curie temperature; above the Curie temperature, catalytic activity remains briefly constant before resuming its trajectory from before the discontinuity at the Curie temperature.[10] In 1942, Olmer experimented with a range of ferromagnetic catalysts (Fe, Co, CMn_3 and BMn among others) for carbon monoxide decomposition, but was unable to see the purported Hedvall effects.[11]

Selwood et al. investigated magnetic influence in the hydrogenation of benzene over mixed nickel/copper catalysts.[12] They reported that catalytic activity decays linearly with decreasing catalyst ferromagnetism. Similar investigations were undertaken by Lielmezs et al. for ethylene hydrogenation over nickel catalysts but with external magnetic fields applied at times.[13] They noted a significant discontinuity in activation energy at the Curie temperature for experiments conducted in the absence of an external field, while for cases with a field applied, irregular oscillations in reactant conversion rate and overall reaction rate were seen. Below the Curie temperature, an external field decreased the rate of ethylene hydrogenation, while the opposite was true above the Curie temperature.[13,14] Additionally, Mehta and Sales reported comparable decreases in the activation energies of nickel carbonylation and nickel oxidation adjacent to the Curie temperature.[15,16] Notwithstanding the efforts discussed above, the area remains poorly researched, and the causes and impact of magnetocatalytic effects have yet to be fully rationalised. Accordingly, the field is ripe for further exploration and scrutiny.

5.1.3 Spinel ferrites

One material to have piqued considerable interest in recent years as a magnetic material is cobalt ferrite, which is the subject of the experiments detailed in this chapter. It exists in the spinel structure with general formula AB_2X_4. In a typical spinel structure, the two cations A and B possess different oxidation states (+2 and +3 respectively), though various alternative combinations of multivalent cations are known. In a spinel ferrite, the magnetic moments of all A cations align in one direction, while the magnetic moments of B cations orient antipodally. Since there are twice the number of B sites as A sites within the structure, there is a net spontaneous magnetisation and the material is ferrimagnetic. The magnetic properties of such spinel ferrites can be tweaked relatively easily by altering the metal cations and ionic distribution throughout the structure.[17,18]

Many synthetic methods have been employed to produce spinel ferrite nanoparticles, including the microemulsion, combustion and polyol methods and nonhydrolytic seed-mediated growth processes.[17,19–23] These methods are popular, as they permit precise control of the size and shape of the resulting nanoparticles. For example, Song et al. synthesised spherical nanocrystals of cobalt ferrite with mean diameter 5 nm by a nonhydrolytic process using acetylacetonate coordination compounds of iron and cobalt. These 5 nm spheres were then employed as seeds for further development of a larger nanocrystalline structure (reaching 9 nm in diameter at greatest extent). Notwithstanding the impressive capabilities of the synthetic methods above, co-precipitation remains a stalwart method to produce cobalt ferrite nanoparticles, primarily due to its simplicity.

The physical properties of a cobalt ferrite sample can be modified by temperature, with calcinations at higher temperature removing smaller nanoparticles in favour of larger aggregations. This shift in particle size properties also modifies the magnetic properties of the material, increasing its Curie temperature and modifying the magnitude of its spontaneous magnetisation. The addition of dopants to the cobalt ferrite structure can also affect physical and magnetic properties. In the cubic crystal structure of spinel ferrites, the overall magnetic order arises from a superexchange interaction—antiferromagnetic coupling between two next-to-nearest cations through an intermediary non-magnetic anion—between the cations in the A and B sublattices. By introducing a non-magnetic cation, for example zinc, which prefers to occupy A sites, superexchange can be hindered, in turn affecting the magnetic properties of the resulting nanoparticles.[24]

Importantly, the degree of the effect depends on the proportion of the substitute cation present. Gul et al. experimented with a range of aluminium-doped cobalt ferrites produced by a sol-gel method, and found that particle size could change from 17 to 27 nm as the aluminium fraction approached half.[25] In contrast, Arulmurugan et al. noted the opposite behaviour when zinc was substituted for up to one half of the cobalt and the particles were produced by co-precipitation. It was seen that increasing the quantity of zinc in the structure decreased the average particle size from 11.7 to 8.9 nm.[26] Preliminary investigations into the tunability of cobalt ferrite magnetic properties by zinc substitution have been undertaken by Yaseneva et al. in 2011, who reported that increasing zinc doping decreased the Curie point of the material.[27] The findings of Yaseneva et al. are of particular relevance to this thesis, as the motivation for the studies reported in this chapter was to exposit the effects of zinc doping.

5.1.4 Research objectives

The studies in this chapter sought to explore whether magnetocatalytic effects might be visible in methanol selective oxidation. It was hoped that the well-understood shell-core catalyst framework developed for MoO_x/Fe_2O_3 (and subsequently for VO_x/Fe_2O_3, see Chapter 3) would be sufficiently adaptable to permit the inclusion of a magnetic core material, which would then render the shell-core catalyst susceptible to magnetic influence. Cursory preliminary experimentation on magnetocatalytic effects on molybdenum-containing catalysts was performed in the Bowker group almost a decade ago, which, while unpublished, was sufficiently encouraging to warrant further study.

This chapter seeks to answer four main questions:

(i) Can a magnetic material be successfully employed as the core moiety with a MoO_x shell in a shell-core catalyst?

(ii) Can the magnetic properties of the material be altered to situate the Curie temperature within the relevant temperature range for methanol oxidation?

(iii) Are magnetocatalytic effects evident during methanol oxidation?

(iv) Does the position of the Curie temperature influence any such magnetocatalytic effects?

These studies will be guided by the knowledge of prior shell-core catalysts based on (non-magnetic) haematite. The reactivity and catalytic behaviour observed in such systems will be particularly helpful when attempting to rationalise the behaviour of magnetic shell-core catalysts.

5.2 Experimental

The experimental conditions and synthetic methods used to produce cobalt ferrites, zinc-doped cobalt ferrites and subsequently the shell-covered catalysts are detailed in Chapter 2. To summarise, all catalyst support materials of any Zn loading were prepared by co-precipitation of various quantities of cobalt nitrate, iron nitrate and zinc nitrate. Incipient wetness impregnation with ammonium heptamolybdate was performed to produce $MoO_x/CoFe_2O_4$ shell-core catalysts, and all samples were calcined at 500°C for 24 hours prior to use.

Since this research was a joint project between Cardiff University and the University of Cape Town, experimentation was split into two stages. The first part of the research, involving the investigation of Zn-doping, *ex situ* catalytic testing and *ex situ* magnetometry, was undertaken at Harwell. The second stage of the project was performed at the University of Cape Town, which involved the use of the *in situ* magnetometer and reactor capable of applying magnetic fields between $-2\,\mathrm{T}$ to $2\,\mathrm{T}$.

5.3 Cobalt ferrite: a suitable core material?

For a shell-core catalyst of type MO_x/Fe_2O_3 (where M = Mo or V), it is essential that the core be effectively isolated and unable to directly participate in catalysis. This is due to the fundamental differences in the selectivities displayed by shell and core components respectively: for MoO_x/Fe_2O_3 catalysts, the shell MoO_x species are selective to formaldehyde, while the Fe_2O_3 core is an eager combustor of methanol, producing CO_2. That such strong differences in selectivity exist between the components is extremely beneficial, as reliable indicators of shell integrity (the degree to which the core is isolated) are accordingly produced in methanol TPD measurements: if CO_2 is seen in TPD, the shell is improperly formed, and the core is exposed.

For the purposes of investigating magnetocatalytic effects with shell-core catalysts, however, haematite is magnetically uninteresting. It was necessary therefore to seek an alternative material, one which exhibits the desired magnetic properties while resembling the reactivity of haematite. This latter consideration is vitally important: any deviations from the expected behaviour of the shell-core model can only be assessed if the core combusts methanol. The most promising candidate was cobalt ferrite, $CoFe_2O_4$, a ferrimagnetic material with a Curie temperature of 440°C.[27] Before continuing further study of cobalt ferrite, it was essential to verify that it resembles the behaviour of haematite in TPD (Figure 5.4).

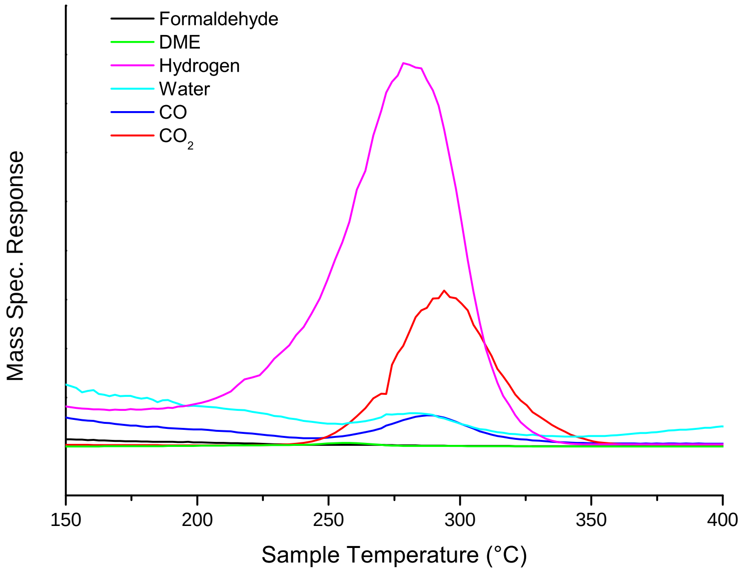

Figure 5.4: TPD data for $CoFe_2O_4$ after methanol dosing, displaying strong methanol combustion. Gas flow: 30 mL/min He. Sample mass: 175 mg.

It is evident in TPD that $CoFe_2O_4$ combusts methanol, producing CO_2 and H_2 as the major products along with smaller quantities of CO. Crucially, no selective products are observed, neither formaldehyde nor DME. From a reactivity perspective, $CoFe_2O_4$ is therefore an excellent substitute for Fe_2O_3 as a core material.

To make the most efficient use of the time available for these studies, it was decided not to investigate cobalt ferrite *per se* in detail, beyond this initial confirmation of appropriate reactivity. Instead, focus was directed at a series of analogous doped cobalt ferrite compounds whose Curie temperatures could be moved to temperatures more relatable to the operating temperatures of methanol oxidation.

5.3.1 Zinc-doped cobalt ferrites

The effects of substituting zinc for cobalt in $CoFe_2O_4$ have been investigated before, revealing a trend between Zn loading and the position of the Curie temperature:[27] the greater the substitution of Zn for Co, the lower the Curie temperature. The resulting structures are labelled zinc-doped cobalt ferrites, with general formula $Zn_xCo_{1-x}Fe_2O_4$. For brevity and clarity, however, throughout this chapter Zn-doped cobalt ferrites are referred to in the text as x ZnCoFe where x = Zn fraction: e.g., $Zn_{0.4}Co_{0.6}Fe_2O_4$ is 0.4 ZnCoFe.

While the greatest attention was given to whether magnetocatalytic effects would be seen at all, it was decided to simultaneously investigate whether the position of the Curie temperature influenced any observed magnetocatalytic effects. In TPD and PFR studies of methanol oxidation over MoO_x/Fe_2O_3 catalysts, the temperature range within which high formaldehyde selectivity is seen spans from 200 to 250°C. Efforts focussed therefore on producing three different loadings of ZnCoFe, namely 0.35, 0.4 and 0.45 Zn fraction, each with a different Curie temperature. These values would lie at the beginning, middle and end of the formaldehyde-producing region respectively, to gauge whether positioning the Curie temperature in and around this region would influence catalytic behaviour. All three samples were calcined at 500°C for 24 hours; while calcination temperature is a known means of modifying Curie temperature position, for these studies Zn loading was to be the only variable.

Characterisation

Although it was found that $CoFe_2O_4$ itself behaves like Fe_2O_3 in the presence of methanol, it was vital to understand whether the incorporation of Zn into the ferrite structure altered its selectivity during methanol oxidation. To assess this, and assure the continued validity of TPD as a means of measuring the degree of shell-core segregation when a shell layer is added, a 0.4 ZnCoFe sample was prepared and measured by TPD (Figure 5.5).

The TPD data for 0.4 ZnCoFe resemble those of unadulterated $CoFe_2O_4$, where CO_2 is produced in large quantities alongside H_2, indicating that combustion remains the predominant process. The two other samples, 0.35 and 0.45 ZnCoFe, were similarly tested by TPD and found to exhibit extremely similar behaviour (Figures 5.6 and 5.7). There are discrepancies between the apparent quantity of hydrogen produced by samples with different Zn loadings, but this is likely attributable to experimental differences from the mass spectrometer between sample measurements and not a signal of significantly different catalytic behaviour between samples. Considering the TPD findings from the three ZnCoFe samples, it can be safely assumed that TPD will again provide reliable indications of the status of the MoO_x shell in any MoO_x/ZnCoFe shell-core catalyst.

XRD analysis of Zn-doped cobalt ferrite is essential to ensure that no significant structural changes are caused by the addition of Zn. In particular, there should be no differences structurally between the three Zn loadings: if they all differ from unadulterated cobalt

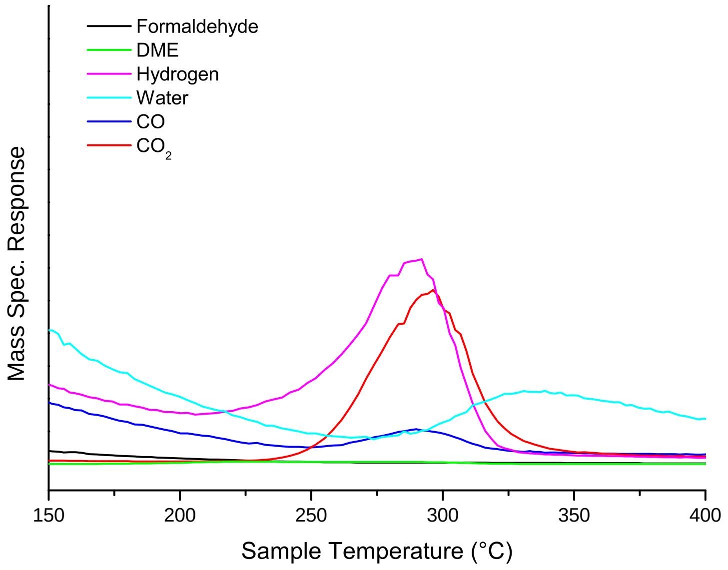

Figure 5.5: TPD data for 0.4 ZnCoFe: no significant differences from ordinary $CoFe_2O_4$ are seen and combustion remains the major process. Gas flow: 30 mL/min He. Sample mass: 175 mg.

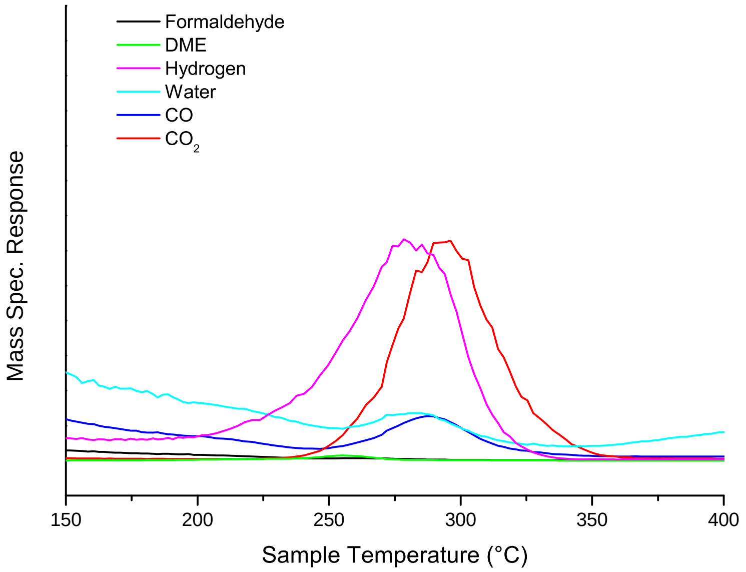

Figure 5.6: TPD data for 0.35 ZnCoFe: no significant differences from ordinary $CoFe_2O_4$ are seen and combustion remains the major process. Gas flow: 30 mL/min He. Sample mass: 175 mg.

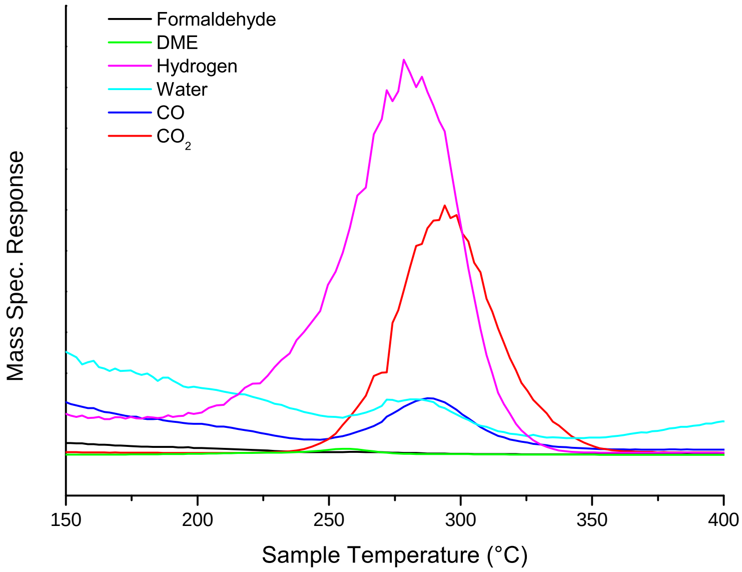

Figure 5.7: TPD data for 0.45 ZnCoFe: no significant differences from ordinary $CoFe_2O_4$ are seen and combustion remains the major process. Gas flow: 30 mL/min He. Sample mass: 175 mg.

ferrite, they must differ uniformly. By XRD, no significant differences were seen between the samples (Figure 5.8), confirming that no structural changes result from increasing the Zn fraction from 0.35 to 0.45. Given the number of published studies on $CoFe_2O_4$, plenty of reference XRD data exist in the literature: the key peaks are found at 2θ values of 18, 30, 35, 37, 44, 53, 57, 63 degrees.[28] The XRD patterns obtained for all three ZnCoFe samples display similar peaks at identical values of 2θ. Accordingly, it can be concluded the inclusion of any amount of Zn below a fraction of 0.45 does not detrimentally affect the overall ferrite spinel structure. This is an important result. With it known that Zn-doped cobalt ferrites behave like, and are structurally indistinguishable from, undoped cobalt ferrites, they can be used in shell-core catalysts with confidence.

XPS data from 0.35, 0.4 and 0.45 ZnCoFe have also been collected, which revealed nothing untoward nor anything unexpected of (Zn-doped) cobalt ferrite (Figures 5.9, 5.10 and 5.11). Comparing the measured binding energies with those reported in the literature indicated that Fe exists as Fe(III), Co as Co(II) and Zn as Zn(II).[29] Importantly, no significant discrepancies between Zn loadings were observed, signifying that no visible changes in metal speciation occur as a function of Zn loading.

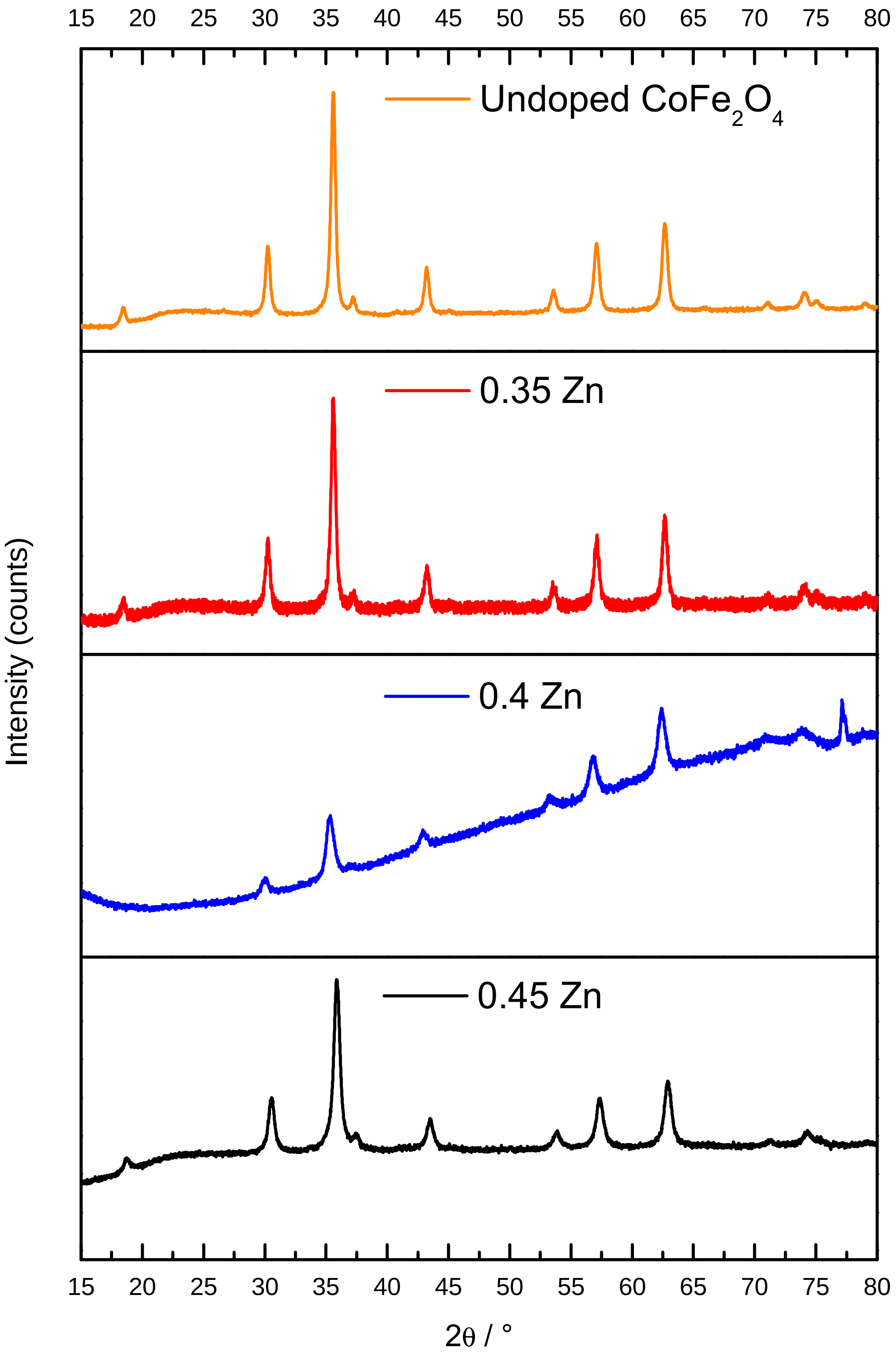

Figure 5.8: XRD patterns for 0.35, 0.4 and 0.45 ZnCoFe. The 0.4 ZnCoFe sample could not be made to remain on the goniometer during the measurement, with powder lost from the sample disc as the angle steepened, causing a rising background; however, the significant peaks from cobalt ferrite are nonetheless visible.

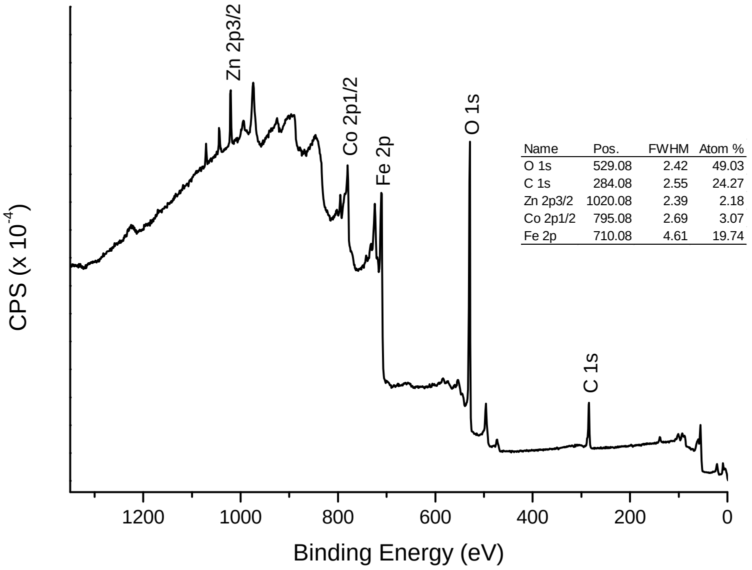

Name	Pos.	FWHM	Atom %
O 1s	529.08	2.42	49.03
C 1s	284.08	2.55	24.27
Zn 2p3/2	1020.08	2.39	2.18
Co 2p1/2	795.08	2.69	3.07
Fe 2p	710.08	4.61	19.74

Figure 5.9: XPS data from 0.35 ZnCoFe.

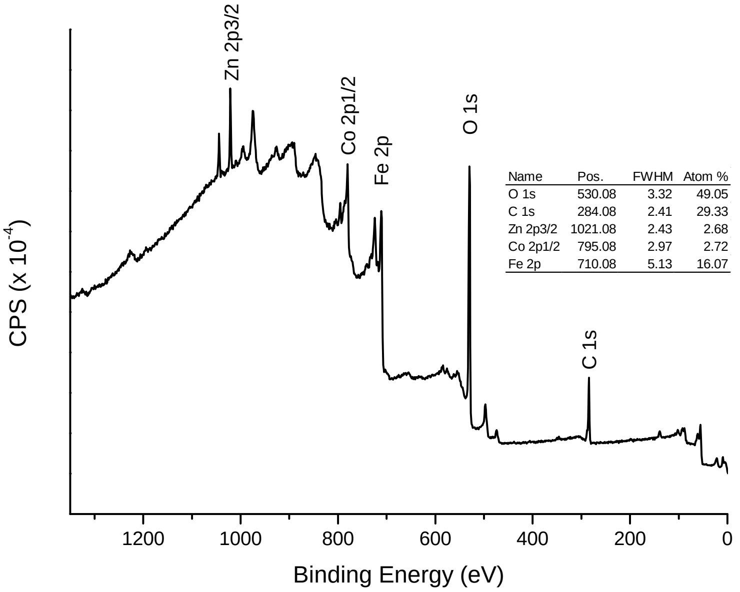

Name	Pos.	FWHM	Atom %
O 1s	530.08	3.32	49.05
C 1s	284.08	2.41	29.33
Zn 2p3/2	1021.08	2.43	2.68
Co 2p1/2	795.08	2.97	2.72
Fe 2p	710.08	5.13	16.07

Figure 5.10: XPS data from 0.40 ZnCoFe.

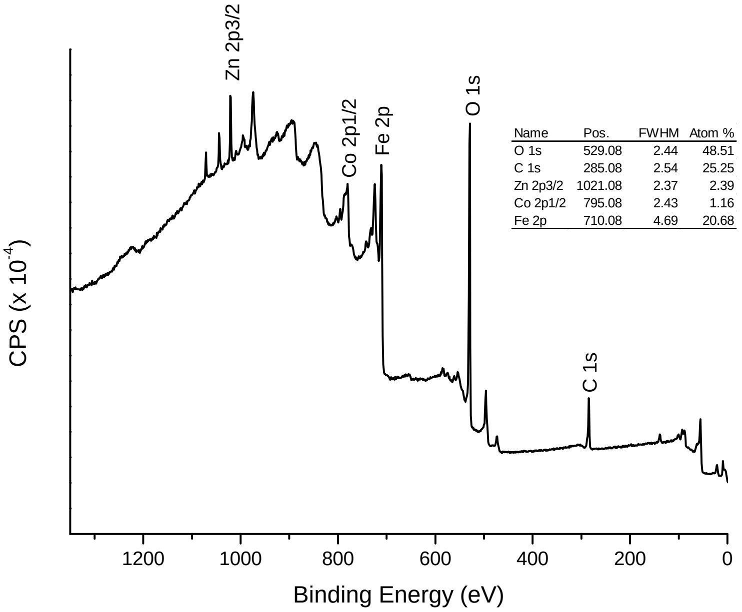

Figure 5.11: XPS data from 0.45 ZnCoFe.

Magnetic properties

Having synthesised three ZnCoFe samples with different Zn loadings, *ex situ* magnetometric measurements were performed. These measurements sought firstly to gauge the value of the Curie temperature in each sample, and secondly to verify that the decrease in Curie temperature was roughly linear with the quantity of Zn present. Each sample was analysed with a benchtop magnetometer, which heated each sample to 400°C while measuring magnetic susceptibility. Encouragingly, the distribution of Curie temperature positions echoed earlier work and confirmed that linear increases in Zn loading afford effectively linear decreases to the position of the Curie temperature (Figure 5.12):[27] the measured values are tabulated to aid comprehension (Table 5.1). The aim was to bracket the formaldehyde-producing temperature region with a Curie temperature value at either extreme and one in the middle of the region: this has been successfully achieved.

Table 5.1: Measured Curie temperature values for 0.35, 0.4 and 0.45 ZnCoFe samples as determined by *ex situ* magnetometry.

Zn loading (decimal fraction)	Recorded T_c (°C)
0.35	281
0.40	245
0.45	195

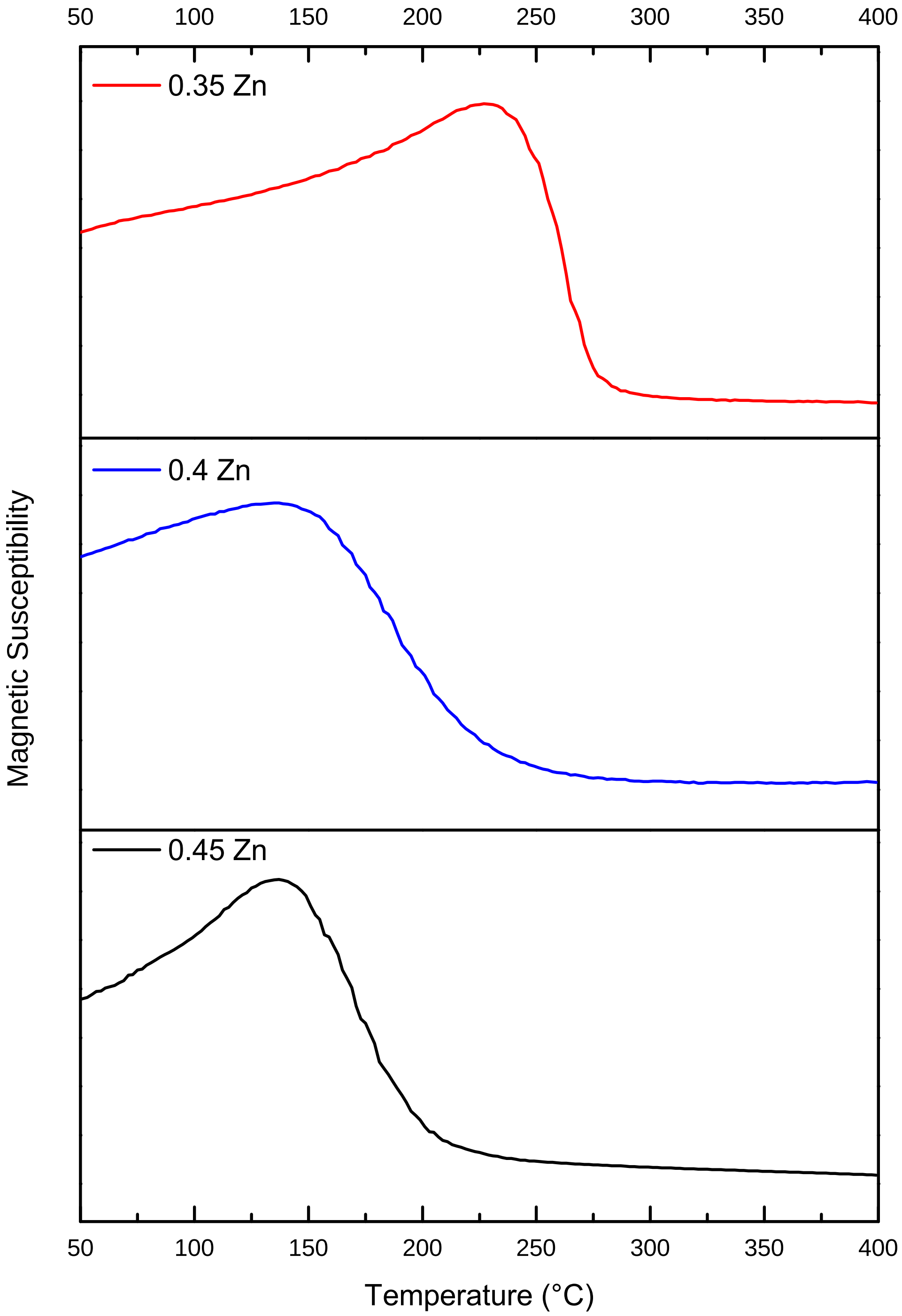

Figure 5.12: Magnetic susceptibility curves as a function of increasing temperature for 0.35, 0.4 and 0.45 ZnCoFe samples. The Curie temperature is determined by drawing a tangent parallel to the downward gradient at the midpoint of the decline in magnetic susceptibility to the abscissa.

5.3.2 Producing MoO_x/Zn-doped cobalt ferrite shell-core catalysts

Having established that cobalt ferrite and Zn-doped cobalt ferrite mimic haematite in terms of reactivity, the next question to answer was whether shell-core formation could proceed with Zn-doped cobalt ferrite cores. For MoO_x/Fe_2O_3 catalysts, 3 ML catalysts were generally used for experimentation, as this was thought to provide an ideal balance between shell material presence at the surface and overthickening of the shell layers (and consequently producing more bulk iron molybdate at the surface); however, other ML coverages were tested at an early stage before focussing on 3 ML. When planning the experiments conducted for this chapter, however, it was not possible to investigate a full range of MoO_x ML coverages on Zn-doped cobalt ferrites due to the time constraints of the student exchange and time available on the *in situ* magnetometer. Consequently, efforts were concentrated on one ML coverage, viz. 6 ML MoO_x. Brief preliminary studies had been conducted on 3 ML $MoO_x/CoFe_2O_4$ catalysts, wherein difficulties in ensuring proper shell-core segregation were encountered. While the causes of these problems were not identified, to maximise the chances of avoiding similar issues a larger ML coverage was chosen. It was considered that the monolayer calculations might be underestimating the quantity of MoO_x precursor required, resulting in insufficient shell material leaving the core exposed. To combat this, catalysts would be produced with a larger quantity of MoO_x for these studies, namely 6 ML.

Similarly to the investigations of MoO_x and VO_x/Fe_2O_3 catalysts, TPD measurements are the most immediately useful, since they reveal key information regarding the status of the shell-core catalyst. The first catalyst to be produced utilised the 0.4 ZnCoFe sample as the core component, onto which 6 ML of MoO_x was deposited by incipient wetness impregnation, after which the catalyst was dried and then calcined at 500°C. No catalysts were prepared with calcination temperatures lower than 500°C. Unlike the earlier studies of MoO_x and VO_x/Fe_2O_3, investigations of the formation process of MoO_x/ZnCoFe were not conducted due to time constraints. Since calcination temperature has a direct impact upon the magnetic properties of the catalyst, great care was taken not to exceed 500°C: higher temperature calcination destroys smaller nanoparticles and raises the Curie temperature. In this instance, the 0.4 ZnCoFe support had previously been calcined, so no further undesirable changes would occur during calcination of the MoO_x-doped catalyst. Once calcined, 6 ML MoO_x/0.4 ZnCoFe was analysed by TPD (Figure 5.13).

Strong selectivity to formaldehyde is witnessed from approximately 170 to 250°C, mimicking the selectivities demonstrated by MoO_x/Fe_2O_3 and VO_x/Fe_2O_3 catalysts; however,

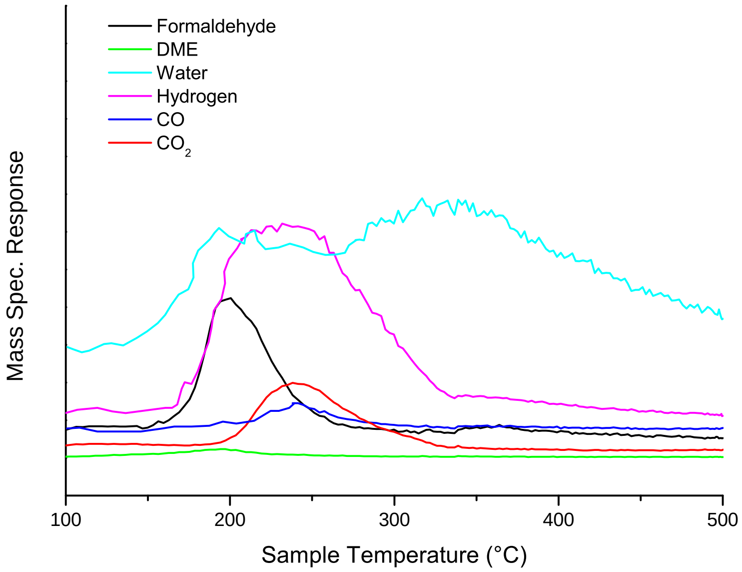

Figure 5.13: TPD data for 6 ML MoO_x/0.4 ZnCoFe. Gas flow: 30 mL/min He. Sample mass: 175 mg.

some CO_2 is also produced. This indicates that at least some portions of the ZnCoFe core are exposed and directly participating in catalysis. Nonetheless, significant portions of the MoO_x shell must be properly formed, for greater selectivity to formaldehyde than CO_2 is seen: given the thermodynamic preference for full combustion, that a greater quantity of formaldehyde is still produced indicates that the core is mostly segregated.

Similar results are seen for the other two catalysts, 6 ML MoO_x/0.35 ZnCoFe and 6 ML MoO_x/0.45 ZnCoFe (Figures 5.14 and 5.15). Some differences are apparent for the 0.35 ZnCoFe-based catalyst, which appears to have two separate smaller regions in which CO_2 is produced, rather than one large peak as for 0.4 and 0.45 ZnCoFe. This could indicate that the shell in 6 ML MoO_x/0.35 ZnCoFe was more effectively formed, but this could also arise from experimental error. Nevertheless, the fundamental TPD trends are alike irrespective of Zn loading. This is a vitally important result: were the proportions of core constituents to affect the resulting catalysis, no sound comparisons between the catalysts could be made.

PFR studies of 6 ML MoO_x/ZnCoFe catalysts were also conducted to reinforce the TPD findings (Figures 5.16, 5.17 and 5.18). No significant differences are discernible between the different Zn loadings, which bolsters the assertion that incorporating Zn into the cobalt ferrite structure does not influence the resultant catalytic properties. Strong selectivity to formaldehyde is seen for all catalysts at temperatures below 250°C, while notable

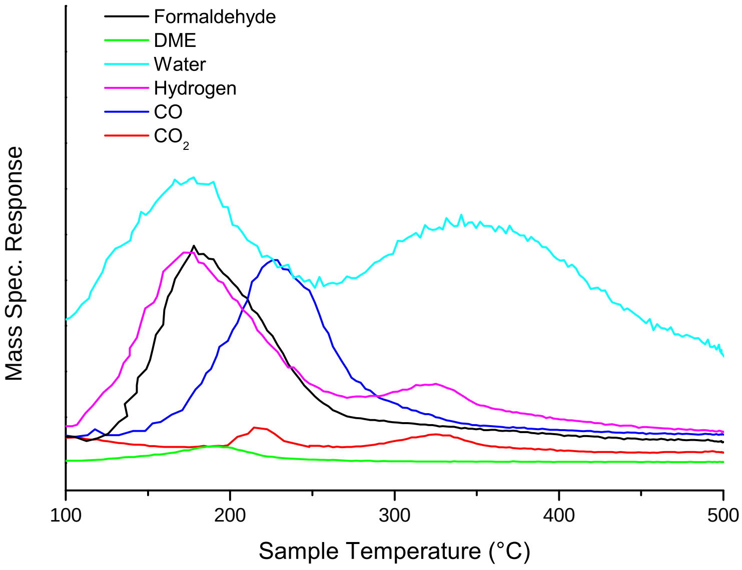

Figure 5.14: TPD data for 6 ML MoO_x/0.35 ZnCoFe. Gas flow: 30 mL/min He. Sample mass: 175 mg.

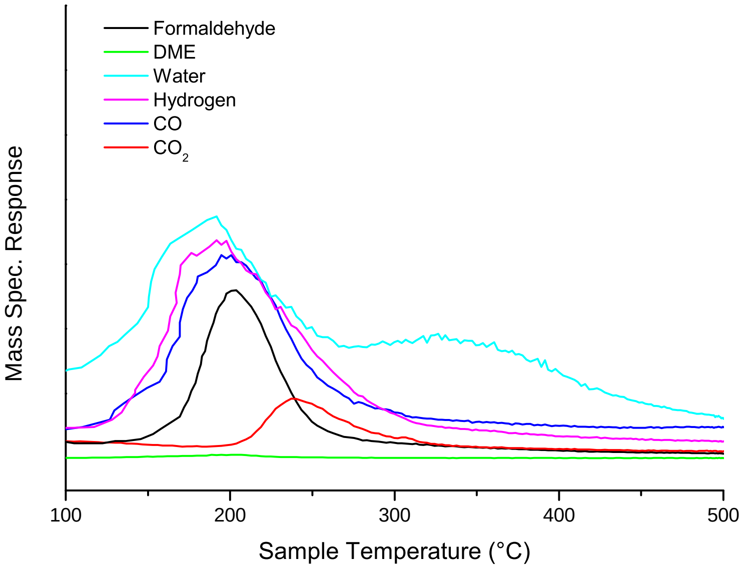

Figure 5.15: TPD data for 6 ML MoO_x/0.45 ZnCoFe. Gas flow: 30 mL/min He. Sample mass: 175 mg.

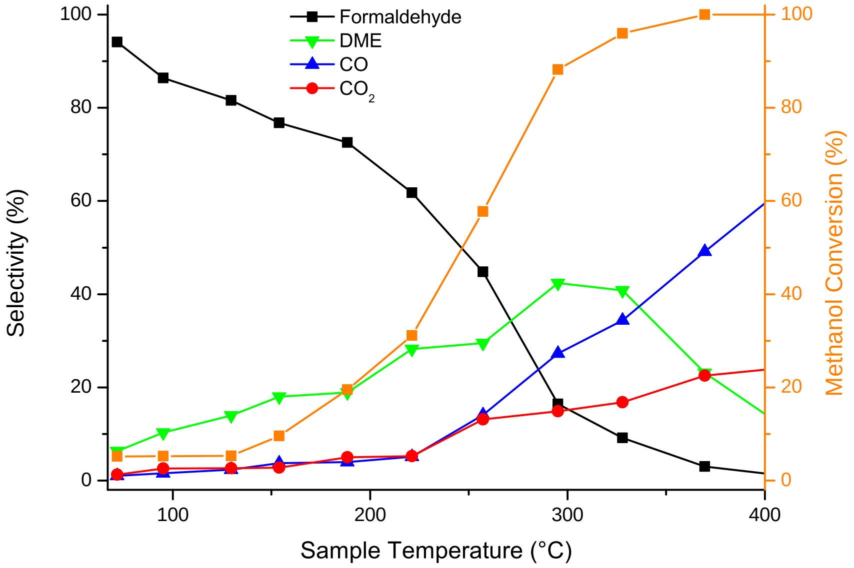

Figure 5.16: PFR data for 6 ML MoO_x/0.35 ZnCoFe. Methanol conversion is shown in orange on the right-hand y-axis. Gas flow: 30 mL/min 10% O_2 in He. Sample mass: 175 mg.

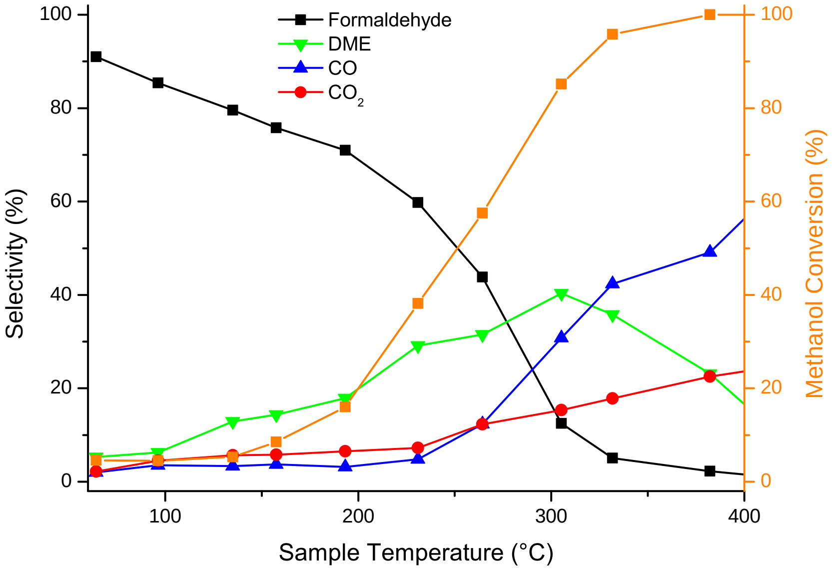

Figure 5.17: PFR data for 6 ML MoO_x/0.40 ZnCoFe. Methanol conversion is shown in orange on the right-hand y-axis. Gas flow: 30 mL/min 10% O_2 in He. Sample mass: 175 mg.

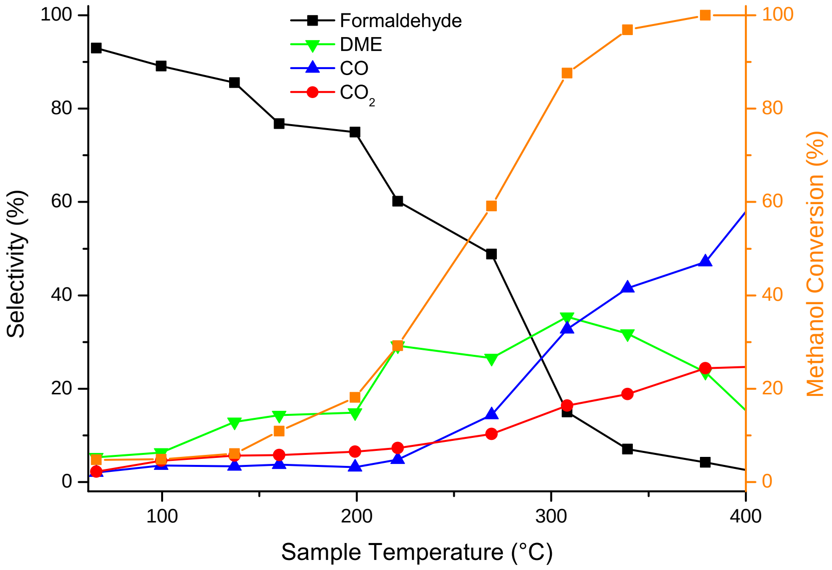

Figure 5.18: PFR data for 6 ML MoO_x/0.45 ZnCoFe. Methanol conversion is shown in orange on the right-hand y-axis. Gas flow: 30 mL/min 10% O_2 in He. Sample mass: 175 mg.

DME selectivity is also observed. Selective oxidation declines at higher temperatures, with CO production predominating above 330°C alongside lesser, but still significant generation of CO_2. Importantly, in all cases CO_2 production does not commence in earnest at temperatures below 240°C. This indicates that a high degree of core segregation has been achieved, as without effective inhibition of core participation, considerable CO_2 production would be visible below 200°C. This tallies with the behaviour seen by TPD, wherein formaldehyde production was greater than (more thermodynamically favourable) complete combustion to CO_2.

While the reactivity trends are promising, it is equally vital to ensure that no structural differences arise from shell-core formation when ZnCoFe is employed. To assess any changes, XRD analysis was performed on samples of the 0.35 ZnCoFe support prior to and after MoO_x incipient wetness impregnation (Figure 5.19). Hearteningly, the XRD patterns do not significantly differ. The XRD pattern for 6 ML MoO_x/0.35 ZnCoFe exhibits superior signal-to-noise, and hence some of the smaller peaks are more discernible than for plain 0.35 ZnCoFe, but no substantive structural alterations upon addition of the MoO_x shell are visible by XRD. Furthermore, no disparities between Zn loadings were seen by XRD, with 0.40 and 0.45 ZnCoFe displaying identical behaviour. While the lack of changes upon shell formation is important *per se*, it is equally significant that no multicomponent bulk phases be formed in preference to the desired shell-core structure: XRD

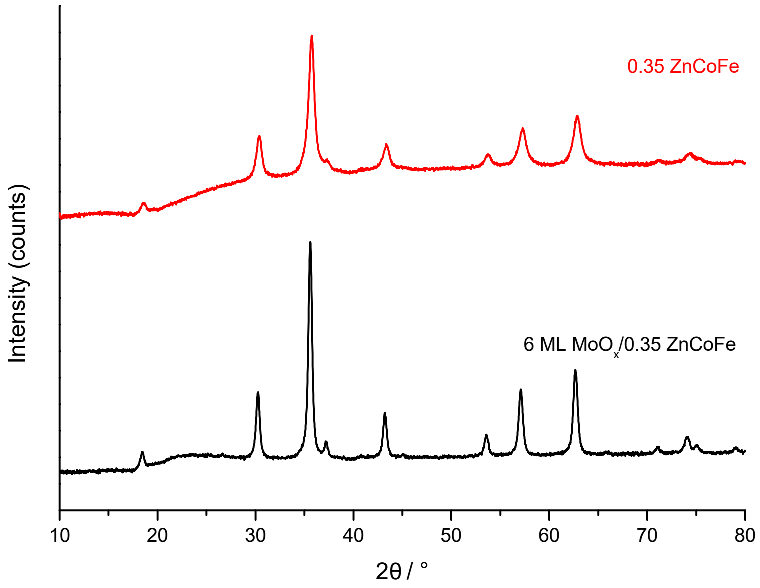

Figure 5.19: A comparison of XRD patterns before and after addition of 6 ML MoO$_x$ to 0.35 ZnCoFe.

reliably demonstrates that this does not occur. Raman analysis was attempted to illuminate sample speciation, but the ZnCoFe samples—jet black in colour—were unsuitable. XPS measurements of all three MoO$_x$/ZnCoFe catalysts were performed on these samples to assess whether any fundamental differences in speciation had arisen from the addition of MoO$_x$ shells (Figures 5.20, 5.21 and 5.22). The Mo present is revealed to exist as Mo(VI), as expected, and no other differences are observed between the MoO$_x$-coated catalysts and the earlier pristine ZnCoFe supports; the sample still resembles cobalt ferrite, with no indications of the presence of any other species.

For these studies, the presence of CO$_2$ is not overly concerning, as the objective of these experiments is not to produce a fully formaldehyde-selective catalyst, but to probe magnetocatalytic effects. To observe any changes in selectivity and to be sure they are genuine changes (and not the result of experimental noise), all reaction products must be present in observable quantities: i.e. in a mass spectrum, the signal from each product must be well clear of the baseline. For the 6 ML MoO$_x$/ZnCoFe catalysts, formaldehyde remains the major product, while all other products during TPD are easily observed: consequently, and pivotally, any changes in these selectivities from magnetic influences during *in situ* magnetometry will be also be easily observed.

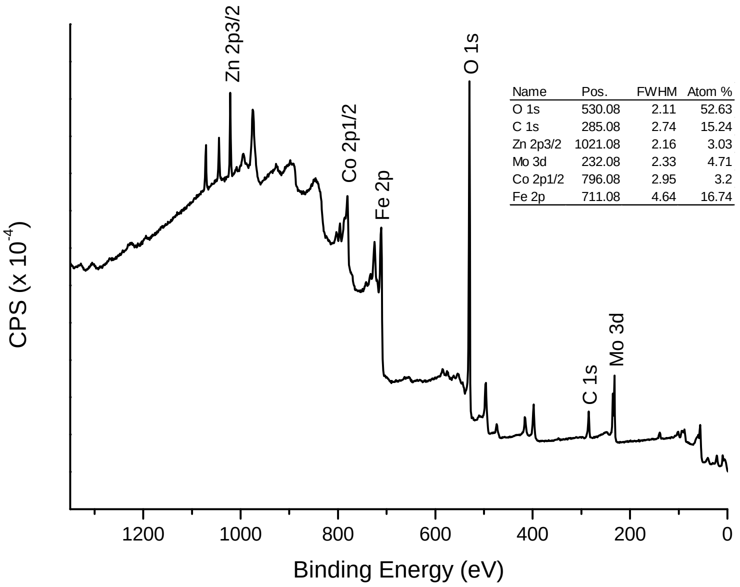

Figure 5.20: XPS data from 6 ML MoO$_x$/0.35 ZnCoFe.

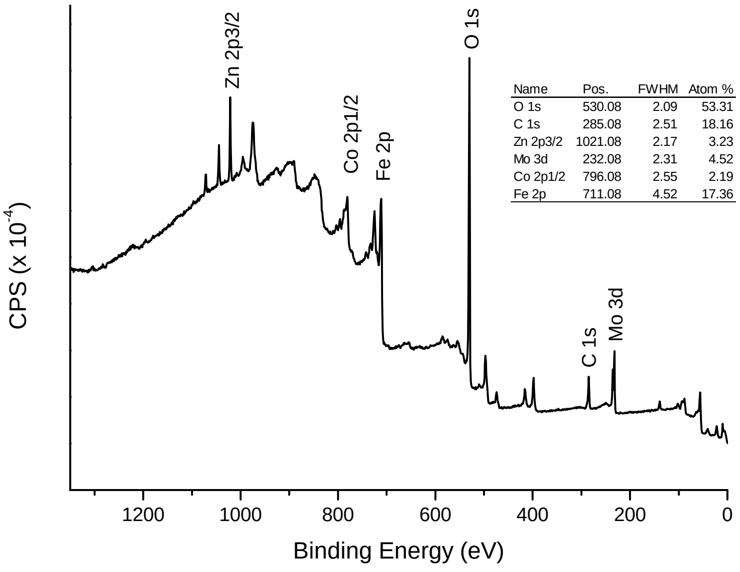

Figure 5.21: XPS data from 6 ML MoO$_x$/0.40 ZnCoFe.

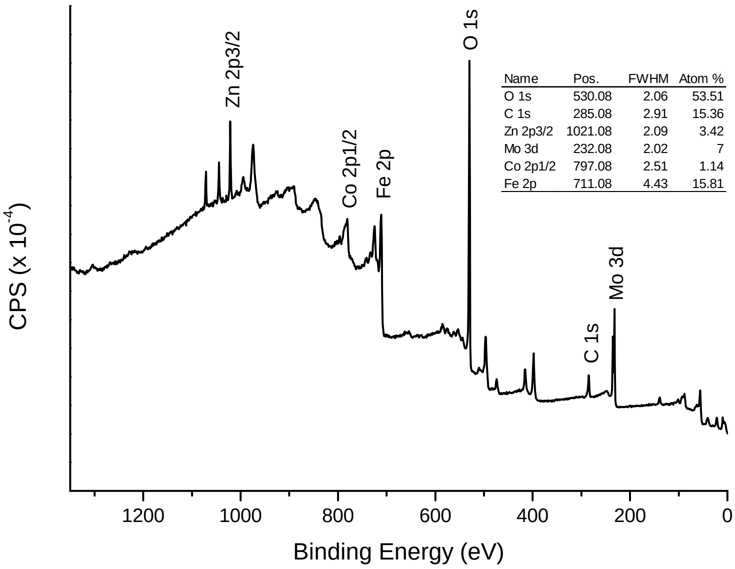

Name	Pos.	FWHM	Atom %
O 1s	530.08	2.06	53.51
C 1s	285.08	2.91	15.36
Zn 2p3/2	1021.08	2.09	3.42
Mo 3d	232.08	2.02	7
Co 2p1/2	797.08	2.51	1.14
Fe 2p	711.08	4.43	15.81

Figure 5.22: XPS data from 6 ML MoO_x/0.45 ZnCoFe.

5.4 *In situ* magnetometry of MoO_x/ZnCoFe catalysts

The range of *ex situ* characterisation performed at Harwell clearly demonstrated the viability of MoO_x/ZnCoFe catalysts, and displayed the similarities between the catalytic behaviours of MoO_x/ZnCoFe and well-understood MoO_x/Fe_2O_3. With confidence in the abilities of MoO_x/ZnCoFe shell-core catalysts in place, experimental work was transferred to the University of Cape Town and its *in situ* magnetometer and reactor. The objectives of the experiments undertaken at UCT were twofold: firstly, to ascertain whether any external magnetocatalytic effect would result from applied magnetic influences; and secondly, to determine whether any internal magnetocatalytic effects arising from the behaviour in the region of the Curie temperature would be present.

At this juncture it is useful, particularly for any future endeavours in this topic, to discuss the technical and experimental challenges encountered during the studies. As for previous *ex situ* reactor measurements, mass spectrometry was the technique of choice for monitoring the progress of methanol oxidation over MoO_x/ZnCoFe. The operation of a mass spectrometer relies on magnetic influences to direct ions to the analyser; however, the magnetometer produces extremely strong magnetic fields, capable of disrupting the selection process inside a mass spectrometer. This produces interference in the resulting mass spectra obtained from the spectrometer, manifesting as vastly greater noise in the data. In retrospect this is obvious; however, these were some of the first experiments performed with the magnetometer using an online mass spectrometer and hence liable to teething problems without the aid of hindsight. Two options were considered to mitigate the effects of the magnetometer on the mass spectrometer, either to install shielding material around the instrument or to physically distance the mass spectrometer from the magnetometer to the greatest extent.

The shielding option, while seemingly attractive, was not practically achievable. The use of a Faraday cage provides a highly effective impediment to the passage of electromagnetic radiation, but its use against static or low frequency magnetic fields (such as are produced by the magnetometer) is fruitless. Magnetic shielding materials are available, for example mu-metal, a ferromagnetic nickel-iron alloy with very high permeability (the ability of a material to support the generation of a magnetic field within itself). The shielded item is protected by the mu-metal encouraging an external magnetic field to alter direction to align with the mu-metal, and thereby flow around the shielded contents and not through them. The efficacy of such shielding depends on the thickness of the shielding layer, the number of layers and—most importantly—the applied field strength. For a 2 T field, an unreasonable thickness of shielding is required to nullify the effects on the mass spectrometer. Alternatively, active shielding can be employed to counteract the effects of a magnetic field, i.e. by applying an equal and opposite magnetic field; however, negating the 2 T field generated by the magnetometer would necessitate a -2 T field generated by equally powerful magnets around the magnetometer. The complexity of active shielding renders it impractical for the experimental setup available at UCT.

The more sensible option was to increase the distance between the mass spectrometer and the magnetometer, as the effects of the magnetic field scale with distance from the field source, though this also introduces further intricacies. With each metre from the magnetometer, the mass spectrometer requires another metre of heated capillary to allow post-reaction gas to reach the instrument. This considerably increases the distance of tubing through which gas must pass, and hence increases the delay time between the catalyst and analysis by the spectrometer. Given that the total flow rate of the gas mixture used during these studies was approximately 30 mL/min (i.e. not fast), when the final layout of equipment was arranged, a five minute delay was evident between changes to the magnetometer/reactor and the resulting changes to the mass spectra. This is far from ideal for catalysis research, but was an unavoidable inconvenience with the setup used for these studies.

Having resolved the significant experimental issues and conducted numerous test reactions, experiments to collect *in situ* measurements could begin. Measurements of catalytic behaviour at and around the Curie temperature will waste the least time from sample cooling between measurement runs for 0.45 ZnCoFe ($T_c = 195$°C) compared to 0.35 ZnCoFe ($T_c = 281$°C): accordingly, in the first instance it was decided to focus on 6 ML MoO_x/0.45 ZnCoFe with the intention of investigating the other Zn loadings later if possible.

5.4.1 External magnetocatalytic effects

The first experiment was designed to assess whether any external magnetocatalytic effect could be seen during methanol oxidation. A 220 mg sample of 6 ML MoO_x/0.45 ZnCoFe was placed into the magnetometer and exposed to a 10% oxygen in helium gas flow, reminiscent of the conditions used for CATLAB PFR studies; this gas mixture was maintained throughout the duration of the experiment. The gas flow from the catalyst was monitored constantly by mass spectrometry to chart any changes in reactant consumption or product quantities (Figure 5.23). A temperature profile was programmed into the experiment, involving a ramp to 100°C followed by a dwell period of two hours, then a further increase to 300°C followed by a two-hour dwell period. At the end of this time, the heating elements were deactivated and the sample was allowed to cool to 80°C. During the latter half of each dwell period, a constant 2 T external magnetic field was applied by the magnetometer (Figure 5.23: shaded areas). For MoO_x/ZnCoFe (and MoO_x/Fe_2O_3) catalysts, the optimal formaldehyde production temperature is below 300°C, while the operating temperature of the equivalent industrial catalysts is typically around 300°C, though can be higher.

At 100°C, very little of interest is observed either before the magnetic field is applied or during field application. This is to be expected, given that methanol conversion is low as the catalyst is scarcely active at 100°C. During the temperature ramp to 300°C, the catalytic activity markedly increases, with 50% conversion occurring at approximately 240°C and 90% conversion by 300°C. This agrees with the behaviour seen by *ex situ* PFR studies. By 300°C, while the products of selective oxidation are formed, they are rapidly oxidised further to produce CO_2. Accordingly, at this temperature the majority products seen by mass spectrometry are CO, CO_2 and hydrogen, though some formaldehyde is still detected. At the midpoint of the 300°C dwell period, the field was applied. Significant changes can be seen immediately upon field application. The mass spectral signal from oxygen decreases, while the signals from CO_2, water and hydrogen increase (confirmed separately by gas chromatography). This indicates a greater consumption of oxygen along

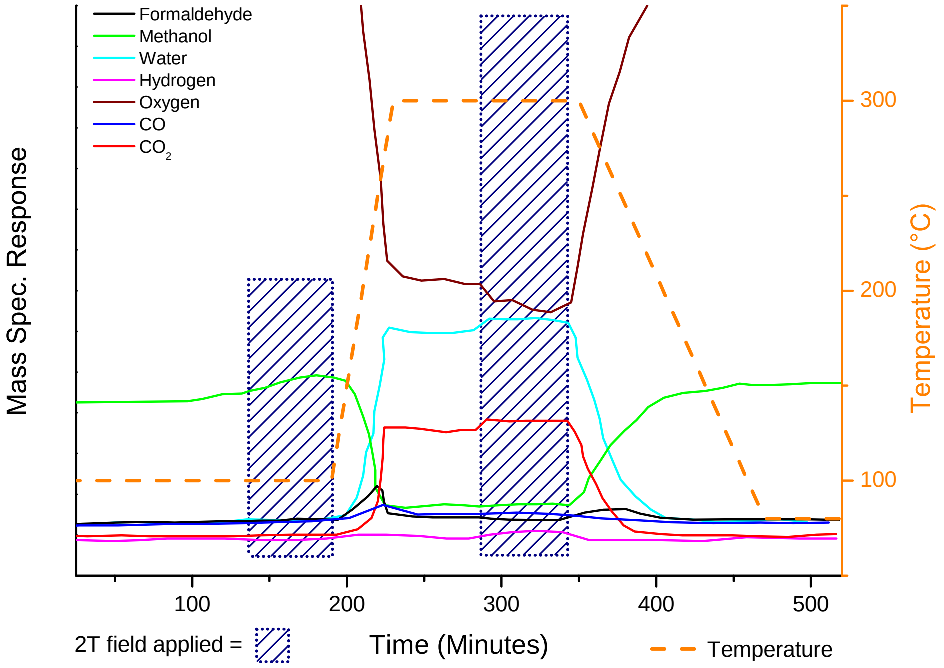

Figure 5.23: Mass spectra from 6 ML MoO_x/0.45 ZnCoFe obtained from the *in situ* magnetometer/reactor to compare reactivity with and without an external magnetic field applied. When applied, the field strength was 2 T: regions during which the field was applied are shown with blue hatching.

with increased generation of combustion products: in other words, combustion is encouraged by the magnetic field. No obvious changes in methanol consumption were evident, signifying that the overall activity of the catalyst is unchanged by the magnetic field; however, the formaldehyde signal was seen to decrease for the duration of field application, counterbalancing the increased combustion. It is apparent that when a magnetic field is applied to 6 ML MoO_x/0.45 ZnCoFe, catalytic selectivity is clearly altered to favour combustion. This is a gripping result indeed. While the increase in selectivity is for combustion, and not selective oxidation, the fact that selectivity is modified is nonetheless an important proof of concept.

Having demonstrated that an external magnetocatalytic effect is evident in methanol oxidation over a MoO_x/0.45 ZnCoFe catalyst, attempts were made to reproduce the effects detailed above in the same sample. Due to electrical failures affecting the instruments and the time constraints of the work, however, it was ultimately not possible to repeat the same experimental procedure to confirm the external magnetocatalytic effect seen. The position of the Curie temperature (and any effects which might occur thereat) were not the focus of investigation in this first experiment, but were for the subsequent experiments.

5.4.2 Internal magnetocatalytic effects

An experiment was designed to probe any internal magnetocatalytic effects which might be present during methanol oxidation, i.e. those which arise from the inherent magnetisation of the catalyst and not from an externally applied field. Two portions of 6 ML MoO_x/0.45 ZnCoFe were subjected to an identical experimental regimen, in which they were heated to 300°C for a dwell period before cooling to room temperature. For one sample, a constant 2 T applied field was maintained for the whole experiment; for the other sample, no magnetic field was applied at any point. The gas flow from the catalyst was constantly monitored by mass spectrometry in both cases, focussing particularly on combustion products in light of the earlier findings: reducing the number of analysed masses afforded greater time resolution, which was important given the transience of literature reported Curie temperature discontinuities. In both cases, nothing of significance was observed while the temperature was increasing to 300°C. During the cooldown after the dwell period, however, a promising discrepancy is seen between the no field and constant field samples (Figures 5.24 and 5.25).

In the absence of an applied field during cooldown, a large spike in combustion products is observed at a temperature corresponding to the Curie temperature of the sample in question (195°C). This is highly reminiscent of the discontinuities reported in the literature by Hedvall and other contemporaneous researchers of magnetocatalytic effects. In contrast, no spikes in combustion products are witnessed when a constant external magnetic field is applied for the duration of the cooldown period. This is a hugely significant result, as it demonstrates the presence of an internal magnetocatalytic effect in the 6 ML MoO_x/0.45 ZnCoFe catalyst.

To rationalise the assertion of an internal magnetocatalytic effect, it is necessary to understand the nature of the magnetisation of the catalysts at various stages in the experiment. During the experiment in which no external field is applied at any point, the magnetisation of the catalyst differs markedly as a function of temperature. Below the Curie temperature, the sample exhibits a spontaneous net magnetisation, while above the Curie temperature this magnetisation is lost, yielding an apparently non-magnetic material. Without a field applied, the catalyst does not regain its magnetisation while it is hotter than its Curie temperature. As the catalyst cools, it approaches its Curie temperature; upon reaching its Curie temperature, an overall spontaneous magnetisation

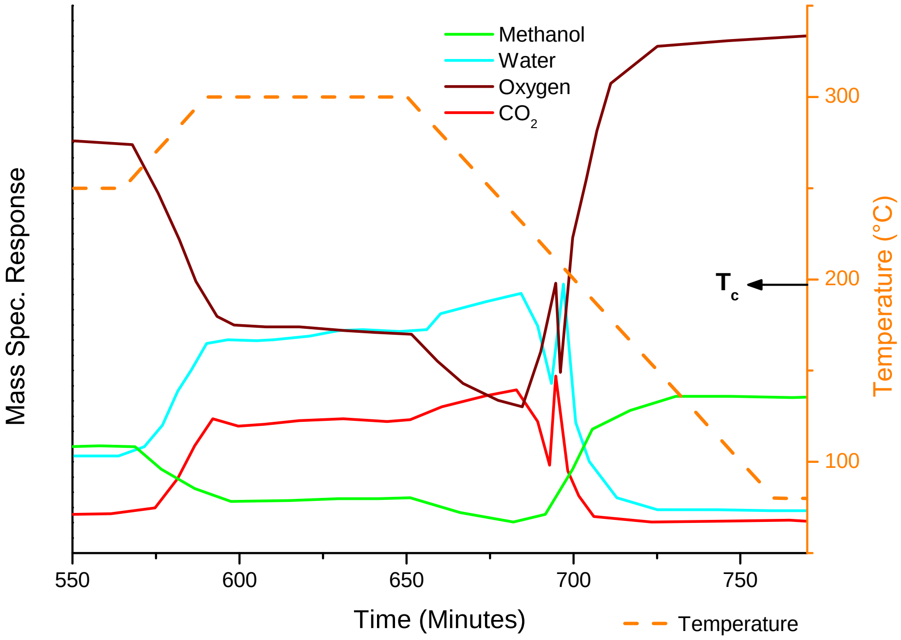

Figure 5.24: Mass spectra obtained during methanol oxidation over 6 ML MoO_x/0.45 ZnCoFe in the absence of an applied field.

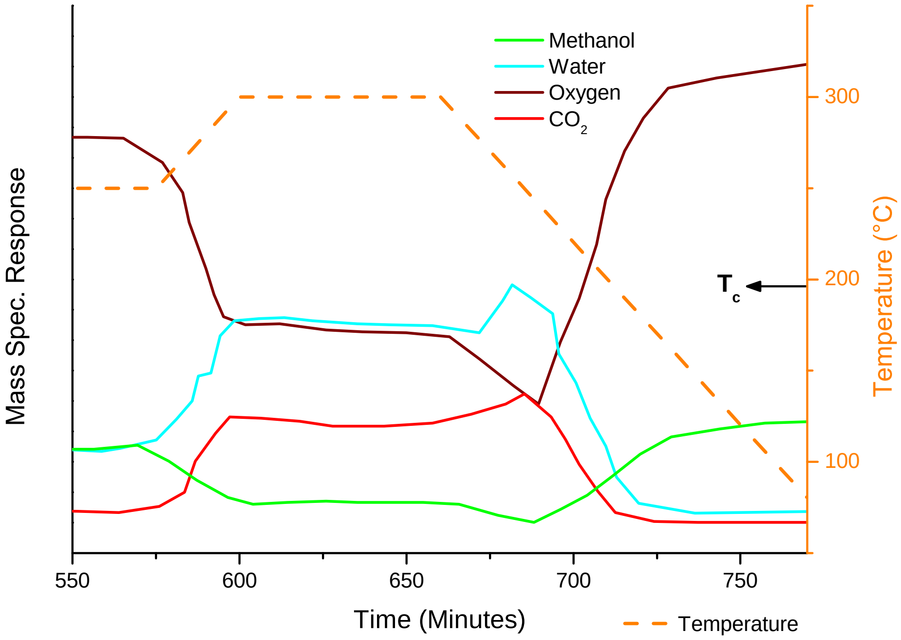

Figure 5.25: Mass spectra obtained during methanol oxidation over 6 ML MoO_x/0.45 ZnCoFe under a constant 2 T applied field.

is suddenly restored to the catalyst and remains with further cooling. When the same experiment is performed with a constant 2 T field in place, however, the sample is magnetised for the entire duration of the experiment. Since the strength of the applied field vastly outweighs the spontaneous magnetisation of the catalyst, at all stages the material is aligned with this field. Accordingly, no structural changes to the magnetic domains occur when passing the Curie temperature due to the continued presence of the applied field. This is important, as it implies that it is the sudden change in the magnetic properties of a material which produces discontinuities in catalytic properties, not long-duration differences between magnetic states.

A subsequent experiment was conducted to assess whether pre-magnetisation of the catalyst imparted any effects during the reaction. In this instance, pre-magnetisation was achieved by exposing the sample to a 2 T field at the start of the experiment for a short time only; the remainder of the reaction (i.e. the majority of it) was performed in the absence of an external field. While pre-magnetisation was not expected to influence the behaviour, it warranted investigation nonetheless. As for the earlier no field experiment, a fleeting but significant jump in combustion selectivity is observed as the sample cools through its Curie temperature (Figure 5.26). It is again useful to consider the magnetisation present in the catalyst during the experiment. While this catalyst is pre-magnetised, the application of a strong magnetic field while the sample is at room temperature does not permit the material to retain its permanent magnetism beyond its Curie temperature. In fact, the pre-magnetised catalyst and the catalyst tested with no field applied at all are identical in their magnetic behaviour: in both cases, as the samples cool through the Curie temperature, they suddenly regain their internal magnetisation. Since the lifetime of the increased combustion is short, and localised only to the Curie temperature, the strong implication is that catalytic discontinuities arise not from enduring differences in magnetic properties, but from transient changes. The corroboration of the internal magnetocatalytic effect for MoO_x/0.45 ZnCoFe in a second experiment greatly boosts confidence in these findings.

By considering the behaviour demonstrated by 6 ML MoO_x/0.45 ZnCoFe in the absence of a magnetic field during cooling, vital additional evidence can be extracted from the first magnetometry experiment discussed earlier (Figure 5.23). During that experiment, a 2 T field was applied to the sample at 300°C—in excess of its Curie temperature—which was removed before cooling. When only a pre-magnetisation was applied, or no field at all, upon passing the Curie temperature of 195°C a sharp increase in combustion is observed. Following exposure to and subsequently the removal of the 2 T field at 300°C, one would

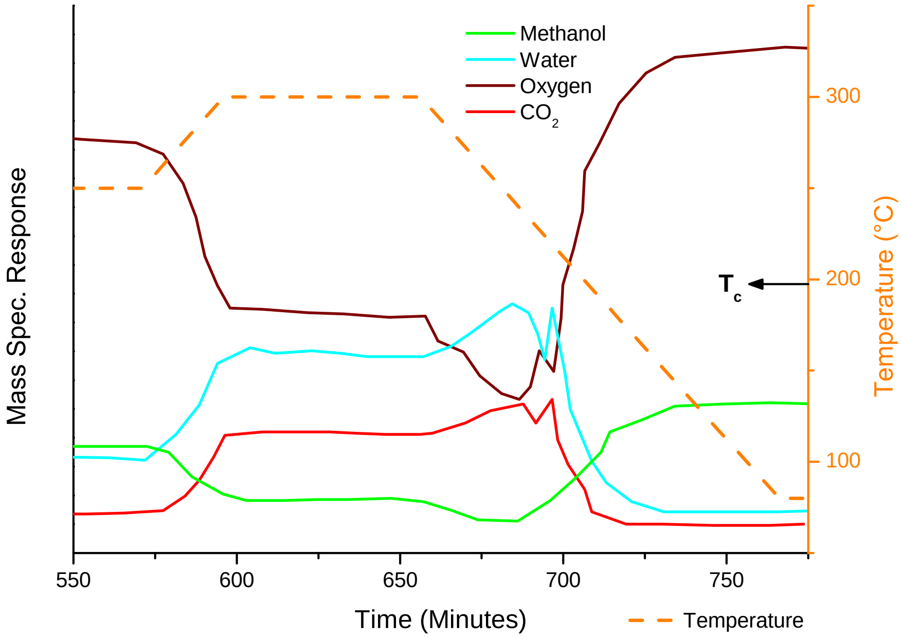

Figure 5.26: Mass spectra obtained during methanol oxidation over a pre-magnetised 6 ML MoO_x/0.45 ZnCoFe catalyst in the absence of an applied field.

expect a similar jump in combustion during cooling; however, no spike in combustion is observed at the Curie temperature (Figure 5.27). While the absence of such a spike may seem to contradict the behaviour detailed above, in actuality it strongly reinforces it.

The key to understanding this apparent disparity lies in the magnetic behaviour of the catalysts during the experiment. When the MoO_x/0.45 ZnCoFe catalyst is heated above its Curie temperature to 300°C, it loses its magnetisation. It remains unmagnetised until the midpoint of the 300°C dwell period, when the 2 T field is applied. Throughout the field application, the sample magnetisation aligns with the external field; however, despite the removal of the field at the end of the dwell period, the magnetic domains in the catalyst are unable to rotate to minimise the overall structural magnetisation due to magnetic hysteresis. Numerous factors contribute to the magnitude of the effects of magnetic hysteresis, of which remanence—the magnetisation remaining in a magnetic material after an external field is removed, also called residual magnetism—is one of the more influential. This value is dictated by the identity of the material in question, but the strength of the applied field is also important: if the applied field is too weak, the effects of hysteresis can be diminished. In this case, a 2 T field is easily powerful enough to elicit full hysteresis effects in the catalyst. The remanence of a neodymium magnet—a considerably

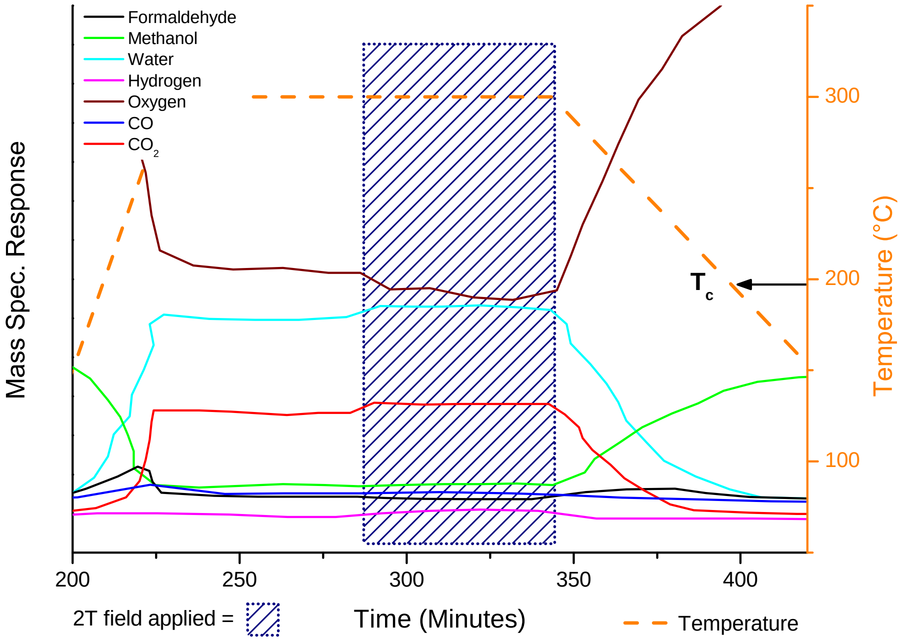

Figure 5.27: Expanded mass spectra from Figure 5.23 focussing on the cooling stage of the experiment. No magnetocatalytic discontinuity is visible at the Curie temperature.

stronger magnet than cobalt ferrite—can reach 1.3 T, requiring fields in excess of this value to induce full hysteresis: consequently, the remanence of weaker cobalt ferrite will require a weaker field to overcome. These effects compel the magnetic domains in the catalyst to remain aligned with the now-removed field, producing a net magnetisation despite the absence of an applied field at temperatures above the Curie temperature. Accordingly, unlike the no field and pre-magnetised catalysts, when the catalyst in this experiment reaches its Curie temperature, there is no diametric shift from an unmagnetised to a magnetised state. Instead, only small changes in the magnitude of magnetisation will occur. From this, it is thought that fundamental shifts in magnetisation at the Curie temperature are required to trigger a discontinuity in catalytic behaviour (i.e. an internal magnetocatalytic effect): when magnetisation scarcely changes, the catalytic properties are unperturbed.

Due to the myriad of technical complications encountered with the experimental setup and the consequent delays, no further experimentation could be undertaken on the *in situ* magnetometer in the time available during the student exchange. In addition, the electromagnets in the instrument developed an irreparable fault shortly thereafter, rendering the magnetometer inoperable for over six months. Consequently, while provision had been made to compensate for lost experimental time by performing further studies beyond the period of the student exchange, this was ultimately impossible.

5.5 Conclusions

The two cardinal objectives of this chapter were to determine whether magnetocatalytic effects could be observed in methanol oxidation over MoO_x shell-core catalysts, and whether the position of the Curie temperature influenced any such effects. To allow these objectives to be fulfilled, two smaller questions required consideration, namely whether a magnetically relevant alternative for haematite as a core material could be employed, and whether Zn-doping could be used in this material to reliably decrease the Curie temperature.

Cobalt ferrite was identified as the most promising candidate on account of its magnetic properties—ferrimagnetic spinel structure, $T_c = 440°C$—and its reactivity, which closely resembles that of haematite. Since the success of shell-core segregation is gauged by differential reactivities in methanol TPD, it was essential that any new core material act akin to haematite to ensure the continued validity of TPD as a measure of shell-core formation. With the reactivity reliably established, experiments were undertaken to modify the Curie temperature of cobalt ferrite by substituting Zn for a portion of the cobalt in cobalt ferrite. Three catalyst loadings were produced, with Zn fractions of 0.35, 0.40 and 0.45 affording Curie temperatures of 281, 245 and 195°C respectively. This is essentially a linear decrease in Curie temperature with a linear increase in Zn loading, and confirms earlier work on Zn-doping. It was vital, however, that the reactivity of the Zn-doped cobalt ferrite catalysts not be affected by the incorporation of Zn dopants: this was clearly demonstrated in TPD data wherein combustion was the dominant behaviour in all cases, showing no differences from unadulterated cobalt ferrite.

Following the examination of cobalt ferrite and Zn-doped cobalt ferrites in isolation, the next stage focussed on the suitability of Zn-doped cobalt ferrite as core materials supporting MoO_x shells in a manner similar to haematite in MoO_x/Fe_2O_3 shell-core catalysts. For the purposes of these studies, 6 ML MoO_x was the shell loading of choice. When each Zn loading sample was coated with 6 ML MoO_x and analysed by TPD, all three indicated good selectivity to formaldehyde, functioning similarly to the analogous MoO_x/Fe_2O_3 catalysts; however, CO_2 was visible in all cases. Importantly, the quantity of CO_2 produced was significantly smaller than that of formaldehyde, signifying that the shell is mostly complete; since combustion to CO_2 is the preferable option, producing more formaldehyde than CO_2 indicates that exposure of the ZnCoFe core is limited. It is not yet understood why the shell is not fully complete. By XRD, no structural differences are apparent between plain ZnCoFe and 6 ML MoO_x/ZnCoFe, but it is possible that the surface environment is not uniformly MoO_x atop ZnCoFe. Instead, small areas of mixed metal oxide compounds (e.g. zinc molybdate or cobalt molybdate) might be present at the surface, disrupting the shell coverage. Further structural investigations are necessary with more specialised and appropriate techniques, such as XAS, to understand the surface speciation of MoO_x/ZnCoFe catalysts.

Convincing evidence of an external magnetocatalytic effect was displayed by 6 ML MoO_x/0.45 ZnCoFe during methanol oxidation when a 2 T field was applied. Combustion selectivity was markedly increased, as determined by an increase in combustion products and a decrease in oxygen and formaldehyde reaching the mass spectrometer. Importantly, this phenomenon is not simply an increase in catalytic activity. The application of a strong external field to a magnetic material can generate inductive heating, and as catalytic activity relies on temperature, any such heating might increase catalytic activity. In this case, however, inductive heating does not occur. A thermocouple was positioned in the sample bed, which reported no temperature fluctuations: in addition, methanol conversion is unchanged after field application. This implies that the change in product distribution arises from modifications to selectivity, not activity. The fundamental cause of the changes in selectivity induced by the external magnetocatalytic effect remains to be determined. It is theorised that external magnetic influences on a magnetic catalyst are able to alter the electronics of the catalyst, and in doing so modify activation energies and hence selectivities. Since the energetic differences between various catalytic pathways can be minute, it is logical that only a small perturbation would need to be induced by an external magnetic field to elicit a significant change in selectivities. While electronic factors are thought to be the significant cause of magnetocatalytic effects, an additional consideration is the physical alignment of a material. It is well known that certain catalysts favour different reactions on different structural faces. If an applied field were to prompt a material to adopt an alignment which rendered certain faces less accessible, selectivity could in turn be affected. Irrespective of the cause of the effect, the existence of a magnetocatalytic effect has been demonstrated in methanol oxidation over 6 ML MoO_x/0.45 ZnCoFe. This is an exciting result, especially given the paucity of reported magnetocatalytic investigations.

Internal magnetocatalytic effects also attracted interest in these studies, and convincing evidence for their existence in MoO_x/ZnCoFe catalysts has been obtained. When 6 ML MoO_x/0.45 ZnCoFe catalysts are heated during methanol oxidation above their Curie temperature of 195°C, catalytic discontinuities are seen upon cooling through 195°C. These manifest as significant, but fleeting boosts to combustion, mirroring the selectivity change for the external magnetocatalytic effect. Crucially, these discontinuities are absent during cooldown in the presence of a constant applied field (i.e. when the catalyst is never unmagnetised during reaction), implying that the rapid recovery of catalyst magnetisation is responsible for the transient selectivity changes.

At time of writing, the studies reported in this chapter represent the first foray into magnetocatalytic effects in methanol oxidation and the first study of cobalt ferrite-containing catalysts as analytical vehicles to probe magnetocatalysis. The results obtained from the *in situ* magnetometer have been highly encouraging, and strengthen the case for further study in this area. The experience gained while conducting experiments with the magnetometer would be of considerable use to anyone performing further experiments. Given the scarcity of available time on the instrument, and that experimental difficulties consumed a considerable portion of it, it is vital to effectively apply the experimental knowledge gained during these studies to future efforts in order to maximise their benefits.

There are many experiments with MoO_x/ZnCoFe catalysts that could be conducted in future to further clarify the nature of magnetocatalytic effects. It is essential to analyse the ZnCoFe catalysts with other Zn loadings to probe the internal magnetocatalytic effect at the earliest opportunity. According to the theory exposited above, in the absence of an applied field the discontinuity encountered at the Curie temperature on cooldown will move with the Curie temperature: e.g. for 6 ML MoO_x/0.40 ZnCoFe the jump in combustion should move to 245°C. This would be a simple experiment to perform, but the result would be extremely telling. An additional experiment of interest would be to probe the effects of different applied magnetic field strengths on the internal magnetocatalytic effect, to chart whether the magnitude of the field is reflected in the magnitude of the changes in selectivity. Alternatively, modifications to the catalyst design could be made, for instance through the use of another shell metal oxide atop ZnCoFe cores. This would assist in understanding whether the external magnetocatalytic effect manifests differently with different catalyst materials. These suggestions are but a few examples of the rich seam of possible future research into magnetocatalysis and magnetocatalytic effects.

References

(1) E. Lenz, *Annalen der Physik und Chemie*, 1834, **107**, 483–494.

(2) D. Griffiths, *Introduction to Electrodynamics*, Pearson, 2013.

(3) L. Néel, *Annales de Géophysique*, 1949, **5**, 99–136.

(4) R. Feynman, R. Leighton and M. Sands, *The Feynman Lectures on Physics: Mainly electromagnetism and matter*, Addison-Wesley Publishing Company, 1965.

(5) J. A. Hedvall, *Chemical Reviews*, 1934, **15**, 139–168.

(6) G. Cohn and J. A. Hedvall, *The Journal of Physical Chemistry*, 1942, **46**, 841–847.

(7) J. A. Hedvall, R. Hedin and O. Persson, *Zeitschrift für Physikalische Chemie*, 1935, **B27**, 196.

(8) J. A. Hedvall and F. Sandford, *Zeitschrift für Physikalische Chemie*, 1938, **B29**, 455.

(9) J. A. Hedvall and H. Byström, *Zeitschrift für Physikalische Chemie*, 1938, **B31**, 163.

(10) H. Forestier and R. Lille, *Comptes rendus de l'Académie des Sciences*, 1937, **204**, 1254–1256.

(11) F. Olmer, *The Journal of Physical Chemistry*, 1942, **46**, 405–414.

(12) P. W. Selwood, *Chemical Reviews*, 1946, **38**, 41–82.

(13) J. Lielmezs and J. Morgan, *Chemical Engineering Science*, 1967, **22**, 781–791.

(14) J. Lielmezs and H. Aleman, *Thermochimica Acta*, 1990, **161**, 267–277.

(15) B. C. Sales and M. B. Maple, *Physical Review Letters*, 1977, **39**, 1636–1639.

(16) R. S. Mehta, M. S. Dresselhaus, G. Dresselhaus and H. J. Zeiger, *Physical Review Letters*, 1979, **43**, 970–973.

(17) D. S. Mathew and R.-S. Juang, *Chemical Engineering Journal*, 2007, **129**, 51–65.

(18) B. J. Rani, M. Ravina, B. Saravanakumar, G. Ravi, V. Ganesh, S. Ravichandran and R. Yuvakkumar, *Nano-Structures & Nano-Objects*, 2018, **14**, 84–91.

(19) C.-H. Yan, Z.-G. Xu, F.-X. Cheng, Z.-M. Wang, L.-D. Sun, C.-S. Liao and J.-T. Jia, *Solid State Communications*, 1999, **111**, 287–291.

(20) M. Rajendran, R. Pullar, A. Bhattacharya, D. Das, S. Chintalapudi and C. Majumdar, *Journal of Magnetism and Magnetic Materials*, 2001, **232**, 71–83.

(21) G. Baldi, D. Bonacchi, C. Innocenti, G. Lorenzi and C. Sangregorio, *Journal of Magnetism and Magnetic Materials*, 2007, **311**, Proceedings of the Sixth International Conference on the Scientific and Clinical Applications of Magnetic Carriers, 10–16.

(22) Q. Song and Z. J. Zhang, *Journal of the American Chemical Society*, 2004, **126**, 6164–6168.

(23) X.-M. Lin and A. C. Samia, *Journal of Magnetism and Magnetic Materials*, 2006, **305**, 100–109.

(24) G. Vaidyanathan, S. Sendhilnathan and R. Arulmurugan, *Journal of Magnetism and Magnetic Materials*, 2007, **313**, 293–299.

(25) I. Gul and A. Maqsood, *Journal of Alloys and Compounds*, 2008, **465**, 227–231.

(26) R. Arulmurugan, G. Vaidyanathan, S. Sendhilnathan and B. Jeyadevan, *Physica B: Condensed Matter*, 2005, **363**, 225–231.

(27) P. Yaseneva, M. Bowker and G. Hutchings, *Physical Chemistry Chemical Physics*, 2011, **13**, 18609–18614.

(28) L. Kumar, P. Kumar, A. Narayan and M. Kar, *International Nano Letters*, 2013, **3**, 8.

(29) M. C. Biesinger, B. P. Payne, A. P. Grosvenor, L. W. Lau, A. R. Gerson and R. S. Smart, *Applied Surface Science*, 2011, **257**, 2717–2730.

Chapter 6

Conclusions and Future Work

Mixed metal oxide catalysts are vital to the vast array of irreplaceable industrial processes underpinning life in the 21st century. This thesis has focussed on one major process, namely the production of formaldehyde from methanol. This process relies on an effective, yet poorly understood, bulk iron molybdate catalyst. For heterogeneous catalysis chemists, the surface, functioning as the boundary between catalyst and reactant, holds the greatest research attention; however, exploring the surface of a catalyst is decidedly nontrivial.

One solution to this difficulty is the shell-core catalyst. In a continuous bulk structure (e.g. iron molybdate), the surface is dwarfed by the bulk as a proportion of the whole structure. This drastically limits the size of the analytical toolbox available to investigate solely the surface layers: only a minority of techniques are inherently surface-sensitive. Moreover, such techniques generally introduce significantly greater complexity than more typical analytical methods, and time for such techniques can be difficult to obtain. The shell-core catalyst model is a means to bypass this, and is achieved in two ways: firstly, when a high surface area core is used, shell-core catalysts can support greater surface areas than their bulk catalyst counterparts, meaning more surface species are present, facilitating their analysis; and secondly, by ensuring that separate metal oxide components are segregated from each other, where they would normally be mixed in a bulk structure. This is the fundamental benefit of the development of shell-core catalysts. If it is known that the shell component contains only one of the two oxides, then element-specific techniques can be employed to retrieve quasi-surface-sensitive information. For example, the original case, the MoO_x/Fe_2O_3 shell-core catalyst, was developed to assist XAS analysis of the iron molybdate catalyst surface. XAS is a powerful element-specific technique, revealing a plethora of valuable chemical and structural information from a material, but crucially it is inherently a bulk technique. While the surface layers of a bulk catalyst are probed by XAS in all cases, they are a small minority of the species present. Accordingly, their contribution to the overall averaged XAS signal will be masked by the contribution from the bulk. If it can be confirmed that all of a specific element is present at the surface, however, then the XAS information obtained must arise from the surface: accordingly, surface-sensitivity can be attained through careful structural control of a material. This thesis has taken the shell-core theme and expanded it in three important new directions.

The first concerned the investigation of alternative metal oxides in shell-core catalysts. Prior to the works reported in this thesis, research had focussed entirely on Mo and its oxides, and then MoO_x/Fe_2O_3 shell-core catalysts, due to the pre-eminence of molybdate catalysts in methanol selective oxidation. Given the research dividends gained from the studies of MoO_x/Fe_2O_3 catalysts, the next step was to probe the suitability of alternative metal oxides as shell components. Molybdates are renowned particularly for methanol selective oxidation and olefin ammoxidation, but many other important industrial processes are catalysed by other metal oxides—e.g. vanadium oxides for the oxidative dehydrogenation of propane—and it was therefore desired to use alternative shell-core catalysts to model other industrially relevant catalysts. Vanadium was selected as the first alternative, mainly due to the catalytic pedigree of vanadium oxides. It is now known that vanadium is a suitable shell material, forming selective VO_x/Fe_2O_3 shell-core catalysts analogously to MoO_x/Fe_2O_3. A range of VO_x/Fe_2O_3 catalysts was investigated, which revealed similar structural trends to MoO_x/Fe_2O_3. Overall, no significant divergences from the anticipated shell-core behaviour were seen: VO_x is an excellent candidate for a shell material. The precise identity of the active site at the surface of VO_x/Fe_2O_3 remains to be determined; however, based on XAS analysis, the surface is likely to consist of VO_4 tetrahedra. In a similar vein, better quality EXAFS measurements have now been performed on MoO_x/Fe_2O_3 catalysts to enhance the existing understanding of the MoO_x surface. In particular, the theory that the active site on MoO_x/Fe_2O_3 catalysts resembles Mo_3O_9 has been tested. Using a model of Mo_3O_9, reliable EXAFS fits were obtained, indicating the model to accurately represent the structure at the surface. This has provided considerable support for a Mo_3O_9-based active site, but EXAFS cannot be conclusive independently; to definitively determine this, further experiments are needed.

Having demonstrated that two metal oxide components could be successfully segregated in MoO_x/Fe_2O_3 and now VO_x/Fe_2O_3, there was hope that this success could be continued with additional metal oxides. Niobium oxides have also been widely explored as potential catalysts, and thus niobium oxide was the third material to be investigated for inclusion in a shell-core catalyst; however, in a reversal of the proverbial trend, the shell-core model is unlucky at the third metal oxide. NbO_x cannot entirely sequester the Fe_2O_3 core, enabling unselective catalysis (i.e. combustion) to occur upon reaction with methanol. Irrespective of the ML coverage employed, NbO_x/Fe_2O_3 catalysts fail to demonstrate the segregation necessary to produce a selective catalyst. Without the surety that full shell-core segregation has occurred, one cannot assume that the information obtained from element-specific measurements originates from the surface layers only. In this respect, NbO_x frustrates the very *raison d'être* of the shell-core model. This is ascribed to the Tamman temperatures of metal oxides. It is apparent that the Tamman temperatures of MoO_x and VO_x are exceeded by a large margin during the 500°C calcination, which permits the spreading of the shell across the Fe_2O_3. In contrast, NbO_x is unable to progress beyond the form adopted during incipient wetness impregnation, as its Tamman temperature is markedly higher than the calcination temperature. It is clear, therefore, that the selection of new metal oxides for shell-core catalysts must consider their Tamman temperatures.

The second new direction was to explore the effects of modifying the Fe_2O_3 core, as opposed to the MoO_x shell, in order to boost surface area. The effects of greater surface area, if no alterations to catalytic selectivities occur, would not be limited to solely MoO_x/Fe_2O_3 catalysts: indeed any shell-core catalyst could benefit. It was known that an approximate doubling of post-calcination surface area could be achieved with relatively little Al content. This thesis sought to continue this research, and particularly to ascertain whether an effective limit on Al loading existed, after which catalytic properties would be negatively impacted.

Further increases in surface area can indeed be obtained with greater quantities of Al in Fe_2O_3, but to the detriment of shell-core uniformity at higher loadings (15% and 20%). Discrepancies were observed in reactivity measurements, implying that the segregation vital to shell-core catalysts had failed. Yet in spite of the appearance of alumina-like reactivity, nothing can be seen by XRD to suggest the presence of any other phases: consequently, these additional phases must be small in size. XAS analysis was conducted to probe the Al environment as a function of Al loading in Fe_2O_3, which revealed that only at 5% loading is Al substitution into Fe_2O_3 observed. At 10%, 15% and 20%, clear phase separation to alumina is visible. Considering the XAS evidence obtained here, and literature evidence for a similar iron oxyhydroxide system, it appears that increasing the concentration of Al in the Fe_2O_3 not only produces more alumina, but also lessens the likelihood that the Al will substitute into the Fe_2O_3 structure. Clearly, there must be an ideal Al loading in Fe_2O_3, at which surface area is maximised but phase separation is not initiated. It would be a highly useful experiment to determine this loading.

The third area covered in this thesis concerned the initial forays into magnetocatalysis in conjunction with the University of Cape Town. As a concept, magnetocatalytic effects had been reported in a few catalytic processes in the 20th century, but few efforts have been made in this topic, and thus far not in methanol oxidation. This was the ideal opportunity to gauge the applicability of the shell-core model to new systems and for new purposes. All previous shell-core catalysts have employed Fe_2O_3 as the core material, but this is weakly ferromagnetic. Instead, to assess the effects of magnetic supports on catalysis, shell-core catalysts were developed using MoO_x shells atop Zn-doped cobalt ferrite cores: the amount of Zn present could be tweaked to alter the position of the Curie temperature. In reactivity terms, the catalysts produce formaldehyde, although crucially a small amount of combustion is visible, implying that shell-core segregation is not entirely achieved. Segregation must be at least partially in place, as a large quantity of formaldehyde is produced, which would be impossible were the core more than slightly exposed.

After determining that MoO_x/ZnCoFe catalysts are effective methanol oxidation catalysts, *in situ* magnetometry was undertaken to scrutinise whether any magnetocatalytic effects were visible. It was determined that the application of a magnetic field during catalysis does influence the distribution of products: a pronounced increase in combustion occurs when a magnetic field is applied, and is sustained for the duration of field application. This was confirmed both spectrometrically and chromatographically. This was a compelling result, and is the first known reliable evidence for an external magnetocatalytic effect in methanol oxidation. While the ideal magnetocatalytic effect might produce an abundance of formaldehyde upon field application, the focus of these studies was gauging the presence of magnetically-induced selectivity alterations, irrespective of their effects.

Strong evidence for the existence of internal magnetocatalytic effects—effects arising from changes in magnetisation within the material and not from an externally applied field—has also been obtained. On cooling down in the absence of an applied magnetic field, a strong spike in combustion is observed at the Curie temperature, i.e. the point at which magnetisation is restored to the ferrite support. Crucially, such a discontinuity is not witnessed when an external field is applied throughout the cooldown period, nor when a strong field has been applied while above the Curie temperature and catalyst magnetisation is maintained by hysteresis. That a spike is only seen in the absence of a field strongly implies that catalytic discontinuities are only encountered when the magnetisation of the ZnCoFe catalyst fundamentally changes, e.g. from unmagnetised to magnetised, and not when magnetisation changes subtly or not at all. Indeed, the existing literature on magnetocatalytic effects, though in different reactions, details remarkably similar behaviour, where fleeting discontinuities occur at points when magnetisation changes significantly. The magnetocatalytic experiments reported in this thesis constitute a preliminary exploration of magnetocatalytic effects, and in light of the highly encouraging results, further research in this area certainly warrants consideration.

In summary, the soundness and utility of the shell-core model have been reliably demonstrated. In terms of future potential, MoO_x/Fe_2O_3 catalysts have been sufficiently explored, but for the final question regarding the active site at the surface. Since MoO_x/Fe_2O_3 represents the surface layers of the iron molybdate industrial catalyst, the active site of MoO_x/Fe_2O_3 will strongly reflect the active site of iron molybdate. If this can be conclusively determined, it may then be possible to reverse-engineer the structural moieties responsible for formaldehyde selectivity to understand how cutting-edge catalysts might be improved. Given the environmental impetus to reduce the emissions from chemical industry, even small improvements to an industrial catalyst can provide significant benefits.

In terms of alternative shell-core catalysts, there are many potential candidates for shell materials. For example, VO_x/Fe_2O_3 catalysts have been shown to achieve the structural segregation required in a shell-core catalyst, but the precise identity of the active site in VO_x/Fe_2O_3 remains to be determined. Moreover, thus far, VO_x/Fe_2O_3 catalysts have only been investigated in the context of methanol oxidation, as this permitted a fair comparison of VO_x/Fe_2O_3 with MoO_x/Fe_2O_3; however, vanadium oxides are not employed in methanol selective oxidation, but instead in other oxidative processes, e.g. propane ODH. It would be wholly worthwhile to assess the abilities of VO_x/Fe_2O_3 catalysts in reactions to which they might be better suited.

Since the Tamman temperature is now known to be a critical factor in the determining whether a metal oxide will achieve the necessary shell-core segregation, it has become slightly easier to screen for potential candidates. By selecting only those metal oxides whose Tamman temperatures are below or near the 500°C calcination temperature, the risk of failing to produce a properly segregated shell-core catalyst is minimised. For example, WO_3 has a Tamman temperature of 590°C, but might be sufficiently mobile at

500°C to achieve shell-core segregation. Alternatively, calcination temperature could be increased, though with an elevated risk of catalyst sintering.

In all cases, whether investigating the shell, the core or both, the *sine qua non* of all shell-core catalysts is the successful segregation of shell and core components. This is the main strength of shell-core model catalysts, since it enables the use of powerful analytical techniques like XAS to understand the surfaces of the bulk catalysts represented by the shell-core model systems. It is, however, also the main weakness. The techniques used throughout this thesis to gauge segregation require a fundamental difference in reactivity between the shell and core component to gauge whether the core is appropriately isolated. Where this is not the case, the degree of segregation cannot be determined. If structural segregation cannot be confirmed, the crucial advantage of the shell-core model is lost.

So far, only single component shells have been investigated; it is worth pursuing whether a multicomponent shell is achievable, since such catalysts could potentially display the beneficial properties of two metal oxides in combination. This could, however, introduce an additional structural challenge. With two shell materials present, it cannot be assumed that they would mix evenly to form a mixed shell; indeed, one might expect that the materials form two single component layers in a stack instead. Whatever the next avenue of research in this topic, it will be well served by the body of knowledge developed throughout this thesis.

Appendix A

Supplementary reactor data

Throughout this thesis, pulsed-flow reaction data have been presented in converted form, i.e. after the resolution of spectral overlaps, calculation of peak integrals and data processing. The resulting processed figures display product selectivity and methanol conversion against sample temperature: these graphs are markedly more useful than unprocessed mass spectra, the comprehension of which is nontrivial. This appendix contains the unprocessed counterparts to the PFR data mentioned in the main thesis. For reference, MS cracking patterns are detailed again below:

Table A.1: MS cracking patterns.

Substance	Cracking fractions (Abundance ‰)
Hydrogen	2 (1000), 1 (21)
Water	18 (1000), 17 (211), 16 (9), 19 (5), 20 (3)
Carbon monoxide	28 (1000), 12 (47), 16 (17), 29 (12), 14 (8), 30 (2), 13 (1)
Formaldehyde	29 (1000), 30 (885), 28 (309), 14 (44), 13 (43), 12 (33), 31 (19), 17 (14)
Methanol	31 (1000), 32 (717), 29 (421), 28 (90), 30 (78), 33 (11), 27 (5)
Oxygen	32 (1000), 16 (36)
Carbon dioxide	44 (1000), 16 (94), 28 (82), 12 (67)
Dimethyl ether	45 (1000), 29 (390), 15 (240), 31 (30), 43 (10), 30 (10), 28 (9), 44 (6)

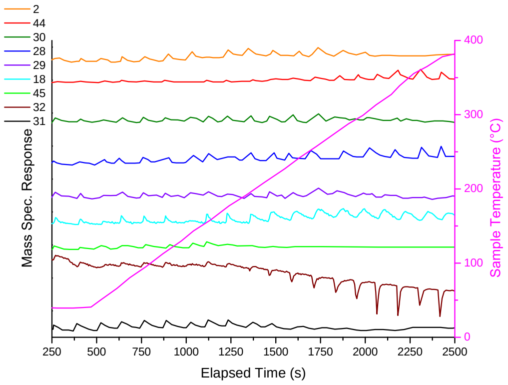

Figure A.1: Unprocessed PFR mass spectra for 1 ML VO_x/Fe_2O_3.

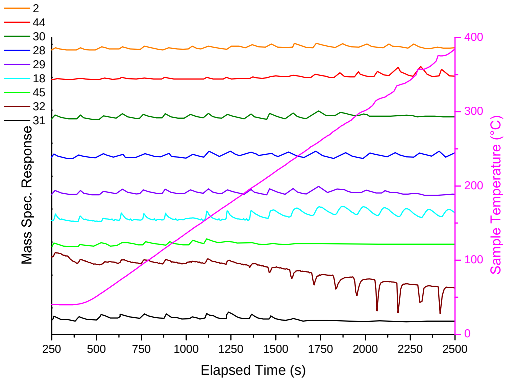

Figure A.2: Unprocessed PFR mass spectra for 3 ML VO_x/Fe_2O_3.

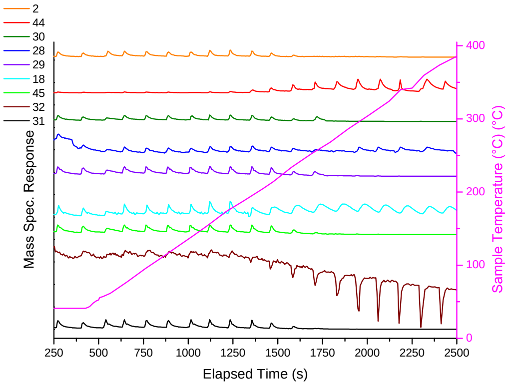

Figure A.3: Unprocessed PFR mass spectra for 1 ML NbO_x/Fe_2O_3.

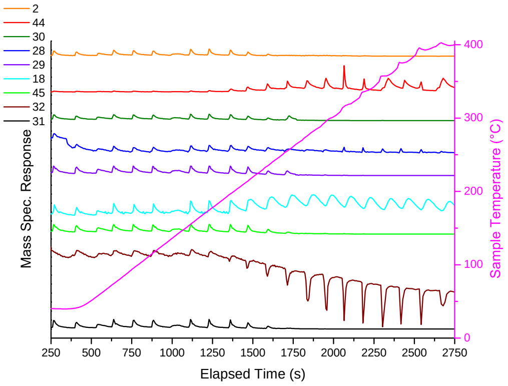

Figure A.4: Unprocessed PFR mass spectra for 3 ML NbO_x/Fe_2O_3.

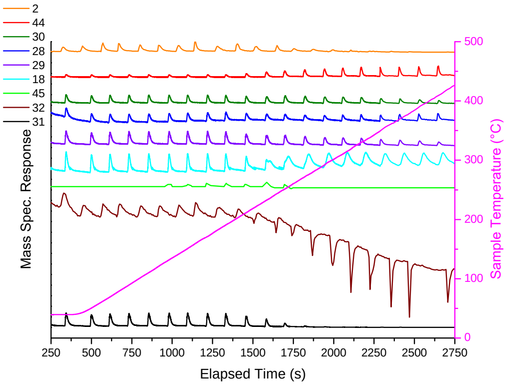

Figure A.5: Unprocessed PFR mass spectra for 3 ML MoO_x/5% HSA Fe_2O_3.

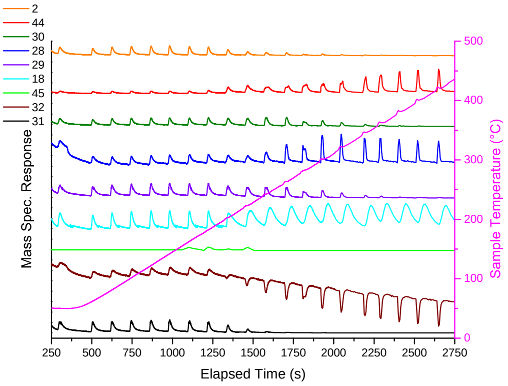

Figure A.6: Unprocessed PFR mass spectra for 3 ML MoO_x/10% HSA Fe_2O_3.

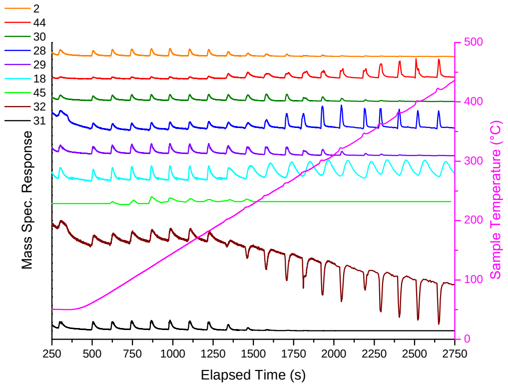

Figure A.7: Unprocessed PFR mass spectra for 3 ML MoO_x/15% HSA Fe_2O_3.

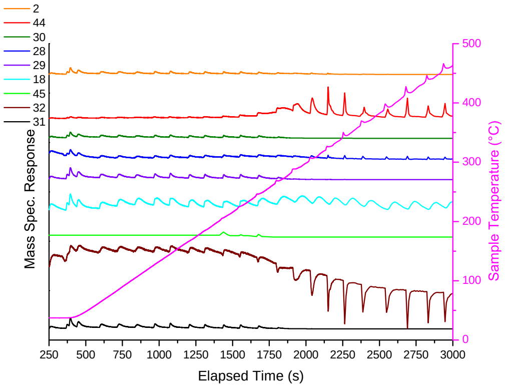

Figure A.8: Unprocessed PFR mass spectra for 3 ML MoO_x/20% HSA Fe_2O_3.

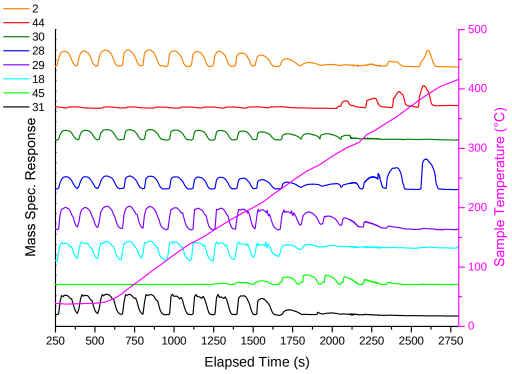

Figure A.9: Unprocessed PFR mass spectra for 6 ML MoO_x/0.35 ZnCoFe.

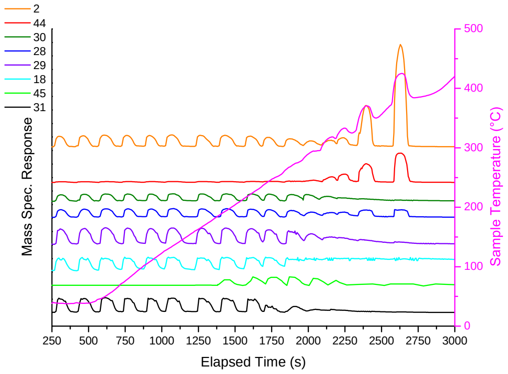

Figure A.10: Unprocessed PFR mass spectra for 6 ML MoO$_x$/0.4 ZnCoFe.

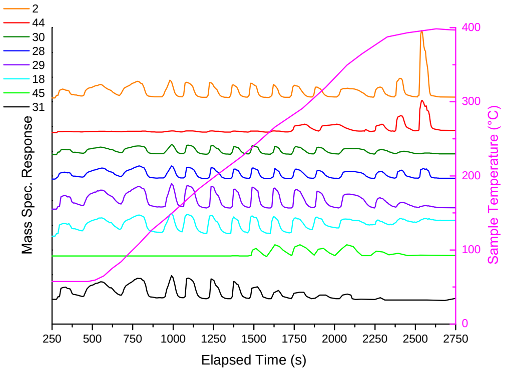

Figure A.11: Unprocessed PFR mass spectra for 6 ML MoO$_x$/0.45 ZnCoFe.

A.0.1 Processing Pulsed Flow Reaction data

This section provides a short walkthrough of the data processing undertaken in this thesis to convert sets of raw PFR data (as would be obtained directly from a mass spectrometer) into the more useful format, wherein selectivity and conversion are displayed against temperature. An example case, using PFR data from Chapter 4 concerning 15% HSA Fe_2O_3, is used below to illustrate the process. Importantly, this is only a brief primer and is tailored towards analysing the selective oxidation of methanol to formaldehyde; for other reactions, this technique may not be appropriate (as detailed in point ii). Four main steps are involved to process PFR data, which are:

(i) Preliminary data sorting;

(ii) Resolution of spectral overlaps;

(iii) Calculation of peak integrals; and

(iv) Computation of selectivity and conversion.

i) Preliminary data sorting

The mass spectrometers used in the experiments reported in this thesis were of MID-type. These require the user to pre-define the masses of interest, which the spectrometer will then monitor. The total number of masses measurable simultaneously differs between different models of mass spectrometer, but in the case of the Hiden CATLAB system, up to 16 masses could be monitored at one time.

After an experiment, mass spectral data can be retrieved and plotted. For the purposes of this guide, Origin graphing software has been used. Other software, such as Microsoft Excel, can be used, but the design of Origin is well suited for the mathematical processing discussed herein. A plot of the masses against time can be prepared without any processing (e.g. Figure A.12 below, which also displays temperature as a function of time), but depending on the software used to control the mass spectrometer, it can be necessary to collate several separate measurement files to produce a general plot.

To those familiar with mass spectra and the products formed in the experiment in question, such a plot already provides significant information. For those unfamiliar with mass spectra and the reaction in question, however, such a figure is difficult to understand. To resolve this, the data can be presented in a more intuitive form.

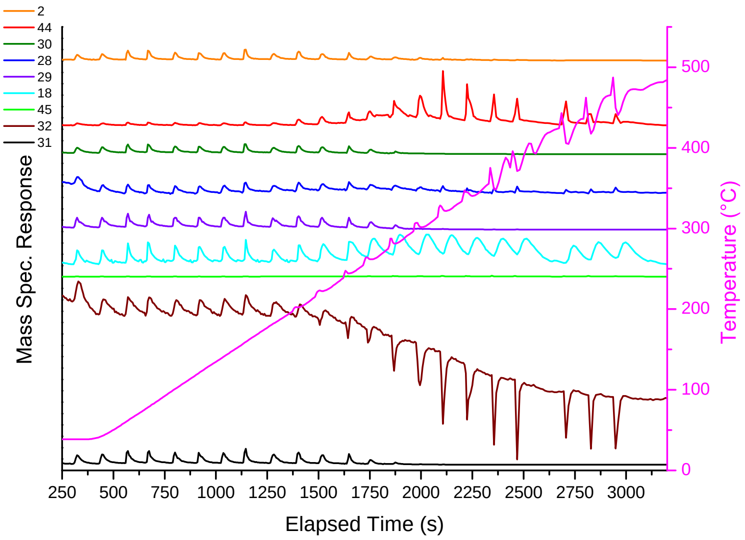

Figure A.12: Unprocessed PFR mass spectra from 15% HSA Fe_2O_3. Gas flow: 30 mL/min 10% O_2 in He. Sample mass: 200 mg.

ii) Resolution of spectral overlaps

It is vital to remember that mass spectral measurements of individual masses are not measuring compounds directly. It is normally the case that spectral overlaps will be present, and accordingly certain masses will be contributed to by more than one species present in the reaction mixture. Some mass spectrometers are capable of reporting the signal from substances, and not from individual masses. In other words, the mass spectrometer can perform the first two stages of the processing detailed in this appendix. For the purposes of these studies, however, no such conversion was performed by the spectrometer.

Using Table A.1 above, or ideally the precise cracking patterns as produced by an individual mass spectrometer, deciphering of the mass spectra can begin. As a demonstration, consider methanol. Methanol has its major peak at mass 31. It also produces cracking fragments at other masses, and the contributions to these other peaks are relative to the size of the major peak at mass 31. The magnitudes of contributions to other masses are expressed as percentages of the major 31 peak. In addition to mass 31, methanol generates peaks at 32 (71.7% the size of the 31 peak); 29 (42.1% the size of the 31 peak); 28 (9.0% the size of the 31 peak); and 30 (7.8% the size of the 31 peak). There are additional fragments, e.g. at 33 and 27, but these are at most 1% the size of the 31 peak, and are therefore insignificant for this processing. In this case, no other reaction product has a significant peak at mass 31. To deconvolute spectral overlaps, there must be at least one unique peak available for each substance (though it need not be the major peak). The total amount of methanol is therefore relatively simple to calculate, by summing the mass 31 peak with (71.7%*Mass 31 size) of the coincident mass 32 signal, (42.1%*Mass 31 size) of the coincident mass 28 signal, and so on.

Another method must be employed when the major peak of a substance is not unique. For example, CO has its major peak at mass 28, with no other significant cracking peaks. In this reaction, methanol, formaldehyde and CO_2 all contribute significant cracking peaks at mass 28. Therefore, the total contribution to the mass 28 peak of CO, m_{CO}, is:

$$m_{\mathrm{CO}} = m_{28} - m_{\mathrm{FA}} - m_{\mathrm{MeOH}} - m_{\mathrm{CO_2}} \tag{A.1}$$

where m_{28} is the mass 28 signal, m_{FA} is the contribution thereto of formaldehyde (30.9% the size of the coincident mass 29 peak), m_{MeOH} is the contribution thereto of methanol (9.0% the size of the coincident mass 31 peak) and $m_{\mathrm{CO_2}}$ is the contribution thereto of CO_2 (8.2% the size of the coincident mass 44 peak).

In summary, either by using a substance with a unique major peak and working through its cracking fragments, or by using a substance with a unique cracking fragment mass and working backwards to its shared major peak, spectral overlaps can be resolved. It can sometimes be necessary to work both forwards from a major peak and backwards from a cracking fragment to a major peak and several iterations may be required to resolve all masses.

Methanol and CO represent examples of the two approaches used to deconvolute mass spectra, but the same overall methodology detailed above can be employed for all substances present to calculate the total mass spectral contribution from each substance, as opposed to each mass. For the selective oxidation of methanol, this process is not unduly difficult; for more complicated reactions, e.g. those involving many different species without unique peaks, this process can be extremely difficult.

iii) Calculation of peak integrals

Having resolved the mass spectra, the data will now appear as a series of pulses corresponding to particular species in the reaction, e.g. methanol, formaldehyde, CO_2, etc. The relative quantities of each substance present are obtained by calculating the area under each peak, namely by integration. The integration limits are fairly simple for PFR data: since each pulse is discrete, being clearly defined by each manual injection of methanol, the edges of the pulse as they appear can be taken to provide the limits between which to integrate (Figure A.13). Sensible selection of the baseline during integration is essential for valid comparison of quantities of the species present. The approach adopted for the studies reported in this thesis was to use the baseline mass spectral signal for each component, i.e. the signal read by the spectrometer over a prolonged period with no methanol added. The ideal time to measure this baseline is at the start of the experiment, where a delay period can establish good background conditions.

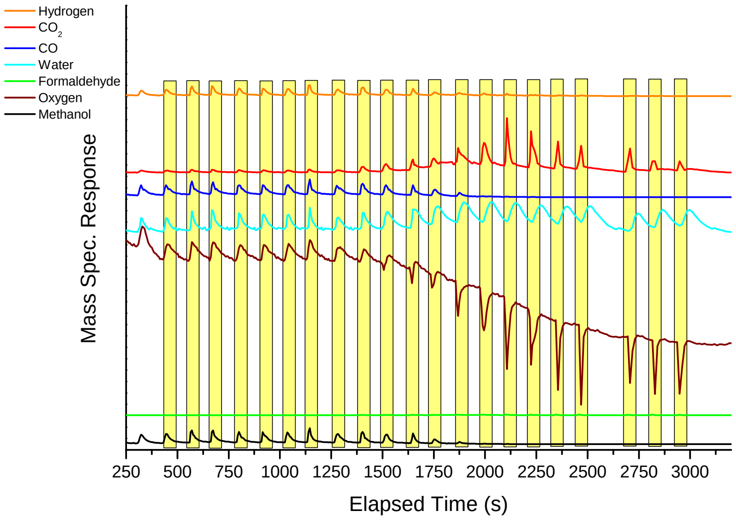

Figure A.13: PFR data from 15% HSA Fe_2O_3 ready for peak integration: the data have been processed to resolve spectral overlaps. The width over which integration is to be performed for each peak is marked in yellow.

The “Peak Analyser” tool of graphing software Origin was used to perform the integration of the data, though it can also perform a range of other mathematical analytical methods. Running this tool on a set of peaks (as shown ready for integration in Figure A.13) yields a numerical value for the area under each peak for each substance.

iv) Computation of selectivity and conversion

The calculated integral values can then be used to calculate product selectivity and methanol conversion for each injection. Methanol conversion can be determined relatively easily by comparing the amount of methanol present at that pulse with the amount of methanol present at zero conversion. For PFR studies in this thesis, zero conversion was taken to be the maximum quantity of methanol present before the heating phase commenced. Expressed mathematically, the quantity of methanol conversion at time t is determined by:

$$X_i = 100 - \left(\frac{n_t}{n_{\text{unreacted}}}\right) \times 100 \tag{A.2}$$

where X_i is conversion expressed as a percentage, n_t is the integral of the methanol pulse at a time t during the reaction and $n_{\text{unreacted}}$ is the integral of the methanol pulse at low temperature with no conversion.

The integral values can also be used to calculate product selectivity at each pulse using the following method:

$$S_p = \left(\frac{S_d}{\sum_i S_i} \right) \times 100 \tag{A.3}$$

where S_p is the selectivity of product p, S_d is the mass spectral integral of the desired species d and $\sum_i S_i$ is the sum of the integrals of all products.

The yield of the reaction can be determined by combining conversion and selectivity thus:

$$Y_p = X_i S_p \tag{A.4}$$

where Y_p is the overall yield of the reaction expressed as a percentage.

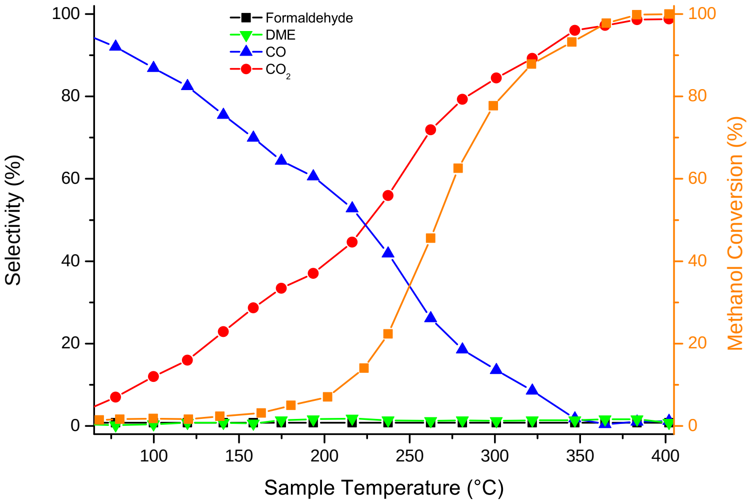

Figure A.14: Processed PFR data from 15% HSA Fe_2O_3. Methanol conversion is on the right-hand y-axis.

The net result, starting from the data displayed in Figure A.12, is displayed in Figure A.14, revealing catalytic selectivity and methanol conversion as functions of temperature (or elapsed time as preferred) on the same graph. This graphical presentation forms a useful way to visualise the data and is better suited to a non-specialist audience than raw mass spectral data, assisting interpretation and discussion.